

MOMENTUM TRANSPORT: INTRINSIC ROTATION AND ZONAL FLOWS IN MICROTURBULENCE IN TOKAMAKS

By
Rameswar Singh

INSTITUTE FOR PLASMA RESEARCH, GUJARAT.

A thesis submitted to the
Board of Studies in Physical Sciences

In partial fulfillment of the requirements

For the Degree of

DOCTOR OF PHILOSOPHY

of

HOMI BHABHA NATIONAL INSTITUTE



December 2012



Homi Bhabha National Institute

Programme: Ph.D.

Board of Studies in PHYSICAL Sciences

1. Name of the Constituent Institution: <u>INSTITUTE FOR PLASMA RESEARCH</u>			
2. Name of the Student:		<u>RAMESWAR SINGH</u>	
3. Enrolment Number:		<u>PHYS 06200704018</u>	
4. Date of Enrolment in HBNI:		<u>12 SEPTEMBER 2007</u>	
5. Date of Submission of Thesis:		<u>14 DECEMBER 2012</u>	
6. Title of the Thesis:		<u>MOMENTUM TRANSPORT, INTRINSIC ROTATION AND ZONAL FLOWS IN MICROTURBULENCE IN TOKAMAKS</u>	
7. Composition of the Doctoral Committee:			
Sr No	Composition	Designation in HBNI	Name
a.	Chairman	SENIOR PROF.	PROF. P. K. KAW
b.	Convener (Guide)	ASSO. PROF.	PROF. R. SINGH
c.	Co-Guide, if any	—	—
d.	Member	ASST. PROF.	DR. R. GANESH
e.	Member	ASST. PROF.	DR. R. SRINIVASAN
f.	The Technology Adviser, if any	Invitee	—
8. Number of Doctoral Committee Meetings held with respective dates: <u>2nd yr - 26/3/10;</u> <u>3rd yr - 26/9/10</u> <u>4th yr - 27/9/11;</u> <u>5th yr + synopsis - 25/7/12</u>			
9. Name and Organization of the Examiner 1: <u>PROF. NIKHIL CHAKRABARTI</u> <u>SAHA INSTITUTE OF NUCLEAR PHYSICS</u> <u>(KOLIKATA)</u> Recommendations of the Examiner 1 (Thesis Evaluation) <u>(i) accepted</u> , (ii) accepted after revisions, or (iii) rejected:			
10. Name and Organization of the Examiner 2: <u>PROF. AVINASH KHARE</u> <u>DELHI UNIVERSITY (NEW DELHI)</u> Recommendations of the Examiner 2 (Thesis Evaluation) <u>(i) accepted</u> , (ii) accepted after revisions, or (iii) rejected:			

Name & Signature of Dean-Academic, CI:

S. Mukherjee
(Dr. S. Mukherjee)

Recommendations of the Viva Voce Board

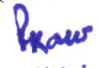
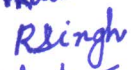



1. Date of Viva Voce Examination: 12 SEPTEMBER 2013
2. Recommendations for the award of the Ph.D. degree: Recommended / Not Recommended
(If Recommended, give summary of main findings and overall quality of thesis)
(If Not Recommended, give reasons for not recommending and guidelines to be communicated by Convener of the Doctoral committee to the student for further work)

I attended the viva-voce exam of Mr. Rameswar Singh which was held in L.P.R. on 12/9/2013. The presentation by Mr. Singh was lucid, clear and succinct. The thesis work is on the generation of toroidal and poloidal flows examined in slab and toroidal geometry using fluid and gyrokinetic model. This work uses extensive analytical and numerical procedures. Specifically the role of K_{\perp} parallel symmetry breaking and the effect of residual stress on generation of toroidal and poloidal flows (which is of significance for transport in fusion devices) has been clearly elucidated. I find this work to be relevant to the present state of fusion research and therefore I recommend it for the award of Ph.D. degree.

In case Not Recommended, another date will be fixed by the Dean-Academic, CI, which shall not be earlier than a month after and not later than six months from the date of first viva.

Date:

Name and Signature of the Viva Voce Board (Doctoral Committee and External Examiner):

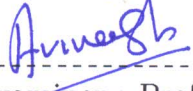
PROF. P. K. KAW	—	
PROF. R. SINGH	—	
DR. R. GANESH	—	
DR. R. SRINIVASAN	—	
PROF. A. KHARE	—	

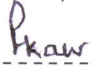
(External Examiner)

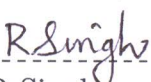
Homi Bhabha National Institute

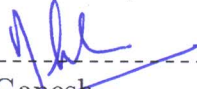
Recommendations of the Viva Voce Board

As members of the Viva Voce Board, we recommend that the dissertation prepared by **Rameswar Singh** entitled "Momentum Transport: Intrinsic Rotation and Zonal Flows in Microturbulence in Tokamaks" may be accepted as fulfilling the dissertation requirement for the Degree of Doctor of Philosophy.


----- Date :12/09/2013
External Examiner : Prof. Avinash Khare
Delhi University, Delhi, India


----- Date :12/09/2013
Chairman : Prof. P K Kaw
Institute For Plasma Research
Bhat, Gandhinagar-382428, India

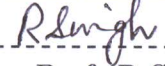

----- Date :12/09/2013
Convener : Prof. R Singh
Institute For Plasma Research
Bhat, Gandhinagar-382428, India


----- Date :12/09/2013
Member : Dr. R Ganesh
Institute For Plasma Research
Bhat, Gandhinagar-382428, India


----- Date :12/09/2013
Member : Dr. R Srinivasan
Institute For Plasma Research
Bhat, Gandhinagar-382428, India

Final approval and acceptance of this dissertation is contingent upon the candidate's submission of the final copies of the dissertation to HBNI.

I hereby certify that I have read this dissertation prepared under my direction and recommend that it may be accepted as fulfilling the dissertation requirement.


----- Date :12/09/2013
Guide : Prof. R Singh
Institute For Plasma Research, Bhat, Gandhinagar-382428, Gujarat, India



Homi Bhabha National Institute

Ph.D. Thesis Evaluation Report

1. Name of the Constituent Institution: Institute for Plasma Research
2. Name of the Student: Rameswar Singh
3. Enrolment No. : PHYS 06200704018
4. Title of the Thesis: Momentum transport: Intrinsic rotation and zonal
5. Board of Studies: Physical Sciences

Recommendations

Tick one of the following:

1. The thesis in its present form is commended for the award of the Ph.D. Degree. ☒
2. The thesis is commended for the award of the Ph.D. degree. However, my suggestions for improving the thesis may be considered at the time of the viva voce examination and if the viva voce board deems it appropriate, the same may be incorporated in the thesis based on the discussions during the viva voce examination. The revised thesis need not be sent to me. ☐
3. The thesis should be revised as per the suggestions enclosed. I would like to see the revised thesis incorporating my suggestions before I give further recommendations. ☐
4. The thesis is not acceptable for the award of the Ph.D. degree. ☐

(Signature):

Name of Examiner: Nikhil Chakrabarti

Date: 7th March, 2013

Please give your detailed report in the attached sheet. You may use additional sheets, if required.

(Nikhil Chakrabarti)
Professor, Plasma
Physics Division

Saha Institute of Nuclear Physics
1/AF, Bidhannagar, Kolkata-64

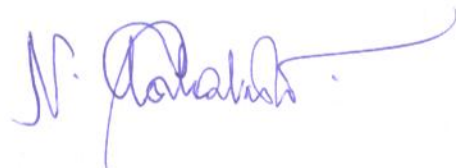
1. Name of the student: Rameswar Singh
 2. Enrolment No. : PHYS 06200704018
 3. Title of the Thesis: Momentum Transport: Intrinsic rotation and Zonal flows in microturbulence in Tokamaks.
 4. Board of Studies: Physical Sciences.
-

Detailed Report

I have read the above mentioned thesis which presents several important issues to characterized the magnetized plasma turbulence in light of flow generation. This thesis presents some original work and in general has been clearly written. The author is careful enough in implementation of ideas and to derive some new and interesting results.

In this thesis, systematic calculations of radial fluxes of turbulent momentum due to the slab ITG mode in the presence of a shear velocity are presented. In presence of these sheared flows the author showed that the eigenfunction is shifted off the mode-rational surface, leading to the symmetry breaking. It has been demonstrated that the poloidal shear flow contributes to toroidal non-diffusive residual flux. As a result the toroidal flow accumulates with the diffusive component which modifies the turbulent viscosity. The identification of toroidal momentum source is a good contribution of this work. Also the toroidal and poloidal shear flow coupling in the radial force balance equation is an interesting finding. The toroidal flow generation does not require shear electric field which seems to be a novel result.

In normal drift wave ordering the polarization drift convection of equilibrium density is normally ignored as compared to $\mathbf{E} \times \mathbf{B}$ convection of equilibrium density. In this thesis importance of such term has been demonstrated. It has been argued that the term which has been considered subdominant may now lead to the formation of residual parallel Reynolds stress due to the finite ρ_s^* driven parallel symmetry breaking. The other important contribution is that in the region of steep density gradient, ρ_s^* effect breaks the reflectional symmetry of the eigenfunction even without radial electric field shear in contrast to the usual belief.



Flux tube simulation of linear ITG mode in presence of finite ballooning angle has been carefully studied. It has been shown that zero ballooning angle is not the maximally growing mode at high wave number region which generates an important question to investigate the cause for the further analysis. Nonlinear simulation with mean $\mathbf{E} \times \mathbf{B}$ shear indicating an intimate relation between heat flux with zonal flow is also an important conclusion.

Electromagnetic toroidal ITG mode and Zonal flow studies is a good piece of work. The nonlinear dispersion relation for the zonal flow is quite instructive. Coupling between poloidal and toroidal zonal flow is very interesting. The self consistent flow fluctuation theory and its application to L-H transition phenomena is similar to the modulational instability mechanism where ITG mode behaves like a pump wave. The work is complete interesting and has practical application in tokamak plasmas.

In my opinion this thesis not only addresses some problems and their solutions but also opens up various questions which is also significant to study further.

In summary, according to me the work presented in this thesis is fully adequate in scope and in quality, as a dissertation for the degree of Doctor of Philosophy (Ph.D.).


March 07, 2013
Nikhil Chakrabarti

(Nikhil Chakrabarti)
Professor, Plasma
Physics Division

Saha Institute of Nuclear Physics
1/AF, Bidhannagar, Kolkata-64

I have some suggestions/ questions for my own understanding and to improve the quality of the thesis.

In general writing mathematical symbol in the running text one must avoid frac command in Latex it looks ugly. The figure legend sometimes not as clear as it is expected.

1. The clarification between Zonal flow and shear flow is not adequate for a reader who is not familiar before.
2. In Eq. (2.16) page 17, there is a typographical error, it will be ∇_y
3. The electromagnetic effect on zonal flow is not illustrated as compared to the electrostatic one.
4. Please see if Eq. (3.39) is dimensionally correct?
5. Chapter 1 page 2 ,.....which are known as (one typo). Also in the same line GAM is introduced without reference.
6. In page 18, while approximating Eq. (2.22) it has been assumed that the mode frequency higher than shearing rate i.e. $\omega \gg V_E'$. Nothing is said about magnetic shear. Since the mode structure is determined by the magnetic shear parameter. Probably a little elaboration may be required.
7. With so much work about the momentum transport, are we at the point where we can start to use this knowledge to change the flow profile as desired? If not, what are the missing ingredients?
8. In Eq. (6.31) can we take $k_{x0} = 0$? In Eq. (6.32) there is no reflection of k_{x0} , why it is needed?
9. Is there any mechanism by which we can have an estimate of the radial scale of zonal flow q_x ?
10. In the background ITG mode when one is estimating the zonal flow growth rate, how can we ensure there is no linear ITG mode growth rate is mixed with this. Since linear ITG mode itself is a growing mode there is a possibility of co-existence of linear ITG as well as shear flow mode.



(Nikhil Chakrabarti)
Professor, Plasma
Physics Division

Saha Institute of Nuclear Physics
1/AF, Bidhannagar, Kolkata-64



Homi Bhabha National Institute

Ph.D. Thesis Evaluation Report

1. **Name of the Constituent Institution:** Institute for Plasma Research
2. **Name of the Student:** Rameswar Singh
3. **Enrolment No. :** PHYS 06200704018
4. **Title of the Thesis:** Momentum transport: Intrinsic rotation and zonal
5. **Board of Studies:** Physical Sciences

Recommendations

Tick one of the following:

1. The thesis in its present form is commended for the award of the Ph.D. Degree. ☒
2. The thesis is commended for the award of the Ph.D. degree. However, my suggestions for improving the thesis may be considered at the time of the viva voce examination and if the viva voce board deems it appropriate, the same may be incorporated in the thesis based on the discussions during the viva voce examination. The revised thesis need not be sent to me. ☐
3. The thesis should be revised as per the suggestions enclosed. I would like to see the revised thesis incorporating my suggestions before I give further recommendations. ☐
4. The thesis is not acceptable for the award of the Ph.D. degree. ☐

(Signature): ~~Your Signature~~ 

Name of Examiner: Prof Avinash Khare

Date: 20/4/2013

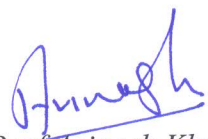
Please give your detailed report in the attached sheet. You may use additional sheets, if required.

1. **Name of the Student:** Rameswar Singh
2. **Enrolment No.:** PHYS 06200704018
3. **Title of the Thesis:** Momentum transport: Intrinsic rotation and zonal
4. **Board of Studies:** Physical Sciences

DETAILED REPORT

Write your comments, if any.

[you can type or insert text box here] Please see the attached document


Name of Examiner: *Prof Avinash Khare*

Signature and Date: 20/4/2013

Detailed report on the thesis of Mr. Rameshwar Singh

I think Mr Singh, in this thesis, has dealt with certain very important aspects of self-consistent dynamics of micro-turbulence and mesoscopic and macroscopic flows. The calculations presented in the thesis are consistent and correct. The results of the thesis are relevant to modern day tokamak research and will definitely lead to further work and extensions. I congratulate Mr Singh and Prof Singh on this excellent task. My detailed comments are as follows

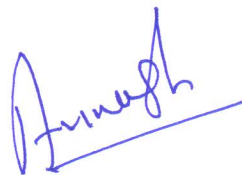
In this thesis Mr Singh has presented several important and interesting aspects of micro-turbulence driven flows in magnetized tokamak plasmas. Specifically he has talked about two types of self-driven flows by ITG turbulence viz., 'intrinsic rotation' and zonal flows.

He has presented careful calculations of radial fluxes of the toroidal and the poloidal momentum and has demonstrated the existence of the residual momentum flux due to the generation of intrinsic rotation. In normal shear configuration, the k_{\parallel} symmetry breaking has been shown to cause a residual parallel momentum flux and the k_r symmetry breaking has been shown to cause a residual poloidal momentum flux. The toroidal and the poloidal momentum fluxes have been shown to be coupled via radial force balance. The macroscopic $E \times B$ shear at leading order and strong density gradients at higher order have been shown to cause k_{\parallel} symmetry breaking by shifting the eigen-mode structure off the rational surface. Comparative study of the density gradient driven momentum flux with other candidates is quite interesting.

Mr. Singh has also extended above described normal shear calculations to reverse shear configuration. This I think is an important extension. Particularly the generation of residual parallel momentum flux by the symmetric eigen-function at q_{\min} qualitatively explains generation of the spontaneous flows.

The thesis also contains important results from the gyrokinetic flux tube simulation of finite ballooning angle effects on the toroidal ITG mode. The growth rate is maximum at ballooning angles other than zero leading to the formation of a short wavelength branch. This has been shown to have important effects on the momentum and the heat transport. Correlation studies among heat flux, momentum flux and the self-consistent zonal flow shear is an important piece of work.

In the study of the electromagnetic effects on the zonal flow generation in toroidal ITG turbulence the competition between the Reynold and the Maxwell stresses producing different behaviour of the ratio of the zonal flow growth rate to the ITG growth rate with respect to plasma beta near and away from marginality has been highlighted. The results obtained are consistent with the observations of the increased nonlinear Dimits upshift of the critical temperature gradient with increasing beta.



It has been shown that the toroidal zonal flow shear and the conventional poloidal zonal flow shear get simultaneously excited via modulational instability. Their dynamics has been shown to be coupled in general when k_{\parallel} symmetry is broken. The effects of the poloidal and the toroidal zonal flow shear on the transient dynamics of L to H transition also been presented.

In the last part of the thesis the author has elegantly investigated stationary solutions of the electrostatic toroidal ITG and poloidal zonal flow systems. Formation of coherent nonlinear structures such as soliton, shocks in the zonal flow field due to trapping of quasi-particles in the effective potential formed by the zonal flow field has been demonstrated..

The contents of the thesis are adequate in scope and quality to be considered as a dissertation for the award of Doctor of Philosophy. I recommend it for the award of PhD degree.

Prof Avinash Khare

20 Apr. 2013




STATEMENT BY AUTHOR

This dissertation has been submitted in partial fulfillment of requirements for an advanced degree at Homi Bhabha National Institute (HBNI) and is deposited in the Library to be made available to borrowers under rules of the HBNI.

Brief quotations from this dissertation are allowable without special permission, provided that accurate acknowledgement of source is made. Requests for permission for extended quotation from or reproduction of this manuscript in whole or in part may be granted by the Competent Authority of HBNI when in his or her judgment the proposed use of the material is in the interests of scholarship. In all other instances, however, permission must be obtained from the author.

Date: 12/09/2013


Rameswar Singh

DECLARATION

I, hereby declare that the investigation presented in the thesis has been carried out by me. The work is original and the work has not been submitted earlier as a whole or in part for a degree/diploma at this or any other Institution or University.


Date: 12/09/2013

Rameswar Singh
Rameswar Singh

CERTIFICATION FROM GUIDE

This is to certify that the corrections as suggested by the Referees in the thesis evaluation report have been incorporated in the copy of the thesis submitted to HBNI.

Date: 12/09/2013


Guide: Prof. R Singh

.....*to my parents*

ACKNOWLEDGEMENTS

Foremost, I would like to express my sincere gratitude to my advisor Prof. R Singh. His continuous support and guidance had been inspiring. His enthusiasm and friendly nature had made this journey possible. I really appreciate his tolerance for listening and answering to my every childlike questions during the initial days of my work. I am also thankful to him for providing me enough independence during this work and involving me in some fruitful collaborations.

I am grateful to Dr. R Ganesh, Dr. R Srinivasan and Prof. P Kaw for being my doctoral committee members. Their comments during my reviews had been quite helpful in improving this work. Discussions with Prof. Kaw had always been enlightening.

I am extremely thankful to Dr. R Ganesh for involving me in collaboration on gyrokinetic simulations with Dr S Brunner and Prof. F Jenko. I am truly indebted and thankful to Dr S Brunner who helped me in learning the gyrokinetic turbulence code GENE with extreme patience during my stay at CRPP-EPFL. Many thanks to Prof. F Jenko and his group from IPP, Garching for fruitful discussions through videoconferencing. I appreciate numerous helps of Edith Grueter, Daniel Brunetti and T Bogdan during my stay at CRPP-EPFL.

I am thankful to Dr. Ö D Gürçan, Prof. P H Diamond, Dr. J Anderson, Prof. H Nordman, Dr. N Bisai, Prof. A Sen and Prof. P Kaw for collaboration on various topics that are included in this thesis.

I would like to thank Dr. P Chattopadhyay, Dr. S K Pathak, Dr. S Sengupta, Dr. D Raju, Dr. M Warriar, Dr. S Pradhan, Dr. H Joshi, Dr. R Srinivasan, Dr. R Ganesh, Dr. N Ramsubramaniam, Dr. Joydeep Ghos, Dr. Asim, Dr. Devendra Sharma, Dr. R Goswami, Dr. S Mukherji, Prof. A Das and Prof. R Jha for their endurance while teaching us during the 1st year course. Many thanks to Prof. A Sen for guiding me during my pre-doctoral project work.

Thanks to Dr. L M Awasthi, Amulya Sanyasi and Pankaj Srivastava for being friendly and helpful towards me on various occasions.

Thanks to the library, computer and administrative staff of IPR for being always cooperative. I thank Mr. Saroj Das, Mr. Shravan Kumar, Ms. Smita Parmar, Mrs. Arundhati Das, Mrs. Pragya Pathak, Mrs. Sutapa Ranjan, Mr. Shailendra Trivedi, Mr. Arvind Singh, Mr. Hemant Joshi, Mr. Gaurav Garg, Mr. Govind Lokhande, Mr. M Sourabhan, Mr. M. H. Vartak, Mr. H. K. Sharma, Mr. H. C. Khanduri, Mr. Hitesh Mehta, Mr. Dinesh Nair, Mr. Silel Shah, and Ms. Shirin Bhesania for their helps on numerous occasions.

I enjoyed the friendly hostel life at IPR. Greetings and best wishes to my dear Pintu da, Ritu di, Manash Paul, Rajneesh Yadav, Anand Srivastava, Bhaskar Chaudhary, Anurag Mishra, Vikrant Saxena, Kishore Karatiparambil, Padduvatti N. Maya, Subhas, Sanjay Mishra, Swati Baruah, Ajai, Jugal Chaudhury, Satyanand Kar, Sharad Yadav, Shekhar T. Goud, Sunita Negi, Kshitish Barada, Deepak Sangwan, Vikram Narang, Prabal Singh Verma, Ashwin Joy, Ujjwal Shinha, Sita Sunder, Sushil, Sanat, Pravesh, Partha, Nishant, Sayak, Manjit, Soumen, Aditya, Iliyas, Vikram Jr, Rana, Veda, Sandeep, Zuber, Rupendra, Mangilal, Bibhuparasad, Varaprasad, Harish, Sameer, Neeraj, Deepa, Akanksha, Vidhi, Dushyant, Anup, Arghya, Bhumika, Debraj, Modhuchandran, Narayan, Amit, Rajnarayan, Ratan, Sonu, Surabhi and Umesh.

My batchmates Pravesh, Sanat and Sushil deserve special thanks for always being supportive for me.

I take this opportunity to thank my teachers during my MSc at Gauhati University, especially, Prof. S A S Ahmed and Prof. N. N. Singh for motivating me to pursue higher studies.

Many thanks to my university friends Samiran Chaterji, Abu Mostako, Nabaratna Bhagawati, Sandeep Chaudhury, Mayur Bawari, Shashi Kalita, Chayanika, Parijat Saikia, Liladhar Chauhan, Rongmon Bordoloi whose company always boosted a positive attitude in me.

Thanks a lot again to Pravesh, Aditya and Sushil for spending their valuable time in proofreading the draft.

At last, my heartfelt gratitude to my parents and family for their goodwill and support all through my life.

Date: 12/09/2013

Rameswar Singh
Rameswar Singh

PUBLICATIONS

Thesis:

1. *Intrinsic toroidal and poloidal flow generation in the background of ITG turbulence*, Rameswar Singh, R Ganesh, R Singh, P Kaw and A Sen, Nuclear Fusion **51** 013002 (2011).
2. *Symmetry breaking effect of density gradient on parallel momentum transport: A new ρ_s^* effect*; Rameswar Singh, R Singh, P Kaw, Ö D Gürcan, P H Diamond and H Nordman, Phys. Plasmas **19** 012301 (2012).
3. *Secondary instability of electromagnetic ion-temperature-gradient modes for zonal flow generation*, Johan Anderson, Hans Nordman, Rameswar Singh, Raghvendra Singh, Phys. Plasmas **18**, 072306 (2011).
4. *Parallel momentum transport in the neighbourhood of q_{min} in reverse shear tokamaks*, Rameswar Singh, R Singh, Hogun Jhang, and P H Diamond, Phys. Plasmas 2013 (submitted).
5. *A new paradigm of coupled intrinsic toroidal zonal flow - ITG turbulence - poloidal zonal flow system*, Rameswar Singh, R Singh, P Kaw, Phys. Plasmas (to be submitted).
6. *Coherent structures in ITG-zonal flow system*, Rameswar Singh, R Singh, P Kaw, and P H Diamond, New J. Phys. 2013 (under review).
7. *Finite ballooning angle effects on ion temperature gradient driven mode and associated transports in gyrokinetic flux tube simulations*, Rameswar Singh, S Brunner, R Ganesh and F Jenko, Phys. Plasmas (to be submitted).

Others:

1. *Low-frequency fluctuations in scrape-off layer of tokamak plasma with limiter biasing*, N. Bisai, Rameswar Singh and R. Singh, J. Plasma Physics, Available on CJO 2011, DOI: 10.1017/S0022377811000158

Abstract

Microturbulence driven by equilibrium density and temperature gradients is responsible for cross field transport of particles and energy deteriorating plasma confinement in tokamaks. Mean shear flows tend to reduce energy and particle transport by enhancing the turbulence decorrelation. These flows can be either externally driven or can be self-generated by turbulence. Self-generated flows can appear at macroscopic scale and mesoscopic scale. Intrinsic toroidal and poloidal rotation without external momentum source belong to the first category while zonal flows in poloidal and toroidal direction belong to the second category. Self generated intrinsic rotation and zonal flows can be viewed as different manifestations of momentum transport in turbulence. This thesis deals with certain features of momentum transport in ion temperature gradient (ITG) driven microturbulence leading to generation of intrinsic rotation and zonal flows using mean field theory. Analytical calculations are mostly performed in sheared slab geometry and numerical simulations are performed in local flux tube geometry using the gyrokinetic turbulence code GENE.

Residual stress is identified as a key ingredient of intrinsic rotation drive whether it is toroidal or poloidal. $\langle k_{\parallel} \rangle$ symmetry breaking drives parallel residual stress while $\langle k_r \rangle$ symmetry breaking drives poloidal stress assisted by radial fluctuating $E \times B$ velocity. (Here $\langle k_{\parallel} \rangle$ represents eigenmode averaged wave number parallel to the equilibrium magnetic field and $\langle k_r \rangle$ represents eigenmode averaged wave number in the radial direction.) This $\langle k_{\parallel} \rangle$ symmetry breaking is achieved by mean $E \times B$ shear and density gradient as a higher order ρ_s^* effect via mode shift off the rational surface. (Here $\rho_s^* = \rho_s/L_n$; ρ_s being ion sound radius and L_n being ion density gradient scale length.) Poloidal residual stress by $\langle k_r \rangle$ symmetry breaking requires mean parallel flow shear. This leads to coupling of parallel and poloidal momentum fluxes and hence of intrinsic toroidal and poloidal rotations. In reverse shear tokamak with non-monotonic safety factor q , $\langle k_{\parallel} \rangle$ symmetry breaking does not require asymmetry of the eigenmode at the minimum of q due to quadratic variation in the poloidal magnetic field there. However the mode symmetry is spontaneously broken due to mean $E \times B$ shear and finite ρ_s^* effects. Polarization drift also drive parallel residual stress at a higher order in ρ_s^* by $\langle k_{\parallel} k_x \rangle$ symmetry breaking which does not require asymmetry of the eigenmode about the rational

surface. However polarization drift fails to drive any poloidal stress. Linear gyrokinetic flux tube simulations show that toroidal ITG instability extend to short wavelength region when growth rates are maximized over all ballooning angles. Finite ballooning angle generates parallel residual momentum flux by breaking the symmetry of the eigenmode about the low field side (LFS) mid plane. Nonlinear simulations with macroscopic $E \times B$ shear show parallel residual momentum flux by symmetry breaking of the eigenmode about the LFS mid plane. $2D$ cross-correlation calculations show some finite spatially local but temporally non-local correlation between momentum flux and root mean square zonal flow shear, but zonal flow shear fails to generate volume averaged parallel momentum flux.

Zonal flow in the poloidal direction is well known to appear as a consequence of modulational instability of the ITG turbulence. Inclusion of electromagnetic effects show that near marginality the ratio of zonal flow growth to ITG mode growth γ_{ZF}/γ_{ITG} increases with β (ratio of thermal pressure to magnetic pressure) whereas for larger η_i , ratio of density and temperature scale lengths, the zonal flow drive reduces due to the competition between Reynolds and Maxwell stresses. Toroidal zonal flows (TZF) get excited via modulational instability similar to poloidal zonal flow (PZF) excitation in ITG turbulence. Toroidal and poloidal zonal flow shears are coupled linearly via non-linear stresses. A $0 - D$ empirical model for time evolution of turbulence intensity, PZF shear, TZF shear, pressure gradient in a input power ramp shows that the input power threshold for L→H transition reduces with PZF→TZF coupling coefficient which depends on $\langle k_{\parallel} \rangle$ symmetry breaking mechanisms. In the strong turbulence regime coherent nonlinear structures like solitons, shocks, nonlinear wave trains appear in poloidal zonal flow field due to Reynolds stresses offered by trapped and untrapped ITG waves.

1	Introduction	1
1.1	Motivation and brief history	1
1.2	Thesis outline	8
2	Intrinsic toroidal and poloidal flow generation in the background of ion temperature gradient turbulence	11
2.1	Introduction	11
2.2	Flow generation and amplification: momentum conservation	14
2.3	Model equations	15
2.4	Momentum flux	20
2.4.1	$E \times B$ Flux	21
2.4.2	Polarization driven flux	24
2.5	Coupled Toroidal and Poloidal Flow Equations	26
2.5.1	Comparison of nondiffusive fluxes	29
2.6	Discussion and conclusions	29
3	Symmetry breaking effects of density gradient on parallel momentum transport: A new ρ_s^* effect	31
3.1	Introduction	31
3.2	Radial Eigenmode Analysis	34
3.3	Momentum flux by Reynolds stresses	39
3.3.1	Comparison with fluxes driven by mean radial electric field shear	41
3.3.2	Comparison with parallel polarization stress/flux	46
3.3.3	Comparison with fluxes driven by turbulence intensity gradient	47
3.4	Results and Discussion	49
4	Momentum transport in the neighborhood of q_{min} in reverse shear tokamak due to ITG turbulence	52
4.1	Introduction	52
4.2	Eigenmode formulation	53
4.3	Eigenmode structures at q_{min}	58

4.3.1	Double mode-rational surface RS-ITG	58
4.3.2	Single mode-rational surface RS-ITG	63
4.3.3	No mode-rational surface or Non-resonant RS-ITG	64
4.4	Momentum flux: General considerations of radial fluxes of parallel and poloidal momentum	67
4.4.1	$E \times B$ Flux	69
4.4.2	Polarization driven flux	71
4.5	Momentum flux in the neighborhood of q -min	72
4.5.1	$E \times B$ flux	72
4.5.2	$E \times B$ Fluxes at q_{min} due to single mode-rational surface mode:	75
4.5.3	Polarization drift driven flux	76
4.5.4	Polarization fluxes at q_{min} due single mode-rational surface mode:	77
4.6	Discussion and conclusions	78
5	Finite ballooning angle and macroscopic ExB shear effects on ion temperature gradient driven mode in gyrokinetic flux tube simu- lations	80
5.1	Introduction	80
5.2	Model Equations	82
5.2.1	Formulation	82
5.2.2	Diagnostics	85
5.3	Results From Linear Gyrokinetics	87
5.3.1	Eigenvalues	87
5.3.2	Mixing length estimates	89
5.3.3	Momentum and heat fluxes	90
5.4	Non-linear gyrokinetic simulations with background ExB shear	96
5.4.1	System description	96
5.4.2	Results	97
5.5	Discussion and Conclusions	101
6	Secondary instability of electromagnetic ion temperature gradient modes for zonal flow generation	105
6.1	Introduction	105

6.2	Electromagnetic toroidal ion temperature gradient driven modes	107
6.3	The model for zonal flow generation	111
6.4	Results and discussion	115
6.5	Conclusions	117
7	A new paradigm of coupled intrinsic toroidal zonal flow - ITG turbulence - poloidal zonal flow system	120
7.1	Introduction	120
7.2	Coupled excitation of PZF and TZF: A new paradigm	121
7.3	Zonal flows suppression by mean shear flows	126
7.4	An extended 0D empirical model: Role of TZF in $L \rightarrow H$ transition	127
7.5	Conclusions	132
8	Coherent non-linear structures in ITG-Zonal flows system	134
8.1	Introduction	134
8.2	Basic turbulence equations	135
8.3	Zonal mode equations	138
8.4	Coherent structures: Stationary solutions	141
8.5	Conclusions	149
9	Conclusions	150
9.1	Summary	150
9.2	Future directions	152
A	Perturbative calculation of eigenfunction at q_{min}	154
B	Derivation of Equation(8.57)	158

List of Figures

1.1	Schematic showing consequences of momentum transport and approaches used to handle different processes.	5
3.1	Real frequencies (a) and growth rates (b) vs k_y obtained from numerical solution of the dispersion relation. The dashed-dotted (---) curve) represents the analytical approximation of the growth rate on the low k_y side of the spectrum only. Parameters: $L_n = 0.05m$, $L_T = 0.020m$, $\hat{s} = 2.0$, $q_{a/2} = 2.0$, $R = 1m$, $a = 0.25m$, $T_e = T_i = 4KeV$, $m_i = 1.6 \times 10^{-27}Kg$, $B = 4.6T$, $r = a/2$	37
3.2	Eigenfunction shifts off the resonant surface due to finite ρ_s^* . The figure shows $Re\phi$ (— curve) , $Im\phi$ (— curve) and $ \phi ^2$ (— curve). The zoomed-in subplot highlights the mode shift. The solid vertical line indicates the peak of the shifted eigenfunction. Parameters: $k_{y,max} = 0.60$, $\gamma_{max} = 2.92$, $\omega_{r,max} = -4.41$ and other parameters are same as in Fig.(3.1). The mode width is $\Delta = 1.59$, the mode shift is $\xi = 5.90e - 03$ and the mode averaged $\langle k_{\parallel} \rangle = 3.15e - 03$	38
3.3	Variation of ρ_s^* induced symmetry breaking driven residual stress $\Pi_{x,\parallel}^{\rho_s^*,res}$ (— curve) and E_r -shear induced symmetry breaking driven residual stress $\Pi_{x,\parallel}^{E_r',res}$ (— curve) with L_n/R . Stresses are computed corresponding to the highest growing mode for every L_n/R . Parameters: $V_E' = 100000s^{-1}$ and other parameters same as in Fig.(3.1).	44
3.4	Relative strength of ρ_s^* induced symmetry breaking driven residual stress to E_r -shear induced symmetry breaking driven residual stress vs L_n/R . Parameters: same as in Fig.(3.3)	44
3.5	Approximate parallel flow levels evaluated at the mid-minor radius ($a/2$) by using $V_{\parallel} = - \int_{a/2}^a dx (\Pi_{x,\parallel}^{res} / \chi_{\parallel}) = (\Pi_{x,\parallel}^{res} / \chi_{\parallel})(a/2)$. The (—) curve represents ρ_s^* driven flow and the (—) curve represents the E_r' driven flow. This shows that at small L_n/R the ρ_s^* driven flow may be comparable to E_r' driven flow.	45

3.6	Schematic showing regions of relative importance of ρ_s^* induced symmetry breaking driven residual parallel momentum and turbulence intensity gradient induced symmetry breaking driven parallel residual flux. The vertical dashed-dotted lines are only for roughly highlighting the regions where the respective fluxes are dominating. . . .	49
4.1	Schematic showing a typical reverse q profile and arrangement of rational surfaces resonating with toroidal mode number $n = 2$. Zero of the radial coordinate is fixed at the position of q_{min} . $q = (q_{min} + c_1(r - c_2)^2)$, $q_{min} = 1/\sqrt{2}$, $c_1 = 10.0$, $c_2 = 0$. Here $r \equiv r/a$ where a is minor radius.	59
4.2	The growing branch of the double rational surface RS-ITG. Fig(a) is the dispersion plot and (b) is growth rate vs k_y . Parameters are: $L_n = 0.020 \times 4$ m, $L_T = 0.020$ m, $V_E' = 0.0$, $V_{ }' = 0.0$, $\hat{s} = 0.0$, $T_e = T_i = 4.0$ keV, $m_i = m_H = 1.67 \times 10^{-27}$ kg, $B = 4.6$ Tesla, $r_0/a = 0.3$ m, $q_0'' = 20$, $R = 2.0$ m, $k_z = 0.7$; $\rho_s = 1.40 \times 10^{-03}$ m	60
4.3	Eigenmode structure of the double rational surface RS-ITG. Solid vertical line indicates the shifted position of the mode. Mode shift = 0.6485, mode width = 8.0394. Parameters: same as in Fig.(4.2), $\omega = -0.672 + i0.7745$	61
4.4	The growing branch of the double rational surface RS-ITG. Fig(a) is the dispersion plot and (b) is growth rate vs k_y . Parameters: same as in Fig.(4.2), $L_n = 0.019 \times 4$ m, $L_T = 0.019$ m, $\hat{V}_E' = 0.01$	62
4.5	Eigenmode structure of the double rational surface RS-ITG. Solid vertical line indicates the shifted position of the mode. Mode shift = 1.08, mode width = 9.42. Parameters: same as in Fig.(4.4), $\omega = -0.40 + i0.517$. Mode shift enhancement due to finite \hat{V}_E' can easily be noticed.	62
4.6	The growing branch of the single rational surface RS-ITG. Fig(a) is the dispersion plot and (b) is growth rate vs k_y . Parameters: same as in Fig.(4.2), $L_n = 0.019 \times 4$ m, $L_T = 0.019$ m, $\hat{V}_E' = 0.01$, $\hat{V}_{ }' = 0.7$, $k_z = 0$	64

4.7	Eigenmode structure of the single rational surface RS-ITG. Solid vertical line indicates the shifted position of the mode. Mode shift = 25.13, mode width = 40.09. Parameters: same as in Fig.(4.4), $\omega = 0.08 + i0.477$, $k_z = 0$. Mode shift enhancement due to finite \hat{V}'_E can easily be noticed.	65
4.8	Growing branch of the non-resonant RS-ITG. Fig(a) is the dispersion plot and (b) is growth rate vs k_y . Parameters: same as in Fig.(4.2).	66
4.9	Eigenmode structure of the non-resonant RS-ITG. Solid vertical line indicates the shifted position of the mode. Mode shift = 0.731081, mode width = 8.53614. Parameters: same as in Fig.(4.8), $\omega = -0.6139 + i0.7885$	66
4.10	Schematic showing three distinct modes in the $k_y - k_z$ space. The nature of the mode is determined by whether the q_{min} is a rational number or not.	68
4.11	First order corrected growing branch of the double rational RS-ITG. Fig.(a) is the dispersion plot and (b) is growth rate vs k_y . Parameters: same as in Fig.(4.2)	68
4.12	First order corrected eigenmode structures of the double rational surface RS-ITG. Parameters: same as in Fig.(4.11), $\omega = -0.75 + i0.77$. Color meanings: (-.-.-) $\text{Re}\phi$, (-.-.-) $\text{Im}\phi$, and (-.-.-) $ \phi ^2$ with 1st order correction and without ρ_s^* effect. (—) $\text{Re}\phi$, (—) $\text{Im}\phi$, and (—) $ \phi ^2$ with 1st order correction and with ρ_s^* effect. (-.-.-) $ \phi ^2$ at zeroth order with ρ_s^* effect. Intensity humps become asymmetric due to ρ_s^* effect.	69
4.13	Double rational surface RS-ITG: (a) Mode average of $k_{ }/k_y$ with and without ρ_s^* . (b) Residual stress vs L_n/R with and without ρ_s^* shift. It appears that ρ_s^* induced symmetry breaking of the eigenfunction has no appreciable effect on $k_{ }$ symmetry breaking. So the $k_{ }$ symmetry breaking and hence the residual stress is dominantly determined by mode width rather than mode shift.	74

4.14	No rational surface RS-ITG: (a) Mode average of k_{\parallel}/k_y with and without ρ_s^* . (b) Residual stress vs L_n/R with and without ρ_s^* shift. It appears that ρ_s^* induced symmetry breaking of the eigenfunction has no appreciable effect on k_{\parallel} symmetry breaking. So the k_{\parallel} symmetry breaking and hence the residual stress is dominantly determined by mode width rather than mode shift.	74
5.1	Linear growth rates γ vs kx_{center} (left) and γ vs θ_0 (right) with k_y as parameter. $kx_{center} = 0$ or $\theta_0 = 0$ is not always the maximum growing mode. Very weakly growing modes or damped mode growth rates in the valley are not well converged as per the rule Equations(5.5) and are obtained from linear regression analysis of the available time series of $ n ^2$ and hence are only approximately correct.	88
5.2	Left: kx_{center} vs k_y at max. growth rates. Right: Ballooning angle at max. growth rate vs k_y	88
5.3	Left: Thin solid lines with * indicates γ for $kx_{center} = 0$, thick solid lines with o represent γ maximized over all kx_{center} i.e., γ_{max} . Right: Corresponding real frequencies.	89
5.4	$\langle k_{\perp}^2 \rangle$ vs k_y (Left) and $\gamma/\langle k_{\perp}^2 \rangle$ vs k_y (Right) at ballooning angles $\theta_0 _{\gamma_{max}}$ corresponding to max growth rates γ_{max}	90
5.5	Left: $\Gamma_{\parallel}/\langle \phi^2 \rangle$ vs θ_0 at $k_y = \{0.3, 0.6\}$, $R/L_T = 9$. The underlined regions indicate damped mode contributions. Right: $\langle k_{\parallel} \rangle$ vs θ_0 showing $\langle k_{\parallel} \rangle$ symmetry breaking by finite θ_0	91
5.6	Γ_{\parallel} vs k_y at ballooning angles $\theta_0 _{\gamma_{max}}$ corresponding to max growth rate and $R/L_T = 9$	91
5.7	Γ_{\parallel} vs z with kx_{center} as parameter at $k_y = 0.3$ and $R/L_T = 9$. The shown values of kx_{center} correspond to $\theta_0/\pi = \{0, -0.05, -0.10, -0.15, 0, 0.05, 0.10, 0.15\}$	92
5.8	Mode parities, at the end of simulation, along the field line when $kx_{center} = 0$ for $k_y = 0.3$ at $R/L_T = 9$	92
5.9	Mode parities, at the end of simulation, along the field line when $\theta_0 = -0.15\pi$ for $k_y = 0.3$ at $R/L_T = 9$	93

5.10	Left: $Q_i / \langle \phi^2 \rangle$ vs θ_0 at $k_y = \{0.3, 0.6\}$, $R/L_T = 9$. The underlined regions correspond to damped modes. Right: $\langle k_\perp^2 \rangle$ vs θ_0	93
5.11	Q_i vs z with kx_{center} as parameter at $k_y = 0.3$ and $R/L_T = 9$. The shown values of kx_{center} correspond to $\theta_0/\pi = \{0, -0.05, -0.10, -0.15, 0, 0.05, 0.10, 0.15\}$	94
5.12	Finite kx_{center} shifts mode away from LFS midplane. The figure highlights the same for $k_y = 0.3$ for few representative cases of growing modes. The shown values of kx_{center} correspond to $\theta_0/\pi = \{0, -0.05, -0.10, -0.15, 0, 0.05, 0.10, 0.15\}$	94
5.13	Q_i vs k_y at ballooning angles $\theta_0 _{\gamma_{max}}$ corresponding to max growth rate and $R/L_T = 9$	95
5.14	Mode parities, at the end of simulation, along the field line when $\theta_0 = 0$ for $k_y = 0.3$ at $R/L_T = 9$	95
5.15	Mode parities, at the end of simulation, along the field line when $\theta_0 = -0.15\pi$ for $k_y = 0.3$ at $R/L_T = 9$	96
5.16	Left: $\Gamma_{ }^{res}$ vs $E \times B$ rate, Middle: $\Gamma_{ }^{res} / \langle \phi^2 \rangle$ vs $E \times B$ rate.	97
5.17	Left: $ \phi ^2(z)$ vs z at various $E \times B$ rates. Right: rms $\omega_{E \times B, zonal}$ vs $E \times B$ rate.	98
5.18	2d Cross-correlations of zonal shear and momentum flux $R_{\omega_{E \times B, zonal} \Gamma_{ }}$ (left); and zonal shear and heat flux $R_{\omega_{E \times B, zonal} Q_i}$ (right), cross-correlations of heat flux and momentum flux $R_{Q_i \Gamma_{ }}$ (bottom).	99
5.19	Left: Cross-correlations $R_{ \phi ^2 Q_i}$. Right: $R_{ \phi ^2 \Gamma_{ }}$	99
5.20	2d Cross-correlations of zonal shear and momentum flux $R_{\omega_{E \times B, zonal} \Gamma_{ }}$ (left) and zonal shear and heat flux $R_{\omega_{E \times B, zonal} Q_i}$ (right), heat flux and momentum flux $R_{Q_i \Gamma_{ }}$ (bottom) at $\gamma_E = 0.30$	100
5.21	2d Cross-correlations $R_{ \phi ^2 Q_i}$ (left) $R_{ \phi ^2 \Gamma_{ }}$ (right) at $\gamma_E = 0.30$	101
5.22	Eigenmode averaged curvatures $\langle \hat{\mathcal{K}}_x \rangle$, $\langle \hat{\mathcal{K}}_y \rangle$ vs kx_{center} (left) and θ_0 (right) for a test case of $k_y = 0.6$ when $R/L_T = 9$. The periodic nature of γ is a reflection of periodic nature of $\hat{\mathcal{K}}_y$	103

6.1	Numerical solution to Equation(6.15) displaying the ITG growth rate (normalized with $\omega_{\star e}$) versus β for $\eta_e = 0$, $q = 1.5$, $s = 0.5$, $k_{\perp}^2 \rho^2 = 0.1$, $\Delta\sqrt{\pi} = 1.0$ with ϵ_n as a parameter. Results are shown for $\eta_i = 3.5$ (dashed line) and $\eta_i = 4.0$ (solid line).	116
6.2	Zonal flow growth rate (normalized with γ_{ITG}) versus β with η_i as a parameter for the same parameters as in Fig.(6.1) as obtained numerically by solving Equation(6.37). A fixed ITG turbulence saturation level $\tilde{\phi} = \tilde{\phi}_0$ was used.	116
6.3	Numerical solution to Equation (6.15) showing the ITG growth rate (normalized with $\omega_{\star e}$) versus η_i for $\eta_e = 0$, $\epsilon_n = 2$, $q = 1.5$, $s = 0.5$, $k_{\perp}^2 \rho^2 = 0.1$, $\Delta\sqrt{\pi} = 1.0$ with β as a parameter. Results are shown for $\beta = 0.1\%$ (dash-dotted line), $\beta = 0.5\%$ (dashed line), $\beta = 1.0\%$ (dashed line) and $\beta = 1.3\%$ (solid line)	118
6.4	Zonal flow growth rate (normalized with γ_{ITG}) versus η_i with β as a parameter for the same parameters as in Fig.(6.3) as obtained numerically by solving Equation(6.37). A ITG turbulence saturation level $\tilde{\phi} = \tilde{\phi}_0$ was used.	118
7.1	Parameters: Common: $a_1 = 0.2$, $a_2 = 0, 0.7$ (solid curves on left, otherwise), $a_3 = 0.0$, $a_4 = 0, 0.7$ (left, right), $a_5 = 0$, $b_1 = 0, 1$ (left, right), $b_{11} = 0, 1.5$ (left, right) , $b_{12} = 0$, $b_2 = 1.0$, $b_3 = 0$, $b_4 = 0, 1$ (left, right), $c_1 = 0$, $c_{11} = 0.0$, $c_{12} = 0.0$, $c_2 = 0$, $c_3 = 0$, $c_4 = 0$, $c_5 = 0$, $d_1 = 1$, $d_2 = 0.5$, $e_1 = 1$, $e_2 = 0$, $V'_{\parallel} = 0$, $m = 1$	130
7.2	Parameters: $a_1 = 0.2$, $a_2 = 0.7$, $a_3 = 0.0$, $a_4 = 0.7$, $a_5 = 0.1$, $b_1 = 1$, $b_{11} = 1.5$, $b_{12} = 0.15$, $b_2 = 1.0$, $b_3 = 0$, $b_4 = 1$, $c_1 = 1$, $c_{11} = 0.01$, $c_{12} = 0.5$ (left panel), $c_{12} = 4.0$ (right panel), $c_2 = 1$, $c_3 = 0$, $c_4 = 1$, $c_5 = 0.5$, $d_1 = 1$, $d_2 = 0.5$, $e_1 = 1$, $e_2 = 0$, $V'_{\parallel} = 0$, $m = 1$	131
7.3	Turbulence intensity ε in different situations explained in the legend	132
8.1	k_x vs x when $v = v_0 \cos(qx)$ (left) and when $v = v_0 \sin(qx)$ (right) with $\tau = 1$, $\epsilon_n = 0.7$, $k_y = 0.2$, $v_0 = 0.1$, $q = 0.2$	144
8.2	Population distributions of trapped and untrapped waves for $\epsilon = 0.3$, $\Delta/f_m = 1.0$	145
8.3	Sketch of Sagdeev Potential for $\kappa = 0.8$ and $\bar{\beta} = 0.5$	147

8.4	Left: Zonal flow soliton. Right: Zonal flow shock	148
-----	-------------------------------------------------------------	-----

Introduction

1.1 Motivation and brief history

Tokamak is a toroidal magnetic confinement fusion device aimed for production of energy via fusion reaction of deuterium and tritium in plasma state. Strong magnetic fields are used to keep the high temperature plasmas detached from the vessel wall. In tokamks the toroidal magnetic field is produced by external coils, while the poloidal field is generated by the plasma itself by inducing a toroidal plasma current as opposed to the stellarator where complex geometry coils are used to generate both toroidal and poloidal magnetic field. The necessary ingredients for the success of fusion reaction are: high temperature T , high particle density n of the enclosed plasma (to ensure large fraction of high-energy particles) and high mean energy confinement time τ_E . The 'ignition condition' is given by the *Lawson Criterion* [1, 2]: $nT\tau_E > 3 \times 10^{21} m^{-3} keVs$. That is the product of the three parameters has to exceed a certain value, so that the energy gain due to nuclear fusion over-compensates the energy loss due to radiation and convection. For typical parameters of $T \approx 10 - 20 keV$ and $n \approx 10^{20} m^{-3}$, the confinement time needs to be of the order of several seconds to allow for a self-sustaining plasma burning. The confinement time, on the other hand, depends on heat diffusivity χ and minor radius a of the tokamak through $\tau_E = a^2/\chi$. Obviously minimum heat loss is desired to get better confinement. Hence study of processes that effects heat and particle confinement becomes extremely important so that optimizations can be done to maximize confinement.

Tokamak plasmas are always found to be in a symbiotic state of turbulence and

flows. The turbulence is usually driven by the release of free energy contained in the equilibrium density and temperature profiles. Whereas the flows are either externally driven e.g., by unbalanced neutral beam injections or it can be self driven. This self generated flows include intrinsic toroidal rotation on macroscale and zonal flows on mesoscale. Intrinsic rotation is referred to spontaneous toroidal rotation without any external momentum source which has been observed in all types of discharges. Zonal flows correspond to poloidally symmetric band-like shear flows[3, 4] and are most dominantly observed in high (H) confinement mode. Zonal flows has two variants: stationary zonal flows and high frequency zonal flows which are also know as geodesic accoustic mode (GAM). Flow generation and momentum/velocity transport are intrinsically connected. Self-generation of flows is viewed as phenomena of self-organization in turbulence by Reynolds stresses. Mean flow self-generation and anomalous momentum transports are prevelent at many places in astrophysical settings such as in accretion disk formation[5], galactic dynamics, zonal flows in the Jovian atmosphere[6]. The phenomenon of tokamak flow self-organization has gained considerable interest and importance in recent years. This is because shear flows reduce outward particle and heat transport by reducing eddy decorrelation length, thus providing better confinement[7, 8, 9, 10]. Both toroidal flow and its shear influence the power threshold for L-H transition[11], and plays importatnt role in formation of internal transport barriers (ITB)[12, 13]. Toroidal rotation is also helpful in suppressing certain types of harmful magnetohydrodynamic(MHD) instabilities, such as resistive wall modes(RWM) [14, 15, 16, 17] whose stability is a major concern for advanced ITER scenerios [18]. RWMs are nothing but the long wavelength MHD external kink modes in the presence of a resistive wall. RWMs stability can facilitate tokamaks to operate at normalized pressure values beyond the no-wall stabilty limit and rotation plays a significant role in achieving this. In present generation tokamaks neutral beam injection(NBI) is the main external driver of rotation. However use of NBI in ITER and other future reactor scale machines to achieve desired rotation is still debatable because of unvoidable bulky size of these machines [19, 20, 21]. Hence self generated rotation will play a vital role in suppression of RWMs. Fortunately Rice scaling predicts a toroidal intrinsic rotation Alfven Mach number of $M_A \geq 0.02$ for ITER plasma and that appears to be sufficient for stabilization of RWMs [22]. This suggests that the RWMs in the ITER plasma will probably be self-stabilized because of spontaneous

rotation itself, which would provide an alternative solution to the NBI problem apart from the active feedback control of RWMs [18]. These findings have sparked extensive theoretical and experimental studies on intrinsic rotation generation.

Experimental efforts over the years have been able to characterize intrinsic toroidal rotation which follow many empirical trends in H-mode[22]: a) rotation is typically co-current, b) the increment in central velocity ΔV_ϕ at the L→H mode transition scales with the increment in stored energy ΔW and plasma current I_p as $\Delta V_\phi \sim \Delta W/I_p$, with no observed dependence on normalized gyroradius $\rho^*(=\rho/a)$ or normalized collisionality $\nu^*(=\nu/\nu_b)$, where a is minor radius and ν_b is bounce frequency, c) co-current rotation initiates at the edge and then propagates inward. L mode plasmas show even more complex behaviour. Core plasma rotation reverses from co-to-counter current when the electron density is increased beyond a critical electron density or toroidal magnetic field ramps in torque free ohmic discharge plasmas such as in TCV[23] and Alcator C-Mod[24, 25, 26, 27]. The rotation reversal critical density increases linearly with plasma current I_p , and decreases with increasing toroidal magnetic field B . A strong correlation has been observed between the reversal density and the density at which the global ohmic L-mode energy confinement changes from the linear to the saturated regime.

Intrinsic rotation and zonal flows can be viewed as different manifestations of radial transport of toroidal and poloidal momentum. Early theories attempted to explain the observed rotation in ICRF plasmas based on orbit shifts of fast ions[28, 29, 30, 31]. But similarity between Ohmic and ICRF H-mode rotation results suggests that it is not a fast ion orbit effect. Among others, neoclassical theories [32, 33] and ion orbit loss based [34] theories are only partly able to explain certain features of edge intrinsic toroidal rotation. The most promising theories are those based on flow generation by turbulent Reynolds stresses[35, 36]. While both neoclassical and turbulent contributions should be considered to predict intrinsic rotation profiles, this thesis focuses only on turbulent momentum fluxes. Tokamak plasmas always exhibit turbulence so turbulent Reynolds stresses are natural ways of exerting local internal torques. Momentum flux differs from heat and particle flux in the sense that it consist of an unique part called residual momentum flux which is not present in heat and particle fluxes. Residual flux differs from diffusive and convective fluxes in the sense that it is independent of mean velocity/momentum and mean velocity/momentum shear.

The mean flows are self sustained only when the residual stress is non zero. This residual stress acts like an internal torque and drives the spontaneous rotation[37]. Self sustained mean flows are the nothing but the so called *Intrinsic Flows*. So searching for nondiffusive elements (i.e., pinch and residual stress) and understanding underlying mechanisms have been the focus in research related to intrinsic rotation generation in tokamaks. The structure of the residual stress has been found to depend on the type of underlying turbulence. Different mechanisms driving the residual stress are seen as different candidate mechanisms driving intrinsic rotation. Some of the mechanisms discovered so far in normal shear tokamak, where the safety factor q is monotonically increasing radially outward, are described below. The first convincing mechanism was given by Gurcan *etal* [37]. They showed that the mean radial electric field shear breaks the reflectional symmetry (about a mode rational surface) in ion temperature gradient (ITG) driven microturbulence which has also been shown by many authors in the past in different contexts. This makes spectrally averaged $\langle k_{\parallel} \rangle$ finite. This in turn makes parallel residual stress finite. This electric field shear driven parallel residual stress generation mechanism has also been reproduced in gyrokinetic simulation [38]. This mechanism of residual stress generation is now popularly known as $\langle k_{\parallel} \rangle$ symmetry breaking mechanism. Later it was realized that having $\langle k_{\parallel} \rangle \neq 0$ is a generic requirement for generating finite residual stress when radial fluctuating velocity is $E \times B$ fluctuating velocity only. Parallel nonlinearity in concert with the gyrokinetic poisson equation has also been shown to generate parallel residual stress [39, 40] by making $\langle k_r k_{\parallel} \rangle \neq 0$ which is a fundamentally different mechanism. Toroidicity[41] and up-down asymmetry in toroidal plasma current[42, 43] also drives parallel residual stress. Tokamak plasmas are also noticed to have poloidal rotation along with intrinsic toroidal rotation[44, 45]. Hence looking for structure of poloidal momentum flux and other mechanisms of residual stress generation in tokamaks with regular q profile and non-monotonic q profile (such as reversed shear case) is highly desirable. Above mechanisms for parallel/toroidal or poloidal rotation are for mean toroidal and poloidal rotation, there can be other variant of toroidal and poloidal flows which appears at mesoscale. While poloidal flows at mesoscale namely zonal flows are well explored theoretically and experimentally, possibility of toroidal flows at mesoscale having characteristics similar to zonal flows can not be overruled. Coming to the zonal flow generation in the poloidal plane, these mesoscale flows

are well known to arise due to modulational instability of the drift wave turbulence. The poloidal Reynolds stress leads to growth of zonal mode as a secondary instability[3]. The zonal flows provide a strong shear stabilization of the turbulent eddies and are hence important for the self-regulation and saturation of the turbulence[46, 47, 48, 49]. Finite β (thermal pressure to magnetic pressure ratio) has stabilizing influence on ITG mode which gives favourable scaling of confinement with β in quasilinear theories[50, 51, 52, 53]. However the role of electromagnetic effects on the generation of zonal flows are not well studied analytically, though many nonlinear simulations of ITG turbulence including electromagnetic effects and zonal flow dynamics have been performed using both gyrokinetic [53, 54, 55, 56, 57, 58] and gyro-fluid models[59, 60]. Reduction of transport levels with increasing β , as reported in recent gyrokinetic simulations[53, 54], could not be explained by the linear theories alone.

Zonal flow shear excited via modulational instability of a test shear by a drift

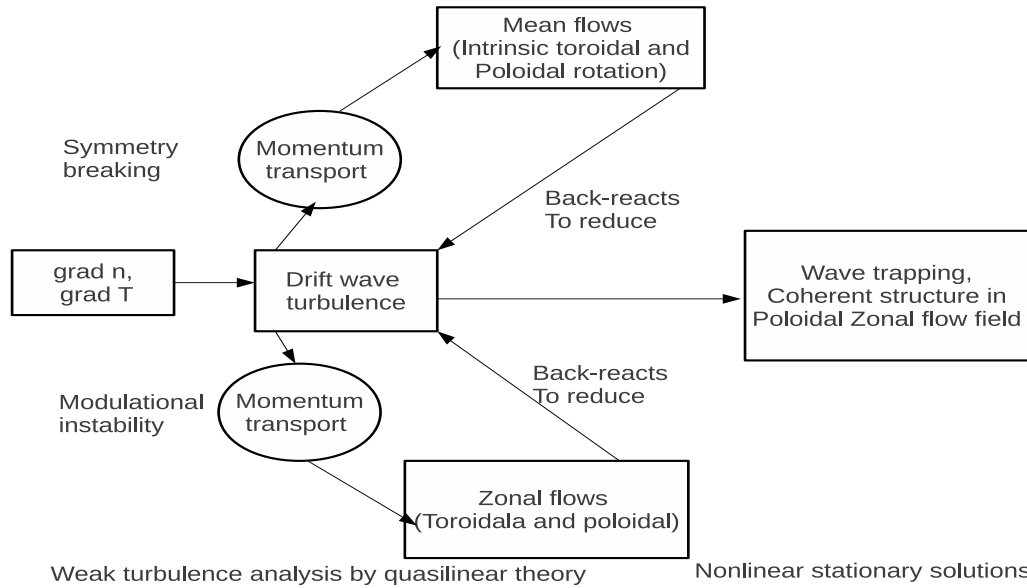


Figure 1.1: Schematic showing consequences of momentum transport and approaches used to handle different processes.

wave spectrum can not keep on increasing indefinitely and hence some saturation

mechanisms are required to limit the growth of zonal flow shear. In presence of an effective collision of ions, which could arise from collision between trapped and passing ion in tokamak core due to high temperature, zonal flows are directly subject to collisional damping [61]. In zero collisionality regime several possibilities can exist. Tertiary linear KH instability which is a secondary KH instability of the zonal flow itself. This will return energy to the $m \neq 0$ fluctuations, thus limiting the zonal flow growth. This mechanism is efficient near marginality[62]. However a follow up study in Ref.[63] shows that zonal flow damping by linear KH instability is not efficient near marginality, but could be significant away from marginality. Moreover Landau damping of KH modes further weakens this effect. Among other routes with no higher order instabilities include the following. a) Flattening of the quasi-particle distribution function (wave action density or wave population density N_k) through \vec{k} -space diffusion. When the zonal flows grow, they shear turbulent eddies of the drift wave and thus generates modes of higher k_r which flatten the N_k spectrum. The flattening then weakens the drive of zonal flow generation causing it to saturate. The main features of this nonlinear feedback can be captured in simple “predator-pray” model by employing quasilinear closure. b) When zonal flow amplitude grows to larger values quasi-particles may get trapped in the effective potential formed by zonal flows profile. The trapping is effective when the bounce frequency ω_b is greater than the growth rate γ of the quasi-particle i.e., $\omega_b > \gamma$. Trapping can lead to saturation of zonal flow by formation of self-consistent zonal flow - turbulence state.

Dominance of different processes can be understood in a unifying framework of shearing and wave kinetics[3]. Quasi-particle bounce frequency ω_b and the dispersion in the wave number Δk of the quasi-particle due to mesoscale zonal flow field serve as key parameters to identify different processes. Δk is typically the width of the island in the phase space for quasi-particle orbit. Chirikov parameter \mathcal{S} is introduced for quasi-particle dynamics in mesoscale zonal flow perturbations as

$$\mathcal{S} = \frac{(\partial v_g / \partial k) \Delta k}{\Delta(\Omega/q)} > 1$$

which is ratio of variation in velocity $(\partial v_g / \partial k) \Delta k$ of quasi-particle over the island width Δk to separation between phase velocities $\Delta(\Omega/q)$ of the modulations. Similarly effective Kubo number \mathcal{K} of quasi-particle is introduced as ratio between

the life time and bounce time of the quasi-particle

$$\mathcal{K} = \omega_b / \gamma$$

Depending on different values of these parameters \mathcal{S} and \mathcal{K} different nonlinear processes become dominant. The values $\mathcal{S} \rightarrow 0$ and $\mathcal{K} \rightarrow 0$ correspond to the case of single zonal flow perturbation and with infinitesimal small amplitude so that there is no island overlapping and quasi-particle trapping. Then simply the method of modulational parametric instability apply. This regime does not yield saturation level of zonal flow. For $\mathcal{S} > 1$ and $\mathcal{K} \ll 1$, the resonances overlap and the quasi-particle trapping is not efficient. The dynamics then become stochastic, with stochastic rays, and random shearing and refraction of drift waves by zonal flows constitute the principal effect of zonal flows on the turbulence. Quasi-linear theory may be used in this regime which yield a picture of diffusive refraction. Higher order extension of the quasilinear theory is possible to account the effects of strong nonlinear deviations of N_k by larger amplitude zonal flows. Retaining terms up to third order produces zonal flow equation with cubic nonlinearity which supports propagating kink soliton like solutions[64]. The regime with $\mathcal{S} \sim 1$ and $\mathcal{K} \sim 1$ correspond to the regime of turbulent trapping. This is a kind of mixed regime with stochasticity and trapping where closely separated quasi-particles remain correlated for times greater than the nonlinear decorrelation time. This causes granulation in N_k . For $\mathcal{S} \ll 1$ and $\mathcal{K} > 1$ there is no island overlapping but trapping is effective. In this case the dynamics is coherent and the quasi-particle moves along its perturbed orbit without decorrelation. Eventually a BGK state[65] of the wave kinetic equation may be reached. Kaw et al [66] in context of disparate scale interaction between Langmuir turbulence and acoustic turbulence showed soliton formation in the envelope of acoustic density modulation by appropriate choice of distribution of trapped and untrapped plasmon (or quasi-particle) density. Then again inspired by the non-Gaussian features such as intermittency, burstiness etc., [67, 68, 69, 70, 71] in turbulent transport in tokamaks, Kaw et al[72] showed that in a strongly non-linear regime in a drift wave - zonal flow system a significant fraction of drift wave trajectories get perturbed by trapping effects in the effective potential formed by zonal flow. Then the Reynolds stress offered by trapped and untrapped drift waves can sustain coherent structures like solitons,

shocks, and nonlinear wave trains in the zonal flow field in the drift wave turbulence. Similar phenomena may also be expected in other disparate scale systems such as toroidal ITG turbulence and zonal flows. These coherent structures might provide alternate saturated states of the ITG turbulence.

In the backdrop of the scopes outlined above this thesis is dedicated to study of some critical issues related to momentum transport in normal and reverse shear tokamaks, possibility of zonal like toroidal flows and its role in L-H transition, electromagnetic effects on zonal flow generation in toroidal ITG turbulence and coherent structure formation in ITG-zonal flow system.

1.2 Thesis outline

This thesis deals with parallel and poloidal momentum transport in tokamaks which manifest as intrinsic toroidal and poloidal rotation and zonal flows. Chapters 2 to 5 present studies on momentum transport relevant to macroscale intrinsic toroidal and poloidal rotation and the Chapters 6 to 8 deals with momentum transport phenomena leading to the generation of mesoscale poloidal and toroidal zonal flows.

Chapter 2: deals with intrinsic toroidal and poloidal flow generation in the background of ion temperature gradient turbulence. In this chapter we have performed a systematic calculation of toroidal/parallel and poloidal Reynolds stresses for electrostatic slab ITG turbulence with adiabatic electron response and macroscopic $E \times B$ shear and parallel flow shear, in fluid theoretical framework. Structure of parallel and poloidal stresses in the low flow shear limit is discussed. Parallel and poloidal symmetry breaking mechanisms of residual stress generation linked to intrinsic rotation in toroidal and poloidal direction are detailed. $E \times B$ leads to generation of parallel residual stress by k_{\parallel} symmetry breaking via radial symmetry breaking of the eigenmode about a mode rational surface. Parallel flow shear generates poloidal residual stress by k_r symmetry breaking via radial symmetry breaking of the eigenmode. Residual parallel polarization stress generated by $k_r k_{\parallel}$ symmetry breaking however, does not require radial asymmetry of the eigenmode. Chapter 3: Divergence of the fluctuating polarization current that arise from the radial gradient of the density of the particles generates a fluctuating current by

their polarization drift motions which is one order higher in ρ_s^* in regular drift wave ordering used in Chapter 2. Inclusion of this higher order term in the ITG eigenmode calculation, leads to a symmetry breaking in k_{\parallel} by breaking of radial symmetry of the eigenmode due to finite ρ_s^* , and therefore a net non-zero residual momentum flux which does not require background $E \times B$ shear. The importance of this effect is discussed by making comparisons with the residual stresses driven by E_r -shear, parallel polarization residual stress (already obtained in Chapter 2) and the turbulence intensity gradient.

Chapter 4: Theories discussed in Chapters 2 and 3 are further extended to reverse shear configuration where the safety factor q profile varies non-monotonically in the minor radial coordinate. Because of the novel configuration of magnetic field and existence of internal transport barrier (ITB), momentum transport studies are done at the minimum of q . At q_{min} the parallel and poloidal symmetry is spontaneously broken without the need of eigenfunction with broken symmetry in radial direction.

Chapter 5: Calculations in the previous Chapters have been performed in sheared slab geometry which captures the effect of radial eigenmode structure only because poloidal variation of equilibrium magnetic field is not considered there. The effect of poloidal eigenmode structure on momentum and heat transport is studied in this Chapter using the gyrokinetic turbulence code GENE. First part of this chapter discovers finite ballooning angle θ_0 effects on toroidal ITG mode in linear flux tube simulations. The k_y spectrum of growth rates maximized over all θ_0 extends to wavelength region $k_y \rho_i > 1$ which disappears at lower values of R/L_T near marginality. Finite θ_0 leads to generation of parallel residual momentum flux by symmetry breaking of the eigenfunction about the low field side (LFS) mid plane. Transport of heat and parallel momentum are discussed in detail.

Second part of this chapter discovers the effects of macroscopic $E \times B$ shear on nonlinear toroidal ITG simulations with adiabatic electrons. Simulations clearly show generation of parallel residual stress by symmetry breaking of the eigenfunction about the low field side mid plane. Role of self-consistently formed zonal flows on parallel momentum flux is analyzed.

Chapter 6: This chapter deals with generation of zonal flows in electromagnetic toroidal ITG turbulence. A two-fluid model for the ions and the electrons are used and the wave kinetic approach is employed for zonal flow generation. The ion fluid

response is used in the limit $\omega \gg k_{\parallel} c_s$ i.e., ignoring the ion parallel compression effect which eliminates the need of parallel ion dynamics. A system of equations is derived which describes the coupling between the background ITG turbulence, using a wave-kinetic equation, and the zonal flow mode driven by Reynolds and Maxwell stress forces. The scaling of the zonal flow growth rate with plasma parameters is studied and the implications for ITG driven transport are discussed.

Chapter 7: Now the ion parallel dynamics is retained in the toroidal ITG equations which facilitate the possibility of excitation of toroidal zonal flows (TZF) by the same modulational instability of the ion temperature gradient (ITG) turbulence that excites poloidal zonal flows (PZF). However, to keep things simple and to dig out the fundamental mechanism of toroidal zonal flow excitation electromagnetic effects are not considered. TZF and PZF dynamics is coupled linearly via non-linear stresses. Then considered the effect of mean poloidal and toroidal shear flows on zonal flows (both toroidal and poloidal) generation. It is found that, in weak shear limit, mean shear flows reduces the growth of zonal flows shear by enhancing the decorrelation of underlying mode propagation.

Based on these observations an extended 0D model is proposed which contains the self-consistent dynamics of turbulence intensity, mean pressure gradient, mean $E \times B$ shear, mean toroidal flow shear, PZF, TZF and input power. Predictions from the model in context of input power threshold and the transients of L to H transition are discussed.

Chapter 8: In this chapter nonlinear stationary solutions of the coupled toroidal ITG-Zonal flow system is investigated. Here, for simplicity the parallel ion dynamics is ignored. The ITG turbulence is described by a wave-kinetic equation for the action density of ITG mode and the longer scale zonal mode is described by a dynamic equation for the $m = n = 0$ component of the potential. Some fraction of drift wave trajectories get trapped in the effective potential formed by the large amplitude zonal flows in the nonlinear regime. This novel effect leads to formation of nonlinear stationary structures in a moving frame. It is shown that the ITG turbulence can self-consistently sustain coherent, radially propagating modulation envelope structures such as solitons, shocks, nonlinear wave trains, etc.

Chapter 9: The results of the entire thesis are summarized in this chapter and future directions are outlined.

2

Intrinsic toroidal and poloidal flow generation in the background of ion temperature gradient turbulence

2.1 Introduction

Anomalous momentum transport is a kind of phenomenon which is prevalent at many places in nature, such as accretion disks, solar atmosphere, galactic dynamics, laboratory and space plasmas etc. In laboratory fusion grade plasmas such momentum transport is manifested in the form of intrinsic or spontaneous rotation[73]. Intrinsic rotation is the toroidal rotation observed without external momentum injection. Though observed in all modes of tokamak discharges, it is most prominent in H-mode discharges. Both toroidal rotation and its shear is observed to influence the power threshold for L-H transition[11]. Toroidal rotation is also found to have stabilizing influence on resistive wall modes (RWMs), which are dangerous MHD modes and it has been estimated that a speed of ~ 200 km/s is needed to stabilize RWMs in ITER. While neutral beam injection (NBI) is a means of generating toroidal rotation in present generation of tokamaks, it is still questionable whether such high toroidal rotation can be produced by NBI in ITER and other future fusion grade machines because of their bulky size. But intrinsic rotation, as suggested by “Rice scaling”, can reach upto ~ 250 km/s in ITER scenario, which appears to be sufficient to stabilize RWMs[22]. This finding has revived the interest of fusion community to understand the generation mech-

anism of intrinsic rotation and its enhancement. However a good and satisfactory explanation of this fundamental phenomenon is still not found. Till date many theories have been advanced to understand the generation mechanism of intrinsic rotation. Sub-neo-classical[32], neoclassical[33], thermal ion orbit loss theory [34] explain certain features of intrinsic rotation. Because the tokamak plasma is always found to be in a turbulent state, theory based on flow generation from turbulent Reynolds stresses[36, 35] also seem to provide a natural and promising mechanism for intrinsic rotation. From this perspective intrinsic rotation can be viewed as specific manifestation of the more general phenomena of mean field generation by turbulent stresses. To name a few, are α effect in magnetic dynamo theory[74], flow generation due to inverse cascade of energy in 2D incompressible fluid turbulence[75, 76] and zonal flow generation in strongly magnetized plasma[3]. Let's now look at the structure of parallel momentum flux

$$\langle mnv_{\parallel}v_r \rangle = m\langle v_{\parallel} \rangle \langle \tilde{v}_r \tilde{n} \rangle + m\langle n \rangle \langle \tilde{v}_r \tilde{v}_{\parallel} \rangle$$

where the first term is the momentum flux due to particle flux, which very sensitively depends on electron response and the second term is Reynolds stress driven momentum flux. The particle flux for adiabatic electron response is zero and will not be considered in further analysis. In the mean field electrodynamics[77], the distinct scale separation between mean and fluctuating magnetic field facilitates the mean electromotive force to be expressed in terms of mean magnetic field and its spatial derivative, thus providing closure. The Reynolds stress term, in the spirit of mean field electrodynamics, is shown to be decomposed as[37, 78]

$$\langle \tilde{v}_r \tilde{v}_{\parallel} \rangle \approx -\chi_{\parallel} \frac{\partial \langle v_{\parallel} \rangle}{\partial r} + V_c \langle v_{\parallel} \rangle + S$$

where the first term is diffusive, second term is convective or pinch and the third term called residual stress is independent of mean parallel flow and its shear. χ_{\parallel} is parallel momentum diffusivity and V_c is radial convective velocity. With this the mean parallel flow equation in cylindrical system for circular flux surfaces, in the presence of external momentum source S_{ext} , can be written as

$$\frac{\partial \langle v_{\parallel} \rangle}{\partial t} + \frac{1}{r} \frac{\partial}{\partial r} \left[r \left(-\chi_{\parallel} \frac{\partial \langle v_{\parallel} \rangle}{\partial r} + V_c \langle v_{\parallel} \rangle + S \right) \right] = S_{ext}$$

which is same as the evolution equation for mean toroidal flow $\langle v_\phi \rangle$ when $B_\theta \ll B_\phi$, where r represents radial coordinate in poloidal plane. Assuming stationary solution and integrating from 0 to r ,

$$-\chi_\parallel \frac{\partial \langle v_\parallel \rangle}{\partial r} + V_c \langle v_\parallel \rangle + S = \hat{S}_{ext}$$

which makes it obvious that residual stress term is isomorphic to integrated external momentum source \hat{S}_{ext} and hence S is an ideal term to drive intrinsic rotation. Earlier diffusive momentum transport has been studied extensively both theoretically [79] and experimentally [80] and it has been established that toroidal momentum diffusivity $\chi_\phi \sim \chi_i$, ion thermal diffusivity. However it should be noted that, whereas some recent gyrokinetic simulations [38] support this scaling, others [81] have shown departure from this. Turbulent momentum pinch has been treated in Refs. [82, 83, 84]. A particular form of residual stress has been shown to arise due to asymmetry of fluctuation spectra induced by mean radial electric field shear and so this mechanism of intrinsic rotation is found to be operative in the region of strong mean radial electric field shear [37, 38]. Perturbation experiments carried out on JT60U tokamak has also demonstrated and confirmed the link between radial electric field shear and intrinsic rotation [85]. It has recently been shown that breaking of up-down symmetry of equilibrium magnetic topology [42, 43] and parallel nonlinearity in gyrokinetic framework [39, 40] are also capable of generating residual stresses.

However these earlier works have not considered about simultaneous generation of mean poloidal flow. Again in the same spirit of mean field electrodynamics we can write poloidal turbulent Reynolds stress as

$$\langle \tilde{v}_r \tilde{v}_y \rangle \approx -\chi_y \frac{\partial \langle v_y \rangle}{\partial r} + V_r \langle v_y \rangle + S_y$$

where as before first term is diagonal diffusive, second term is off-diagonal convective/pinch and the third term is off-diagonal poloidal residual stress. χ_y is poloidal momentum diffusivity and V_r is radial convective/pinch velocity. Here the residual stress term S_y is independent of mean poloidal flow $\langle v_y \rangle$ and its shear $\langle v'_y \rangle$ but may depend on mean toroidal flow $\langle v_\parallel \rangle$ and its shear $\langle v'_\parallel \rangle$. That is, off-diagonal part for one type of stress may serve as diagonal part for the other, hence providing

coupling between toroidal and poloidal flow generation mechanisms. In this chapter we have performed a systematic calculation of toroidal and poloidal Reynolds stresses for electrostatic ITG turbulence with adiabatic electron response, in fluid theoretical framework, and found that toroidal and poloidal flow generation mechanisms and their evolutions are naturally coupled. We also find that while a “seed” poloidal flow is necessary to generate the toroidal residual stress due to $E \times B$ drift, the polarization drift can generate residual stress even in absence of “seed” poloidal flows. While turbulent $E \times B$ drift is found to generate poloidal stress (and hence poloidal rotation), by means of asymmetric eigen spectrum and radially propagating nature of basic mode [86], no appreciable mean poloidal stress is generated by polarization drift.

This chapter is organized as follows. In Section 2.2 toroidal and poloidal momentum conservation theorem is derived. In Section 2.3 radial eigenmode analysis is done where potential eigenfunction and eigenmode dispersion relation, in presence of seed flows, is derived which is used in Section 2.4 to evaluate the contributions to toroidal and poloidal momentum fluxes due to $E \times B$ and polarization drift, for slow and fast modes. In Section 2.5 toroidal and poloidal coupled flow equations are written using the exact expressions for various Reynolds stresses calculated in the previous section. The chapter ends with conclusions and discussion in Section 2.6.

2.2 Flow generation and amplification: momentum conservation

In this section the equations for mean toroidal and poloidal flow evolution equations are derived in slab geometry where x represents radial, y represents poloidal and z represents toroidal coordinates. We separate temporal and perpendicular spatial scales into a set of “fast” variables, (\vec{x}_\perp, t) , associated with the microturbulence and a set of “slow” variables (\vec{X}_\perp, T) , typical of slowly evolving equilibrium profiles[87]. Treating these fast and slow variables as independent one can decom-

pose the perpendicular space and time derivatives in the form

$$\vec{\nabla}_{\perp} \rightarrow \vec{\nabla}_{\perp}^{(0)} + \epsilon \vec{\nabla}_{\perp}^{(1)}, \quad \frac{\partial}{\partial t} \rightarrow \epsilon \frac{\partial}{\partial t} + \epsilon^2 \frac{\partial}{\partial T}, \quad \nabla_{\parallel} \rightarrow \epsilon \nabla_{\parallel} \quad (2.1)$$

where $\epsilon \sim (\rho_s/L_n) \sim (\omega/\omega_{ci}) \sim (k_{\parallel}/k_y) \ll 1$ in drift wave ordering. Here $\vec{\nabla}_{\perp}^{(0)}$ corresponds to a derivative with respect to \vec{x}_{\perp} and $\vec{\nabla}_{\perp}^{(1)}$ corresponds to a derivative with respect to \vec{X}_{\perp} . Furthermore, for any field f and its fluctuation $\delta f(x, t, X, T)$, we may define a space-time average over the fast scales such that $\langle \delta f(x, t, X, T) \rangle = 0$, but functions of only slow variables are left unaltered, i.e., $\langle f(X, T) \rangle = f(X, T)$. Similarly, averages over the fast scales annihilate derivatives of fast variables as well as derivatives along magnetic field lines but commute with slow derivatives, i.e., $\langle \vec{\nabla}_{\perp}^{(0)} f \rangle = \langle \nabla_{\parallel} f \rangle = 0$, but $\langle \vec{\nabla}_{\perp}^{(1)} f \rangle = \vec{\nabla}_{\perp}^{(1)} \langle f \rangle$. Using above tools to the momentum equation

$$m_i n_i \left(\frac{\partial}{\partial t} + \vec{V}_i \cdot \vec{\nabla} \right) \vec{V}_i = e n_i (\vec{E} + \vec{V}_i \times \vec{B}) - \vec{\nabla} P_i \quad (2.2)$$

the evolution equation for mean toroidal and poloidal flows are obtained up to order ϵ^4 as

$$\frac{\partial \langle V_{\parallel} \rangle}{\partial T} + \frac{\partial}{\partial X} \langle \delta v_{Ex} \delta v_{\parallel} \rangle + \frac{\partial}{\partial X} \langle \delta v_{polx} \delta v_{\parallel} \rangle = 0 \quad (2.3)$$

and

$$\frac{\partial \langle V_y \rangle}{\partial T} + \frac{\partial}{\partial X} \langle \delta v_{Ex} \delta v_{Ey} \rangle + \frac{\partial}{\partial X} \langle \delta v_{polx} \delta v_{Ey} \rangle = 0 \quad (2.4)$$

which are coupled through the radial force balance equation

$$\langle V_y \rangle = -\frac{E_x}{B_z} + \frac{1}{n_0 e B_z} \frac{dP_0}{dX} + \frac{\langle V_z \rangle B_y}{B_z} \quad (2.5)$$

Note that, though the third term in above mean toroidal and poloidal momentum equation is nominally one order higher it will be shown in Section 2.5.1 that under certain conditions the second and third terms can become comparable.

2.3 Model equations

In this section the linear eigenfunction for electrostatic ITG instability in the presence of mean flows is derived. In the following we derive a simplified set of fluid equations governing the electrostatic ion temperature gradient driven instability in

the presence of poloidal and toroidal sheared seed flows, under the assumption of 1) quasi-neutrality $\delta\tilde{n}_e = \delta\tilde{n}_i$, 2) constant electron temperature, 3) zero resistivity, 4) zero electron inertia for $c_i \leq \frac{\omega}{k_{\parallel}} < c_e$, 4) $\omega \ll \omega_{ci}$ and 5) $\eta_i > 1$, ITG mode dominated regime. Here $c_{i,e} = \sqrt{\frac{T_{0i,e}}{m_{i,e}}}$ is the ion(i)/electron(e) thermal speed, $T_{0i,e}$ are ion(i)/electron(e) temperature, $m_{i,e}$ is ion/electron mass, ω is a typical frequency, $\omega_{ci} = \frac{eB}{m_i}$ is ion cyclotron frequency and $\eta_i = \frac{L_n}{L_{T_i}}$ is the ratio of density and ion temperature scale lengths, $L_n^{-1} = -\frac{d \ln n_0}{dx}$ and $L_{T_i}^{-1} = -\frac{d \ln T_{i0}}{dx}$ respectively. We consider a sheared slab configuration of magnetic field \vec{B} and an equilibrium flow velocity lying in the (y,z) plane and all equilibrium quantities varying in x direction

$$\vec{B} = B(\hat{z} + \frac{x - x_0}{L_s}\hat{y}) \quad (2.6)$$

which represents neighborhood of a rational surface situated at x_0 , where $L_s^{-1} = \frac{B'_y}{B}$ is magnetic shear scale length. $\hat{x}, \hat{y}, \hat{z}$ are unit vectors in (x, y, z) orthogonal Cartesian coordinate system. For fluctuations localized on a particular rational surface at $x = x_0$, the mean ion flow velocity \vec{V}_{i0} may be expanded as

$$\vec{V}_{i0}(x) = \vec{V}_{i0}(x_0) + (x - x_0) \left(\frac{\partial \vec{V}_{i0}}{\partial x} \right) + \dots \quad (2.7)$$

We will describe the system of equations in inertial frame moving with constant velocity $\vec{V}_{i0}(x_0)$. The electron response is adiabatic

$$\frac{\delta n_e}{n_0} = \frac{e\delta\phi}{T_e} \quad (2.8)$$

The ion response is determined by the continuity equation, the momentum equation and the pressure evolution equation

$$\frac{\partial n_i}{\partial t} + \vec{\nabla} \cdot (n_i \vec{V}_i) = 0 \quad (2.9)$$

$$m_i n_i \left(\frac{\partial}{\partial t} + \vec{V}_i \cdot \vec{\nabla} \right) \vec{V}_i = e n_i (\vec{E} + \vec{V}_i \times \vec{B}) - \vec{\nabla} P_i \quad (2.10)$$

$$\left(\frac{\partial}{\partial t} + \vec{V}_i \cdot \vec{\nabla} \right) P_i + \gamma P_i \vec{\nabla} \cdot \vec{V}_i = 0 \quad (2.11)$$

where n , m , V , \vec{E} , \vec{B} , P are density, mass, velocity, electric field, magnetic field, and pressure respectively and subscript i stands for ion. The perpendicular ion dynamics, in drift wave regime $\omega \ll \omega_{ci}$, with equilibrium flows are due to $\vec{E} \times \vec{B}$, ion diamagnetic drift and polarization drifts :

$$\vec{V}_{i\perp} = \vec{V}_E + \vec{V}_{*i} + \vec{V}_{pol} \quad (2.12)$$

where $E \times B$ and diamagnetic drifts are of first order and polarization drift term is of second order in (ω/ω_{ci}) which are given by

$$\vec{V}_E = \frac{\vec{B} \times \vec{\nabla} \phi}{B^2} \quad (2.13)$$

$$\vec{V}_{*i} = \frac{\vec{B} \times \vec{\nabla} P_i}{en_i B^2} \quad (2.14)$$

$$\vec{V}_{pol} = -\frac{1}{B\omega_{ci}} \left(\frac{\partial}{\partial t} + (\vec{V}_E + \vec{V}_{*pi}) \cdot \vec{\nabla} \right) \vec{\nabla}_{\perp} \phi \quad (2.15)$$

In the limit when the equilibrium scale is larger than perturbation scale, we can separate equilibrium and fluctuating parts in Equations(2.9-2.11) as $f_i = f_{i0}(\vec{x}) + \delta f_i(\vec{x}, t)$. Then the perturbed nonlinear continuity, momentum and pressure equation for ions becomes as follows.

$$\begin{aligned} & \left(\frac{\partial}{\partial t} + x\hat{V}'_{E0} \cdot \vec{\nabla} \right) n_i + \nabla_y \phi - \left(\frac{\partial}{\partial t} + x\hat{V}'_{E0} \cdot \vec{\nabla} - K\nabla_y \right) \nabla_{\perp}^2 \phi + \nabla_{\parallel} v \\ & + \hat{\Phi}_0'' \nabla_x \nabla_y p + \hat{\Phi}_0''' \nabla_y (\phi + p) + [\phi, n] - [\phi + p, \nabla_{\perp}^2 \phi] - \left[\frac{\partial p}{\partial x}, \frac{\partial \phi}{\partial x} \right] \\ & - \left[\frac{\partial p}{\partial y}, \frac{\partial \phi}{\partial y} \right] = 0 \end{aligned} \quad (2.16)$$

$$\left(\frac{\partial}{\partial t} + x\hat{V}'_{E0} \nabla_y \right) v - \hat{V}'_{\parallel 0} \nabla_y \phi + \nabla_{\parallel} (p + \phi) + [\phi, v] = 0 \quad (2.17)$$

$$\left(\frac{\partial}{\partial t} + x\hat{V}'_{E0} \nabla_y \right) p + K\nabla_y \phi + \Gamma \nabla_{\parallel} v + [\phi, p] = 0 \quad (2.18)$$

Linearizing the set of Equations(2.16-2.18), we get

$$\left(\frac{\partial}{\partial t} + x\hat{V}'_{E0} \nabla_y \right) (1 - \nabla_{\perp}^2) \phi + (1 + K\nabla_{\perp}^2) \nabla_y \phi + \nabla_{\parallel} v = 0 \quad (2.19)$$

$$\left(\frac{\partial}{\partial t} + x\hat{V}'_{E0}\nabla_y\right)v - \hat{V}'_{\parallel 0}\nabla_y\phi + \nabla_{\parallel}(p + \phi) = 0 \quad (2.20)$$

$$\left(\frac{\partial}{\partial t} + x\hat{V}'_{E0}\nabla_y\right)p + K\nabla_y\phi + \Gamma\nabla_{\parallel}v = 0 \quad (2.21)$$

where normalization is

$$x = (x-x_0)/\rho_s, \quad y = y/\rho_s, \quad z = z/L_n, \quad t = tc_s/L_n, \quad \phi = (e\delta\phi/T_e)(L_n/\rho_s), \quad n_i = (\delta n_i/n_0)(L_n/\rho_s) \\ v = (\delta v_{\parallel i}/c_s)(L_n/\rho_s), \quad p = (\tau_i\delta p_i/P_{i0})(L_n/\rho_s), \quad L_n\nabla_{\parallel} \equiv \nabla_{\parallel} = \frac{\partial}{\partial z} + xs\frac{\partial}{\partial y} \text{ and the non dimensional parameters are } \eta_i = L_n/L_T, \quad K = \tau_i(1 + \eta_i) = \tau_i\alpha_i, \tau_i = T_{0i}/T_{0e}, \quad \Gamma = \gamma\tau_i, \quad s = L_n/L_s, \quad \hat{V}'_{E0} = (L_n/c_s)V'_{E0}, \quad \hat{V}'_{\parallel 0} = (L_n/c_s)V'_{\parallel 0}, \quad \rho_s = c_s/\omega_{ci}.$$

Now considering the perturbation of the form $f = f_k(x)\exp(ik_y y - i\omega t)$, where k_y and ω are normalized as $k_y = k_y\rho_s, \omega = \omega/(c_s/L_n)$, the above set of Equations(2.19-2.21) form an eigenvalue problem in x direction in ϕ_k

$$\frac{d^2\phi_k}{dx^2} + \left[-k_y^2 + \frac{k_y - \omega}{\tau_i\alpha_i k_y + \omega - xk_y\hat{V}'_{E0}} + k_y^2 \frac{(sx)^2}{(\omega - xk_y\hat{V}'_{E0})^2 - \Gamma(sx)^2} \right] \phi_k \\ + xk_y \left[\frac{\hat{V}'_{E0}}{\tau_i\alpha_i k_y + \omega - xk_y\hat{V}'_{E0}} - \frac{\hat{V}'_{\parallel 0}}{(\omega - xk_y\hat{V}'_{E0})(\tau_i\alpha_i k_y + \omega - xk_y\hat{V}'_{E0})} \right] \phi_k = 0 \quad (2.22)$$

For flow shear frequency much smaller than the mode frequency Equation(2.22) simplifies to

$$\frac{d^2\phi_k}{dx^2} + \left[-k_y^2 + \frac{k_y - \omega}{\tau_i\alpha_i k_y + \omega} + k_y^2 \frac{(sx)^2}{\omega^2} + xk_y \left[\frac{\hat{V}'_{E0}}{\tau_i\alpha_i k_y + \omega} - \frac{\hat{V}'_{\parallel 0}}{\omega(\tau_i\alpha_i k_y + \omega)} \right] \right] \phi_k = 0 \quad (2.23)$$

which can be written as

$$\frac{d^2\phi_k}{dx^2} + (A_1 + A_2x + A_3x^2) \phi_k = 0 \quad (2.24)$$

where

$$A_1 = \frac{k_y - \omega}{\tau_i\alpha_i k_y + \omega} - k_y^2, A_2 = \frac{k_y}{\tau_i\alpha_i k_y + \omega} \left(\hat{V}'_{E0} - k_y s \frac{\hat{V}'_{\parallel 0}}{\omega} \right), A_3 = \left(\frac{k_y s}{\omega} \right)^2 \quad (2.25)$$

Using the transformation

$$\xi = (-A_3)^{1/4} \left(x + \frac{A_2}{2A_3} \right) \quad (2.26)$$

above Equation(2.24) becomes

$$\frac{d^2 \phi_k}{d\xi^2} + (E - \xi^2) \phi_k = 0 \quad (2.27)$$

where $E = \left(A_1 - \frac{A_2^2}{4A_3} \right) / \sqrt{(-A_3)}$ The solution of Equation(2.27) is

$$\phi_{kl} = \phi_0 \exp\left(-\frac{\xi^2}{2}\right) H_l(\xi) \quad (2.28)$$

with

$$E = 2l + 1, l = 0, 1, 2, 3, \dots etc \quad (2.29)$$

Being the most dominant we will consider the $l = 0$ mode for which the eigen function in x is

$$\phi_k = \phi_0 \exp \left[-\frac{1}{2} i \sqrt{A_3} \left(x + \frac{A_2}{2A_3} \right)^2 \right] \quad (2.30)$$

and the corresponding eigenmode dispersion relation is

$$\omega^2 (1 + k_y^2) + \omega k_y (-1 + k_y^2 \tau_i \alpha_i + i s) + i s \tau_i \alpha_i k_y^2 = -\frac{\omega k_y^2 \left[\frac{\omega}{s k_y} \hat{V}'_{E0} - \hat{V}'_{\parallel 0} \right]^2}{4 (\tau_i \alpha_i k_y + \omega)} \quad (2.31)$$

Equation 2.30 shows that the eigenfunction is shifted off the mode rational surface in the presence of background sheared flows and it has a propagating wave nature as well. In the limit $\hat{V}'_{E0} = \hat{V}'_{\parallel 0} = 0$ and $s \ll 1$ and for long wavelength mode satisfying $|k_y^2 \tau_i \alpha_i| \ll 1$ we get the purely a growing mode

$$\omega = i s \tau_i \alpha_i k_y \quad (slow \quad mode) \quad (2.32)$$

Taking this as the zeroth order ω i.e. ω_0 and taking other parameters perturbatively can get the next order frequency ω_1 which carries the effect of flows. Using the

ordering: $|k_y^2 \tau_i \alpha_i| \equiv \epsilon |k_y^2 \tau_i \alpha_i|$, $s \equiv \epsilon s$, $\left(\frac{\omega}{s k_y} \hat{V}'_{E0} - \hat{V}'_{\parallel 0}\right)^2 \equiv \epsilon \left(\frac{\omega}{s k_y} \hat{V}'_{E0} - \hat{V}'_{\parallel 0}\right)^2$, we get

$$\omega_{1r} = -s^2 k_y \tau_i \alpha_i [1 + \tau_i \alpha_i (1 + k_y^2)] + 0.5 s \tau_i \alpha_i k_y \hat{V}'_{E0} \hat{V}'_{\parallel 0} \quad (2.33)$$

$$\omega_{1i} = s \tau_i \alpha_i k_y \left[\tau_i \alpha_i k_y^2 + \frac{1}{4 \tau_i \alpha_i} \left[- \left(\tau_i \alpha_i \hat{V}'_{E0} \right)^2 + \hat{V}_{\parallel 0}'^2 \right] \right] \quad (2.34)$$

This shows that growth rate decreases with increasing \hat{V}'_{E0} where as it increases with increasing $\hat{V}'_{\parallel 0}$. This could be due to K-H instability. However, this is not prime focus of the present work and will be discussed somewhere else. Anyway for calculating turbulent parallel momentum flux we will use the purely growing status of this mode. When $\hat{V}'_{E0} = \hat{V}'_{\parallel 0} = 0$ and under the assumption that $|1 - k_y^2 \tau_i \alpha_i| \lesssim s \ll 1$ the fastest growing mode occurs at $k_y^2 = (\tau_i \alpha_i)^{-1}$ which is given by

$$\omega = (-1 + i) \sqrt{\frac{s}{2(1 + k_y^2)}} \quad (fast \quad mode) \quad (2.35)$$

2.4 Momentum flux

In this section we calculate toroidal and poloidal quasi-linear momentum fluxes due to $E \times B$ drift and polarization drift. Assuming flow shear frequency much smaller than the mode frequency the linear response for δv_{\parallel} , in dimensional form, from Equations(2.20,2.21) is obtained to be

$$\delta v_{\parallel, k} = \left(\frac{c_s \rho_s}{L_n} \right) \frac{k_y}{\omega} \left[-\hat{V}'_{\parallel 0} + \frac{k_{\parallel}}{k_y} \left[1 - \frac{\omega_{*pi}}{\omega} \right] \right] \phi_k \quad (2.36)$$

The response for $\delta v_{y, k}$ is obtained from Equations(2.12,2.13) as

$$\delta v_{y, k} = \delta v_{Ey, k} = i \left(\frac{c_s \rho_s}{L_n} \right) k_x \phi_k \quad (2.37)$$

The response for $\delta v_{pol, k}$ is obtained from Equation(2.15) as

$$\delta v_{pol, k} = -c_s \left(\frac{\rho_s}{L_n} \right)^2 \omega k_x \phi_k \quad (2.38)$$

where $\omega_{*pi} = -\tau_i \alpha_i k_y$, $k_x = -i \partial \ln \phi_k / \partial x$. Further we will make use of the following definition for averaging

$$\langle AB \rangle = \sum_{\vec{k}} A_{\vec{k}}^* B_{\vec{k}} = \sum_{\vec{k}} A_{-\vec{k}} B_{\vec{k}} \quad (2.39)$$

for two fluctuating fields A and B when they do not contain explicit time derivatives. To proceed further we use

$$\sum_{\vec{k}} = \sum_{k_y} \int dk_{\parallel} = \sum_{k_y} k_y s \int_{-\infty}^{+\infty} dx \quad (2.40)$$

to carry out the $\sum_{\vec{k}}$.

2.4.1 $E \times B$ Flux

From linear responses for $\delta v_{\parallel,k}$ from Equation(2.36) and for δv_{Ex} from Equation(2.13) we obtain a quasilinear form of toroidal Reynolds stress (with seed flows)

$$\langle \delta v_{Ex} \delta v_{\parallel} \rangle = Re \left(\frac{c_s \rho_s}{L_n} \right)^2 \sum_{\vec{k}} i \frac{k_y^2}{\omega} \left[-\hat{V}'_{\parallel 0} + \frac{k_{\parallel}}{k_y} \left[1 - \frac{\omega_{*pi}}{\omega} \right] \right] |\phi_k|^2 \quad (2.41)$$

the first term is diffusive and the second term, being independent of V_{\parallel} and V'_{\parallel} , is non-diffusive residual flux. Since $k_{\parallel} = k_y s x$ so, $\langle k_{\parallel} / k_y \rangle$ survives when scalar potential ϕ_k possess odd parity about a mode-rational surface and poloidal stress is

$$\langle \delta v_{Ex} \delta v_y \rangle = -Re \sum_{\vec{k}} \left(\frac{c_s \rho_s}{L_n} \right)^2 k_y k_x |\phi_k|^2 \quad (2.42)$$

It is obvious that poloidal flux survives only if $k_x \neq 0$. In case of standing eigenmodes k_x is imaginary and hence mean flow can not be generated. If k_x is linear in x , as happens to be for electrostatic drift waves, another turbulence characteristic necessary for poloidal flow generation is that of radial asymmetry of fluctuation spectrum about mode-rational surface. This is analogous to $\langle k_{\parallel} \rangle$ symmetry breaking and hence may be termed as $\langle k_x \rangle$ symmetry breaking. Note that in Equation(2.42) the diamagnetic advecting velocity δv_{*x} does not appear because of the

well known “gyro-viscous cancellation”. The advected diamagnetic velocity δv_{*y} is not considered under the assumption of weaker diamagnetic velocity fluctuation i.e., $\delta v_{*y} \ll \delta v_{Ey}$. We now calculate toroidal and poloidal stresses explicitly for slow Equation(2.32) and fast Equation(2.35) modes.

Slow mode

Using Equations (2.32) and (2.25), various parameters are

$$\sqrt{A_3} = \frac{k_y s}{\omega} = \frac{1}{i\tau_i \alpha_i} \quad (2.43)$$

$$\frac{A_2}{2A_3} \cong -\frac{1}{2} \left(\tau_i \alpha_i \hat{V}'_{E0} + i\hat{V}'_{\parallel 0} \right), (s \ll 1) \quad (2.44)$$

And hence using Equation(2.44) the eigenfunction Equation(2.30) becomes

$$\phi_k = \phi_{0ks} \exp \left[-\frac{1}{2} \left(\frac{x - \xi_{ks}}{\Delta_{ks}} \right)^2 \right] \exp \left[i \frac{\hat{V}'_{\parallel 0}}{2\tau_i \alpha_i} x \right] \quad (2.45)$$

for which the radial wave number is

$$k_x = i \frac{x - \xi_{ks}}{\Delta_{ks}^2} + \frac{\hat{V}'_{\parallel 0}}{2\tau_i \alpha_i} \quad (2.46)$$

Note that Equation(2.45) represents spatially bound growing mode with a finite Rek_x whose mode half-width is $\Delta_{ks} = \sqrt{\tau_i \alpha_i}$ and is shifted by $\xi_k = \tau_i \alpha_i \hat{V}'_{E0}/2$ from the mode rational surface. Also a finite real Rek_x of the eigenmode is equivalent to having a finite radial group velocity because the eigenfunction actually represents a wave packet rather than a single wave. From Equation(2.45) the square amplitude of the mode is

$$|\phi_k|^2 = |\phi_{0ks}|^2 \exp \left[-\left(\frac{x - \xi_{ks}}{\Delta_{ks}} \right)^2 \right] \quad (2.47)$$

Using Equations(2.32) and (2.47) in Equation(2.41) the toroidal Reynolds stress from $E \times B$ drift for slow mode is

$$\langle \delta v_{Ex} \delta v_{\parallel} \rangle = \sum_{k_y} \left(\frac{c_s \rho_s}{L_n} \right)^2 k_y^2 \left[-\hat{V}'_{\parallel 0} + s\xi_{ks} \right] \sqrt{\pi}/\Delta_{ks} |\phi_{0ks}|^2 \quad (2.48)$$

and the poloidal stress due to $E \times B$ drift for slow mode is

$$\langle \delta v_{Ex} \delta v_y \rangle = - \sum_{k_y} \left(\frac{c_s \rho_s}{L_n} \right)^2 k_y^2 s \left(\hat{V}'_{\parallel 0} / 2 \Delta_{ks} \right) |\phi_{0ks}|^2 \quad (2.49)$$

which is purely non-diffusive flux, and hence is capable to produce intrinsic mean poloidal rotation.

Fast mode

We now evaluate the eigenfunction for fast ITG mode. For computing eigenfunction various parameters, using Equations (2.35) and (2.25), are

$$i\sqrt{A_3} = (1 - i) \sqrt{\frac{s(1 + \tau_i \alpha_i)}{2(\tau_i \alpha_i)^2}}, \frac{A_2}{2A_3} = -\frac{i\tau_i \alpha_i \hat{V}'_{E0}}{2s(\tau_i \alpha_i + 1)} \quad (2.50)$$

In the limit when $\hat{V}'_{E0} \gg \hat{V}'_{\parallel 0}(\tau_i \alpha_i)^{-1} \sqrt{2s(1 + \tau_i \alpha_i)}$ and $\tau_i \alpha_i k_y \gg \omega$. Corresponding fast growing eigenfunction turns out to be

$$\phi_k = \phi_{0kf} \exp \left[-\frac{1}{2} \left(\frac{x - \xi_{kf}}{\Delta_{kf}} \right)^2 \right] \exp \left[\frac{i}{2} \left(\frac{x + \xi_{kf}}{\Delta_{kf}} \right)^2 \right] \quad (2.51)$$

for which the radial wave number is

$$k_x = i \frac{x - \xi_{kf}}{\Delta_{kf}^2} + \frac{x + \xi_{kf}}{\Delta_{kf}^2} \quad (2.52)$$

where $\xi_{kf} = \tau_i \alpha_i \hat{V}'_{E0} / 2s(\tau_i \alpha_i + 1)$ is the mode shift off the rational surface and $\Delta_{kf}^{-2} = \sqrt{s(\tau_i \alpha_i + 1) / 2(\tau_i \alpha_i)^2}$ where Δ_{kf} is half-width of the mode. Here again the existence of finite $Re k_x$ is equivalent to having a finite radial group velocity. The square of the amplitude of the fast eigenmode is

$$|\phi_k|^2 = |\phi_{0kf}|^2 \exp \left[-\left(\frac{x - \xi_{kf}}{\Delta_{kf}} \right)^2 \right] \quad (2.53)$$

Toroidal stress due to $E \times B$ drift for fast mode is

$$\langle \delta v_{Ex} \delta v_{\parallel} \rangle = \sum_{k_y} \left(\frac{c_s \rho_s}{L_n} \right)^2 \frac{k_y^3 s}{2\gamma_f} \left[-\hat{V}'_{\parallel 0} + \left(1 + \frac{\omega_{*pi}}{\gamma_f} \right) s \xi_{kf} \right] \Delta_{kf} \sqrt{\pi} |\phi_{0kf}|^2 \quad (2.54)$$

The appearance of γ_f in the denominator can be traced back to the particular form of the fast mode frequency Equation(2.35) by writing it in the form $\omega = (-1+i)\gamma_f$. Poloidal stress due to $E \times B$ drift for fast mode is

$$\langle \delta v_{Ex} \delta v_y \rangle = - \sum_{k_y} \left(\frac{c_s \rho_s}{L_n} \right)^2 k_y^2 s \left[2 \frac{\xi_{kf}}{\Delta_{kf}} \right] \sqrt{\pi} |\phi_{0kf}|^2 \quad (2.55)$$

which does not contain a non-diffusive component for the assumptions made in this section. This means either no or very weak intrinsic poloidal flow, compared to intrinsic toroidal flow, is generated due to fast modes. It is also obvious that fast mode is dominant for intrinsic toroidal rotation generation whereas slow mode is dominant for intrinsic poloidal rotation generation. From above analysis of $E \times B$ flux few points are in order. The residual toroidal flux is proportional to mean electric field shear, and hence to mean pressure gradient, and so this mechanism of flow generation is active in high pressure gradient region, typical to the edge of H-mode plasma.

2.4.2 Polarization driven flux

From linear responses for $\delta v_{\parallel,k}$, $\delta v_{y,k}$, δv_{polx} from Equations(2.36), (2.37) and (2.15) respectively, we obtain a quasilinear form of toroidal stress

$$\begin{aligned} \langle \delta v_{polx} \delta v_{\parallel} \rangle &= -c_s^2 \left(\frac{\rho_s}{L_n} \right)^3 \frac{\partial}{\partial T} \langle \frac{\partial \phi}{\partial x} \delta v_{\parallel} \rangle \\ &+ c_s^2 \left(\frac{\rho_s}{L_n} \right)^3 Re \sum_{\vec{k}} \left[\hat{V}'_{\parallel 0} k_x^* k_y - k_x^* k_{\parallel} \left[1 - \frac{\omega_{*pi}}{\omega} \right] \right] |\phi_k|^2 \end{aligned} \quad (2.56)$$

and poloidal stress

$$\langle \delta v_{polx} \delta v_y \rangle = -c_s^2 \left(\frac{\rho_s}{L_n} \right)^3 \frac{\partial}{\partial T} \left[\frac{1}{2} \left\langle \left(\frac{\partial \phi}{\partial x} \right)^2 \right\rangle \right] \quad (2.57)$$

where $Re(f)$ means real part of (f) and the angular braces indicates average over fast space-time scale. Equation(2.56) reveals that the time asymptotic polarization drift induced residual stress survives when the spectral average $\langle k_{\parallel} k_x \rangle \neq 0$ which is always satisfied because $k_{\parallel} \propto x$ and $k_x \propto x$ in general, and due to the shifted gaussian structure of the fluctuation spectrum. Equation(2.57) suggests that poloidal momentum flux due to polarization drift vanishes for stationary solutions. Moreover, the time derivatives in Equations(2.56) and (2.57) are of ϵ^4 order and so they are not considered in our further discussions. Now we calculate toroidal stresses due to polarization drift explicitly for slow (Equation(2.32)) and fast (Equation(2.35)) modes.

Slow mode

From Equations(2.47), (2.56), and (2.57) we obtain toroidal stress

$$\langle \delta v_{polx} \delta v_{\parallel} \rangle = \sum_{k_y} c_s^2 \left(\frac{\rho_s}{L_n} \right)^3 k_y^2 \left[\frac{\hat{V}'_{\parallel 0} k_y}{2\tau_i \alpha_i} \hat{V}'_{\parallel 0} \Delta_{ks} \sqrt{\pi} - \frac{\Delta_{ks}}{2} \sqrt{\pi} \right] |\phi_{0ks}|^2 + O(\epsilon^4) \quad (2.58)$$

where it is clearly seen that the diffusive component of flux is modulated by the propagating wave nature of the eigenmode. The effect of eigenmode shift on toroidal momentum conductivity comes at a higher order ϵ^4 . The eigenmode shift also contributes to the non-diffusive non-pinch component of the toroidal momentum flux for slow mode but at even higher order ϵ^5 and hence the effect of spectral shift off the mode rational surface here can be ignored in the total toroidal momentum flux budget. The term independent of $\hat{V}'_{\parallel 0}$ and ξ_{ks} is identified as a purely “seedless” contribution to total toroidal momentum flux which we term as “seedless” residual flux.

Fast mode

Similarly from Equations(2.53), (2.56), and (2.57), we obtain toroidal stress

$$\langle \delta v_{pol} \delta v_{\parallel} \rangle = \sum_{k_y} c_s^2 \left(\frac{\rho_s}{L_n} \right)^3 (k_y s)^2 \left[2 \frac{\xi_{kf}}{s \Delta_{kf}} \hat{V}'_{\parallel 0} - \left(1 + \frac{\omega_{*pi}}{\gamma_f} \right) \frac{\Delta_{kf}}{2} \right] \sqrt{\pi} |\phi_{0kf}|^2 + O(\epsilon^5) \quad (2.59)$$

Here, again the origin of γ_f in the denominator is because of the particular form of the fast mode frequency Equation(2.35) where real and imaginary parts are equal in magnitude. The diffusive flux shown in the above expression is of ϵ^4 order and hence will not be considered in momentum flux budget. We strongly emphasize that in the limit of vanishing “seed flows” the polarization drift driven toroidal momentum fluxes are residual in nature which we term here as “seedless” residual flux which, being independent of mean radial electric field shear, is likely to be active in wide parameter regime and may complement the toroidal flow generation mechanism in weak mean electric field shear region or flat pressure profile region.

2.5 Coupled Toroidal and Poloidal Flow Equations

Using expressions for toroidal and poloidal stresses obtained in the previous section, we obtain coupled toroidal and poloidal flow equations, from Equations(2.3,2.4) as

$$\frac{\partial \langle V_{\parallel} \rangle}{\partial T} + \frac{\partial}{\partial X} \left[- \left(\chi_{\parallel E} + \chi_{\parallel pol} \right) \frac{\partial V_{\parallel}}{\partial X} - \chi_y \frac{\partial V_y}{\partial X} + S_{\parallel E} + S_{\parallel pol} \right] = 0 \quad (2.60)$$

where for the slow mode

$$\chi_{\parallel E} = \sum_{k_y} \left(\frac{c_s \rho_s}{L_n} \right)^2 k_y^2 \frac{\sqrt{\pi}}{\Delta_{ks}} \frac{L_n}{c_s} |\phi_{0ks}|^2 + \sum_{k_y} \left(\frac{c_s \rho_s}{L_n} \right)^2 k_y s \frac{B_y}{B} \frac{\tau_i \alpha_i}{2} \frac{\sqrt{\pi}}{\Delta_{ks}} \frac{L_n}{c_s} |\phi_{0ks}|^2 \quad (2.61)$$

$$\chi_{\parallel pol} = - \sum_{k_y} c_s^2 \left(\frac{\rho_s}{L_n} \right)^3 k_y^2 s \hat{V}'_{\parallel 0} \frac{\sqrt{\pi}}{2 \Delta_{ks}} \frac{L_n}{c_s} |\phi_{0ks}|^2 \quad (2.62)$$

$$\chi_y^{\parallel} = - \sum_{k_y} \left(\frac{c_s \rho_s}{L_n} \right)^2 k_y s \frac{\tau_i \alpha_i}{2} \frac{\sqrt{\pi}}{\Delta_{ks}} \frac{L_n}{c_s} |\phi_{0ks}|^2 \quad (2.63)$$

$$S_{\parallel E} = - \sum_{k_y} \left(\frac{c_s \rho_s}{L_n} \right)^2 k_y^2 s \frac{\tau_i \alpha_i}{2} \frac{\sqrt{\pi}}{\Delta_{ks}} V'_{*pi} \frac{L_n}{c_s} |\phi_{0ks}|^2 \quad (2.64)$$

$$S_{\parallel pol} = - \sum_{k_y} c_s^2 \left(\frac{\rho_s}{L_n} \right)^3 k_y^2 s \Delta_{ks} \frac{\sqrt{\pi}}{2} |\phi_{0ks}|^2 \quad (2.65)$$

and for the fast mode,

$$\chi_{\parallel E}^{\parallel} = \sum_{k_y} \left(\frac{c_s \rho_s}{L_n} \right)^2 \frac{k_y^3 s}{2\gamma_f} \left[1 + \left(1 + \frac{\omega_{*pi}}{\gamma_f} \right) \frac{B_y}{B} \frac{\tau_i \alpha_i}{2(1 + \tau_i \alpha_i)} \right] \sqrt{\pi} \Delta_{kf} \frac{L_n}{c_s} |\phi_{0ks}|^2 \quad (2.66)$$

$$\chi_{\parallel pol}^{\parallel} = 0 \quad (2.67)$$

$$\chi_y^{\parallel} = - \sum_{k_y} \left(\frac{c_s \rho_s}{L_n} \right)^2 \frac{k_y^3 s}{2\gamma_f} \left[1 + \frac{\omega_{*pi}}{\gamma_f} \right] \frac{\tau_i \alpha_i}{2(1 + \tau_i \alpha_i)} \sqrt{\pi} \Delta_{kf} \frac{L_n}{c_s} |\phi_{0ks}|^2 \quad (2.68)$$

$$S_{\parallel E} = - \sum_{k_y} \left(\frac{c_s \rho_s}{L_n} \right)^2 \frac{k_y^3 s}{2\gamma_f} \left[1 + \frac{\omega_{*pi}}{\gamma_f} \right] \frac{\tau_i \alpha_i}{2(1 + \tau_i \alpha_i)} V'_{*pi} \sqrt{\pi} \Delta_{kf} \frac{L_n}{c_s} |\phi_{0ks}|^2 \quad (2.69)$$

$$S_{\parallel pol} = - \sum_{k_y} c_s^2 \left(\frac{\rho_s}{L_n} \right)^3 (k_y s)^2 \left[1 + \frac{\omega_{*pi}}{\gamma_f} \right] \Delta_{kf} \frac{\sqrt{\pi}}{2} |\phi_{0ks}|^2 \quad (2.70)$$

and

$$\frac{\partial \langle V_y \rangle}{\partial T} + \frac{\partial}{\partial X} \left[- \left(\chi_{\parallel E}^y + \chi_{\parallel pol}^y \right) \frac{\partial V_{\parallel}}{\partial X} - \chi_y^y \frac{\partial V_y}{\partial X} + S_{yE} + S_{ypol} \right] + \nu_{neo} V_y = 0 \quad (2.71)$$

where for slow mode

$$\chi_{\parallel E}^y = \sum_{k_y} \left(\frac{c_s \rho_s}{L_n} \right)^2 k_y s \frac{\sqrt{\pi}}{2\Delta_{ks}} \frac{L_n}{c_s} |\phi_{0ks}|^2 \quad (2.72)$$

$$\chi_{\parallel pol}^y = 0 \quad (2.73)$$

$$\chi_y^y = 0 \quad (2.74)$$

$$S_{yE} = 0 \quad (2.75)$$

$$S_{ypol} = 0 \quad (2.76)$$

and for fast mode

$$\chi_{\parallel E}^y = \sum_{k_y} \left(\frac{c_s \rho_s}{L_n} \right)^2 k_y^2 s \frac{B_y}{B} \frac{\tau_i \alpha_i}{2s(1 + \tau_i \alpha_i)} \frac{2\sqrt{\pi}}{\Delta_{kf}} \frac{L_n}{c_s} |\phi_{0ks}|^2 \quad (2.77)$$

$$\chi_{\parallel pol}^y = 0 \quad (2.78)$$

$$\chi_y^y = \sum_{k_y} \left(\frac{c_s \rho_s}{L_n} \right)^2 k_y^2 s \frac{\tau_i \alpha_i}{2s(1 + \tau_i \alpha_i)} \frac{2\sqrt{\pi}}{\Delta_{kf}} \frac{L_n}{c_s} |\phi_{0ks}|^2 \quad (2.79)$$

$$S_{yE} = \sum_{k_y} \left(\frac{c_s \rho_s}{L_n} \right)^2 k_y^2 s \frac{\tau_i \alpha_i}{2s(1 + \tau_i \alpha_i)} V'_{*pi} \frac{2\sqrt{\pi}}{\Delta_{kf}} \frac{L_n}{c_s} |\phi_{0ks}|^2 \quad (2.80)$$

$$S_{ypol} = 0 \quad (2.81)$$

where use has been made of the radial force balance equation in the form

$$\frac{\partial V_{Ey}}{\partial X} = \frac{\partial V_y}{\partial X} - \frac{\partial V_{*y}}{\partial X} - \frac{\partial}{\partial X} \left(\frac{B_y}{B} V_{\parallel} \right) \quad (2.82)$$

Note that a neoclassical damping term $\nu_{neo} V_y$ is included in the poloidal flow Equation(2.71) for saturation of flow. The coupling of toroidal and poloidal flow dynamics is appreciable in the following limits. a) For slow mode: when $k_y \approx s(B_y/B)(\tau_i \alpha_i)/2$ in Equation(2.61) and $V_y' \sim V_{\parallel}'(B_y/B) \sim V_{*pi}'$ in Equation(2.60). b) For fast mode: when $(1 + \frac{\omega_{*pi}}{\gamma_f})(B_y/B)(\tau_i \alpha_i)/(2(1 + \tau_i \alpha_i)) \sim 1$ in Equation(2.67) and $V_y' \sim V_{\parallel}'(B_y/B) \sim V_{*pi}'$ in Equation(2.60). Similarly from poloidal flow Equation(2.71) and the expressions following Equation(2.77), for fast mode, the flow

coupling is appreciable when $V_y' \sim V_{\parallel}'(B_y/B) \sim V_{*pi}'$.

2.5.1 Comparison of nondiffusive fluxes

Let's now compare various toroidal and poloidal non-diffusive fluxes, in order to see under what condition the contribution due to polarization drift be important. Estimating the magnitude of radial electric field shear by diamagnetic term in the radial force balance equation i.e, $\hat{V}_{E0}' \approx (\rho_s/L_n)\tau_i\alpha_i$, we get from residual component in Equation(2.48) and “seedless” residual component in Equation(2.58) and from residual component in Equation(2.54) and “seedless” residual component in Equation(2.59), respectively

$$\left| \frac{S_{\parallel, pol, slow}}{S_{\parallel, E, slow}} \right| \approx \frac{1}{\tau_i \alpha_i} \quad (2.83)$$

$$and \quad \left| \frac{S_{\parallel, pol, fast}}{S_{\parallel, E, fast}} \right| \approx \sqrt{2} s^{3/2} \frac{\sqrt{1 + \tau_i \alpha_i}}{\tau_i \alpha_i} \quad (2.84)$$

where S stands for respective residual components of toroidal and poloidal fluxes and γ_f is the fast mode linear growth rate. One observation that immediately follows from Equations(2.83) and (2.84) is that polarization drift driven toroidal momentum flux increasingly gains relative importance in weak temperature gradient region where radial electric field shear driven flux becomes vanishingly small. Above comparison also shows that the polarization driven flux is more active for slow mode compared to fast mode. As shown in Equations(2.56) and (2.57), the polarization drift driven poloidal stress vanishes for stationary state whereas corresponding parallel stress remains finite so one may conclude that the toroidal flow is stronger.

2.6 Discussion and conclusions

We performed systematic calculations of radial fluxes of turbulent momentum due to slab ITG mode in the presence of a mean velocity field. We see that in the presence of sheared seed flows the eigenfunction and the eigenspectrum is shifted off the mode rational surface, leading to $\langle k_{\parallel} \rangle$ symmetry breaking. Here it must be noted that fluctuation spectrum shift is proportional to both toroidal and poloidal

seed flow shear in general (see Equation(2.30)), but only the poloidal flow shear contributes to toroidal non-diffusive residual flux and the toroidal flow shear simply adds up with the diffusive component modifying the effective turbulent toroidal viscosity χ_ϕ . This makes residual stress non-zero which acts as a local toroidal momentum source to drive it further. Looking at the poloidal flow generation mechanism we see that like $\langle k_\parallel \rangle$ symmetry breaking “ $\langle k_x \rangle$ symmetry breaking” also produces non-diffusive residual poloidal momentum flux which is proportional to parallel seed flow shear. But because toroidal and poloidal flow shear are coupled by the radial force balance equation, the mean toroidal and poloidal flow dynamics gets naturally coupled. The principal results of this chapter are

- The coupled set of equations for evolution of mean toroidal and poloidal flows were derived (see Equations(2.60) and (2.71)).
- A novel non-diffusive residual component to the radial flux of toroidal and poloidal momentum has been derived, which arises from polarization drift in fluid theoretical framework. Though nominally it is higher order in expansion in $\epsilon \sim \omega/\omega_{ci} \sim \rho_s/L_n$, detailed analysis (Section2.5.1) shows that the polarization driven flux can become comparable to mean electric field shear driven flux in weak pressure gradient region and hence it complements to $E \times B$ shear driven flow generation mechanism in weak pressure gradient region. That is, if $E \times B$ shear is absent then polarization driven toroidal stress is alone capable to produce toroidal flow.
- This mechanism for toroidal flow generation does not require a mean electric field shear and it is due to $\langle k_\parallel k_x \rangle \neq 0$ which is fundamentally different from $\langle k_\parallel \rangle$ symmetry breaking mechanism. It is found that in steady state the polarization drift driven poloidal Reynolds stress vanishes and hence no residual stress is offered by polarization drift.

Next chapter presents another mechanism of k_\parallel symmetry breaking by steep density gradient alone which is independent of the density gradient contribution to the symmetry breaking coming from the radial $E \times B$ shear via the radial force balance relation.

Symmetry breaking effects of density gradient on parallel momentum transport: A new ρ_s^* effect

3.1 Introduction

It is now understood that a breaking of the symmetry of the underlying microturbulence is necessary in order for the turbulence to generate a net wave-momentum, whose flux is then tied to the transport of the bulk plasma momentum[88]. In addition to a diffusive component, the plasma momentum flux, consists of two separate kinds of off-diagonal pieces. The diffusive momentum flux has been studied extensively both theoretically [79, 89] and experimentally [80] and established momentum diffusivity $\chi_\phi \sim \chi_i$, ion thermal diffusivity except with some departure from this scaling noted in recent gyrokinetic simulation [81]. The effects of curvature in a tokamak, result in a pinch-like contribution[90, 84, 91, 92, 93], mainly via a turbulent equipartition (TEP) mechanism[91]. While this term transports momentum (especially when the rotation is already sufficiently large), its effect on rotation itself is not too pronounced. In contrast a residual stress term can be driven by various different mechanisms including Alfvén waves [94], intensity gradients [95], up-down asymmetry of current [42, 43] and toroidicity [41]. And the residual stress due to a self-consistent $E \times B$ shear that feedback from the pressure gradient through the radial force balance is a possible mechanism that may explain the intrinsic L-H spin-up[96]. Experiments on JT-60U by Yoshida *et al* [85] also

seems to support this pressure gradient scaling. However the discovery of I mode [97], where particle transport is like L mode and energy transport is like H mode, and a recent follow up experiment by Rice *et al* [24] in Alcator C-Mod suggests that gradient in temperature rather than gradient in pressure is the main driver of intrinsic rotation. Experiments on the Large Helical Device (LHD) with ITB also demonstrates temperature gradient as the driver of toroidal intrinsic rotation [98]. Recent gyro-kinetic simulations [89, 99, 100] have verified certain aspects of mean $E \times B$ shear driven mechanism and also highlighted the role of the intensity gradient [95] as a mechanism for driving residual stress. Wang *et al* [99, 101], in gyrokinetic simulations, have also demonstrated nonlinear residual stress generation in collisionless trapped electron mode turbulence. The fundamental similarity underlying all the above mentioned residual stress generation mechanisms is the symmetry breaking in k_{\parallel} (i.e., $\langle k_{\parallel} \rangle \neq 0$ where $\langle \rangle$ indicates average over fluctuation spectrum) by macroscopic gradients. Different means of breaking $\langle k_{\parallel} \rangle$ symmetry has lead to different mechanisms of residual stress generation. For example, $\langle k_{\parallel} \rangle$ symmetry breaking by asymmetrizing the eigenfunction via mean $E \times B$ shear [96, 102]. A fundamentally different mechanism of residual stress generation based on $\langle k_{\parallel} k_x \rangle$ symmetry breaking has also been shown to be driven by polarization drift [39, 40, 102] which does not require asymmetry in eigenfunction. The residual stress is the key driver of intrinsic rotation be it toroidal or azimuthal [102]. The connection between azimuthal intrinsic rotation and directly measured azimuthal residual stress has been demonstrated by Yan *et al* [103] in CSDX plasmas. The residual stress combined with proper boundary condition can explain intrinsic spin-up of the core. However a recent experiment [104] shows that all the features of intrinsic rotation can not be explained just by fluid turbulent stresses. While the effect of temperature gradient seems to be more pronounced on the experimental observations of intrinsic rotation. The density gradient can also generate residual stress. Furthermore, the mechanism for the generation of this residual stress is more direct, and the symmetry breaking is more general in the case of drift waves. Here, we will discuss the effect of finite ρ_s^* , and show that the ITG eigenmode has a broken symmetry in the case of sharp density gradients (e.g. as in an H-mode).

The analytical derivation presented in this chapter is performed in simple slab geometry. This is considered as a local piece-wise linear approximation to a small part of the plasma in the vicinity of the low field side of the tokamak. While

this approach does not capture the exact form of the eigenmode it represents the local processes as long as the microturbulence is sufficiently small scale with their eigenmodes tightly packed.

The process that leads to symmetry breaking due to finite ρ_s^* , arises from the well known expression for the divergence of polarization current, which enter the quasi-neutrality equation in the usual dimensionless units (i.e. $x \rightarrow x/\rho_i$, $\phi \rightarrow e\Phi/T_i$ etc.) as:

$$\nabla_{\perp} \cdot \left[n \frac{D}{Dt} \vec{\nabla}_{\perp} \phi \right] + \nabla_{\parallel} J_{\parallel} = 0$$

while part of the above perpendicular divergence gives rise to the usual definition of vorticity, part of it leads to a nonlinear term which survives in the linear limit due to the existence of the background density gradient. This term is normally small since it involves both the density gradient and the D/Dt , (and for drift waves $D/Dt \sim \omega_*$ already). However, it can become important when the background flow is sufficiently large (i.e. $V_0 k > \omega_*$) or if the density gradient is sufficiently large (i.e. an H-mode pedestal for instance). Physically, this term comes from the fluctuating radial gradient of the polarization current that arise from the radial gradient of the density of the particles that generate this fluctuating current (by their fluctuating polarization drift motions). We will show that the inclusion of this term in the ITG eigenmode calculation, leads to a symmetry breaking in k_{\parallel} , and therefore a net non-zero momentum flux, which has in principle the form of a residual stress. To justify further the importance of this effect we show the comparisons of this with the residual stresses driven by E_r -shear, parallel polarization residual stress and the intensity gradient. It is shown that for fixed E_r -shear the ρ_s^* induced residual stress may become comparable to E_r -shear driven residual stress in the region of small L_n . ρ_s^* induced residual stress turns out to be of the same order as the parallel polarization stress in the regular drift wave ordering where $\rho_s^* \sim \omega/\omega_{ci} \ll 1$, ω is typical mode frequency and ω_{ci} is the ion gyro frequency. And comparison with turbulence intensity gradient driven residual stress shows that ρ_s^* driven residual stress dominates at the sharp density gradient region whereas the intensity gradient driven residual stress dominates at the strong profile curvature regions such as head and the foot of the ITB or the H-mode pedestal.

The rest of the chapter is organized as follows. In Section 3.2, we start with the

derivation of a simple set of reduced fluid equations, and continue with deriving an eigenmode equation corresponding to this system. In the final part of the Section 3.2 we present the solution of this eigen-mode equation, which displays a characteristic shift from the mode rational surface on which it is localized. In Section 3.3 we discuss the effect of this mode shift on momentum transport via the symmetry breaking mechanism, and compare this with the effect due to $E \times B$ shear, parallel polarization stress and the turbulence intensity gradient driven residual stress. We conclude and discuss the implications of our work in Section 3.4.

3.2 Radial Eigenmode Analysis

In this section the linear eigenfunction for electrostatic ITG instability in the presence of mean flows is derived. A simplified set of fluid equations that describes the ion temperature gradient driven instability in the electrostatic regime is derived in the presence of poloidal and toroidal sheared flows. The assumptions made are 1) quasi-neutrality $\delta \tilde{n}_e = \delta \tilde{n}_i$, 2) constant electron temperature, 3) zero resistivity, 4) zero electron inertia for $c_i \leq \frac{\omega}{k_{\parallel}} < c_e$, and 4) $\omega \ll \omega_{ci}$, where $c_{i,e} = \sqrt{\frac{T_{0i,e}}{m_{i,e}}}$ is the ion(i)/electron(e) thermal speed, $T_{0i,e}$ are ion(i)/electron(e) temperatures, $m_{i,e}$ is ion/electron mass, ω is a typical frequency, $\omega_{ci} = \frac{eB}{m_i}$ is ion cyclotron frequency and $\eta_i = \frac{L_n}{L_{T_i}}$ is the ratio of density and ion temperature scale lengths, $L_n^{-1} = -\frac{d \ln n_0}{dx}$ and $L_{T_{si}}^{-1} = -\frac{d \ln T_{i0}}{dx}$ respectively. For concreteness we closely follow the Ref.[102]. We use (x, y, z) orthogonal Cartesian coordinate system, with unit vectors $\hat{x}, \hat{y}, \hat{z}$, situated at a rational surface. All the equilibrium quantities are considered to vary in x direction only. We consider a sheared slab configuration of magnetic field \vec{B} in the neighborhood of a rational surface situated at x_0 ,

$$\vec{B} = B(\hat{z} + \frac{x - x_0}{L_s} \hat{y}) \quad (3.1)$$

where $L_s^{-1} = \frac{B'_y}{B}$ is magnetic shear scale length. We also consider a mean ion flow field \vec{V}_{i0} lying in the (x, y) plane. For fluctuations localized on a particular rational surface at $x = x_0$, the mean ion flow velocity may be expanded as

$$\vec{V}_{i0}(x) = \vec{V}_{i0}(x_0) + (x - x_0) \left(\frac{\partial \vec{V}_{i0}}{\partial x} \right) + \dots \quad (3.2)$$

We will describe the system of equations in inertial frame moving with constant velocity $\vec{V}_{i0}(x_0)$. The perturbed linearized continuity, momentum and pressure equations for ions can be obtained as :

$$\left(\frac{\partial}{\partial t} + x\hat{V}'_{E0}\nabla_y\right)(1 - \nabla_\perp^2 + \rho_s^*\nabla_x)\phi + [1 + K(\nabla_\perp^2 - \rho_s^*\nabla_x)]\nabla_y\phi + \nabla_\parallel v = 0 \quad (3.3)$$

$$\left(\frac{\partial}{\partial t} + x\hat{V}'_{E0}\nabla_y\right)v - \hat{V}'_{\parallel 0}\nabla_y\phi + \nabla_\parallel(p + \phi) = 0 \quad (3.4)$$

$$\left(\frac{\partial}{\partial t} + x\hat{V}'_{E0}\nabla_y\right)p + K\nabla_y\phi + \Gamma\nabla_\parallel v = 0 \quad (3.5)$$

where normalizations are chosen such that

$x = (x - x_0)/\rho_s$, $y = y/\rho_s$, $z = z/L_n$, $t = tc_s/L_n$, $\phi = (e\delta\phi/T_e)(L_n/\rho_s)$, $n_i = (\delta n_i/n_0)(L_n/\rho_s)$, $v = (\delta v_{\parallel i}/c_s)(L_n/\rho_s)$, $p = (\tau_i\delta p_i/P_{i0})(L_n/\rho_s)$, $L_n\nabla_\parallel \equiv \nabla_\parallel = \frac{\partial}{\partial z} + xs\frac{\partial}{\partial y}$ with the nondimensional parameters: $\eta_i = L_n/L_T$, $K = \tau_i(1 + \eta_i) = \tau_i\alpha_i$, $\tau_i = T_{0i}/T_{0e}$, $\Gamma = \gamma\tau_i$, $s = L_n/L_s$, $\hat{V}'_{E0} = (L_n/c_s)V'_{E0}$, $\hat{V}'_{\parallel 0} = (L_n/c_s)V'_{\parallel 0}$, $\rho_s = c_s/\omega_{ci}$, and $\rho_s^* = \rho_s/L_n$. The difference between the above set of linear equations and that obtained in the past references [105, 106, 107, 102] etc. is in the ion continuity Equation(3.3) which now contains an additional term proportional to ρ_s^* . However, Dubin *et al* [108] has retained such term in their gyrokinetic formulation to ensure energy conservation. This term arises from the density gradient dependent part $\vec{V}_{pol} \cdot \vec{\nabla} n_0$ of the divergence of ion polarization current density $\vec{\nabla} \cdot (n_0 \vec{V}_{pol})$. As can be obviously seen in the Equation(3.3) this term is one order higher in ρ_s^* in the regular drift wave ordering scheme and hence it is normally not considered in drift wave theory. But it is clear that this term can become significant in strong particle density gradient regions such as in the H-mode pedestal. Also the above set of fluid equations are in fact a subset of the general gyro-fluid system of equations, which can also be derived by taking the moments of the gyro-kinetic equation[109]. The effect of this ρ_s^* term on the eigenmode structure is derived in the following. We consider the perturbation of the form $f = f_k(x)\exp(ik_y y - i\omega t)$, where k_y and ω are normalized as $k_y = k_y\rho_s$, $\omega = \omega/(c_s/L_n)$, the above set of Equations(3.3-3.5)

form an eigenvalue problem in the x direction for the Fourier amplitude ϕ_k

$$\begin{aligned} \frac{d^2\phi_k}{dx^2} - \rho_s^* \frac{d\phi_k}{dx} + \left[-k_y^2 + \frac{k_y - \omega}{\tau_i \alpha_i k_y + \omega - x k_y \hat{V}'_{E0}} + k_y^2 \frac{(sx)^2}{(\omega - x k_y \hat{V}'_{E0})^2 - \Gamma(sx)^2} \right. \\ \left. + x k_y \left[\frac{\hat{V}'_{E0}}{\tau_i \alpha_i k_y + \omega - x k_y \hat{V}'_{E0}} - \frac{\hat{V}'_{\parallel 0}}{(\omega - x k_y \hat{V}'_{E0})(\tau_i \alpha_i k_y + \omega - x k_y \hat{V}'_{E0})} \right] \right] \phi_k = 0 \end{aligned} \quad (3.6)$$

For shearing rate is much smaller than the mode frequency Equation(3.6) simplifies to

$$\begin{aligned} \frac{d^2\phi_k}{dx^2} - \rho_s^* \frac{d\phi_k}{dx} + \left[-k_y^2 + \frac{k_y - \omega}{\tau_i \alpha_i k_y + \omega} + k_y^2 \frac{(xs)^2}{\omega^2} \right. \\ \left. + x k_y \left[\frac{\hat{V}'_{E0}}{\tau_i \alpha_i k_y + \omega} - \frac{\hat{V}'_{\parallel 0}}{\omega(\tau_i \alpha_i k_y + \omega)} \right] \right] \phi_k = 0 \end{aligned} \quad (3.7)$$

which can be written as

$$\frac{d^2\phi_k}{dx^2} - \rho_s^* \frac{d\phi_k}{dx} + (A_1 + A_2 x + A_3 x^2) \phi_k = 0 \quad (3.8)$$

where

$$A_1 = \frac{k_y - \omega}{\tau_i \alpha_i k_y + \omega} - k_y^2, A_2 = \frac{k_y}{\tau_i \alpha_i k_y + \omega} \left(\hat{V}'_{E0} - k_y s \frac{\hat{V}'_{\parallel 0}}{\omega} \right), A_3 = \left(\frac{k_y s}{\omega} \right)^2 \quad (3.9)$$

The total eigen function satisfying Equation(3.8) for the $l = 0$ radial quantum number, can be obtained as

$$\phi_k = \Phi_0 \exp \left[-\frac{1}{2} i \sqrt{A_3} \left(x + \frac{A_2}{2A_3} \right)^2 \right] \exp \left[\frac{1}{2} \rho_s^* \left(x + \frac{A_2}{2A_3} \right) \right] \quad (3.10)$$

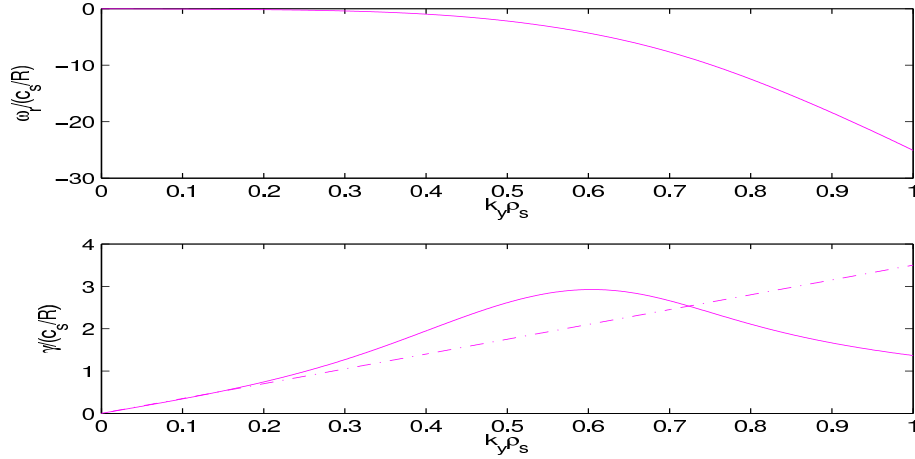


Figure 3.1: Real frequencies (a) and growth rates (b) vs k_y obtained from numerical solution of the dispersion relation. The dashed-dotted (---) curve represents the analytical approximation of the growth rate on the low k_y side of the spectrum only. Parameters: $L_n = 0.05m$, $L_T = 0.020m$, $\hat{s} = 2.0$, $q_{a/2} = 2.0$, $R = 1m$, $a = 0.25m$, $T_e = T_i = 4KeV$, $m_i = 1.6 \times 10^{-27} Kg$, $B = 4.6T$, $r = a/2$.

and the corresponding eigenmode dispersion relation is

$$\begin{aligned} & \omega^2 (1 + k_y^2) + \omega (k_y (-1 + k_y^2 \tau_i \alpha_i) + is|k_y|) + is\tau_i \alpha_i k_y |k_y| \\ &= -\frac{\omega k_y^2 \left[\frac{\omega}{sk_y} \hat{V}'_{E0} - \hat{V}'_{||0} \right]^2}{4(\tau_i \alpha_i k_y + \omega)} - \frac{1}{4} \rho_s^{*2} \omega (\tau_i \alpha_i k_y + \omega) \end{aligned} \quad (3.11)$$

Equation(3.10) shows that the eigenfunction is shifted off the mode rational surface, even in the absence of background shear flows, due to finite ρ_s^* . In the absence of shear flows the above equation becomes

$$\phi_k = \Phi_0 \exp \left[-\frac{1}{2} \left(\frac{x - \xi_{*k}}{\Delta_k} \right)^2 \right] \exp \left[-i \frac{1}{2} Re \sqrt{A_3} x^2 \right] \quad (3.12)$$

where a factor of $\exp(-\rho_s^{*2}/2Im\sqrt{A_3})$ has been absorbed in the amplitude Φ_0 . Mode width $\Delta_k^{-2} = -Im\sqrt{A_3} = |k_y|s\gamma/|\omega|^2$ and mode shift off the rational surface is $\xi_{*k} = -\rho_s^*/2Im\sqrt{A_3} = \rho_s^*|\omega|^2/(2|k_y|s\gamma) = \rho_s^*\Delta_k^2/2$. Also the real part of the radial wave number is $Re(k_x) = -\frac{1}{2}Re\sqrt{A_3}x$ and $\omega = \omega_r + i\gamma$.

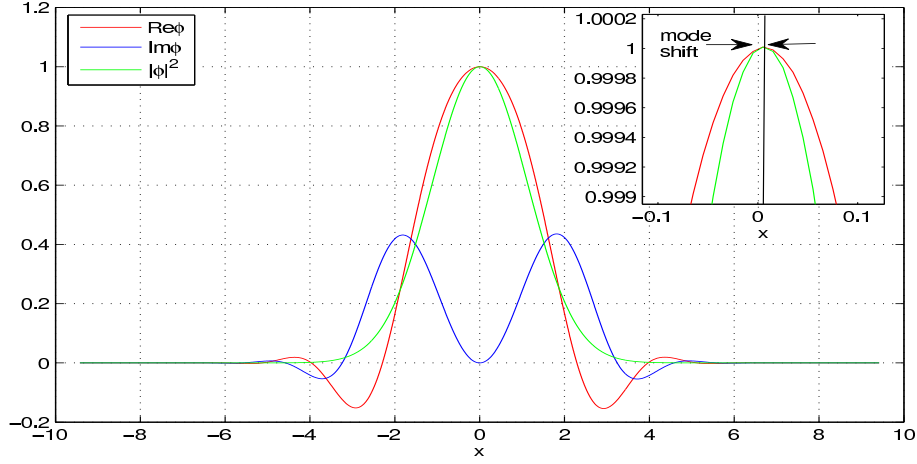


Figure 3.2: Eigenfunction shifts off the resonant surface due to finite ρ_s^* . The figure shows $Re\phi$ (— curve) , $Im\phi$ (— curve) and $|\phi|^2$ (— curve). The zoomed-in subplot highlights the mode shift. The solid vertical line indicates the peak of the shifted eigenfunction. Parameters: $k_{y,max} = 0.60$, $\gamma_{max} = 2.92$, $\omega_{r,max} = -4.41$ and other parameters are same as in Fig.(3.1). The mode width is $\Delta = 1.59$, the mode shift is $\xi = 5.90e - 03$ and the mode averaged $\langle k_{\parallel} \rangle = 3.15e - 03$.

From dispersion relation Equation(3.11) one can pick up a slow mode, on the low k_y side of the spectrum, as

$$\omega = \frac{is\tau_i\alpha_i|k_y|}{1 - k_y^2\tau_i\alpha_i - (1/4)\rho_s^{*2}\tau_i\alpha_i} \approx is\tau_i\alpha_i|k_y| \quad (3.13)$$

The dispersion relation Equation(3.11) is rewritten in a form where the frequency is normalized by c_s/R and L_s is written as $L_s = qR(1/\hat{s})$. Here R is the tokamak major radius, $\hat{s} = rq'/q$ is the shear in safety factor q . The resulting dispersion relation with $\hat{V}'_{E0} = \hat{V}'_{\parallel 0} = 0$ is solved numerically using the Matlab root finding routines. The Fig.(3.1) shows the plots of real frequency and growth rates vs k_y . Next we computed the eigenfunction Equation(3.10) for the highest growth rate. Fig.(3.2) shows the shift of eigenmode structure off the mode rational surface without mean flows.

3.3 Momentum flux by Reynolds stresses

The net radial flux of parallel momentum $\langle nv_r v_{\parallel} \rangle$ is broadly composed of particle flux driven momentum flux $\langle v_{\parallel} \rangle \langle \delta n \delta v_r \rangle$, Reynolds stress driven momentum flux $\langle n \rangle \langle \delta v_r \delta v_{\parallel} \rangle$ and mean radial flow driven momentum flux $\langle v_r \rangle \langle \delta n \delta v_{\parallel} \rangle$ and triple correlation $\langle \delta n \delta v_r \delta v_{\parallel} \rangle$. Since particle flux vanishes for adiabatic electron response and there are no mean radial flows, in this section we calculate the momentum flux due to parallel Reynolds stress carried by fluctuating $E \times B$ drift. We first compute the flux driven by only ρ_s^* induced symmetry breaking of the eigenfunction. Then in the subsequent subsections comparisons are made with E_r shear induced symmetry breaking driven residual stress, parallel polarization stress and turbulence intensity gradient induced symmetry breaking driven residual stress respectively, to gain a feeling for the importance of the new effect reported here. From Equations(3.4) and (3.5), we get the parallel velocity response as

$$\delta v_{\parallel,k} = \left(\frac{c_s \rho_s}{L_n} \right) \frac{k_y}{\omega} \left[-\hat{V}'_{\parallel 0} + \frac{k_{\parallel}}{k_y} \left[1 - \frac{\omega_{*pi}}{\omega} \right] \right] \phi_k \quad (3.14)$$

The parallel Reynolds stress due to fluctuating $E \times B$ drift, using Equation(3.14) for the parallel velocity fluctuation response, is obtained as

$$\langle \delta v_{Ex} \delta v_{\parallel} \rangle = Re \left(\frac{c_s \rho_s}{L_n} \right)^2 \sum_{\vec{k}} i \frac{k_y^2}{\omega} \left[-\hat{V}'_{\parallel 0} + \frac{k_{\parallel}}{k_y} \left[1 - \frac{\omega_{*pi}}{\omega} \right] \right] |\phi_k|^2 \quad (3.15)$$

where $\langle \dots \rangle$ indicates averaging over fast space-time scale. From above Equation(3.15) the diffusive parallel momentum flux is

$$\Pi_{\parallel,x}^{diff} = mn_0 \langle \delta v_{Ex} \delta v_{\parallel} \rangle_{diff} = -\chi_{\parallel} mn_0 \frac{dV_{\parallel}}{dx} \quad (3.16)$$

where the diffusivity is given by

$$\chi_{\parallel} = \left(\frac{c_s \rho_s}{L_n} \right)^2 \sum_{k_y} k_y^2 \frac{\sqrt{\pi} L_n}{\Delta_k c_s} |\phi_{0k}|^2 \quad (3.17)$$

The residual flux is given by

$$\Pi_{\parallel,x}^{res} = mn_0 \langle \delta v_{Ex} \delta v_{\parallel} \rangle_{res} = mn_0 \left(\frac{c_s \rho_s}{L_n} \right)^2 \sum_{\vec{k}} k_y k_{\parallel} \left[\frac{\gamma}{|\omega|^2} + \frac{\omega_{*pi} 2\gamma \omega_r}{|\omega|^2} \right] |\phi_k|^2 \quad (3.18)$$

For the particular slow mode Equation(3.13), where $\omega_r = 0$, the above residual flux expression becomes

$$\Pi_{\parallel,x}^{res} = mn_0 \left(\frac{c_s \rho_s}{L_n} \right)^2 \sum_{k_y} k_y |k_y| s \frac{\gamma}{|\omega|^2} \langle k_{\parallel} \rangle \quad (3.19)$$

where the spectrum average of k_{\parallel} is defined as

$$\langle k_{\parallel} \rangle = \langle k_{\parallel} |\phi_k|^2 \rangle_x \quad (3.20)$$

where we have made use of $\sum_{\vec{k}}(\dots) = \sum_{k_y} |k_y| s \langle (\dots) \rangle_x = \sum_{k_y} |k_y| s \int_{-\infty}^{+\infty} dx (\dots)$ to evaluate the summation over \vec{k} for tightly packed modes. Further using $k_{\parallel} = k_y s x$ and $\langle x |\phi_k|^2 \rangle_x = \xi_{*k} \Delta_k \sqrt{\pi} |\phi_{0k}|^2$ gives the parallel residual flux as

$$\Pi_{\parallel,x}^{res} = mn_0 \left(\frac{c_s \rho_s}{L_n} \right)^2 \sum_{k_y} \frac{1}{2} k_y^2 \rho_s^* s \Delta_k \sqrt{\pi} |\phi_{0k}|^2 \quad (3.21)$$

This clearly shows parallel residual flux generation due to finite ρ_s^* effect. The parallel residual flux to parallel diffusivity ratio is

$$\frac{\Pi_{\parallel,x}^{res}}{\chi_{\parallel}} = mn_0 s \frac{c_s}{L_n} \frac{\langle x |\phi_k|^2 \rangle_x}{\langle |\phi_k|^2 \rangle_x} = mn_0 s \xi_{*k} \frac{c_s}{L_n} = \frac{1}{2} mn_0 s \frac{c_s}{L_n} \rho_s^* \Delta_k^2 \quad (3.22)$$

This demonstrates parallel mean flow generation via microturbulence due to finite ρ_s^* effect.

3.3.1 Comparison with fluxes driven by mean radial electric field shear

Following Chapter 2 the slow mode eigenfunction, with mean $E \times B$ shear present and ignoring the ρ_s^* term, is given by

$$\phi_k^E = \phi_{0ks} \exp \left[-\frac{1}{2} \left(\frac{x - \xi_{Ek}}{\Delta_{ks}} \right)^2 \right] \exp \left[i \frac{|k_y|}{k_y} \frac{\hat{V}'_{\parallel 0}}{2\tau_i \alpha_i} x \right] \quad (3.23)$$

where $\xi_{Ek} = \Delta_{ks}^2 \hat{V}'_{E0}/2$ and $\Delta_{ks}^2 = \tau_i \alpha_i$. The slow mode frequency turns out to be

$$\omega = i s \tau_i \alpha_i |k_y| \quad (3.24)$$

In the above and in the following equations the subscript or superscript E indicates corresponding quantities with mean $E \times B$ shear only. Using Equations (3.15), (3.23) and (3.24), the parallel momentum diffusivity χ_{\parallel}^E is given by

$$\chi_{\parallel}^E = \left(\frac{c_s \rho_s}{L_n} \right)^2 \sum_{k_y} k_y^2 \frac{\sqrt{\pi}}{\Delta_{ks}} \frac{L_n}{c_s} |\phi_{0ks}|^2 \quad (3.25)$$

and the parallel residual momentum flux $\Pi_{\parallel,x}^{E,res}$ can be written in the form

$$\Pi_{\parallel,x}^{E,res} = m n_0 \left(\frac{c_s \rho_s}{L_n} \right)^2 \sum_{k_y} k_y |k_y| s \frac{\gamma}{|\omega|^2} \langle k_{\parallel} \rangle_E \quad (3.26)$$

where

$$\langle k_{\parallel} \rangle_E = k_y s \langle x |\phi_k^E|^2 \rangle_x = k_y s \xi_{Ek} \Delta_k \sqrt{\pi} |\phi_{0k}|^2 \quad (3.27)$$

and $\xi_{Ek} = \Delta_{ks}^2 \hat{V}'_{E0}/2$. Plugging the above form of $\langle k_{\parallel} \rangle_E$ and the mode frequency Equation (3.24) gives the form of the residual stress as

$$\Pi_{\parallel,x}^{E,res} = m n_0 \left(\frac{c_s \rho_s}{L_n} \right)^2 \sum_{k_y} k_y^2 s \xi_{ks} \sqrt{\pi} / \Delta_{ks} |\phi_{0ks}|^2 \quad (3.28)$$

Comparing Equation(3.17) and Equation(3.25) we get

$$\frac{\chi_{\parallel}}{\chi_{\parallel}^E} = 1 \quad (3.29)$$

That is the parallel momentum diffusivity remains unaltered. This is because the summand in the Equation(3.17) contains $|\phi_k|^2$ and no other multiples of function of x . Eigenfunction symmetry breaking has no role in determining parallel diffusivity χ_{\parallel} as long as the turbulence intensity is homogeneous. Again from Equations(3.21) and (3.26) we get

$$\frac{\Pi_{\parallel,x}^{res}}{\Pi_{\parallel,x}^{E,res}} = \frac{\langle k_{\parallel} \rangle}{\langle k_{\parallel} \rangle_E} = \frac{\rho_s^*}{\hat{V}_{E0}'} \quad (3.30)$$

Here we have made use of $\Delta_{ks} = \Delta_k$ because the mode width is determined by $\sqrt{A_3}$ which is the same in both cases of the momentum flux calculation. Equation(3.30) suggests that ρ_s^* induced $\langle k_{\parallel} \rangle$ symmetry breaking driven residual flux may become comparable to E_r -shear induced $\langle k_{\parallel} \rangle$ symmetry breaking driven residual flux in strong density gradient regions such as ITB and pedestal in H-mode plasma.

Note that, a similar result is expected if one considers the zonal $E \times B$ shear as a source of symmetry breaking, since in a quasi-steady state, the zonal flow shear level can be roughly determined by the balance of zonal shear frequency V_{E0}' with linear growth rate γ , (that is $V_{E,ZF}' \approx \gamma \propto \rho_s^*$). This means that the ρ_s^* effect introduced here can be viewed as linked to the zonal $E \times B$ shear induced symmetry breaking mechanism.

In a more rigorous computation of the ZF shear driven residual stress, since the screening length of the ZF would be proportional to the poloidal gyro-radius the effect would probably be more pronounced. A quick way to realize this fact is as follows. \hat{V}_{E0}' may result from the Rosenbluth Hinton (R H) neoclassical residual zonal flow [110]. The corresponding potential is

$$\frac{e\phi}{T_i} = \frac{1}{1 + 1.6q^2/\epsilon^{1/2}} \int dt S_{ik} / (k_{\perp}^2 a_i^2) \quad (3.31)$$

where $\epsilon = r/R$, running minor radius and $a_i^2 = (T_i/m_i)/\omega_{ci}^2$. Now we estimate the \hat{V}'_{E0} , the $E \times B$ shear required for asymmetric eigenfunction as follows

$$\hat{V}'_{E0} = \frac{L_n}{c_s} V'_{E0} \approx \frac{L_n}{c_s} \frac{1}{L_\phi^2} c_s \rho_s \left(\frac{e\phi}{T_e} \right) \quad (3.32)$$

where L_ϕ is potential scale length. We assume $\int dt S_{ik} / (k_\perp^2 a_i^2) = 1$. Then the ratio of ρ_s^* induced residual stress to $E \times B$ shear driven residual stress becomes

$$\frac{\Pi_{\parallel,x}^{res}}{\Pi_{\parallel,x}^{E_{R.H},res}} = \frac{\rho_s^*}{\hat{V}'_{E0}} = \frac{L_\phi^2}{L_n^2} \frac{1}{(e\phi/T_e)} = \frac{L_\phi^2}{L_n^2} \frac{(1 + 1.6q^2/\epsilon^{1/2})}{\tau_i} \quad (3.33)$$

where $\tau_i = T_i/T_e$. In neoclassical theory $L_n \sim L_\phi$, therefore

$$\frac{\Pi_{\parallel,x}^{res}}{\Pi_{\parallel,x}^{E_{R.H},res}} = \frac{(1 + 1.6q^2/\epsilon^{1/2})}{\tau_i} > 1 \quad (3.34)$$

This implies that the ρ_s^* induced residual stress is stronger than the R H residual zonal flow driven residual stress. This is as expected because the actual level of zonal flow in the turbulent case is higher than in the neoclassical case.

To get a feeling for the importance of the ρ_s^* induced $\langle k_\parallel \rangle$ symmetry breaking driven residual stress relative to the E_r -shear induced $\langle k_\parallel \rangle$ symmetry breaking driven residual stress, the expression for $\Pi_{\parallel,x}^{res}$ in Equation(3.18) is estimated numerically for the highest growing mode ($k_{y,max}$, γ_{max} , $\omega_{r,max}$). Here $k_{y,max}$ is the wave number corresponding to the highest growth γ_{max} and the $\omega_{r,max}$ is the corresponding real frequency. The variation of $\Pi_{\parallel,x}^{res}$ and $\Pi_{\parallel,x}^{E_{R.H},res}$ with L_n/R is shown in the Fig.(3.3). It shows that for fixed V'_E the term $\Pi_{\parallel,x}^{res}$ can be dominant over the $\Pi_{\parallel,x}^{E_{R.H},res}$ term for low values of L_n/R typical to ITBs. The Fig.(3.4) also conveys the same message.

Next approximate flow levels generated by the these two stresses are evaluated separately. Using the no-slip boundary condition $V(a) = 0$ to the zero net flux equation

$$\chi_\parallel \frac{dV_\parallel}{dx} = \Pi_{\parallel,x}^{res} \quad (3.35)$$

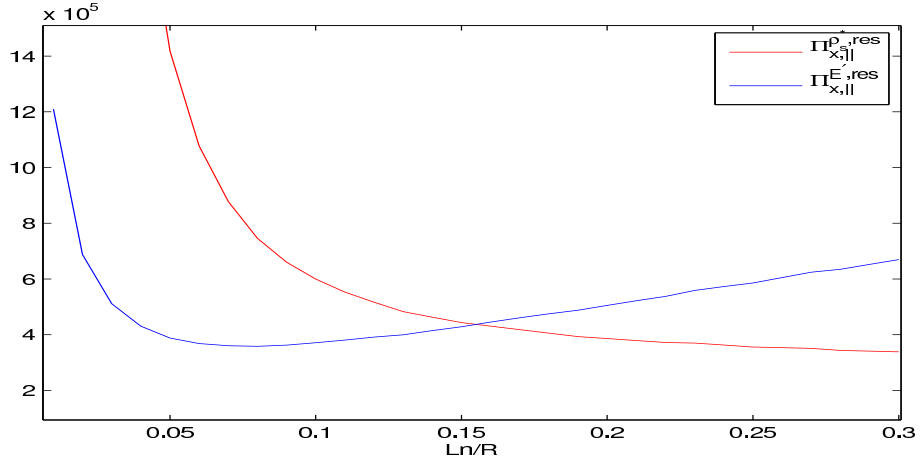


Figure 3.3: Variation of ρ_s^* induced symmetry breaking driven residual stress $\Pi_{x,||}^{\rho_s^*,res}$ (— red curve) and E_r -shear induced symmetry breaking driven residual stress $\Pi_{x,||}^{E_r',res}$ (— blue curve) with L_n/R . Stresses are computed corresponding to the highest growing mode for every L_n/R . Parameters: $V_E' = 100000s^{-1}$ and other parameters same as in Fig.(3.1).

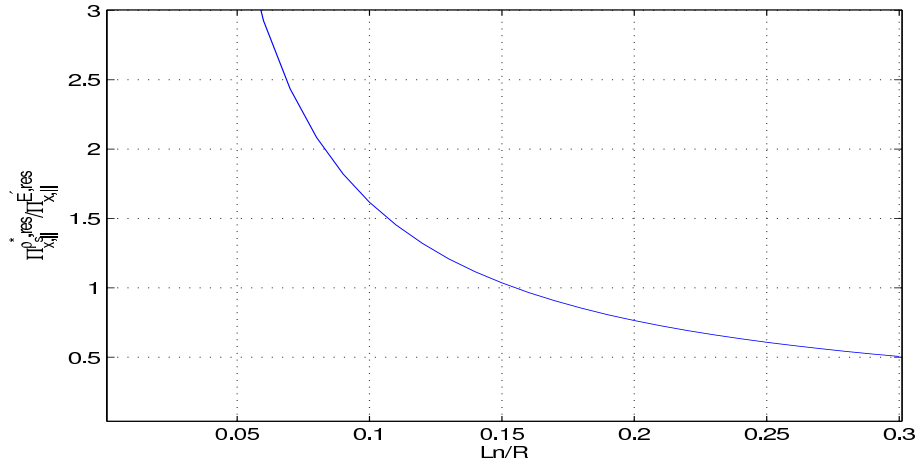


Figure 3.4: Relative strength of ρ_s^* induced symmetry breaking driven residual stress to E_r -shear induced symmetry breaking driven residual stress vs L_n/R . Parameters: same as in Fig.(3.3)

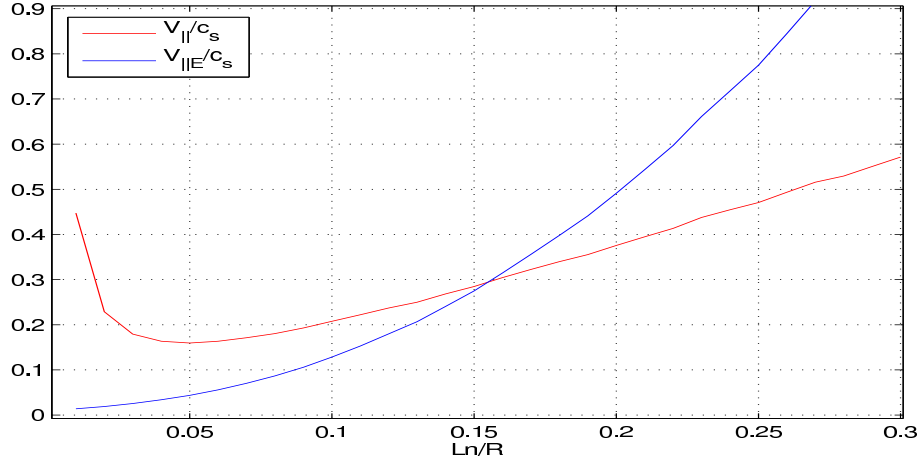


Figure 3.5: Approximate parallel flow levels evaluated at the mid-minor radius ($a/2$) by using $V_{\parallel} = -\int_{a/2}^a dx (\Pi_{x,\parallel}^{res}/\chi_{\parallel}) = (\Pi_{x,\parallel}^{res}/\chi_{\parallel})(a/2)$. The (—) curve represents ρ_s^* driven flow and the (—) curve represents the E_r' driven flow. This shows that at small L_n/R the ρ_s^* driven flow may be comparable to E_r' driven flow.

yields the intrinsic parallel flow level as

$$V_{\parallel}(x) = -\int_x^a dx' \frac{\Pi_{\parallel,x}^{res}(x')}{\chi_{\parallel}(x')} \quad (3.36)$$

This means that the intrinsic parallel flow is determined the synergistic effects of mean profiles embedded in $\Pi_{\parallel,x}^{res}$ and χ_{\parallel} . To get numbers for V_{\parallel} we used the following crude approximation

$$|V_{\parallel}(a/2)| = \frac{\Pi_{\parallel,x}^{res}}{\chi_{\parallel}} \left(\frac{a}{2} \right) \quad (3.37)$$

instead of the exact Equation(3.36). The typical flow levels thus obtained are shown in Fig.(3.5). It is accepted that this estimation is far from rigorous. Anyway the Fig.(3.5) shows that at small L_n/R the flow driven by ρ_s^* induced $\langle k_{\parallel} \rangle$ symmetry breaking can become comparable to flow driven by E_r' -shear induced by $\langle k_{\parallel} \rangle$ symmetry breaking.

3.3.2 Comparison with parallel polarization stress/flux

The time asymptotic form of the parallel polarization stress can be obtained as

$$\langle \delta v_{polx} \delta v_{\parallel} \rangle = c_s^2 \left(\frac{\rho_s}{L_n} \right)^3 Re \sum_{\vec{k}} \left[\hat{V}'_{\parallel 0} k_x^* k_y - k_x^* k_{\parallel} \left[1 - \frac{\omega_{*pi}}{\omega} \right] \right] |\phi_k|^2 \quad (3.38)$$

where $k_x = -i\partial_x \ln \phi_k$ and $Re(...)$ stands for real part of the expression in (...). The radial wavenumber k_x as obtained from the eigenfunction Equation(3.23) is

$$k_x = i \frac{x - \xi_{ks}}{\Delta_{ks}^2} + \frac{|k_y|}{k_y} \frac{\hat{V}'_{\parallel 0}}{2\tau_i \alpha_i} \quad (3.39)$$

Now using the Equation(3.39) for k_x , Equation(3.24) for the slow mode eigenfrequency and Equation(3.23) for the slow mode eigenfunction it is straightforward to show that

$$\langle \delta v_{polx} \delta v_{\parallel} \rangle = \sum_{k_y} c_s^2 \left(\frac{\rho_s}{L_n} \right)^3 k_y^2 s \left[\frac{\hat{V}'_{\parallel 0}}{2\tau_i \alpha_i} \hat{V}'_{\parallel 0} \Delta_{ks} \sqrt{\pi} + \frac{\Delta_{ks}}{2} \sqrt{\pi} \right] |\phi_{0ks}|^2 + O(\epsilon^4) \quad (3.40)$$

where $\epsilon \sim (\rho_s/L_n) \sim (\omega/\omega_{ci}) \sim (k_{\parallel}/k_y) \ll 1$ in drift wave ordering. Here the diffusive flux appears to be nonlinear, the diffusivity being proportional to the parallel flow shear, due to the fact that real part of the radial wavenumber k_x is dominantly determined by the parallel flow shear for the slow mode. Comparing the leading order residual parallel polarization stress with the ρ_s^* induced symmetry breaking driven residual stress Equation(3.21) yields

$$\frac{\Pi_{\parallel, x}^{res}}{\Pi_{\parallel, x}^{pol, res}} = 1 \quad (3.41)$$

This shows that the ρ_s^* induced symmetry breaking driven residual flux is of the same order as to the leading order parallel polarization flux.

3.3.3 Comparison with fluxes driven by turbulence intensity gradient

Now suppose that there is gradient in the fluctuation intensity introduced by mean profile gradients. We will take the following simple minded expansion of fluctuation intensity $|\phi_{ok}|^2 \equiv \epsilon(x)$,

$$\epsilon(x) = \epsilon(0) + x\epsilon(0)' + \dots \quad (3.42)$$

In the following we will examine the effect of fluctuation intensity gradient on the parallel diffusivity and residual stress separately. Including Equation(3.42) in the parallel diffusivity expression yields

$$\chi_{\parallel} = \left(\frac{c_s \rho_s}{L_n} \right)^2 \sum_{k_y} \frac{k_y^2 |k_y| \gamma s}{|\omega|^2} \frac{L_n}{c_s} (\epsilon(0) + \epsilon(0)' \xi) \Delta \sqrt{\pi} \quad (3.43)$$

Comparison of diffusivities for the two cases of ρ_s^* and ϵ' yields

$$\frac{\chi_{\parallel}}{\chi_{\parallel}^{\epsilon'}} = 1 \quad (3.44)$$

The residual flux takes the form

$$\Pi_{\parallel,x}^{res} = mn_0 \langle \delta v_{Ex} \delta v_{\parallel} \rangle_{res} = mn_0 \left(\frac{c_s \rho_s}{L_n} \right)^2 \sum_{\vec{k}} k_y |k_y| \left[\frac{\gamma}{|\omega|^2} + \frac{\omega_{*pi}^2 \gamma \omega_r}{|\omega^2|^2} \right] \langle k_{\parallel} \rangle \quad (3.45)$$

where

$$\langle k_{\parallel} \rangle = k_y s \left(\epsilon(0) \xi \Delta \sqrt{\pi} + \epsilon(0)' \left(\Delta^3 \frac{\sqrt{\pi}}{2} + \Delta \xi^2 \sqrt{\pi} \right) + \dots \right) \quad (3.46)$$

In case of no spectral shift and no intensity gradient $\langle k_{\parallel} \rangle$ vanish and hence the residual stress vanish. In case of finite spectral shift and uniform turbulence intensity above expression recovers the original well know expression for $\langle k_{\parallel} \rangle$. The $\langle k_{\parallel} \rangle$ may be enhanced or reduced over the uniform intensity case depending upon the sign of the turbulence intensity gradient $\epsilon(0)'$. Also, in the case of vanishing spectral shift the sign of $\langle k_{\parallel} \rangle$ is determined by the sign of $\epsilon(0)'$ and the sign of $\langle k_{\parallel} \rangle$ determines the sign of the residual flux $\Pi_{\parallel,x}^{res}$. Comparison of residual stresses

equals the comparison of $\langle k_{\parallel} \rangle$ for respective cases. So

$$\frac{\Pi_{\parallel,x}^{res}}{\Pi_{\parallel,x}^{\epsilon',res}} = \frac{\langle k_{\parallel} \rangle_{\rho_s^*}}{\langle k_{\parallel} \rangle_{\epsilon'}} = \frac{\epsilon \rho_s^*}{\epsilon'} = \frac{L_{\epsilon}}{L_n} \quad (3.47)$$

where $L_{\epsilon} = \epsilon/\epsilon'$ and $L_n = -n/n'$ are turbulence intensity scale length and density scale length respectively. Now it will be interesting to see in which region along the equilibrium profiles these two scale lengths can become comparable. For convenience we will follow the Ref[95] and write a few steps for clarity. The turbulence intensity is related to equilibrium profile gradients and so the turbulence intensity gradient is related to profile curvatures. For example the, differentiating the Ficks law for heat flux

$$Q = -\chi_0 \epsilon \frac{\partial T}{\partial x} \quad (3.48)$$

for constant heat flux Q gives the turbulence intensity scale length as

$$L_{\epsilon}^{-1} = \frac{1}{\epsilon} \frac{\partial \epsilon}{\partial x} = \frac{\epsilon \chi_0}{Q} \frac{\partial^2 T}{\partial x^2} \quad (3.49)$$

Then the flux ratio Equation(3.47) turns out to be

$$\frac{\Pi_{\parallel,x}^{res}}{\Pi_{\parallel,x}^{\epsilon',res}} = \frac{\langle k_{\parallel} \rangle_{\rho_s^*}}{\langle k_{\parallel} \rangle_{\epsilon'}} = \frac{\epsilon \rho_s^*}{\epsilon'} = \frac{L_{\epsilon}}{L_n} \propto -\frac{Q}{\chi_0 \epsilon n_0} \frac{n'_0}{T''_0} \quad (3.50)$$

This shows that the ρ_s^* effect can be more important at the center of the pedestal or ITB where gradient is stronger than curvature. Whereas turbulence intensity gradient driven parallel momentum flux can be more important at the pedestal/ITB head and foot. Note that this curvature dependence could as well have been shown with particle flux but because electrons are considered adiabatic, so it is not attempted. This shows that the ρ_s^* induced symmetry breaking driven residual stress/flux can become comparable to turbulence intensity gradient induced induced symmetry breaking driven residual stress/flux in strong density gradient region such as ITB or density pedestal in H-mode (see Fig.(3.6)).

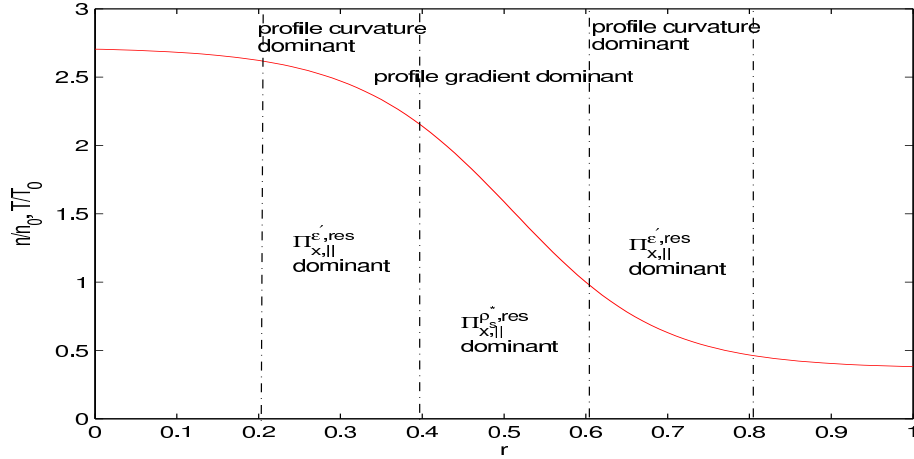


Figure 3.6: Schematic showing regions of relative importance of ρ_s^* induced symmetry breaking driven residual parallel momentum and turbulence intensity gradient induced symmetry breaking driven parallel residual flux. The vertical dashed-dotted lines are only for roughly highlighting the regions where the respective fluxes are dominating.

3.4 Results and Discussion

We presented a clear derivation of the residual stress arising from the $k_{||}$ symmetry breaking via the shift of the eigenmode off of a mode rational surface, with a fluid system of equations in a simple slab geometry. It shows that the physical process which manifests itself as an asymmetry of the eigenmode in the extended poloidal direction in the ballooning representation or as a radial shift of the eigenmode in a cylindrical formulation, can be captured in a simple slab model in local fluid approximation. This allows one to focus on individual effects for which the global mode structure is not expected to be very important. It is well known that the background density gradient together with fluctuating ion polarization drifts generate a term that accompany plasma vorticity and is proportional to the density gradient. Being one order higher in ρ_s^* this term is usually not considered in the usual drift wave ordering. We considered the effect of this term using the formulation that we have developed. This term is expected to be important in the regions where the density gradient is large such as H mode pedestal or ITBs. Following are the principal results of this chapter.

- The new term considered here leads to the formation of residual parallel Reynolds stress, via finite ρ_s^* driven parallel symmetry breaking. The mode structure shifts radially off of a resonance surface. Thus when the effects of all neighboring modes, which are similarly shifted are considered, it generates a net k_{\parallel} . This then gives rise to a net Reynolds stress, which transport momentum even in the absence of any net momentum. Comparing this term with the more conventional $E \times B$ shear driven residual stress term, we find that the ratio is basically given by the ratio:

$$\frac{\Pi_{\parallel,x}^{res}}{\Pi_{\parallel,x}^{E,res}} \propto \rho_s^{*2} \frac{\Omega_i}{V'_{E0}}$$

Note that in the usual gyrokinetic ordering $\frac{\rho}{L_n} \sim \frac{\omega}{\Omega_i}$, and the condition for the shear suppression to become important is roughly $\omega/V'_{E0} \sim 1$. Which suggests that the term that we introduce here is an order higher than the $E \times B$ shear driven term in terms of ρ_s^* . While it is true that a sharper density gradient will reduce this difference, the sharper density gradients are also usually accompanied by deeper E_r wells.

Nevertheless, the term is important for completeness. It needs to be included in a detailed analysis. It also has explicit density gradient dependence. As such, it complements the part of the $E \times B$ shear that comes from the profile gradients in the radial force balance.

- V'_E may also be interpreted as zonal flow shear which is generated by polarization current. The ρ_s^* effect also originates from the polarization current. The zonal shear level can be estimated via mixing length as being roughly proportional to ρ_s^* , so that ρ_s^* effect introduced here, can be thought of as being linked to the zonal $E \times B$ shear induced symmetry breaking. The ρ_s^* induced residual stress is expected to be stronger than the R H neoclassical residual zonal flow shear induced residual stress.
- Comparing ρ_s^* driven residual stress with the parallel polarization stress shows that they are of the same order. In particular

$$\frac{\Pi_{\parallel,x}^{res}}{\Pi_{\parallel,x}^{pol,res}} = 1$$

for the slow mode branch.

- Similarly comparison with turbulence gradient induced residual stress shows that

$$\frac{\Pi_{\parallel,x}^{res}}{\Pi_{\parallel,x}^{\epsilon',res}} = \frac{\langle k_{\parallel} \rangle_{\rho_s^*}}{\langle k_{\parallel} \rangle_{\epsilon'}} = \frac{\epsilon \rho_s^*}{\epsilon'} = \frac{L_{\epsilon}}{L_n}$$

where L_{ϵ} and L_n are turbulence intensity gradient length scale and density gradient length scale respectively. L_{ϵ} is decided by the profile curvatures. In the sharp gradient region L_n is small, curvature is weak and so L_{ϵ} is large. This means that the ρ_s^* driven residual stress overtakes the turbulence intensity inhomogeneity driven residual stress in the sharp density gradient and weak curvature regions along the mean profiles. In contrast, near the “corners”, where curvature is large, the intensity gradient term will be larger.

- For homogeneous turbulence intensity the parallel momentum diffusivity is found not to show any response to this new ρ_s^* effect reported here. This is because the momentum diffusivity does not depend on the broken symmetry of the eigenfunction. However broken symmetry of the eigenfunction together with turbulence intensity inhomogeneity does renormalize the parallel momentum diffusivity (eg., see Equation(3.43)).

Now in the next Chapter, the momentum transport studies presented in the Chapters 2 and 3 are extended to reverse shear configuration.

4

Momentum transport in the neighborhood of q_{min} in reverse shear tokamak due to ITG turbulence

4.1 Introduction

All the works presented in the previous Chapters 2 and 3 applies only to normal to shear tokamaks with a monotonically increasing q profile. In this chapter we focus our studies on toroidal and poloidal momentum transport at and about minimum of q . Because of the novel configuration of magnetic field and existence of internal transport barrier (ITB), it forms the most natural place to focus momentum transport studies in reverse shear configuration. The calculations are performed in sheared slab geometry where magnetic curvature effects are not considered. As seen in the Chapter 3 the ρ_s^* effect becomes important at ITB because of short density scale length. We have computed the ITG eigenfunction for reverse shear case including the ρ_s^* effect. It is found that the symmetry of the eigenfunction is naturally broken by ρ_s^* effect even in absence of mean radial electric field shear. This actually complements the ρ_s^* order shift coming from radial electric field shear driven shift through radial force balance. Three different types of modes are found at q_{min} depending on whether for given mode number (m, n) it resonates once or twice or does not resonate. These are single rational surface reverse shear mode, double rational surface reverse shear mode and no rational surface or non-resonant reverse shear mode. When $q_{min} = m/n$ is a rational number the mode (m, n)

has $k_z = 0$ and it's a single rational surface mode resonating at the q_{min} . When $q_{min} \neq m/n$ the mode (m, n) is either a double rational surface mode or a non-resonant mode.

Toroidal and poloidal Reynolds stresses due to both turbulent $E \times B$ and polarization drift have been computed. We have generalized the definition of spectrally averaged $\langle k_{\parallel} \rangle$ and $\langle Re k_x \rangle$ which takes care for both shear and curvature in q . It is seen that reflectional symmetry breaking of the eigenmode is not a necessary condition for the survival of residual parallel stress at q_{min} . That is $\langle k_{\parallel} \rangle \neq 0$ and $\langle Re k_x \rangle \neq 0$ even for symmetric eigenfunction. This means spontaneous toroidal and poloidal flow generation at q_{min} . Anyway, the mode structure naturally turns out have broken symmetry due to finite ρ_s^* and mean $E \times B$ flow shear (i.e., $V_E' \neq 0$). This modifies the turbulent fluxes. However, the ρ_s^* symmetry breaking of the eigenfunction is seen to have a little contribution to turbulent $E \times B$ drift driven parallel residual stress due to double rational surface RS-ITG and non-resonant RS-ITG. The residual stress is dominantly determined by mode width for $k_{\parallel} \propto x^2$.

The rest of the chapter is organized as follows. Section(4.2) contains the eigenmode formulation of the problem where a general linear mode structure and the corresponding eigenmode dispersion relation are calculated. The three different types of ITG modes spanning the entire (k_y, k_z) space at q_{min} are discussed in detail in Section(4.3). A general calculation of toroidal and poloidal momentum fluxes carried by turbulent $E \times B$ drift and polarization drift are derived in Section(4.4). Momentum fluxes at and about q_{min} are calculated in Section(4.5). Finally discussion and conclusions are made in the Section(4.6).

4.2 Eigenmode formulation

The magnetic field near minimum q can be expressed as [111]

$$\vec{B} = B \left(\hat{z} - \frac{\hat{s}x}{q_0 R} \left(1 + \frac{\hat{s}_d x}{\hat{s}} \right) \hat{y} \right) \quad (4.1)$$

where $\hat{s} = r q_0' / q_0$ is shear in q , $\hat{s}_d = r q_0'' / 2 q_0$ is curvature in q , q_0 is value of q at $r = r_0$, $x = r - r_0$ and r_0 is the location a reference surface not necessarily a

rational surface.

$$\vec{V}_{i0}(x) = \vec{V}_{i0}(r_0) + x \left(\frac{\partial \vec{V}_{i0}}{\partial x} \right) + \dots \quad (4.2)$$

From Equations(4.1) k_{\parallel} becomes

$$k_{\parallel} = k_z - \frac{k_y \hat{s} x}{q_0 R} \left(1 + \frac{\hat{s}_d x}{\hat{s}} \right) \quad (4.3)$$

Normalizing k_{\parallel} and k_z by L_n ; k_y , x , \hat{s}_d by ρ_s i.e., $(k_{\parallel}, k_z) \equiv (k_{\parallel}, k_z)L_n$; $(k_y, \hat{s}_d) \equiv (k_y, \hat{s}_d)\rho_s$ and $x \equiv x/\rho_s$ Equation(4.3) becomes

$$k_{\parallel} = k_z - \frac{k_y \hat{s} x L_n}{q_0 R} \left(1 + \frac{\hat{s}_d x}{\hat{s}} \right) \quad (4.4)$$

Note that finite \hat{s}_d makes rational surfaces near q - minimum non-degenerate. This makes k_z an important parameter compared to normal shear slab ITG problem. Following [112, 113, 114, 115] the perturbed ion continuity, parallel momentum and pressure equations describing the fluid ITG instability are as follows.

$$\left(\frac{\partial}{\partial t} + x \hat{V}'_{E0} \nabla_y \right) (1 - \nabla_{\perp}^2 + \frac{\rho_s}{L_n} \nabla_x) \phi + \left[1 + K \left(\nabla_{\perp}^2 - \frac{\rho_s}{L_n} \nabla_x \right) \right] \nabla_y \phi + \nabla_{\parallel} v = 0 \quad (4.5)$$

where ρ_s^* terms are kept as they can be important at ITB at q_{min} where density gradient is strong. This term arises from the divergence of polarization current when there is background density gradient, apart from the regular vorticity term. Usually this term is small in regular drift wave ordering, but it can become significant at places where density gradient is strong such as ITB at q_{min} . The parallel velocity and pressure fluctuation equations are, respectively

$$\left(\frac{\partial}{\partial t} + x \hat{V}'_{E0} \nabla_y \right) v - \hat{V}'_{\parallel 0} \nabla_y \phi + \nabla_{\parallel} (p + \phi) = 0 \quad (4.6)$$

$$\left(\frac{\partial}{\partial t} + x \hat{V}'_{E0} \nabla_y \right) p + K \nabla_y \phi + \Gamma \nabla_{\parallel} v = 0 \quad (4.7)$$

where normalization is

$$x = (x - x_0)/\rho_s, \quad y = y/\rho_s, \quad z = z/L_n, \quad t = t c_s/L_n, \quad \phi = (e \delta \phi / T_e)(L_n/\rho_s), \quad n_i = (\delta n_i / n_0)(L_n/\rho_s) \\ v = (\delta v_{\parallel i} / c_s)(L_n/\rho_s), \quad p = (\tau_i \delta p_i / P_{i0})(L_n/\rho_s), \quad L_n \nabla_{\parallel} \equiv \nabla_{\parallel} = \frac{\partial}{\partial z} + x s \frac{\partial}{\partial y} \text{ and the non-dimensional parameters are } \eta_i = L_n/L_T, \quad K = \tau_i(1 +$$

$$\eta_i) = \tau_i \alpha_i, \tau_i = T_{0i}/T_{0e}, \quad \Gamma = \gamma \tau_i, \quad s = L_n/L_s, \quad \hat{V}'_{E0} = (L_n/c_s)V'_{E0}, \quad \hat{V}'_{\parallel 0} = (L_n/c_s)V'_{\parallel 0}, \quad \rho_s = c_s/\omega_{ci}.$$

Now considering the perturbation of the form $f = f_k(x) \exp(ik_y y + ik_z z - i\omega t)$, where normalized $k_{y,z}$ and ω are $k_y = k_y \rho_s, k_z = k_z L_n, \omega = \omega/(c_s/L_n)$, the above set of Equations(4.5-4.7) form an eigenvalue problem in x direction in ϕ_k

$$\frac{d^2 \phi_k}{dx^2} - \rho_s^* \frac{d\phi_k}{dx} + U(x, \Omega) \phi_k = 0 \quad (4.8)$$

where

$$U(x, \Omega) = -k_y^2 + \frac{1 - \hat{\Omega}}{K + \hat{\Omega}} + \frac{(k_{\parallel}/k_y)^2 (K + \hat{\Omega}) - (k_{\parallel}/k_y) \hat{\Omega} \hat{V}'_{\parallel}}{(K + \hat{\Omega}) (\hat{\Omega}^2 - \Gamma (k_{\parallel}/k_y)^2)} \quad (4.9)$$

where $\hat{\Omega} = \Omega - x \hat{V}'_E$, $\hat{V}'_{E,\parallel} = L_n V'_{E,\parallel}/c_s$, $\Omega = \omega/k_y$, $\omega_{*e} = c_s k_y/L_n$, $c_s = \sqrt{T_e/m_i}$, $K = \tau_i(1 + \eta_i)$, $\tau_i = T_i/T_e$, $\eta_i = \frac{L_n}{L_{T_i}}$, $\Gamma = \gamma \tau_i$, and $\gamma = C_p/C_v$. For $\Gamma \rightarrow 0$ and $E \times B$ shearing rate much smaller than mode frequency the Expression(4.9) for effective potential becomes

$$U(x, \Omega) = A_1 + A_2 x + A_3 x^2 + A_4 x^3 + A_5 x^4 \quad (4.10)$$

where

$$A_1 = -k_y^2 + \frac{k_y - \omega}{K k_y + \omega} + \frac{k_z^2}{\omega^2} - \frac{k_y k_z \hat{V}'_{\parallel}}{\omega (K k_y + \omega)} \quad (4.11)$$

$$A_2 = \left(k_y \frac{\hat{V}'_E}{K k_y + \omega} - \frac{1}{\omega^2} \frac{2 k_y k_z \hat{s} L_n}{q_0 R} \right) + \frac{k_y}{\omega (K k_y + \omega)} \frac{k_y \hat{s} L_n \hat{V}'_{\parallel}}{q_0 R} \quad (4.12)$$

$$A_3 = \frac{1}{\omega^2} \left\{ \left(\frac{k_y \hat{s} L_n}{q_0 R} \right)^2 - \frac{2 k_y k_z \hat{s} L_n}{q_0 R} \right\} + \frac{k_y}{\omega (K k_y + \omega)} \frac{k_y \hat{s} L_n \hat{V}'_{\parallel}}{q_0 R} \quad (4.13)$$

$$A_4 = \frac{1}{\omega^2} \frac{k_y \hat{s} L_n}{q_0 R} \frac{2 k_y \hat{s} L_n}{q_0 R} \quad (4.14)$$

$$A_5 = \frac{1}{\omega^2} \left(\frac{k_y \hat{s} L_n}{q_0 R} \right)^2 \quad (4.15)$$

Keeping terms upto x^2 in Equation(4.10) and using

$$\xi = (-A_3)^{1/4} \left(x + \frac{A_2}{2A_3} \right) \quad (4.16)$$

and following [115] the eigenmode Equation(4.8) becomes

$$\frac{d^2 \phi_k}{d\xi^2} - (-A_3)^{-1/4} \rho_s^* \frac{d\phi_k}{d\xi} + (E - \xi^2) \phi_k = 0 \quad (4.17)$$

where $E = \left(A_1 - \frac{A_2^2}{4A_3} \right) / \sqrt{(-A_3)}$.

$$\phi_k = \Phi_k \exp \left(\frac{1}{2} \int (-A_3)^{-1/4} \rho_s^* d\xi \right) \quad (4.18)$$

the Equation(4.17) transforms into

$$\frac{d^2 \Phi_k}{d\xi^2} + (E^* - \xi^2) \Phi_k = 0 \quad (4.19)$$

where now

$$E^* = E - \left(\frac{(-A_3)^{-1/4} \rho_s^*}{2} \right)^2 \quad (4.20)$$

The solution of Equation(4.19) is

$$\Phi_{kl} = \Phi_0 \exp\left(-\frac{\xi^2}{2}\right) H_l(\xi) \quad (4.21)$$

with

$$E^* = 2l + 1, l = 0, 1, 2, 3, \dots etc \quad (4.22)$$

Being the most dominant we will consider the $l = 0$ mode for which the eigen function in x is

$$\Phi_k = \Phi_0 \exp \left[-\frac{1}{2} i \sqrt{A_3} \left(x + \frac{A_2}{2A_3} \right)^2 \right] \quad (4.23)$$

And so the total eigen function Equation(4.18), for the $l = 0$ radial quantum number, becomes

$$\phi_k = \Phi_0 \exp \left[-\frac{1}{2} i \sqrt{A_3} \left(x + \frac{A_2}{2A_3} \right)^2 \right] \exp \left[\frac{1}{2} \rho_s^* \left(x + \frac{A_2}{2A_3} \right) \right] \quad (4.24)$$

Equation(4.24) shows that the eigenfunction is shifted off the mode rational surface even in the absence of background shear flows due to finite ρ_s^* . The eigenfunction Equation(4.24) can be rewritten as

$$\phi_k = \Phi_0 \exp \left[-\frac{1}{2} i \sqrt{A_3} \left(x + \frac{A_2}{2A_3} - \frac{\rho_s^*}{2\sqrt{-A_3}} \right)^2 \right] \exp \left[i \frac{1}{2} \sqrt{A_3} \left(\frac{\rho_s^*}{2\sqrt{-A_3}} \right)^2 \right] \quad (4.25)$$

and the corresponding eigenmode dispersion relation from

$$1 = \frac{\left(A_1 - \frac{A_2^2}{4A_3} \right)}{\sqrt{(-A_3)}} - \left(\frac{(-A_3)^{-1/4} \rho_s^*}{2} \right)^2 \quad (4.26)$$

is obtained to be

$$\begin{aligned} & -k_y^2 + \frac{1 - \Omega}{K + \Omega} + \frac{k_z^2}{k_y^2 \Omega^2} - \frac{k_z \hat{V}'_{\parallel}}{k_y \Omega (K + \Omega)} - \frac{1}{4} \left\{ \frac{\hat{V}'_E}{K + \Omega} - \frac{1}{k_y^2 \Omega^2} \frac{2k_y k_z \hat{s} L_n}{q_0 R} + \frac{1}{k_y \Omega (K + \Omega)} \right. \\ & \times \left. \frac{k_y \hat{s} L_n \hat{V}'_{\parallel}}{q_0 R} \right\}^2 \left[\frac{1}{k_y^2 \Omega^2} \left\{ \left(\frac{k_y \hat{s} L_n}{q_0 R} \right)^2 - \frac{2k_y k_z \hat{s}_d L_n}{q_0 R} \right\} + \frac{1}{k_y \Omega (K + \Omega)} \frac{k_y \hat{s}_d L_n \hat{V}'_{\parallel}}{q_0 R} \right]^{-1} \\ & - \left(\frac{\rho_s^*}{2} \right)^2 = i \left\{ \frac{1}{k_y^2 \Omega^2} \left(\left(\frac{k_y \hat{s} L_n}{q_0 R} \right)^2 - \frac{2k_y k_z \hat{s}_d L_n}{q_0 R} \right) + \frac{1}{k_y \Omega (K + \Omega)} \frac{k_y \hat{s}_d L_n \hat{V}'_{\parallel}}{q_0 R} \right\}^{1/2} \end{aligned} \quad (4.27)$$

Separating the real and imaginary parts of the phase of the exponential in Equation(4.25), a further useful form of the eigenfunction Equation(4.25) can be obtained as

$$\phi_k = \Phi_0 \exp \left[-\frac{1}{2} \left(\frac{x - \xi_{*k}}{\Delta_k} \right)^2 \right] \exp \left[-\frac{i}{2} Re \sqrt{A_3} \left(x + Re \frac{A_2}{2A_3} - \frac{Im \sqrt{A_3}}{Re \sqrt{A_3}} Im \frac{A_2}{2A_3} \right)^2 \right] \quad (4.28)$$

where the generalized expression for the mode shift ξ_{*k} off the reference surface is

given by

$$\xi_{*k} = - \left[Re \frac{A_2}{2A_3} + \frac{Re\sqrt{A_3}}{Im\sqrt{A_3}} Im \frac{A_2}{2A_3} + \frac{\rho_s^*}{2Im\sqrt{A_3}} \right] \quad (4.29)$$

and the generalized expression for the half mode width Δ_k is given by

$$\Delta_k^{-2} = -Im\sqrt{A_3} \quad (4.30)$$

Also note that a factor of

$$\exp \left\{ -\frac{i}{2} \sqrt{A_3} \left[\left(1 + \left(\frac{Re\sqrt{A_3}}{Im\sqrt{A_3}} \right)^2 \right) \left(Im \frac{A_2}{2A_3} + \frac{\rho_s^* Re\sqrt{A_3}}{2|\sqrt{A_3}|^2} \right)^2 + \left(\frac{\rho_s^*}{2\sqrt{A_3}} \right)^2 \right] \right\} \quad (4.31)$$

have been absorbed in the mode amplitude Φ_0 in the eigenfunction Equation(4.28). This suggests that turbulence intensity naturally acquires a gradient, because A_2 and A_3 depends on mean profiles. Gurcan *etal*[95] have shown k_{\parallel} symmetry breaking due to turbulence intensity gradient, assuming gradient in turbulence. This factor Equation(4.31) is probably a direct analytical evidence for that. From Equation(4.28) it is also clear that ρ_s^* has no role in generating Rek_x of the mode.

4.3 Eigenmode structures at q_{min}

Depending on the shape of q profile the mode (m, n) may resonate one or many points in radial location. For the typical reverse shear profiles of q the mode (m, n) may resonate at one or two radial points at which $q(r) = m/n$ is satisfied as shown in Fig.(4.1). In the following we classify modes according to the number of resonating rational surfaces.

4.3.1 Double mode-rational surface RS-ITG

At minimum- q $\hat{s} = 0$. Let's now consider the case where q_{min} is not a rational number i.e., $q_{min} \neq m/n$ then $k_z = (m - nq_{min})/qR \neq 0$, and also consider $k_z/k_y > 0$. Then the mode has two rational surfaces on both sides of q_{min} position. The location of the mode rational surfaces are obtained from the quadratic roots of the Equation(4.4) by setting $\hat{s} = 0$. The location of rational surfaces, given by

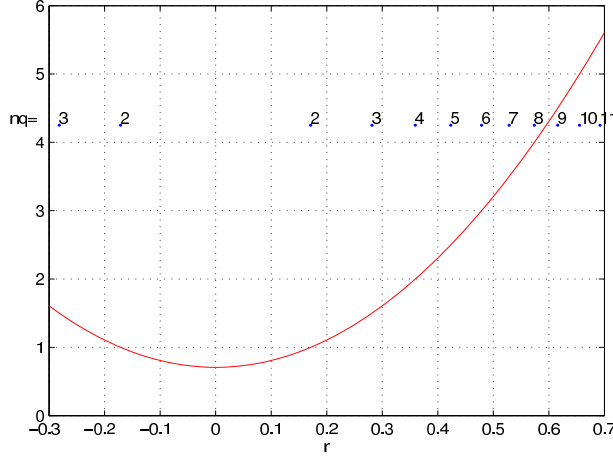


Figure 4.1: Schematic showing a typical reverse q profile and arrangement of rational surfaces resonating with toroidal mode number $n = 2$. Zero of the radial coordinate is fixed at the position of q_{min} . $q = (q_{min} + c_1(r - c_2)^2)$, $q_{min} = 1/\sqrt{2}$, $c_1 = 10.0$, $c_2 = 0$. Here $r \equiv r/a$ where a is minor radius.

$x = \pm \sqrt{(k_z/k_y)(q_0 R/\hat{s}_d L_n)}$, are obtained to be symmetrically distributed about the position of q_{min} . The strong temperature and density gradients at ITB at q_{min} are also associated with wells in E_r . But it is not very clear whether the minimum of the well coincide with the position of q_{min} . In case it coincides then the $E'_r|_{r=r_{min}} = 0$. Then taking $\hat{V}'_E = \hat{V}'_{||} = 0$ the $l = 0$ radial eigenmode Equation(4.25) becomes

$$\phi = \phi_0 \exp \left[-\frac{i}{2} \sqrt{A_3} \left(x - \frac{\rho_s^*}{2\sqrt{-A_3}} \right)^2 \right] \exp \left[i \frac{1}{2} \sqrt{A_3} \left(\frac{\rho_s^*}{2\sqrt{-A_3}} \right)^2 \right] \quad (4.32)$$

where

$$A_3 = -\frac{1}{\omega^2} \frac{2|k_y k_z| \hat{s}_d L_n}{q_0 R} \quad (4.33)$$

Equation(4.32) can further be expressed as

$$\phi_k = \Phi_0 \exp \left[-\frac{1}{2} \left(\frac{x - \xi_{*k}}{\Delta_k} \right)^2 \right] \exp \left[-i \frac{1}{2} Re \sqrt{A_3} x^2 \right] \quad (4.34)$$

where a factor of $\exp(-\rho_s^{*2}/2Im\sqrt{A_3})$ has been absorbed in the amplitude Φ_0 . This represents an eigenmode with the envelope shifted from the position of q-min ($x = 0$) and radially propagating as well. This is because $\omega = \omega_r + i\gamma$ is complex in general. Mode width $\Delta_k^{-2} = -Im\sqrt{A_3}$ and mode shift off the rational surface is $\xi_{*k} = -\rho_s^*/2Im\sqrt{A_3}$. Note that the shift is coming from finite ρ_s^* which can

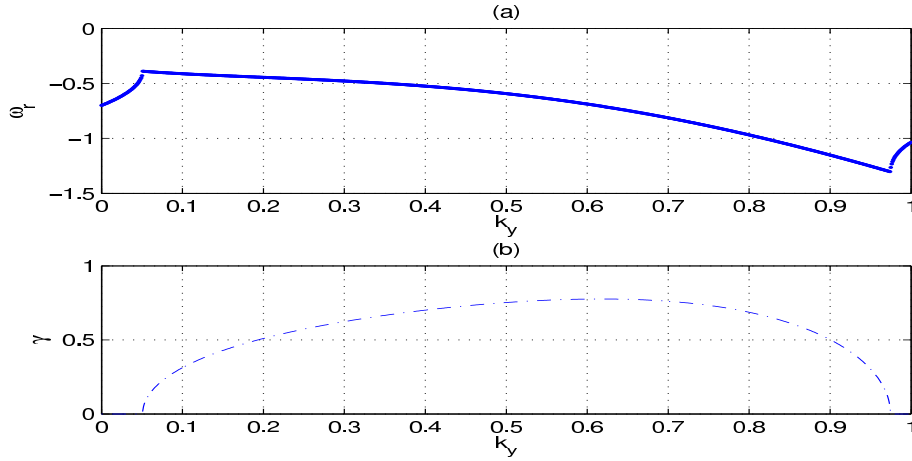


Figure 4.2: The growing branch of the double rational surface RS-ITG. Fig(a) is the dispersion plot and (b) is growth rate vs k_y . Parameters are: $L_n = 0.020 \times 4$ m, $L_T = 0.020$ m, $V'_E = 0.0$, $V'_\parallel = 0.0$, $\hat{s} = 0.0$, $T_e = T_i = 4.0$ keV, $m_i = m_H = 1.67 \times 10^{-27}$ kg, $B = 4.6$ Tesla, $r_0/a = 0.3$ m, $q_0'' = 20$, $R = 2.0$ m, $k_z = 0.7$; $\rho_s = 1.40 \times 10^{-03}$ m

actually be pronounced at ITB at the minimum of q . The eigenmode dispersion relation satisfied by this mode is obtained from Equation(4.27) as

$$-k_y^2 + \frac{k_y - \omega}{Kk_y + \omega} + \frac{k_z^2}{\omega^2} - \left(\frac{\rho_s^*}{2}\right)^2 = \frac{1}{\omega} \left(\frac{2|k_y k_z| \hat{s}_d L_n}{q_0 R}\right)^{1/2} \quad (4.35)$$

Plots of eigenfunction Equation(4.32) for the growing branch (see Fig.(4.2)) of the dispersion relation Equation(4.35) are shown in Fig.(4.3) for $k_z = 0.7$. The mode shift due to ρ_s is highlighted.

In the other case when minimum of E_r well does not coincide with q_{min} position $E'_r|_{r=r_{min}} \neq 0$. Let us then consider the double rational surface mode with $\hat{V}'_E = \hat{V}'_\parallel \neq 0$. We will consider the limit when $-2k_z(Kk_y + \omega) \gg \omega k_y \hat{V}'_\parallel$ for analytical tractability of the problem. Under this condition the last term in the Equation.(4.13) for A_3 is negligible. This allows us to write the eigenfunction in the form of Equation(4.28), where now

$$Re \sqrt{A_3} = \frac{\gamma}{|\omega|^2} \sqrt{\frac{2|k_y k_z| \hat{s}_d L_n}{q_0 R}} \quad (4.36)$$

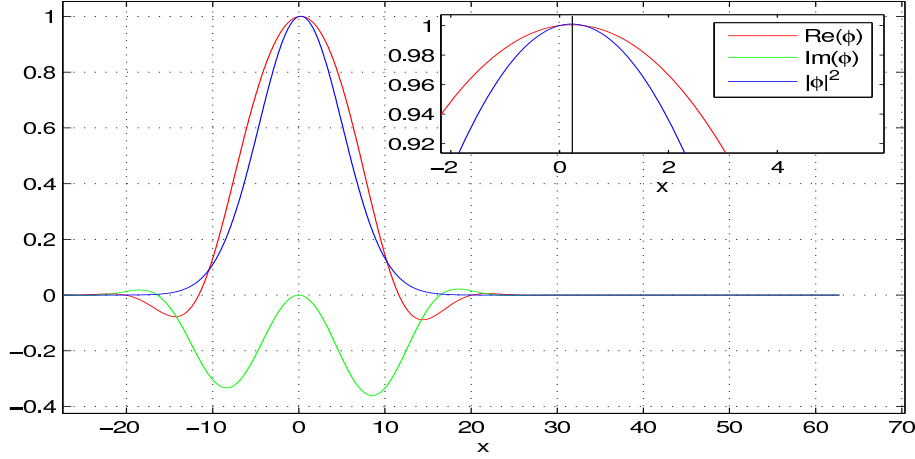


Figure 4.3: Eigenmode structure of the double rational surface RS-ITG. Solid vertical line indicates the shifted position of the mode. Mode shift = 0.6485, mode width = 8.0394. Parameters: same as in Fig.(4.2), $\omega = -0.672 + i0.7745$

and

$$Re \frac{A_2}{2A_3} - \frac{Im \sqrt{A_3}}{Re \sqrt{A_3}} Im \frac{A_2}{2A_3} = -\frac{k_y \hat{V}'_E (Kk_y |\omega|^2 + |\omega|^4 / \omega_r)}{4|k_y k_z| |Kk_y + \omega|^2} \frac{q_0 R}{\hat{s}_d L_n} \quad (4.37)$$

The mode shift including the ρ_s^* term, from Equation(4.29), is given by

$$\xi_{*k} = -\frac{k_y \hat{V}'_E Kk_y |\omega|^2}{4|k_y k_z| |Kk_y + \omega|^2} \frac{q_0 R}{\hat{s}_d L_n} - \frac{\rho_s^* |\omega|^2}{2\omega_r} \sqrt{\frac{q_0 R}{2|k_y k_z| \hat{s}_d L_n}} \quad (4.38)$$

In this case the eigenmode dispersion relation becomes

$$\begin{aligned} -k_y^2 + \frac{k_y - \omega}{Kk_y + \omega} + \frac{k_z^2}{\omega^2} + \frac{1}{4} \left(\frac{\omega k_y \hat{V}'_E}{Kk_y + \omega} \right)^2 \left(\frac{q_0 R}{2|k_y k_z| \hat{s}_d L_n} \right) - \left(\frac{\rho_s^*}{2} \right)^2 \\ = \frac{1}{\omega} \left(\frac{2|k_y k_z| \hat{s}_d L_n}{q_0 R} \right)^{1/2} \end{aligned} \quad (4.39)$$

The growing branch of the dispersion relation Equation(4.39) is shown in the Fig.(4.4). The corresponding eigenfunction is shown in Fig.(4.5) where the enhanced mode shift due to V'_E is clearly visible.

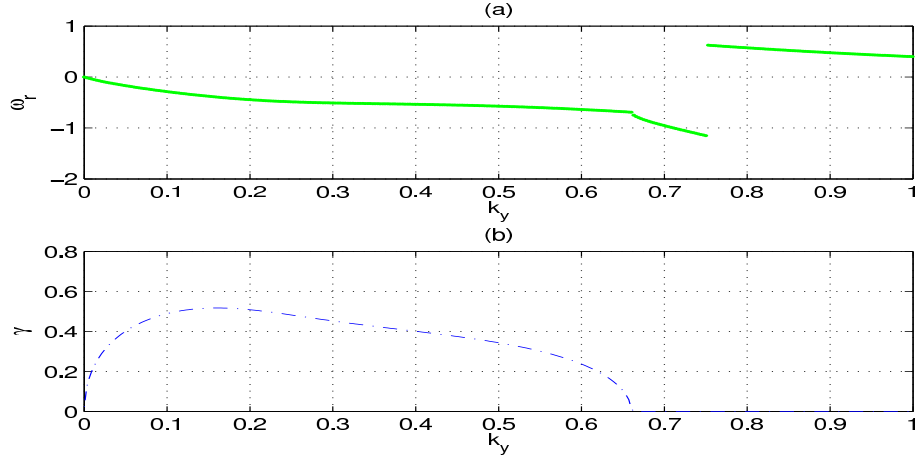


Figure 4.4: The growing branch of the double rational surface RS-ITG. Fig(a) is the dispersion plot and (b) is growth rate vs k_y . Parameters: same as in Fig.(4.2), $L_n = 0.019 \times 4$ m, $L_T = 0.019$ m, $\hat{V}'_E = 0.01$

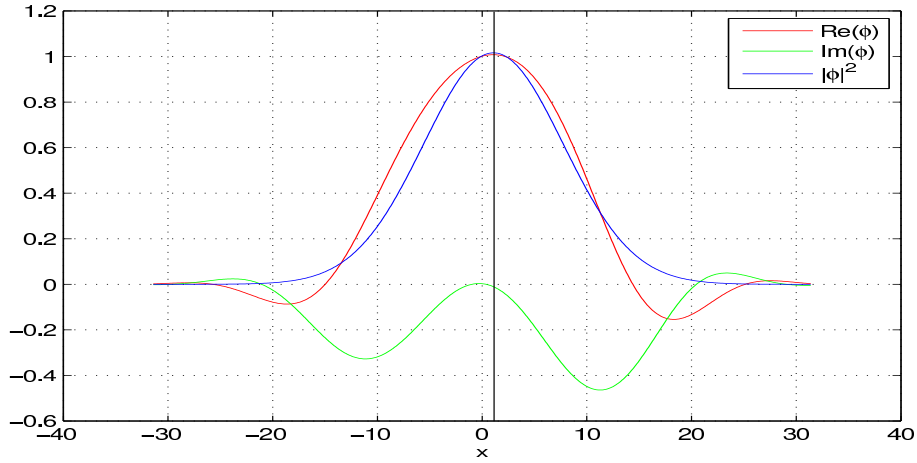


Figure 4.5: Eigenmode structure of the double rational surface RS-ITG. Solid vertical line indicates the shifted position of the mode. Mode shift = 1.08, mode width = 9.42. Parameters: same as in Fig.(4.4), $\omega = -0.40 + i0.517$. Mode shift enhancement due to finite \hat{V}'_E can easily be noticed.

4.3.2 Single mode-rational surface RS-ITG

When q_{min} is rational number i.e., $q_{min} = m/n$ then $k_z = (m - nq_{min})/qR = 0$. The roots of the quadratic Equation(4.4) are then repeated and equals to 0. This means that the mode has single rational surface resonating at q_{min} . For $\hat{V}'_E \neq 0, \hat{V}'_{\parallel} \neq 0$ the $l = 0$ radial eigenmode(4.28) becomes

$$\phi_k = \Phi_0 \exp \left[-\frac{1}{2} \left(\frac{x - \xi_{*k}}{\Delta_k} \right)^2 \right] \exp \left[-\frac{i}{2} Re \sqrt{A_3} \left(x + Re \frac{A_2}{2A_3} - \frac{Im \sqrt{A_3}}{Re \sqrt{A_3}} Im \frac{A_2}{2A_3} \right)^2 \right] \quad (4.40)$$

$$k_x = -i \partial \ln \phi_k / \partial x = -\sqrt{A_3} \left(x + \frac{A_2}{2A_3} \right) \quad (4.41)$$

where the mode shift off the rational surface is given by

$$\begin{aligned} \xi_{*k} = - \left[\omega_r - \gamma \frac{Re \sqrt{\omega (\omega + K k_y)}}{Im \sqrt{\omega (\omega + K k_y)}} \right] \frac{q_0 R}{2 k_y \hat{s}_d L_n} \frac{\hat{V}'_E}{\hat{V}'_{\parallel}} \\ + \frac{\rho_s^*}{k_y} \frac{|\sqrt{\omega (\omega + K k_y)}|^2}{Im \sqrt{\omega (\omega + K k_y)}} \frac{q_0 R}{2 k_y \hat{s}_d L_n} \frac{1}{\hat{V}'_{\parallel}} \end{aligned} \quad (4.42)$$

and the half mode width is given by

$$\Delta_k^{-2} = -Im \left(\sqrt{\frac{k_y^2}{\omega (\omega + K k_y)} \frac{\hat{s}_d L_n \hat{V}'_{\parallel}}{q_0 R}} \right) \quad (4.43)$$

Surprisingly, the mode shift is determined by the ratio $\hat{V}'_E/\hat{V}'_{\parallel}$ and the mode width is determined by \hat{V}'_{\parallel} at min-q. The second term in the Equation(4.42) is a ρ_s^* effect on symmetry breaking. Another surprising observation here is that for $\hat{V}'_{\parallel} \rightarrow 0$ the mode shift ξ as well as the mode width Δ both $\rightarrow \infty$. This means that this particular mode exists only when \hat{V}'_{\parallel} is finite. The dispersion relation of single

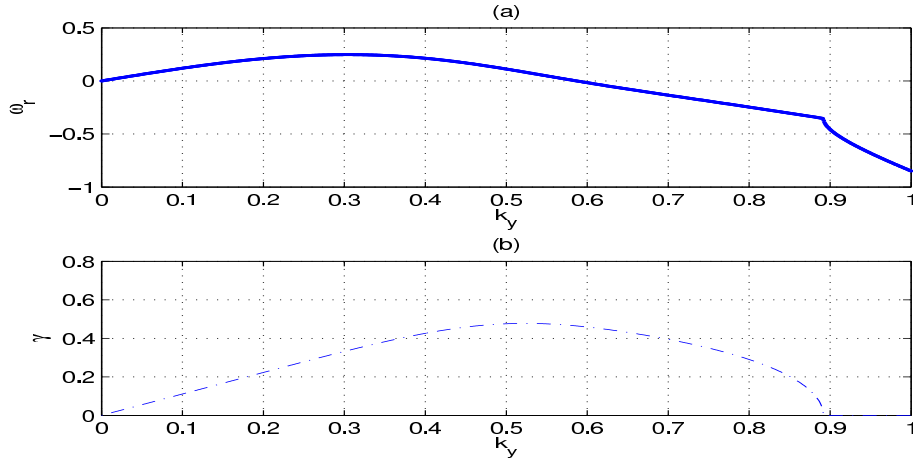


Figure 4.6: The growing branch of the single rational surface RS-ITG. Fig(a) is the dispersion plot and (b) is growth rate vs k_y . Parameters: same as in Fig.(4.2), $L_n = 0.019 \times 4$ m, $L_T = 0.019$ m, $\hat{V}'_E = 0.01$, $\hat{V}'_{\parallel} = 0.7$, $k_z = 0$

rational single rational surface RS-ITG is

$$\begin{aligned} \omega^3 \left(1 + k_y^2 + \frac{\hat{V}_E'^2}{4} \frac{q_0 R}{\hat{s}_d L_n \hat{V}'_{\parallel}} \right) - 2\omega^2 k_y (1 - K k_y^2) \left(1 + k_y^2 + \frac{\hat{V}_E'^2}{4} \frac{q_0 R}{\hat{s}_d L_n \hat{V}'_{\parallel}} \right) \\ + \omega k_y^2 \left(1 - K k_y^2 + \frac{\hat{s}_d L_n \hat{V}'_{\parallel}}{q_0 R} \right) + K k_y^3 \frac{\hat{s}_d L_n \hat{V}'_{\parallel}}{q_0 R} = 0 \quad (4.44) \end{aligned}$$

Plots for the growing branch of the dispersion relation Equation(4.44) and the corresponding eigenfunction are shown in Fig.(4.6) and Fig.(4.7) respectively.

4.3.3 No mode-rational surface or Non-resonant RS-ITG

When $k_z/k_y < 0$ or $k_z k_y < 0$ i.e. when k_z and k_y are of opposite sign the quadratic Equation(4.4) gives imaginary roots for x , given by $x = \pm i \sqrt{(|k_z/k_y|)(q_0 R/\hat{s}_d L_n)}$, and the resulting configuration has no mode-rational surfaces. The mode does not resonate anywhere along the minor radius for the given q profile. For $\hat{V}'_E = 0$ and $\hat{V}'_{\parallel} = 0$ and $k_z k_y = -|k_z k_y|$ the eigenfunction is given by

$$\phi_k = \Phi_0 \exp \left[-\frac{1}{2} \left(\frac{x - \xi_{*k}}{\Delta_k} \right)^2 \right] \exp \left[-i \frac{1}{2} Re \sqrt{A_3} x^2 \right] \quad (4.45)$$

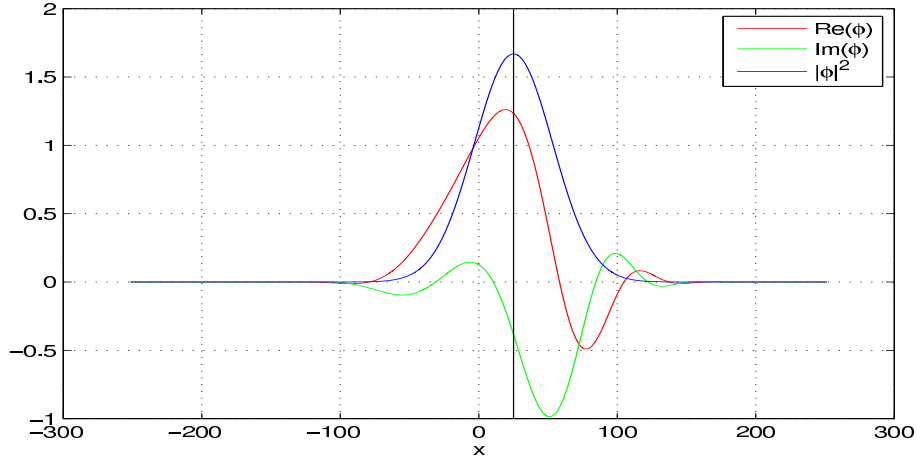


Figure 4.7: Eigenmode structure of the single rational surface RS-ITG. Solid vertical line indicates the shifted position of the mode. Mode shift = 25.13, mode width = 40.09. Parameters: same as in Fig.(4.4), $\omega = 0.08 + i0.477$, $k_z = 0$. Mode shift enhancement due to finite \hat{V}'_E can easily be noticed.

where now

$$A_3 = \frac{1}{\omega^2} \frac{2|k_y k_z| \hat{s}_d L_n}{q_0 R} \quad (4.46)$$

and the mode width given by $\Delta_k^{-2} = -Im\sqrt{A_3}$ now depends on the growth rate γ . The eigenmode dispersion relation is given by

$$-k_y^2 + \frac{k_y - \omega}{K k_y + \omega} + \frac{k_z^2}{\omega^2} - \left(\frac{\rho_s^*}{2}\right)^2 = \frac{i}{\omega} \left(\frac{2|k_y k_z| \hat{s}_d L_n}{q_0 R}\right)^{1/2} \quad (4.47)$$

A plot of the growing branch of the dispersion relation Equation(4.47) is shown in Fig.(4.8). The corresponding eigenfunction is shown in Fig.(4.9).

In the other case when minimum of E_r well does not coincide with q_{min} position $E'_r|_{r=r_{min}} \neq 0$. Let us then consider this mode with $\hat{V}'_E = \hat{V}'_{||} \neq 0$. We will consider the limit when $-2k_z(Kk_y + \omega) \gg \omega k_y \hat{V}'_{||}$ for analytical tractability of the problem. Under this condition the last term in the Equation(4.13) for A_3 is negligible. This allows us to write the eigenfunction in the form of Equation(4.28) where now

$$Re\sqrt{A_3} = \frac{\omega_r}{|\omega|^2} \sqrt{\frac{2|k_y k_z| \hat{s}_d L_n}{q_0 R}} \quad (4.48)$$

and

$$Re \frac{A_2}{2A_3} - \frac{Im\sqrt{A_3}}{Re\sqrt{A_3}} Im \frac{A_2}{2A_3} = \frac{k_y \hat{V}'_E (Kk_y|\omega|^2 + |\omega|^4/\omega_r)}{4|k_z k_y| |Kk_y + \omega|^2} \frac{q_0 R}{\hat{s}_d L_n} \quad (4.49)$$

The mode shift including the ρ_s^* term, from Equation(4.29), is given by

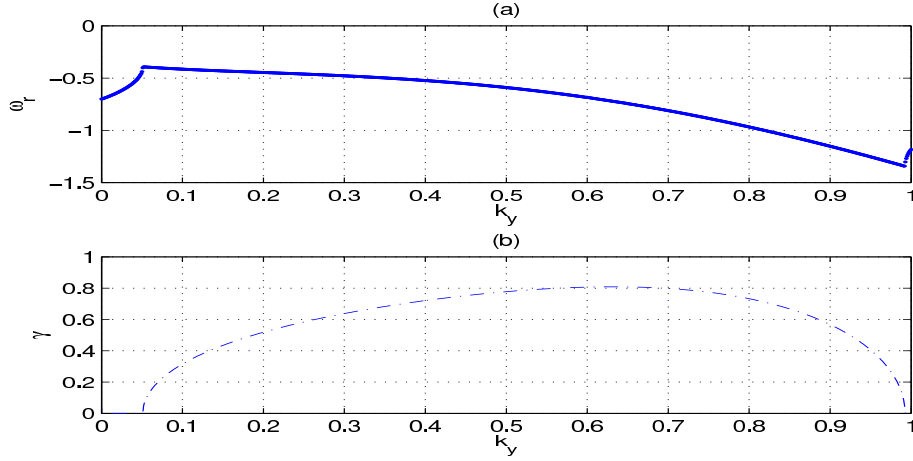


Figure 4.8: Growing branch of the non-resonant RS-ITG. Fig(a) is the dispersion plot and (b) is growth rate vs k_y . Parameters: same as in Fig.(4.2).

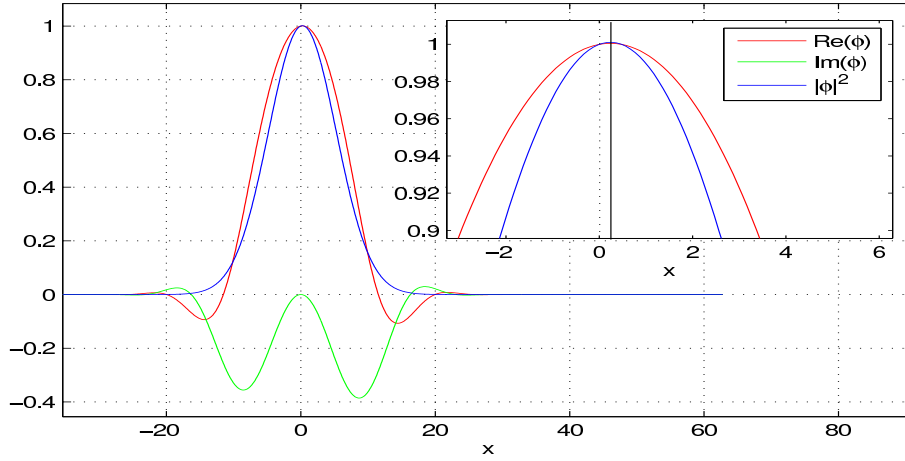


Figure 4.9: Eigenmode structure of the non-resonant RS-ITG. Solid vertical line indicates the shifted position of the mode. Mode shift = 0.731081, mode width = 8.53614. Parameters: same as in Fig.(4.8), $\omega = -0.6139 + i0.7885$.

$$\xi_{*k} = \frac{k_y \hat{V}'_E K k_y |\omega|^2}{4 |k_z k_y| |K k_y + \omega|^2} \frac{q_0 R}{\hat{s}_d L_n} + \frac{\rho_s^* |\omega|^2}{2\gamma} \sqrt{\frac{q_0 R}{2 |k_y k_z| \hat{s}_d L_n}} \quad (4.50)$$

In this case the eigenmode dispersion relation becomes

$$\begin{aligned} -k_y^2 + \frac{k_y - \omega}{K k_y + \omega} + \frac{k_z^2}{\omega^2} + \frac{1}{4} \left(\frac{\omega k_y \hat{V}'_E}{K k_y + \omega} \right)^2 \left(\frac{q_0 R}{2 |k_y k_z| \hat{s}_d L_n} \right) - \left(\frac{\rho_s^*}{2} \right)^2 \\ = \frac{i}{\omega} \left(\frac{2 |k_y k_z| \hat{s}_d L_n}{q_0 R} \right)^{1/2} \end{aligned} \quad (4.51)$$

In the (k_y, k_z) space the double rational surface mode lies in the 1st and the 3rd quadrant, the non-resonant mode lies in the 2nd and the 4th quadrant. The single rational surface mode lies on the k_y axis only where $k_z = 0$.

In this picture these three modes are complementary to each other which fills up the entire (k_y, k_z) space (see Fig.(4.10)).

A higher order calculation of the mode structure is performed in Appendix A. The eigenvalue Equation(4.8) with the quartic potential Equation(4.10) for $\hat{V}'_E, \hat{V}'_{||} = 0$ is solved analytically by perturbative method. The eigenfunction Equation(A.25) corrected up to first order shows double hump about the q_{min} position as can be seen in the Fig.(4.12). The ρ_s^* effect is seen to have two fold effect on mode structure. First, it shifts the mode centroid off the reference surface and second, asymmetrizes mode intensity about the q_{min} position. However the dispersion character and growth rates, with 1st order corrections, do not significantly differ from their respective 0th order counterparts.

4.4 Momentum flux: General considerations of radial fluxes of parallel and poloidal momentum

In this section we calculate toroidal and poloidal quasilinear momentum fluxes due to $E \times B$ drift and polarization drift. Assuming flow shear frequency much smaller than the mode frequency the linear response for $\delta v_{||}$, in dimensional form, is obtained to be

$$\delta v_{||,k} = \left(\frac{c_s \rho_s}{L_n} \right) \frac{k_y}{\omega} \left[-\hat{V}'_{||0} + \frac{k_{||}}{k_y} \left[1 - \frac{\omega_{*pi}}{\omega} \right] \right] \phi_k \quad (4.52)$$

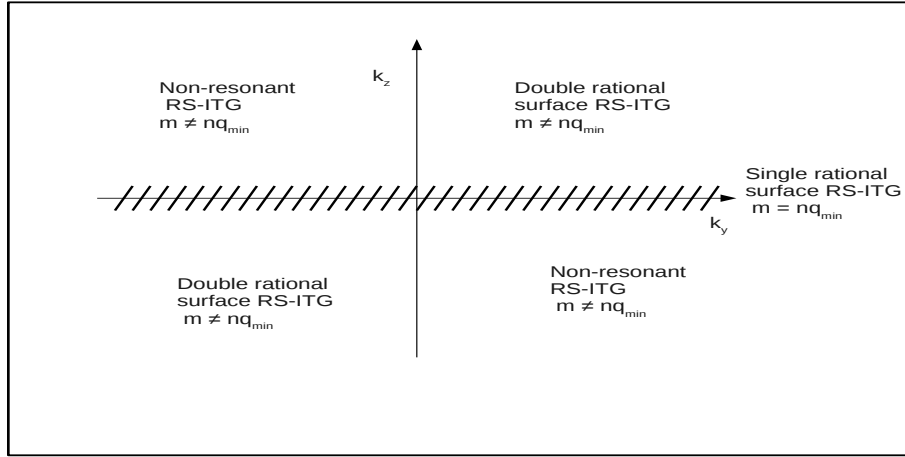


Figure 4.10: Schematic showing three distinct modes in the $k_y - k_z$ space. The nature of the mode is determined by whether the q_{min} is a rational number or not.

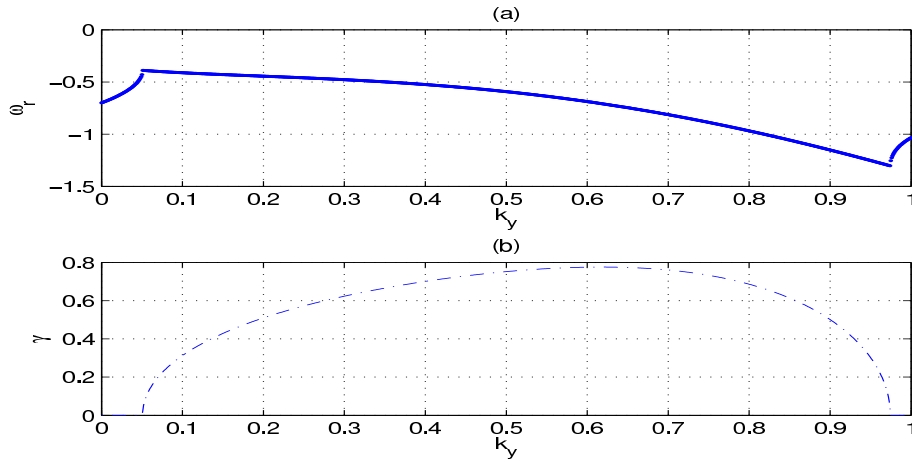


Figure 4.11: First order corrected growing branch of the double rational RS-ITG. Fig.(a) is the dispersion plot and (b) is growth rate vs k_y . Parameters: same as in Fig.(4.2)

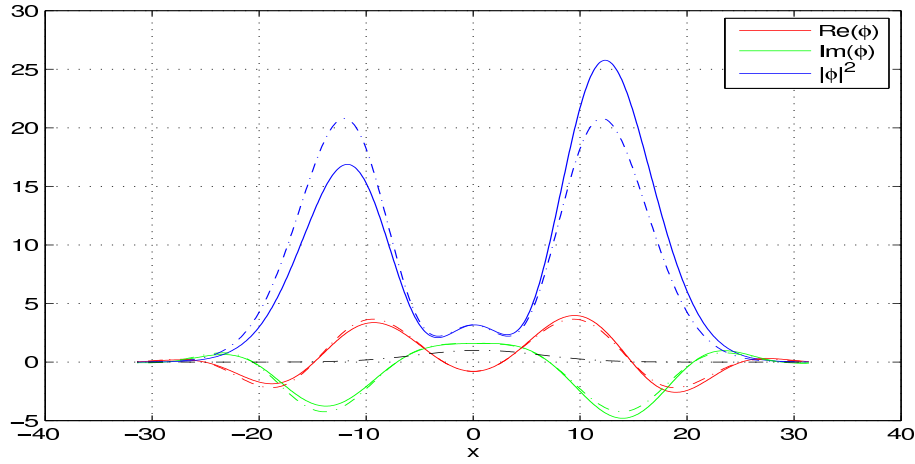


Figure 4.12: First order corrected eigenmode structures of the double rational surface RS-ITG. Parameters: same as in Fig.(4.11), $\omega = -0.75 + i0.77$. Color meanings: (---) $\text{Re}\phi$, (---) $\text{Im}\phi$, and (---) $|\phi|^2$ with 1st order correction and without ρ_s^* effect. (—) $\text{Re}\phi$, (—) $\text{Im}\phi$, and (—) $|\phi|^2$ with 1st order correction and with ρ_s^* effect. (-.-.-) $|\phi|^2$ at zeroth order with ρ_s^* effect. Intensity humps become asymmetric due to ρ_s^* effect.

The response for $\delta v_{y,k}$ is obtained from

$$\delta v_{y,k} = \delta v_{Ey,k} = i \left(\frac{c_s \rho_s}{L_n} \right) k_x \phi_k \quad (4.53)$$

The response for $\delta v_{polx,k}$ is obtained from

$$\delta v_{polx,k} = -c_s \left(\frac{\rho_s}{L_n} \right)^2 \omega k_x \phi_k \quad (4.54)$$

where $\omega_{*pi} = -\tau_i \alpha_i k_y$, $k_x = -i \partial \ln \phi_k / \partial x$, $\omega = \omega / (c_s / L_n)$.

4.4.1 $E \times B$ Flux

From linear responses for $\delta v_{\parallel,k}$ from Equation(4.52) and for δv_{Ex} we obtain a quasilinear form of toroidal Reynolds stress

$$\langle \delta v_{Ex} \delta v_{\parallel} \rangle = \text{Re} \left(\frac{c_s \rho_s}{L_n} \right)^2 \sum_{\vec{k}} i \frac{k_y^2}{\omega} \left[-\hat{V}'_{\parallel 0} + \frac{k_{\parallel}}{k_y} \left[1 - \frac{\omega_{*pi}}{\omega} \right] \right] |\phi_k|^2 \quad (4.55)$$

the first term is diffusive and the second term, being independent of $V_{||}$ and $V'_{||}$, is non-diffusive residual flux. Since $k_{||}$ is given by Equation(4.4) we define, for fixed k_z ,

$$\sum_{\vec{k}}(...) \rightarrow \sum_{k_y} \int dk_{||}(...) = - \sum_{k_y} (|k_y| \hat{s} L_n / q_0 R) (\langle (...) \rangle_{\hat{s}} + 2 \hat{s}_d / \hat{s} \langle (...) \rangle_{\hat{s}_d}) \quad (4.56)$$

where

$$\langle (...) \rangle_{\hat{s}} = \int dx (...) \quad (4.57)$$

and

$$\langle (...) \rangle_{\hat{s}_d} = \int dx |x| (...) \quad (4.58)$$

The modulus on k_y and x is put so that the nature of the summand or integrand with respect to k_y and x do not change while evaluating the summation over \vec{k} . We can write the spectral average of $k_{||}$ as

$$\langle k_{||} \rangle = \langle k_{||} |\phi_k|^2 \rangle_{\hat{s}} + 2 \hat{s}_d / \hat{s} \langle k_{||} |\phi_k|^2 \rangle_{\hat{s}_d} \quad (4.59)$$

So, $\langle k_{||} \rangle$ survives even when scalar potential ϕ_k is symmetric about a reference surface. This means that eigenfunctions with broken symmetry is no more a strong requirement for residual stress generation. This is attributed to the novel magnetic field structure about q_{min} .

The poloidal stress is given by

$$\langle \delta v_{Ex} \delta v_y \rangle = -Re \sum_{\vec{k}} \left(\frac{c_s \rho_s}{L_n} \right)^2 k_y k_x |\phi_k|^2 \quad (4.60)$$

It is obvious that poloidal flux survives only if $\langle Re k_x \rangle \neq 0$. Here we are defining the spectral average of $\langle Re k_x \rangle$ as

$$\langle Re k_x \rangle = \langle Re k_x |\phi_k|^2 \rangle_{\hat{s}} + 2 \hat{s}_d / \hat{s} \langle Re k_x |\phi_k|^2 \rangle_{\hat{s}_d} \quad (4.61)$$

In case of standing eigenmodes k_x is imaginary and hence mean flow can not be generated. Now because of the novel property of the magnetic field near q minimum radial asymmetry in turbulence is no more a strong requirement for

survival of poloidal flux.

4.4.2 Polarization driven flux

From linear responses for $\delta v_{\parallel,k}$, $\delta v_{y,k}$, $\delta v_{polx,k}$ from Equation(4.52), (4.53) and (4.54) respectively we obtain a quasilinear form of toroidal stress

$$\begin{aligned} \langle \delta v_{polx} \delta v_{\parallel} \rangle &= -c_s^2 \left(\frac{\rho_s}{L_n} \right)^3 \frac{\partial}{\partial T} \left\langle \frac{\partial \phi}{\partial x} \delta v_{\parallel} \right\rangle \\ &+ c_s^2 \left(\frac{\rho_s}{L_n} \right)^3 Re \sum_{\vec{k}} \left[\hat{V}'_{\parallel 0} k_x^* k_y - k_x^* k_{\parallel} \left[1 - \frac{\omega_{*pi}}{\omega} \right] \right] |\phi_k|^2 \end{aligned} \quad (4.62)$$

and poloidal stress

$$\langle \delta v_{polx} \delta v_y \rangle = -c_s^2 \left(\frac{\rho_s}{L_n} \right)^3 \frac{\partial}{\partial T} \left[\frac{1}{2} \left\langle \left(\frac{\partial \phi}{\partial x} \right)^2 \right\rangle \right] \quad (4.63)$$

where $Re(f)$ means real part of (f) and the angular braces indicates average over fast space-time scale. The poloidal polarization stress vanish in steady state. A cursory look at Equation(4.62) reveals that the polarization drift induced residual stress survives when the spectral average $\langle k_{\parallel} k_x \rangle$ defined as

$$\langle k_{\parallel} k_x \rangle = \langle k_{\parallel} k_x |\phi_k|^2 \rangle_{\hat{s}} + 2 \frac{\hat{s}_d}{\hat{s}} \langle k_{\parallel} k_x |\phi_k|^2 \rangle_{\hat{s}_d} \neq 0 \quad (4.64)$$

which is always satisfied because $k_{\parallel} \propto x$ and $k_x \propto x$ in general, and shifted Gaussian structure of the fluctuation spectrum in general. But a close look at the above equation reveals that broken symmetry in eigenfunction is not a strict requirement for survival of parallel polarization residual stress. However, microturbulence with broken symmetry will do have an effect on the momentum fluxes be it toroidal or poloidal. In the following we will examine the momentum fluxes at minimum q and in the neighborhood of minimum q separately.

4.5 Momentum flux in the neighborhood of q-min

4.5.1 $E \times B$ flux

The diffusive component of toroidal Reynolds stress is given by

$$\Pi_{\parallel,E}^{Diff} = Re \left(\frac{c_s \rho_s}{L_n} \right)^2 \sum_{k_y} \left(-\frac{|k_y| \hat{s} L_n}{q_0 R} \right) i \frac{k_y^2}{\omega} (-\hat{V}'_{\parallel 0}) \left(\langle |\phi_k|^2 \rangle_{\hat{s}} + 2 \frac{\hat{s}_d}{\hat{s}} \langle |\phi_k|^2 \rangle_{\hat{s}_d} \right) \quad (4.65)$$

The non-diffusive component is given by

$$\Pi_{\parallel,E}^{NDiff} = Re \left(\frac{c_s \rho_s}{L_n} \right)^2 \sum_{k_y} \left(-\frac{|k_y| \hat{s} L_n}{q_0 R} \right) i \frac{k_y^2}{\omega} \left[1 - \frac{\omega_{*pi}}{\omega} \right] \langle \frac{k_{\parallel}}{k_y} \rangle \quad (4.66)$$

where the spectral average $\langle \frac{k_{\parallel}}{k_y} \rangle$ is given by

$$\langle \frac{k_{\parallel}}{k_y} \rangle = \langle \frac{k_{\parallel}}{k_y} |\phi_k|^2 \rangle_{\hat{s}} + 2 \frac{\hat{s}_d}{\hat{s}} \langle \frac{k_{\parallel}}{k_y} |\phi_k|^2 \rangle_{\hat{s}_d} \quad (4.67)$$

Now

$$\langle \frac{k_{\parallel}}{k_y} |\phi_k|^2 \rangle_{\hat{s}} = \frac{k_z}{k_y} \langle |\phi_k|^2 \rangle_{\hat{s}} - \frac{L_n}{q_0 R} [\hat{s} \langle x |\phi_k|^2 \rangle_{\hat{s}} + \hat{s}_d \langle x^2 |\phi_k|^2 \rangle_{\hat{s}}] \quad (4.68)$$

and

$$\langle \frac{k_{\parallel}}{k_y} |\phi_k|^2 \rangle_{\hat{s}_d} = \frac{k_z}{k_y} \langle |\phi_k|^2 \rangle_{\hat{s}_d} - \frac{L_n}{q_0 R} [\hat{s} \langle x |\phi_k|^2 \rangle_{\hat{s}_d} + \hat{s}_d \langle x^2 |\phi_k|^2 \rangle_{\hat{s}_d}] \quad (4.69)$$

where

$$\langle |\phi_k|^2 \rangle_{\hat{s}} = \Delta_k \sqrt{\pi} |\phi_{0k}|^2 \quad (4.70)$$

$$\langle x |\phi_k|^2 \rangle_{\hat{s}} = \Delta_k \xi_k \sqrt{\pi} |\phi_{0k}|^2 \quad (4.71)$$

$$\langle x^2 |\phi_k|^2 \rangle_{\hat{s}} = \left[\Delta_k^3 \frac{\sqrt{\pi}}{2} + \Delta_k \xi_k^2 \sqrt{\pi} \right] |\phi_{0k}|^2 \quad (4.72)$$

and

$$\langle |\phi_k|^2 \rangle_{\hat{s}_d} = \Delta_k^2 |\phi_{0k}|^2 \quad (4.73)$$

$$\langle x |\phi_k|^2 \rangle_{\hat{s}_d} = 2\Delta_k \xi_k \sqrt{\pi} |\phi_{0k}|^2 \quad (4.74)$$

$$\langle x^2 |\phi_k|^2 \rangle_{\hat{s}_d} = [\Delta_k^4 + 3\Delta_k^2 \xi_k^2 + \Delta_k \xi_k^3 \sqrt{\pi}] |\phi_{0k}|^2 \quad (4.75)$$

A closer look at Equations(4.67 - 4.75) clearly unfolds the fact that reflectional symmetry breaking of the eigen function is not strictly necessary for the survival of parallel residual stress.

The poloidal Reynolds stress is

$$\langle \delta v_{Ex} \delta v_y \rangle = Re \sum_{k_y} \left(\frac{c_s \rho_s}{L_n} \right)^2 k_y \left(\frac{|k_y| \hat{s} L_n}{q_0 R} \right) \langle Re k_x \rangle \quad (4.76)$$

where the spectral average $\langle Re k_x \rangle$ is obtained as

$$\langle Re k_x \rangle = \langle Re k_x |\phi_k|^2 \rangle_{\hat{s}} + 2\hat{s}_d / \hat{s} \langle Re k_x |\phi_k|^2 \rangle_{\hat{s}_d} \quad (4.77)$$

where again

$$\langle Re k_x |\phi_k|^2 \rangle_{\hat{s}} = -Re \sqrt{A_3} \left[\langle x |\phi_k|^2 \rangle_{\hat{s}} + \left(Re \frac{A_2}{2A_3} - \frac{Im \sqrt{A_3}}{Re \sqrt{A_3}} Im \frac{A_2}{2A_3} \right) \langle |\phi_k|^2 \rangle_{\hat{s}} \right] \quad (4.78)$$

and

$$\langle Re k_x |\phi_k|^2 \rangle_{\hat{s}_d} = -Re \sqrt{A_3} \left[\langle x |\phi_k|^2 \rangle_{\hat{s}_d} + \left(Re \frac{A_2}{2A_3} - \frac{Im \sqrt{A_3}}{Re \sqrt{A_3}} Im \frac{A_2}{2A_3} \right) \langle |\phi_k|^2 \rangle_{\hat{s}_d} \right] \quad (4.79)$$

This shows that spectrally averaged $Re k_x$ has to be finite for poloidal stress to be finite. In turn this may demand some specific turbulence characteristics to be fulfilled. Equations (4.77 - 4.79) shows that asymmetry in turbulence spectrum is not a necessary condition for survival of spectrally averaged $Re k_x$. However turbulence with broken symmetry does effect the magnitude of poloidal momentum flux.

Taking $V'_E = 0$ and considering ρ_s^* as the only source of symmetry breaking of the eigenfunction the $\langle k_{||}/k_y \rangle$ and hence the residual stress is seen to decrease with L_n/R for both double rational surface RS-ITG (Fig.(4.13)) and non-resonant

RS-ITG(Fig.(4.14)). However the the ρ_s^* induced symmetry breaking of the eigen-

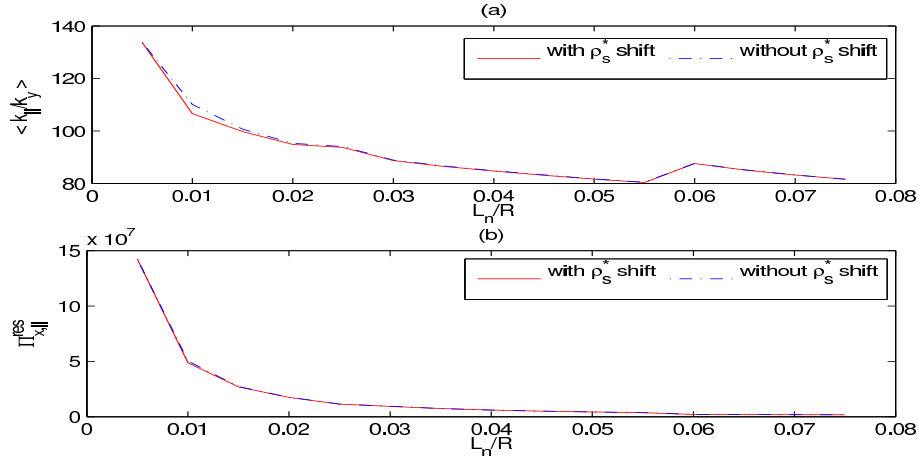


Figure 4.13: Double rational surface RS-ITG: (a) Mode average of k_{\parallel}/k_y with and without ρ_s^* . (b) Residual stress vs L_n/R with and without ρ_s^* shift. It appears that ρ_s^* induced symmetry breaking of the eigenfunction has no appreciable effect on k_{\parallel} symmetry breaking. So the k_{\parallel} symmetry breaking and hence the residual stress is dominantly determined by mode width rather than mode shift.

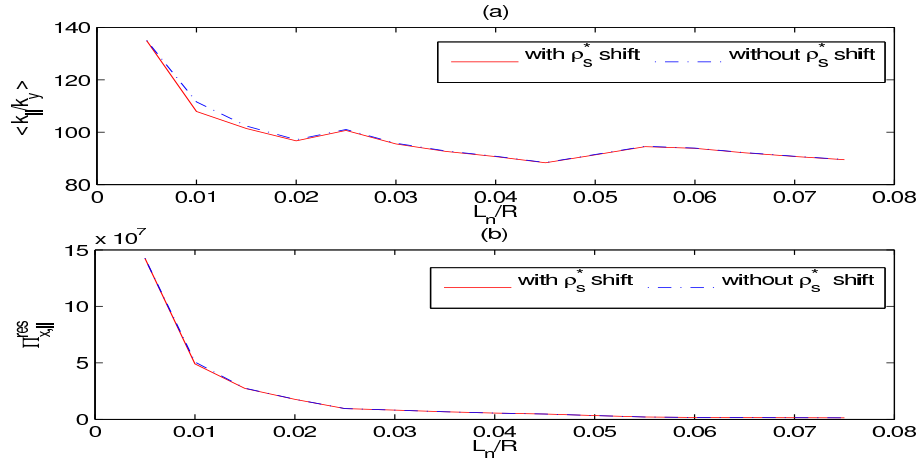


Figure 4.14: No rational surface RS-ITG: (a) Mode average of k_{\parallel}/k_y with and without ρ_s^* . (b) Residual stress vs L_n/R with and without ρ_s^* shift. It appears that ρ_s^* induced symmetry breaking of the eigenfunction has no appreciable effect on k_{\parallel} symmetry breaking. So the k_{\parallel} symmetry breaking and hence the residual stress is dominantly determined by mode width rather than mode shift.

function is seen to have very little contribution to $\langle k_{\parallel}/k_y \rangle$ and residual stress and are dominantly determined by mode width coming through quadratic dependence of parallel wave number on distance from q_{min} position, i.e., $k_{\parallel} \propto x^2$. Symmetry breaking of the eigenfunction due to strong $E \times B$ radial shear (see Fig.(4.5)) will have significant effect/contribution on/to the residual stress (not shown in the figures). Anyway, the most important point is that the dependence $k_{\parallel} \propto x^2$ is alone capable of generating finite residual stress at q_{min} whose origin is rooted in the novelty of the magnetic field structure at and about q_{min} .

In the following subsection we are calculating the toroidal and poloidal momentum fluxes driven by single and double rational surface modes at q_{min} , respectively, due to $E \times B$ drift.

4.5.2 $E \times B$ Fluxes at q_{min} due to single mode-rational surface mode:

$$k_z = 0, \hat{s} = 0$$

Parallel fluxes

The diffusive component is

$$\Pi_{\parallel, E}^{Diffusive} = -\chi_{\parallel} \frac{dV_{\parallel}}{dx} \quad (4.80)$$

where now the diffusivity is

$$\chi_{\parallel} = Re \left(\frac{c_s \rho_s}{L_n} \right)^2 \sum_{k_y} \left(-\frac{|k_y| \hat{s}_d L_n}{q_0 R} \right) i \frac{k_y^2}{\omega} 2 \langle |\phi_k|^2 \rangle_{\hat{s}_d} \quad (4.81)$$

The non-diffusive component as obtained from Equation(4.66) is

$$\Pi_{\parallel, E}^{Res} = Re \left(\frac{c_s \rho_s}{L_n} \right)^2 \sum_{k_y} |k_y| \left(\frac{\hat{s}_d L_n}{q_0 R} \right)^2 i \frac{k_y^2}{\omega} \left[1 - \frac{\omega_{*pi}}{\omega} \right] 2 \langle x^2 |\phi_k|^2 \rangle_{\hat{s}_d} \quad (4.82)$$

Poloidal fluxes

$$\langle \delta v_{Ex} \delta v_y \rangle = \sum_{k_y} \left(\frac{c_s \rho_s}{L_n} \right)^2 k_y \left(\frac{|k_y| \hat{s}_d L_n}{q_0 R} \right) 2 \langle Re k_x |\phi_k|^2 \rangle_{\hat{s}_d} \quad (4.83)$$

In the following subsection we are calculating parallel and poloidal polarization stresses.

4.5.3 Polarization drift driven flux

Parallel fluxes

The parallel diffusive polarization stress is

$$\Pi_{\parallel, pol}^{Diff} = -\chi_{\parallel, pol} \frac{dV_{\parallel}}{dx} \quad (4.84)$$

where

$$\chi_{\parallel, pol} = c_s^2 \left(\frac{\rho_s}{L_n} \right)^3 Re \sum_{k_y} \left(-\frac{\hat{s}_d L_n |k_y|}{q_0 R} \right) k_y \langle Re k_x^* \rangle \quad (4.85)$$

and the spectrally averaged $Re k_x^*$ is actually given by

$$\langle Re k_x^* \rangle = \langle Re k_x \rangle \quad (4.86)$$

and $\langle Re k_x \rangle_{\hat{s}}$ has already been calculated in the previous section. The non-diffusive component of parallel polarization stress is given by

$$\Pi_{\parallel, pol}^{NDiff} = c_s^2 \left(\frac{\rho_s}{L_n} \right)^3 Re \sum_{k_y} \left(\frac{|k_y| \hat{s}_d L_n}{q_0 R} \right) k_y \left[1 - \frac{\omega_{*pi}}{\omega} \right] \langle k_x^* k_{\parallel} \rangle \quad (4.87)$$

where the spectral average $\langle k_x^* k_{\parallel} \rangle$ is given by

$$\langle k_x^* k_{\parallel} \rangle = \langle k_x^* k_{\parallel} |\phi_k|^2 \rangle_{\hat{s}} + 2\hat{s}_d / \hat{s} \langle k_x^* k_{\parallel} |\phi_k|^2 \rangle_{\hat{s}_d} \quad (4.88)$$

Now $k_x^* k_{||}$ can be expressed as

$$k_x^* k_{||} = A + Bx + Cx^2 + Dx^3 \quad (4.89)$$

where the coefficients A , B , C and D are complex in general and are given by

$$A = k_z \left[\frac{i\xi_k}{\Delta_k^2} - Re\sqrt{A_3} \left(Re\frac{A_2}{2A_3} - \frac{Im\sqrt{A_3}}{Re\sqrt{A_3}} Im\frac{A_2}{2A_3} \right) \right] \quad (4.90)$$

$$B = -k_z \left(\frac{i}{\Delta_k^2} + Re\sqrt{A_3} \right) - \frac{k_y \hat{s} L_n}{q_0 R} \frac{A}{k_z} \quad (4.91)$$

$$C = \left[\left(\frac{i}{\Delta_k^2} + Re\sqrt{A_3} \right) - \frac{i\xi_k}{\Delta_k^2} - \frac{\hat{s}_d}{\hat{s}} Re\sqrt{A_3} \left(Re\frac{A_2}{2A_3} - \frac{Im\sqrt{A_3}}{Re\sqrt{A_3}} Im\frac{A_2}{2A_3} \right) \right] \times \frac{k_y \hat{s} L_n}{q_0 R} \quad (4.92)$$

$$D = \left(\frac{i}{\Delta_k^2} + Re\sqrt{A_3} \right) \frac{k_y \hat{s}_d L_n}{q_0 R} \quad (4.93)$$

Poloidal fluxes

The time asymptotic poloidal polarization stress is

$$\langle \delta v_{pol,x} \delta v_y \rangle = 0 \quad (4.94)$$

4.5.4 Polarization fluxes at q_{min} due single mode-rational surface mode:

For single rational surface mode $k_z = 0$, and at q_{min} position $\hat{s} = 0$. Then the turbulent parallel polarization diffusivity turns out to be

$$\chi_{||,pol} = c_s^2 \left(\frac{\rho_s}{L_n} \right)^3 Re \sum_{k_y} \left(-\frac{\hat{s}_d L_n |k_y|}{q_0 R} \right) k_y 2 \langle Re k_x^* |\phi_k|^2 \rangle_{\hat{s}_d} \quad (4.95)$$

The non-diffusive component is obtained from Equation(4.87)

$$\Pi_{||,pol}^{NDiff} = -c_s^2 \left(\frac{\rho_s}{L_n} \right)^3 Re \sum_{k_y} \frac{|k_y| \hat{s}_d L_n}{q_0 R} k_y \left[1 - \frac{\omega_{*pi}}{\omega} \right] 2 \langle k_x^* k_{||} |\phi_k|^2 \rangle_{\hat{s}_d} \quad (4.96)$$

where now

$$\langle k_x^* k_{||} |\phi_k|^2 \rangle_{\hat{s}_d} = C \langle x^2 |\phi_k|^2 \rangle_{\hat{s}_d} + D \langle x^3 |\phi_k|^2 \rangle_{\hat{s}_d} \quad (4.97)$$

and

$$C = -Re\sqrt{A_3} \left(Re\frac{A_2}{2A_3} - \frac{Im\sqrt{A_3}}{Re\sqrt{A_3}} Im\frac{A_2}{2A_3} \right) \frac{k_y \hat{s}_d L_n}{q_0 R} \quad (4.98)$$

$$D = \left(\frac{i}{\Delta_k^2} + Re\sqrt{A_3} \right) \frac{k_y \hat{s}_d L_n}{q_0 R} \quad (4.99)$$

The first term remains finite even for symmetric turbulence spectrum the second term does demand broken symmetry in turbulence spectrum for its survival.

4.6 Discussion and conclusions

We presented a neat derivation of possible slab eigenmodes driven by ion temperature gradient at the minimum of the safety factor q . The dynamics of electrons is considered to be adiabatic. The steep density gradient at the ITB at the q_{min} makes ρ_s^* finite. Inclusion of finite ρ_s^* effect breaks the reflectional symmetry of the eigenfunction even without finite radial electric field shear. Anyway, the finite ρ_s^* and $E \times B$ shear together determine the effective shift of the eigenmode of the q_{min} position. Three different types of reverse shear modes are found at q_{min} depending on whether k_z is 0 or not and relative sign between k_y and k_z . These are single mode-rational surface RS-ITG, double mode-rational surface RS-ITG and non-resonant RS-ITG. The single mode-rational surface RS-ITG lies on the k_y axis ($k_z = 0$), the double mode-rational surface RS-ITG lies in the first and the third quadrants, and the non-resonant RS-ITG lies in the second and the fourth quadrants respectively in the (k_y, k_z) space (see Fig.(4.10)).

Parallel and poloidal Reynolds stresses driven by single mode-rational surface RS-ITG were calculated for both turbulent $E \times B$ drift and polarization drift. The expression for spectrally averaged $k_{||}$ is generalized to include both shear and curvature in safety factor q . It is found that broken symmetry of the eigenfunction is not a strict requirement for the survival of parallel and poloidal residual Reynolds stresses at q_{min} . This is because the $\langle k_{||} \rangle$ survives even for symmetric eigenfunction

at q_{min} . This is attributed to the fact that $k_{\parallel} \propto x^2$ at q_{min} . The ρ_s^* induced symmetry breaking of the eigenfunction (of double rational surface and non-resonant RS-ITG) appears to have insignificantly low effect on turbulent $E \times B$ drift driven parallel residual stress/flux which is dominantly determined by the mode width for $k_{\parallel} \propto x^2$ (see Fig.(4.13) and Fig.(4.14)). The turbulent $E \times B$ drift driven poloidal Reynolds stress survives by making $\langle Re k_x \rangle \neq 0$ i.e., by $\langle Re k_x \rangle$ symmetry breaking. The residual parallel polarization stress survives when $\langle k_x k_{\parallel} \rangle \neq 0$ i.e., by $\langle k_x k_{\parallel} \rangle$ symmetry breaking. The time asymptotic poloidal polarization stress is found to vanish. These symmetry breakings do not necessarily require broken symmetry of the eigenfunction (see Equations(4.78, 4.79); Equation(4.88) and (4.89)). However, the eigenfunction naturally turns out to be asymmetric and this modifies the magnitude of parallel and poloidal momentum fluxes.

In the following chapter gyrokinetic flux tube simulation studies on momentum and heat transport by finite ballooning angle and background $E \times B$ shear in toroidal ITG turbulence are presented.

5

Finite ballooning angle and macroscopic ExB shear effects on ion temperature gradient driven mode in gyrokinetic flux tube simulations

5.1 Introduction

Sheared slab calculations of momentum transport presented in the previous chapters did not consider the effects of poloidal variation of equilibrium magnetic field and hence the effects of poloidal eigenmode structure on transport properties was missing. Such an effect can be studied via ballooning formalism in leading order. However, here gyrokinetic flux tube simulations[116, 117] are used as first principle calculations to serve our purpose. Flux tube simulations, taking advantage of the short perpendicular wavelength and long parallel wavelength i.e. ($k_{\perp} \gg k_{\parallel}$) of these microinstabilities, makes use of the field aligned coordinate system to reduce computational burden [118]. A flux tube is a curved and and sheared box centered around a field line that makes an integral number of poloidal turns around the torus, thus sampling the entire flux surface. The equilibrium quantities are Taylor expanded to first order in the perpendicular coordinates around the central field line (or box center). The values and first derivatives of equilibrium quantities, together with the metric coefficients that describe the shaping of the box, are taken to be constant over the perpendicular extent of the box. Only parallel

variations are taken into account. Such a local approximation is valid when the radial extent of the box is small compared to the machine size. Profile shearing effects, important when ρ^* is finite, are not captured in this formulation. Periodic boundary conditions are used in radial (x) and binormal (y) directions i.e., $f(x+L_x, y, z) = f(x, y, z)$ and $f(x, y+L_y, z) = f(x, y, z)$, where L_x (L_y) represents simulation box length in radial (binormal) direction. The box lengths are chosen to be bigger than the correlation lengths of the turbulent fields in the corresponding directions. Such periodic boundary conditions, allow us to take Fourier representation for the x and y directions. The poloidal angle is used to parametrize the parallel direction z . The magnetic shear \hat{s} causes coupling of radial modes and leads to the parallel boundary condition $f(k_x, k_y, z + L_z) = (-1)^{nN} f(k'_x, k_y, z)$ where $k'_x = (m + nN)k_x^{min}$ and $k_y = mk_y^{min}$ and $k_x = nk_x^{min}$; m and n takes values $0, \pm 1, \pm 2, \dots$ and $k_{x,y}^{min} = 2\pi/L_{x,y}$. $N = 2\pi k_y \hat{s} k_y^{min} / k_x^{min}$ is also an integer. The parallel mode structure is formed by coupling all the k_x modes for a given k_y where each fourier mode (k_x, k_y) balloon at poloidal angle $\theta_k = -k_x/k_y \hat{s}$ called ballooning angle. So a set $\{k_x\} \equiv \{\dots, -k_x^{min}, 0, +k_x^{min}, \dots\}$ forms mode structure in z or θ that is symmetric about low field side (LFS) mid plane ($\theta = 0$). Shifting each of the elements in $\{k_x\}$ by some nonzero values rotates the mode structure in θ and stationing it away from LFS mid plane. That is a shift in the k_x values balloons the mode in θ at $\theta_0 = -k_{x,center}/k_y \hat{s}$, where $k_{x,center}$ represents the central k_x mode. First part of this chapter explores the effects of finite $k_{x,center}$ on linear eigenvalues spectrum and associated transports of heat and momentum.

The k_y spectrum of the eigenvalues differ significantly when $\theta_0 \neq 0$ from that of the commonly considered case of $\theta_0 = 0$. Finite growth rates in the usually stable region ($k_y > 1$) leads to development short wavelength (SW) branch when maximum growth rates in θ_0 scan are considered. This SWITG branch dies out on reduction of equilibrium temperature gradient. This behavior is similar to SWITG reported by authors [119, 120, 121, 122] in the past but the fundamental striking difference between our and past works is that past works considered extremely high temperature gradients ($R/L_T = 25$ with $R/L_n = 10$), which might be prevalent in pedestal and transport barriers, and $\theta_0 = 0$ whereas our results are for regular temperature gradients but at finite θ_0 . The SW branch is damped out towards lower temperature gradients but max growth rates still showing marked difference from zero ballooning angle growth rates. Impact of finite θ_0 on associated heat

and parallel momentum flux are discussed.

Second half of this chapter discusses symmetry breaking effects of background macroscopic $E \times B$ shear on parallel momentum transport in nonlinear gyrokinetic simulations. The role of self-consistently formed zonal shear is investigated. The chapter is organized as follows. Section 5.2 contains formulation of the gyrokinetic equations in field aligned coordinates as solved in GENE. Diagnostics used to extract various information are also described in this section. Results of linear flux tube simulations for ITG mode are delineated in Section 5.3. Finally discussion and conclusions are made in Section 5.5.

5.2 Model Equations

5.2.1 Formulation

The general perturbed gyrokinetic equation being solved in GENE is written in field aligned coordinate (x, y, z) as follows [123]

$$\begin{aligned}
 & \frac{\partial \hat{g}_{1j}}{\partial \hat{t}} + \frac{1}{\hat{C}} \frac{\hat{B}_0}{\hat{B}_{0\parallel}^*} \left[\hat{\omega}_{nj} + \hat{\omega}_{Tj} \left(\frac{\hat{v}_{\parallel j}^2 + \hat{\mu}_j \hat{B}_0}{\tau_{0j}} - \frac{3}{2} \right) \right] \hat{F}_{0j} \frac{\partial \hat{\chi}_{1j}}{\partial \hat{y}} + \frac{1}{\hat{C}} \frac{\hat{B}_0}{\hat{B}_{0\parallel}^*} \left(\frac{\partial \hat{\chi}_{j1}}{\partial \hat{x}} \hat{\Gamma}_{j,y} \right. \\
 & \left. - \frac{\partial \hat{\chi}_{j1}}{\partial \hat{y}} \hat{\Gamma}_{j,x} \right) + \frac{\hat{B}_0}{\hat{B}_{0\parallel}^*} \frac{\hat{T}_{0j}(x_0)}{Z_j} \frac{\hat{\mu}_j \hat{B}_0 + 2\hat{v}_{\parallel}^2}{\hat{B}_0} \left(\hat{\mathcal{K}}_x \hat{\Gamma}_{j,x} + \hat{\mathcal{K}}_y \hat{\Gamma}_{j,y} \right) + \hat{v}_{Tj}(x_0) \frac{\hat{C}}{\hat{j}_{xyz} \hat{B}_0} \hat{v}_{\parallel j} \hat{\Gamma}_{j,z} \\
 & - \frac{\hat{B}_0}{\hat{B}_{0\parallel}^*} \frac{\hat{T}_{0j}(x_0)}{Z_j \hat{B}_0} \frac{\hat{v}_{\parallel}^2}{\hat{C}} \beta_{ref} \frac{\hat{p}_0}{\hat{B}_0} \hat{\omega}_{pj} \hat{\Gamma}_{j,y} - \frac{\hat{v}_{Tj}(x_0)}{2} \frac{\hat{C}}{\hat{j}_{xyz} \hat{B}_0} \hat{\mu}_j \frac{\partial \hat{B}_0}{\partial \hat{z}} \frac{\partial \hat{F}_{j1}}{\partial v_{\parallel}} \\
 & - \frac{\hat{B}_0}{\hat{B}_{0\parallel}^*} \frac{\hat{T}_{0j}(x_0)}{Z_j} \frac{\hat{\mu}_j \hat{B}_0 + 2\hat{v}_{\parallel}^2}{\hat{B}_0} \left[\hat{\omega}_{nj} + \hat{\omega}_{Tj} \left(\frac{\hat{v}_{\parallel j}^2 + \hat{\mu}_j \hat{B}_0}{\tau_{0j}} - \frac{3}{2} \right) \right] \hat{F}_{0j} = 0 \quad (5.1)
 \end{aligned}$$

where we used the definitions $\tau_{0j}(x) = T_{0j}(x)/T_{0j}(x_0)$, $\mathcal{N}_{0j}(x) = n_{0j}(x)/n_{0j}(x_0)$, $Z_j = q_j/e$. The distribution functions are normalized as

$$\hat{F}_{0j} = \frac{c_{ref}^3 \hat{v}_{Tj}^3(x_0)}{n_{ref} \hat{n}_{0j}(x_0)} F_{0j} \quad \hat{F}_{1j} = \frac{L_{ref}}{\rho_{ref}} \frac{c_{ref}^3 \hat{v}_{Tj}^3(x_0)}{n_{ref} \hat{n}_{0j}(x_0)} F_{1j}$$

Chapter 5. Finite ballooning angle and macroscopic ExB shear effects on ion temperature gradient driven mode in gyrokinetic flux tube simulations

The electromagnetic fields are normalized as

$$\hat{\Phi}_1 = \frac{L_{ref}}{\rho_{ref}} \frac{T_{ref}}{e} \Phi_1 \quad \hat{A}_{1||} = \frac{L_{ref}}{\rho_{ref}} B_{ref} \rho_{ref} A_{1||}$$

Space time variables are normalized as $\hat{t} = t c_{ref} / L_{ref}$, $\hat{x} = x / \rho_{ref}$, $\hat{y} = y / \rho_{ref}$, $\hat{z} = z$, $\hat{x}_{eq} = x / L_{ref}$. The velocity variables are normalized as

$$\hat{v}_{||j} = \frac{v_{||}}{\hat{v}_T(x_0) c_{ref}} \quad \hat{\mu}_j = \frac{\mu B_{ref}}{\hat{T}_{0,j}(x_0) T_{ref}} ; v_{Tj}(x) = \sqrt{2T_{0j}(x)/m_j} = c_{ref} \hat{v}_{Tj}(x)$$

Equilibrium density and temperature are normalized as $\hat{T}_{0j}(x) = T_{0j}(x)/T_{ref}$, $\hat{n}_{0j}(x) = n_{0j}(x)/n_{ref}$. The equilibrium geometric quantities are normalized as $\hat{\gamma}_1 = \gamma_1$, $(\hat{\gamma}_2, \hat{\gamma}_3) = (\gamma_2, \gamma_3)L_{ref}$, $\hat{J}^{xyz} = J^{xyz}/L_{ref}$. Here γ 's are defined using metric coefficients g^{ij} : $\gamma_1 = g^{xx}g^{yy} - (g^{xy})^2$, $\gamma_2 = g^{xy}g^{yz} - g^{xy}g^{xz}$, $\gamma_3 = g^{xy}g^{yz} - g^{yy}g^{xz}$.

The dependent variables are defined as

$$\begin{aligned} \hat{g}_{1j} &= \hat{F}_{1j} + \frac{Z_j \hat{v}_{Tj}(x_0)}{\hat{T}_{0j}(x)} \hat{v}_{||j} \hat{F}_{0j} \hat{A}_{1||} \\ \Gamma_{\hat{\alpha},j} &= \partial_{\hat{\alpha}} \hat{f}_{1j} + \frac{Z_j}{\hat{T}_{0j}(x)} \partial_{\hat{\alpha}} \hat{\Phi}_1 \hat{F}_{0j} \\ \hat{F}_{0j} &= \frac{\mathcal{N}_{0j}(x)}{[\pi \tau_{0j}(x)]^{3/2}} \exp\left(-\frac{(\hat{v}_{||j}^2 + \hat{\mu}_j \hat{B}_0(x, z))}{\tau_{0j}(x)}\right) \\ \hat{\chi}_j &= \hat{\Phi}_1 - \hat{v}_{Tj}(x_0) \hat{v}_{||j} \hat{A}_{1||} \end{aligned}$$

The over-bar indicates a gyro-averaged quantity.

Also,

$$\begin{aligned} \hat{\mathcal{K}}_x &= -\frac{1}{\hat{C}} \frac{\hat{\gamma}_2}{\hat{\gamma}_1} \frac{\partial \hat{B}_0}{\partial \hat{z}} \\ \hat{\mathcal{K}}_y &= \frac{1}{\hat{C}} \left(\frac{\partial \hat{B}_0}{\partial \hat{x}_{eq}} - \frac{\hat{\gamma}_3}{\hat{\gamma}_1} \frac{\partial \hat{B}_0}{\partial \hat{z}} \right) \end{aligned}$$

$$\hat{B}_{0||}^* = \hat{B}_0 \left(1 + \beta_{ref} \sqrt{\frac{\hat{m}_j \hat{T}_{0j}(x_0)}{2}} \frac{\hat{j}_{0||}}{Z_j \hat{B}_0^2} \hat{v}_{||j} \right) \quad \hat{j}_{0||} = \frac{j_{0||}}{e n_{ref} c_{ref}}$$

$$\hat{\omega}_{nj} = L_{ref}/L_{nj} = -L_{ref}n'_{j0}/n_{j0}, \quad \hat{\omega}_{Tj} = L_{ref}/L_{Tj} = -L_{ref}T'_{j0}/T_{j0}, \quad \hat{C} = C/B_{ref}, \quad \vec{B} = C\vec{\nabla}x \times \vec{\nabla}y.$$

The gyrokinetic Poisson and Ampere's equations are used to determine the self-consistent electromagnetic fields. Quasineutrality $\sum_j Z_j n_{1,j} = 0$ for adiabatic electron response reads

$$\begin{aligned} -\frac{\hat{n}_{0e}}{\hat{T}_{0e}} \left(\hat{\Phi}_1 - \langle \hat{\Phi}_1 \rangle \right) + \sum_{j \neq e} \left\{ \pi Z_j \hat{n}_{0j}(x_0) \int \hat{B}_{0||}^* \hat{F}_{1j} d\hat{v}_{||} d\hat{\mu}_j \right. \\ \left. - \frac{Z_j^2 \hat{n}_{0j}}{\hat{T}_{0j}} \left[\hat{\Phi}_1 - \frac{\hat{B}_0}{\tau_{0j}} \int \hat{\Phi}_1 \exp\left(-\frac{\hat{\mu}_j \hat{B}_0}{\hat{\tau}_{0j}}\right) d\hat{\mu}_j \right] \right\} = 0 \end{aligned} \quad (5.2)$$

Ampere's law reads

$$\begin{aligned} -\hat{\nabla}_{\perp}^2 \hat{A}_{1||} = -\sum_j \left\{ \frac{\beta_{ref}}{2} Z_j \hat{n}_{0j}(x_0) \hat{v}_{Tj}(x_0) \pi \int \hat{B}_{0||}^* \hat{F}_{1j} d\hat{v}_{||} d\hat{\mu}_j \right. \\ \left. - \frac{\beta_{ref}^2}{4} \frac{\hat{n}_{0j} \hat{j}_{0||}}{\hat{B}_0^2} Z_j \left[\hat{\Phi}_1 - \frac{\hat{B}_0}{\tau_{0j}} \int \hat{\Phi}_1 \exp\left(-\frac{\hat{\mu}_j \hat{B}_0}{\hat{\tau}_{0j}}\right) d\hat{\mu}_j \right] \right\} \end{aligned} \quad (5.3)$$

The above gyrokinetic Vlasov - Maxwell equation are solved for the analytical $\hat{s} - \alpha$ geometry in flux tube approximation for which the normalized metric and equilibrium magnetic field are approximated by

$$g^{ij} = \begin{pmatrix} 1 & \hat{s}\hat{z} - \alpha_{MHD} \sin\hat{z} & 0 \\ \hat{s}\hat{z} - \alpha_{MHD} \sin\hat{z} & 1 + (\hat{s}\hat{z} - \alpha_{MHD} \sin\hat{z})^2 & L_{ref}/r_0 \\ 0 & L_{ref}/r_0 & (L_{ref}/r_0)^2 \end{pmatrix}$$

$$\hat{B}_0 = \frac{1}{1 + \epsilon_t \cos\hat{z}} \quad \partial_{\hat{z}} \hat{B}_0 = \hat{B}_0^2 \epsilon_t \sin\hat{z} \quad \hat{J} = \frac{1}{\hat{B}_0} \quad \epsilon_t = \frac{r_0}{R}$$

This leads to the following curvature terms

$$\hat{\mathcal{K}}_x = -\frac{L_{ref}}{R} \sin\hat{z} \quad \hat{\mathcal{K}}_y = -\frac{L_{ref}}{R} (\cos\hat{z} + \sin\hat{z}(\hat{s}\hat{z} - \alpha_{MHD} \sin\hat{z}))$$

In flux tube simulation approach the radial dependencies of the equilibrium

quantities in above equations are removed:

$$\begin{aligned} \hat{C}(x), \hat{B}_0(x, z), \hat{B}_{0||}^*(x, z, v_{||}), \hat{\mathcal{K}}_{x,y}(x, z), \hat{J}_{xyz}(x, z) &\rightarrow \hat{C}, \hat{B}_0(z), \hat{B}_{0||}^*(z, v_{||}), \hat{\mathcal{K}}_{x,y}(z), \hat{J}_{xyz}(z) \\ \hat{\omega}_{nj}(x), \hat{\omega}_{Tj}(x), \hat{n}_{0j}(x), \hat{p}_0(x) &\rightarrow \hat{\omega}_{nj}, \hat{\omega}_{Tj}, \hat{n}_{0j}, \hat{p}_0 \end{aligned}$$

The x and y directions are Fourier transformed due to periodic boundary conditions in respective directions.

5.2.2 Diagnostics

Eigenvalues

Since all the k_x grid points are coupled via the parallel boundary condition, the linear eigenvalues are computed as follows[124].

$$\lambda(k_y) = \frac{\sum_{k_x, z} w(k_x, k_y, z) \lambda(k_x, k_y, z)}{\sum_{k_x, z} w(k_x, k_y, z)} \text{ where } \lambda(k_x, k_y, z) = \ln \left(\frac{\phi(t_n)}{\phi(t_{n-1})} \right) / \Delta t \quad (5.4)$$

The result $\lambda = \gamma + i\omega$ represents the combined growth rate and real frequency of the mode k_y . The convergence criterion for a given k_y is that the scatter of $\lambda(k_x, k_y, z)$ is below a certain, adjustable limit c_p connected to the precision of the value for λ :

$$\frac{\sum_{k_x, z} w(k_x, k_y, z) |\lambda(k_x, k_y, z) - \lambda(k_y)|^2}{\sum_{k_x, z} w(k_x, k_y, z)} < c_p \quad (5.5)$$

Here $c_p = 10^{-3}$ has been taken for all computations. The weight function is taken to be $w(k_x, k_y, z) = \phi(t_{n-1})$.

Mode averaged quantities

Mode averaged quantities such as k_{\perp}^2 are calculated as follows:

$$\langle k_{\perp}^2 \rangle (k_y) = \frac{\int dz J(z) \sum_{k_x} k_{\perp}^2 |\phi(k_x, k_y, z)|^2}{\int dz J(z) \sum_{k_x} |\phi(k_x, k_y, z)|^2} \quad (5.6)$$

where $k_{\perp}^2 = g^{xx} k_x^2 + 2g^{xy} k_x k_y + g^{yy} k_y^2$. $J(z)$ is the Jacobian and g^{ij} are the metric coefficients.

Momentum and heat fluxes

The generic structure of any flux Γ_{AB} in terms of it's spectral components $A(\vec{k})$ and $B(\vec{k})$ is given by

$$\begin{aligned}\Gamma_{AB}(z) &= \langle A(x, y, z) B(x, y, z) \rangle_{xy} = \frac{\int dx dy A(x, y, z) B(x, y, z)}{\int dx dy} \\ &= \sum_{k_x, k_y} A(k_x, k_y, z) B(k_x, k_y, z)\end{aligned}\quad (5.7)$$

Summation over k_y extends over all +ve and -ve k_y modes while GENE outputs for +ve k_y 's only. Hence using the complex conjugation properties of Fourier amplitudes (i.e., $A^*(\vec{k}) = A(-\vec{k})$) the above expression is reduced to the following form which uses only $k_y \geq 0$.

$$\Gamma_{AB}(z) = \sum_{k_x} A(k_x, 0, z) B(k_x, 0, z) + 2Re \sum_{k_x} \sum_{k_y > 0} A^*(k_x, k_y, z) B(k_x, k_y, z) \quad (5.8)$$

Volume averaged fluxes are calculated as follows:

$$\Gamma_{AB} = \frac{\int dz J(z) \Gamma_{AB}(z)}{\int dz J(z)} \quad (5.9)$$

Substituting

$$A = \hat{v}_\chi^x = -\frac{1}{\hat{C}} \frac{\partial \hat{\Phi}_1}{\partial \hat{y}} \text{ and } B = \hat{n}_{j0} \hat{T}_{j0} \left(\frac{3}{2} \hat{n}_{j1}(\vec{x}, t) + \hat{T}_{\parallel j1}(\vec{x}, t)/2 + \hat{T}_{\perp j1}(\vec{x}, t) \right) \quad (5.10)$$

yields the electrostatic heat flux for the jth species in gyro-Bohm units $Q_{gB} = p_{ref} c_{ref} \rho_{ref}^2 / L_{ref}^2$. Similarly parallel momentum flux is obtained in gyro-Bohm units $\Gamma_{gB} = m_{ref} n_{ref} c_{ref}^2 \rho_{ref}^2 / L_{ref}^2$, by making the following substitution.

$$A = \hat{v}_\chi^x = -\frac{1}{\hat{C}} \frac{\partial \hat{\Phi}_1}{\partial \hat{y}} \text{ and } B = \hat{m}_j \hat{n}_{j0} \hat{u}_{\parallel,1}(\vec{x}, t) \quad (5.11)$$

where quantities with subscript 1 indicate perturbations and with subscript 0 indicate equilibrium quantities. Parallel velocity density fluctuation $\hat{u}_{\parallel,1}$ is obtained from the parallel velocity moment of the perturbed distribution and density fluctuation \hat{n}_{j1} is obtained from the zeroth moment of the perturbed distribution

function.

5.3 Results From Linear Gyrokinetics

In this section we present the results from the flux tube simulations using the GENE code for the linear electrostatic ion temperature gradient (ITG) mode with adiabatic electron response. Various parameters and reference values are tabulated below. Magnetic shear $\hat{s} = 1$, inverse aspect ratio $\epsilon_t = r_0/R_0 = 0.16$, major radius $R_0/L_{ref} = 1$, safety factor, $q_0 = 2$, density gradient $L_{ref}/L_n = 3$, and temperature gradient $L_{ref}/L_T = 9$ unless stated otherwise. The reference quantities are $L_{ref} = R_0 = 1.65 m$, $B_{ref} = B_0 = 1 T$, $Q_{ref} = e = 1.6e-19 C$, $m_{ref} = m_i = 3.34e-27 kg$, $T_{ref} = T_{e0} = 350 eV$, $n_{ref} = n_i = 3.5e+19 m^{-3}$, $c_{ref} = 129487.19 m/s$, $\rho_{ref} = 0.0027029701 m$. We would stress here that the marked difference between the parameters chosen here and the previous works on conventional SWITG is that the later considered very high temperature and density gradients $R/L_T = 25$ and $R/L_n = 10$.

5.3.1 Eigenvalues

Fig.(5.1) shows kx_{center} scan of linear growth rates at different binormal wavenumbers k_y . The figure has a couple of features that need explanation. The growth rates are periodic in kx_{center} or θ_0 for any k_y . This is due to the fact that non-zero kx_{center} shifts the eigenmode away from LFS mid-plane where it sees a different magnetic curvature and hence different growth rate. 2π periodicity of curvature term in θ or z leads to $2\pi k_y \hat{s}$ periodicity of the growth rates in kx_{center} . Another surprising feature of Fig.(5.1) is that $kx_{center} = 0$ is not often the maximum growing mode. Low k_y modes show maximum growth at $kx_{center} = 0$ while high k_y modes show maximum growth rate at $kx_{center} \neq 0$. That is high k_y modes have maximum growth rates when the eigenmode is shifted away from the LFS mid plane. Values of kx_{center} and ballooning angle θ_0 corresponding to maximum growth rates viz., $kx_{center,max}$ and $\theta_0|_{\gamma_{max}}$ respectively, against k_y are shown in Fig.(5.2).

When growth rates maximized over all kx_{center} or θ_0 are considered the ITG mode instability window in k_y broadens way beyond $k_y > 1$ in the short wavelength (SW) regime as shown in Fig.(5.3). But the SW branch disappears at lower temperature

Chapter 5. Finite ballooning angle and macroscopic ExB shear effects on ion temperature gradient driven mode in gyrokinetic flux tube simulations

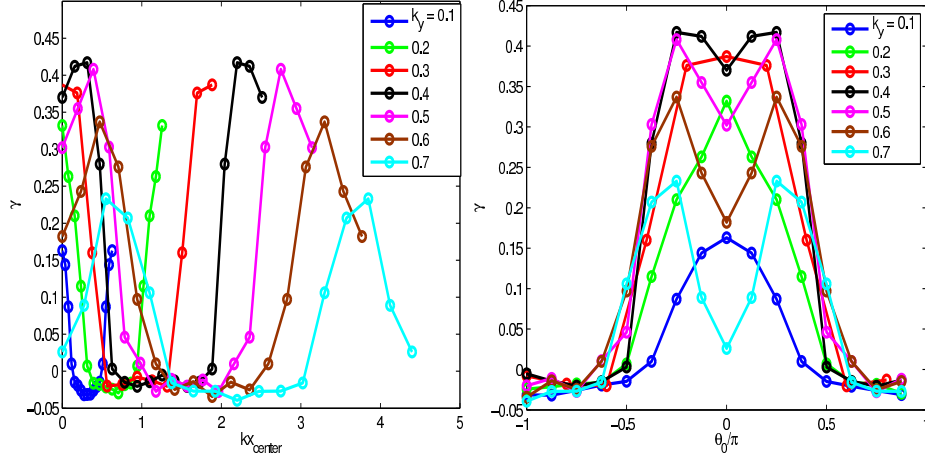


Figure 5.1: Linear growth rates γ vs kx_{center} (left) and γ vs θ_0 (right) with k_y as parameter. $kx_{center} = 0$ or $\theta_0 = 0$ is not always the maximum growing mode. Very weakly growing modes or damped mode growth rates in the valley are not well converged as per the rule Equations(5.5) and are obtained from linear regression analysis of the available time series of $|n|^2$ and hence are only approximately correct.

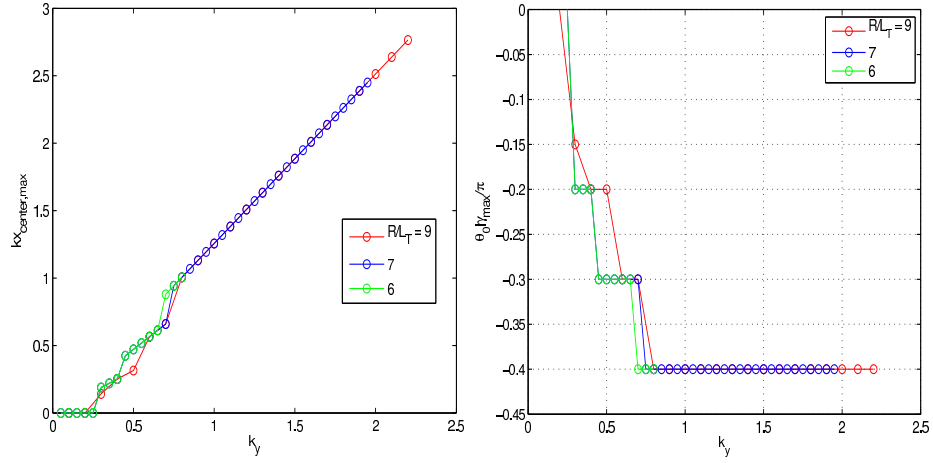


Figure 5.2: Left: kx_{center} vs ky at max. growth rates. Right: Ballooning angle at max. growth rate vs k_y

gradients. This behavior is similar to $\theta_0 = 0$ SWITG driven by extremely large temperature gradients (in fact very large density gradient such that diamagnetic frequency exceeds the mode frequency and for η_i to stay above marginality the needed temperature gradient becomes tremendously high. For example Fig.(10) in

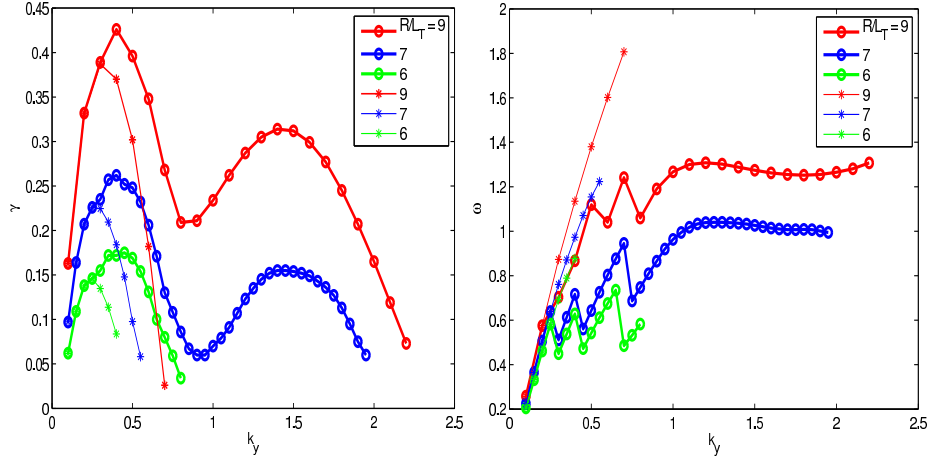


Figure 5.3: Left: Thin solid lines with * indicates γ for $kx_{center} = 0$, thick solid lines with o represent γ maximized over all kx_{center} i.e., γ_{max} . Right: Corresponding real frequencies.

ref[119] shows that the instability exists for $R/L_n > 6$ at $\eta_i = 2.5$ which translates to $R/L_T > 15$!). However, the appearance of SW branch in our case, despite having normal temperature gradients, is due to the fact that at high k_y the growth rates maximized over all θ_0 's are significantly higher than that at $\theta_0 = 0$ (Fig.(5.1)).

5.3.2 Mixing length estimates

Mixing length estimates are generally used to project estimate of heat diffusivity in nonlinearly saturated turbulence from linear mode calculations. Certainly these calculations are not full proof but often gives an idea of what can be expected in a nonlinearly saturated turbulence regime. Hence the k_y spectrum of mixing length estimates for different values of temperature gradient are calculated. Fig.(5.4) shows that mixing length values of the SW branch is not much significant compared to the long wavelength part even though estimates due to γ_{max} are higher than that of modes at $\theta_0 = 0$. It is important to note that the mixing length spectra peaks at $k_y = 0.1$ in all three cases of R/L_T and do not show any peak characteristic of SW branch on high k_y side. The observed monotonically decreasing k_y spectrum of the mixing length estimates is a consequence of monotonically increasing k_y spectrum of $\langle k_\perp^2 \rangle$ as shown in the adjoining left figure in Fig.(5.4).

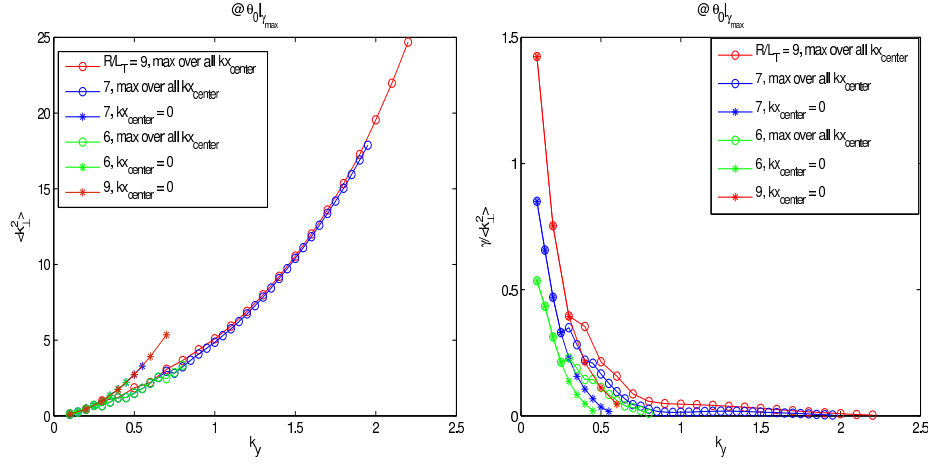


Figure 5.4: $\langle k_{\perp}^2 \rangle$ vs k_y (Left) and $\gamma / \langle k_{\perp}^2 \rangle$ vs k_y (Right) at ballooning angles $\theta_0|_{\gamma_{max}}$ corresponding to max growth rates γ_{max} .

5.3.3 Momentum and heat fluxes

Parallel momentum fluxes Γ_{\parallel} normalized by mode intensity $\langle \phi^2 \rangle$ at $k_y = 0.3$ as a function of θ_0 are shown in left panel of Fig.(5.5). $\Gamma_{\parallel} / \langle \phi^2 \rangle$ is seen to have odd parity with respect to θ_0 . This indicates momentum flux reversal with mode tilt angle which may have important implication for understanding of intrinsic toroidal rotation reversal[125, 23]. The odd parity of parallel momentum flux is a consequence of odd parity of the eigenmode averaged parallel wavenumber. The right panel of Fig.(5.5) clearly demonstrates generation of parallel momentum flux due to breaking of k_{\parallel} symmetry by breaking of eigenmode symmetry caused by finite θ_0 . The k_y spectrum of Γ_{\parallel} (unnormalized) exhibit peaks at $k_y = 0.5$ and 1.5 characteristic of long wavelength and short wavelength peaks in growth rate spectra. This is depicted in Fig.(5.6) for γ_{max} . To nail down the origin of parallel momentum flux by finite θ_0 z profiles of $\Gamma_{\parallel} / \langle \phi^2 \rangle$ and mode parities of electrostatic potential ϕ and parallel velocity density u_{\parallel} in z are calculated. Fig.(5.7) structure of normalized parallel momentum flux in z at different values of θ_0 . It is seen that $\Gamma_{\parallel} / \langle \phi^2 \rangle$ is locally finite but exactly antisymmetric about $z = 0$ when $\theta_0 = 0$. This characteristic can be understood from the even parity of ϕ and odd parity of u_{\parallel} when $\theta_0 = 0$ as shown in Fig.(5.8). In physical words a mode centered on the LFS mid plane drives parallel momentum flux locally in the

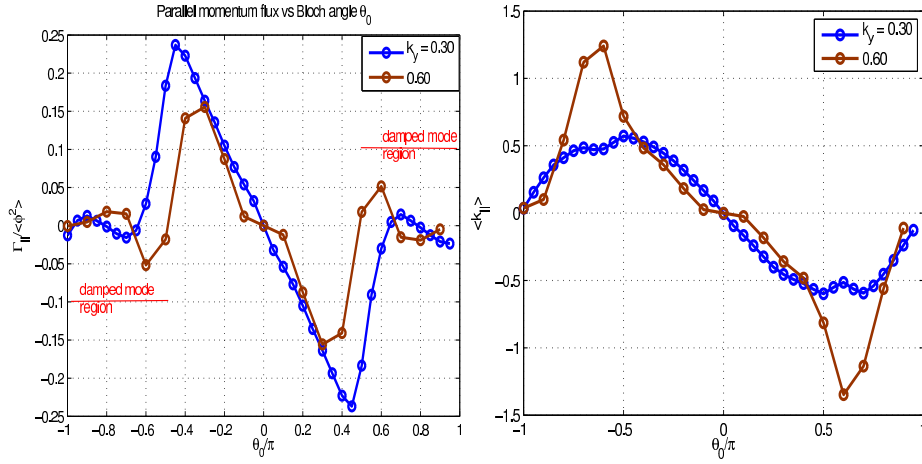


Figure 5.5: Left: $\Gamma_{\parallel} / \langle \phi^2 \rangle$ vs θ_0 at $k_y = \{0.3, 0.6\}$, $R/L_T = 9$. The underlined regions indicate damped mode contributions. Right: $\langle k_{\parallel} \rangle$ vs θ_0 showing $\langle k_{\parallel} \rangle$ symmetry breaking by finite θ_0 .

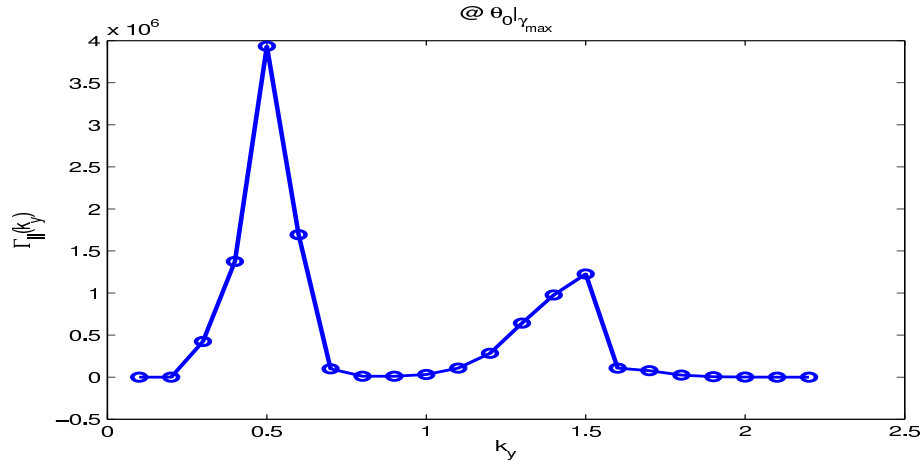


Figure 5.6: Γ_{\parallel} vs k_y at ballooning angles $\theta_0|_{\gamma_{max}}$ corresponding to max growth rate and $R/L_T = 9$.

poloidal angle but flux in the upper plane is exactly canceled by flux in the lower plane to give no net poloidally averaged parallel momentum flux. At a finite θ_0 the z profile of $\Gamma_{\parallel} / \langle \phi^2 \rangle$ losses this antisymmetry property in z hence flux in the upper plane is not exactly canceled by flux in the lower plane constituting a net parallel momentum flux. Again, the loss of antisymmetry of $\Gamma_{\parallel} / \langle \phi^2 \rangle$ can be understood from the breaking of symmetry of ϕ and anti-symmetry of u_{\parallel} about

the LFS mid plane (i.e., $z = 0$) at finite θ_0 as shown in Fig.(5.9).

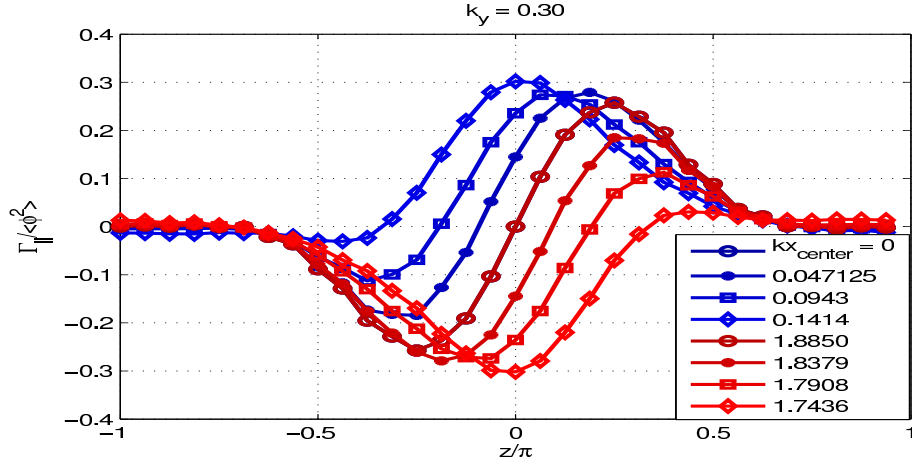


Figure 5.7: $\Gamma_{||}$ vs z with kx_{center} as parameter at $k_y = 0.3$ and $R/L_T = 9$. The shown values of kx_{center} correspond to $\theta_0/\pi = \{0, -0.05, -0.10, -0.15, 0, 0.05, 0.10, 0.15\}$.

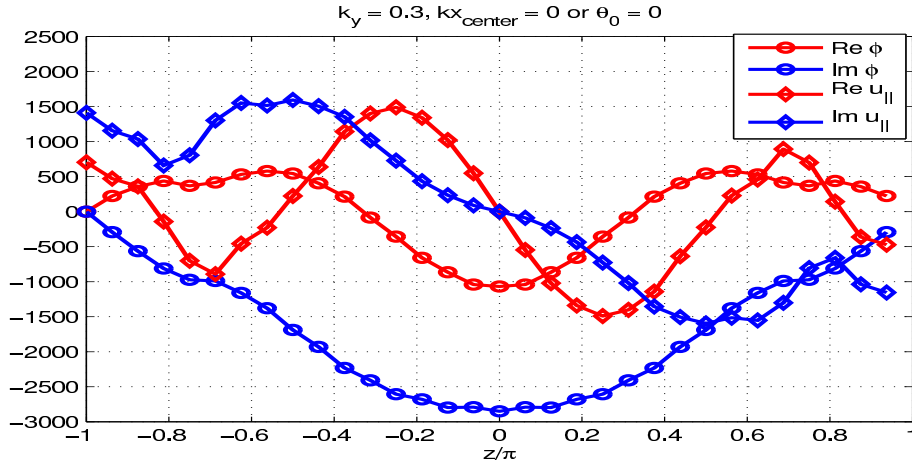


Figure 5.8: Mode parities, at the end of simulation, along the field line when $kx_{center} = 0$ for $k_y = 0.3$ at $R/L_T = 9$.

Normalized heat flux $Q_i / \langle \phi^2 \rangle$ exhibits even parity in θ_0 with a nonzero minimum at $\theta_0 = 0$. Fig.(5.10) shows $Q_i / \langle \phi^2 \rangle$ vs θ_0 for a test case of $k_y = 0.3$ and $R/L_T = 9$. $Q_i / \langle \phi^2 \rangle$ increases with θ_0 up to $\theta_0 = \pm 0.45\pi$ and then decreases rapidly to vanishingly small values as $\theta_0 \rightarrow \pm\pi$ in the damped eigenmode region.

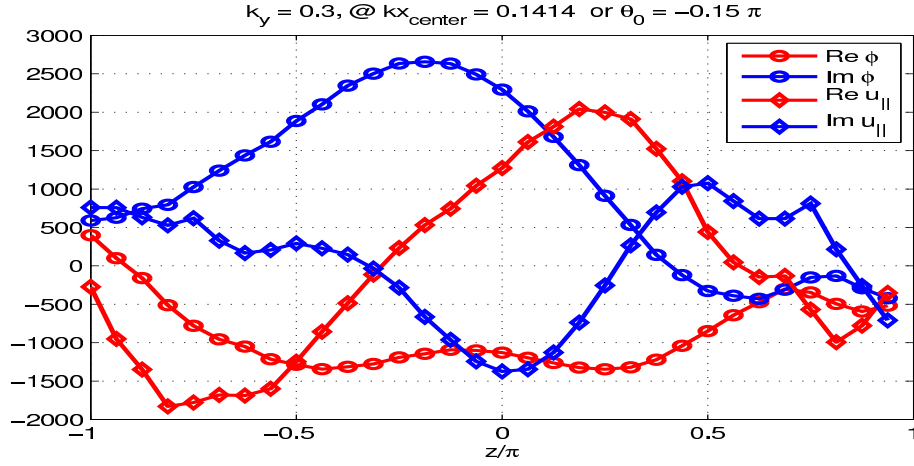


Figure 5.9: Mode parities, at the end of simulation, along the field line when $\theta_0 = -0.15\pi$ for $k_y = 0.3$ at $R/L_T = 9$.

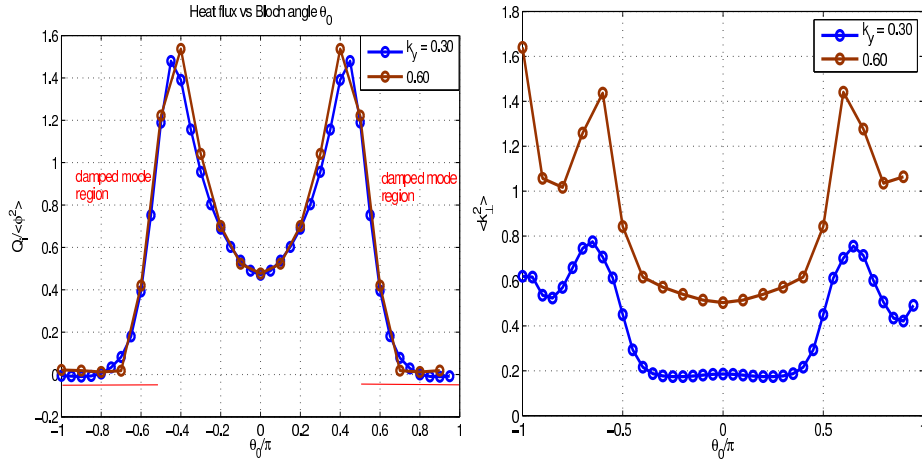


Figure 5.10: Left: $Q_i / \langle \phi^2 \rangle$ vs θ_0 at $k_y = \{0.3, 0.6\}$, $R/L_T = 9$. The underlined regions correspond to damped modes. Right: $\langle k_\perp^2 \rangle$ vs θ_0 .

Heat flux distribution in poloidal angle z is shown for different eigenmode ballooning angles are shown in Fig.(5.11). Heat flux z profile is seen to follow the z profile of mode intensity (Fig.(5.12)). Heat flux profile is exactly symmetric about $z = 0$ when $\theta_0 = 0$. At finite θ_0 eigenmode intensity is shifted either below or above the LFS mid plane depending on the it's sign which is also reflected in the poloidal structure of the heat flux. Like k_y spectrum of parallel momentum flux, the k_y spectrum of ion heat flux in Fig.(5.13) shows peaks at $k_y = 0.5$ and 1.5 character-

istic of long and short wavelength growth spectra respectively. The even parity

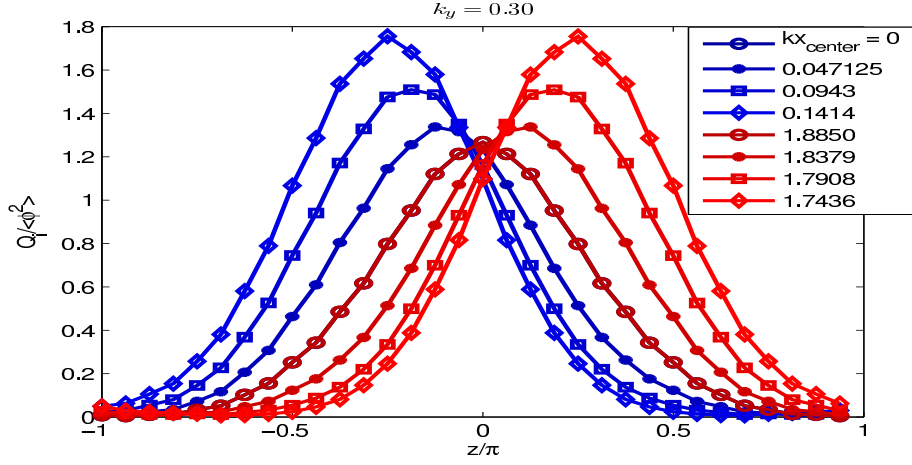


Figure 5.11: Q_i vs z with kx_{center} as parameter at $k_y = 0.3$ and $R/L_T = 9$. The shown values of kx_{center} correspond to $\theta_0/\pi = \{0, -0.05, -0.10, -0.15, 0, 0.05, 0.10, 0.15\}$.

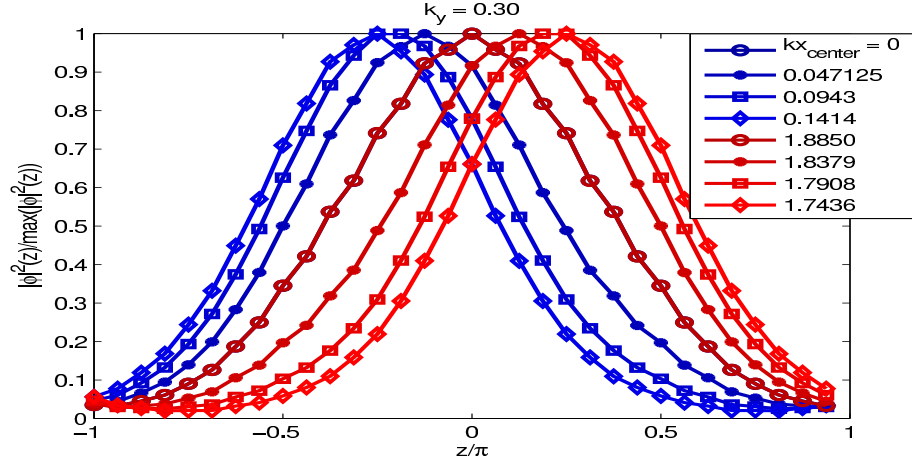


Figure 5.12: Finite kx_{center} shifts mode away from LFS midplane. The figure highlights the same for $k_y = 0.3$ for few representative cases of growing modes. The shown values of kx_{center} correspond to $\theta_0/\pi = \{0, -0.05, -0.10, -0.15, 0, 0.05, 0.10, 0.15\}$.

of heat flux with respect to θ_0 could be understood from the fact that potential fluctuation ϕ , parallel temperature fluctuation $T_{||}$ and perpendicular temperature

fluctuations T_{\perp} all have same even parity when $\theta_0 = 0$ as shown in Fig.(5.14). This symmetry is broken when $\theta_0 \neq 0$ and the fluctuation intensity in all fields maximizes at position other than $z = 0$ as shown in Fig.(5.15) for an example of $\theta_0 = -0.15\pi$.

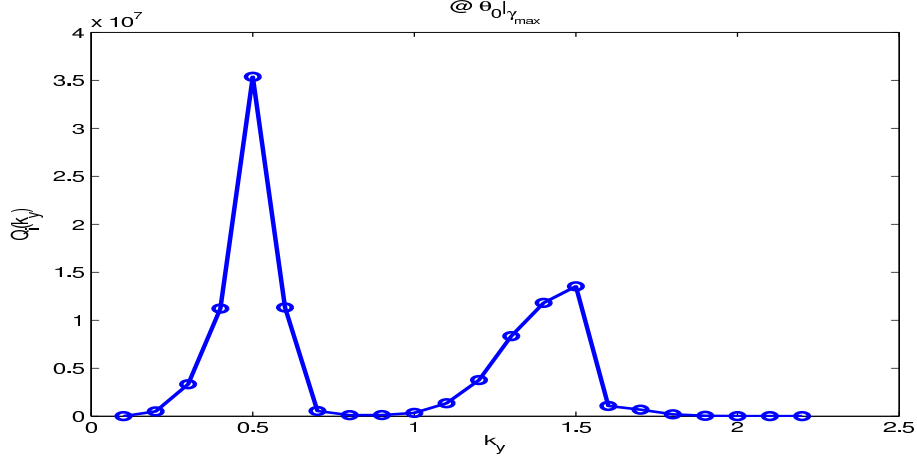


Figure 5.13: Q_i vs k_y at ballooning angles $\theta_0|_{\gamma_{max}}$ corresponding to max growth rate and $R/L_T = 9$.

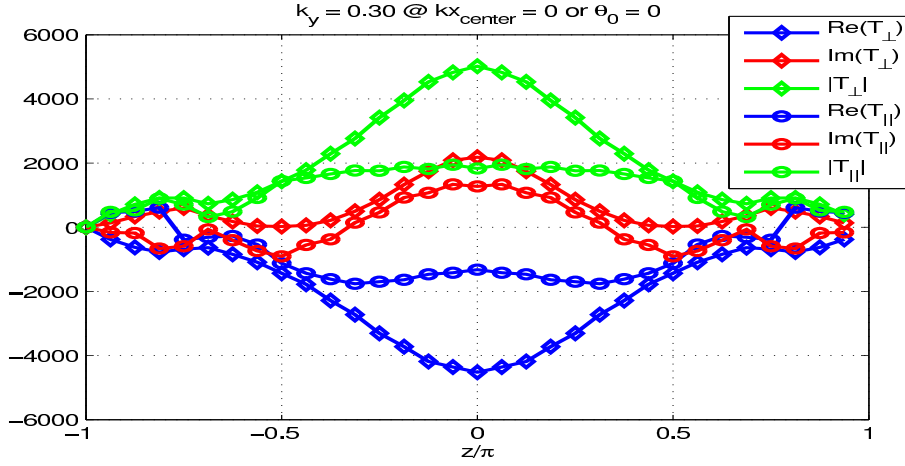


Figure 5.14: Mode parities, at the end of simulation, along the field line when $\theta_0 = 0$ for $k_y = 0.3$ at $R/L_T = 9$.

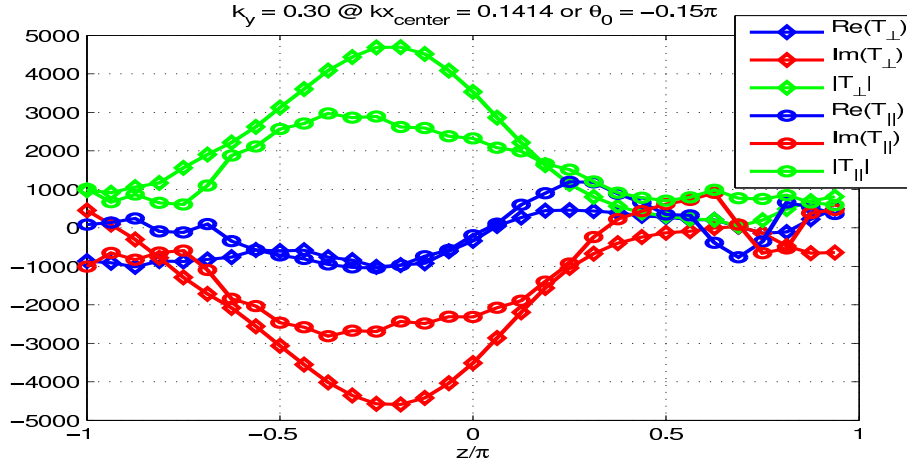


Figure 5.15: Mode parities, at the end of simulation, along the field line when $\theta_0 = -0.15\pi$ for $k_y = 0.3$ at $R/L_T = 9$.

5.4 Non-linear gyrokinetic simulations with background ExB shear

Effects of $E \times B$ shear on ion temperature gradient (ITG) driven turbulence in context of basic linear growth properties and turbulent heat transport has been studied quite extensively [126, 105, 127, 128, 129, 130, 131]. Parallel momentum transport driven by $E \times B$ shear and parallel flow shear has been studied quite well in Ref.[100]. However the connection of self-consistently generated zonal flow shear with residual momentum flux, if any, has not been studied well in flux tube simulations. This section shows that the zonal flow shear itself fails to drive flux tube averaged parallel momentum flux.

5.4.1 System description

Nonlinear gyrokinetic simulations in toroidal geometry are performed with the Vlasov flux tube code GENE. All simulations were done for collisionless Waltz standard case[128, 132, 129] with temperature scale length $R/L_T = 9$, density scale length $R/L_n = 3$, safety factor $q = 2$, magnetic shear $\hat{s} = 1$ and inverse aspect ratio $\epsilon = r/R = 0.16$ unless stated otherwise. The geometry used is the analytical $s - \alpha$ model, which assumes circular flux surfaces with the magnetohydrodynamic

parameter $\alpha = 0$. Unless otherwise stated all simulations are performed with $n_{k_y} = 48$ binormal modes, $n_{k_x} = 128$ radial modes. The number of grid points in parallel velocity $v_{||}$, magnetic moment μ and along the field line z are $n_v = 32$, $n_\mu = 16$, $n_z = 16$.

5.4.2 Results

Parallel momentum fluxes are calculated with and without zonal flow shear as a function of $E \times B$ shearing rates γ_E as shown in the left panel of Fig.(5.16). It is seen that the momentum flux without zonal flows is much higher than that with zonal flows. Momentum flux initially increases with shearing rate at smaller values of the later but starts to roll over at larger values of shearing rate. This could be understood from the fact that with increasing shearing rate the enhancement of the symmetry breaking of the eigenmode about the LFS mid plane is accompanied by the reduction in mode intensity as shown in left panel of Fig.(5.17). Right panel of Fig.(5.16) also reflects the symmetry breaking contribution of $E \times B$ shear to momentum flux.

The root mean square value of zonal shearing rate goes down with background

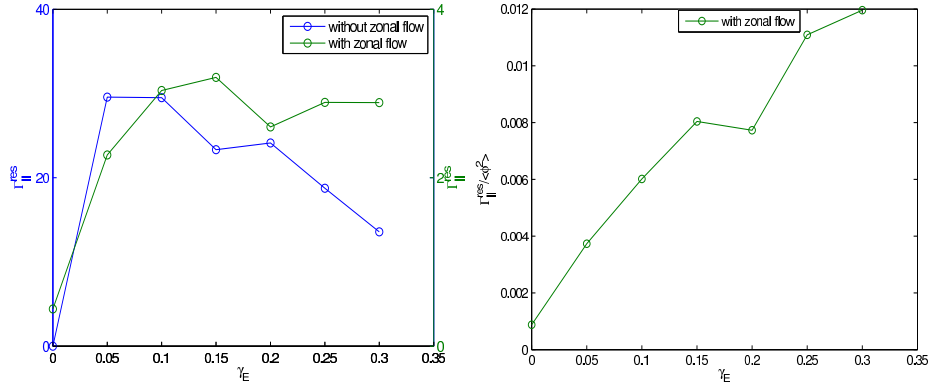


Figure 5.16: Left: $\Gamma_{||}^{res}$ vs $E \times B$ rate, Middle: $\Gamma_{||}^{res} / \langle \phi^2 \rangle$ vs $E \times B$ rate.

$E \times B$ shearing rate as shown in right panel of Fig.(5.17). Background $E \times B$ shear and zonal flow shear both are stabilizing but the former one has symmetry breaking properties in addition.

Now we present 2D space-time correlation studies among $\Gamma_{||}$, Q_i , $\omega_{E \times B, zonal}$, and

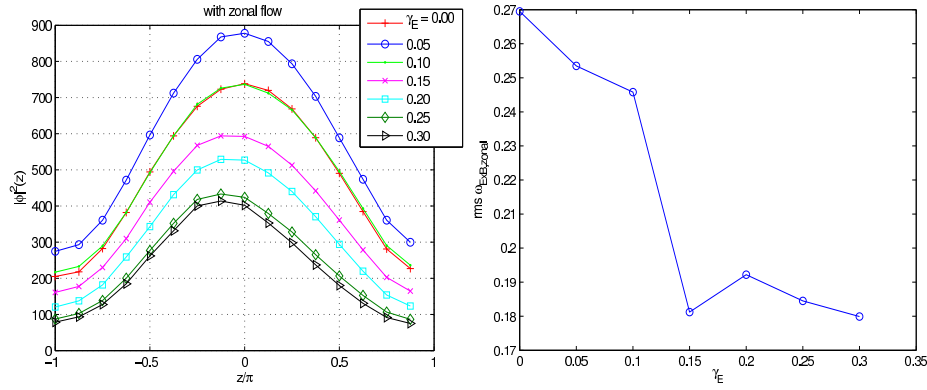


Figure 5.17: Left: $|\phi|^2(z)$ vs z at various $E \times B$ rates. Right: rms $\omega_{E \times B, \text{zonal}}$ vs $E \times B$ rate.

$|\phi|^2$ with and without macroscopic $E \times B$ shear. Results without $E \times B$ shear are discussed first. 2D space time cross correlations between Γ_{\parallel} and $\omega_{E \times B, \text{zonal}}$ are calculated in Fig.(5.18) to ascertain role of zonal flow shear in generating parallel momentum flux locally in radial position x . Left panel of Fig.(5.18) shows that the maximum of the correlation function is situated at $\Delta x = 0$ and $\Delta t \neq 0$ with the maximum value being 0.15. To make sense of the strength of the correlation value, cross correlations between heat Q_i and $\omega_{E \times B, \text{zonal}}$ are calculated as show in left panel of Fig.(5.18). The maximum value is 0.20 with the maximum centered away from the origin at $\Delta x \neq 0, \Delta t \neq 0$. Hence compared to the correlation value of zonal shear and heat flux we conclude that zonal flow shear and parallel momentum flux are locally correlated in x but non-locally in t . Bottom panel of Fig.(5.18) shows that Γ_{\parallel} and Q_i are not correlated. Fig.(5.19) shows that compared to correlation between Q_i and $|\phi|^2$ correlation between Γ_{\parallel} and $|\phi|^2$ is poor.

On introducing finite $E \times B$ shear the first eye catching difference effect that appears in correlation diagrams is that now the streak like structure diminish in the other diagonal direction. This could be related to the fact that avalanche direction symmetry (when $\gamma_E = 0$) is broken and is dominantly determined by the radial electric field direction. With background $E \times B$ shearing rate $\gamma_E = 0.30$ the correlation between $\omega_{E \times B, \text{zonal}}$ and Γ_{\parallel} is still maintained as compared to the correlation between $\omega_{E \times B, \text{zonal}}$ and Q_i which is depicted in the left and right plots of Fig.(5.20). The bottom plot in Fig.(5.20) shows a high correlation between Q_i and Γ_{\parallel} . This indicates that the momentum and heat transport channels get coupled at finite

Chapter 5. Finite ballooning angle and macroscopic ExB shear effects on ion temperature gradient driven mode in gyrokinetic flux tube simulations

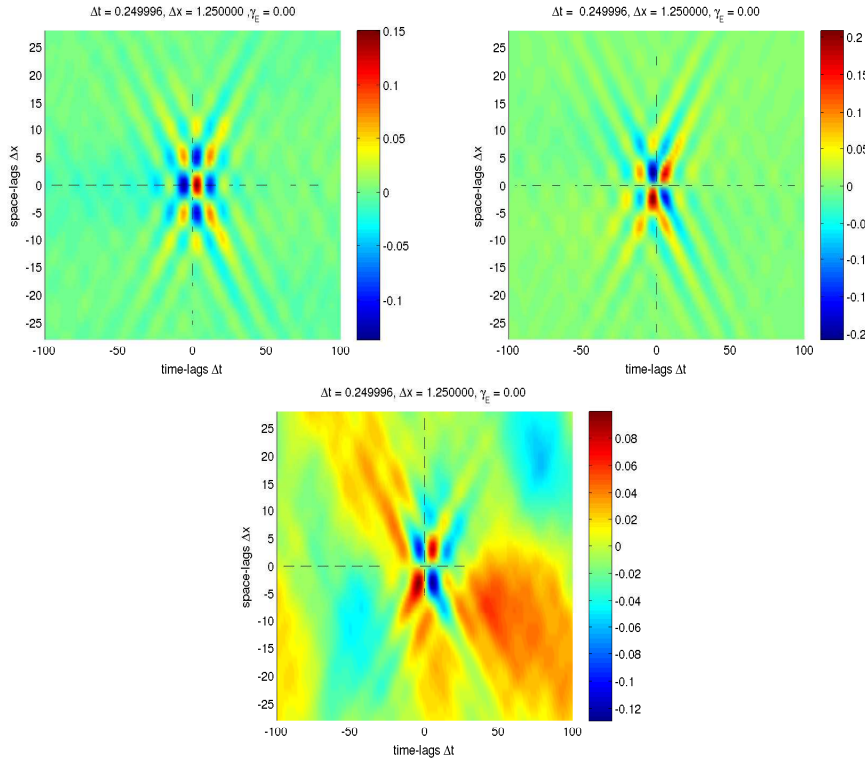


Figure 5.18: 2d Cross-correlations of zonal shear and momentum flux $R_{\omega_{E \times B, zonal} \Gamma_{||}}$ (left); and zonal shear and heat flux $R_{\omega_{E \times B, zonal} Q_i}$ (right), cross-correlations of heat flux and momentum flux $R_{Q_i \Gamma_{||}}$ (bottom).

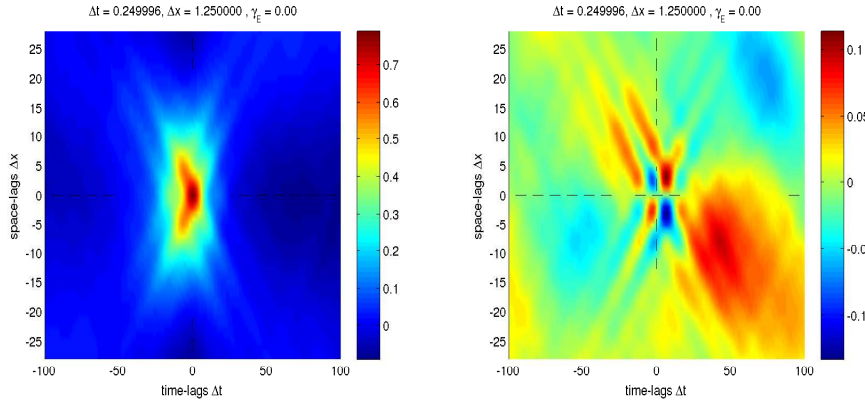


Figure 5.19: Left: Cross-correlations $R_{|\phi|^2 Q_i}$. Right: $R_{|\phi|^2 \Gamma_{||}}$.

Chapter 5. Finite ballooning angle and macroscopic ExB shear effects on ion temperature gradient driven mode in gyrokinetic flux tube simulations

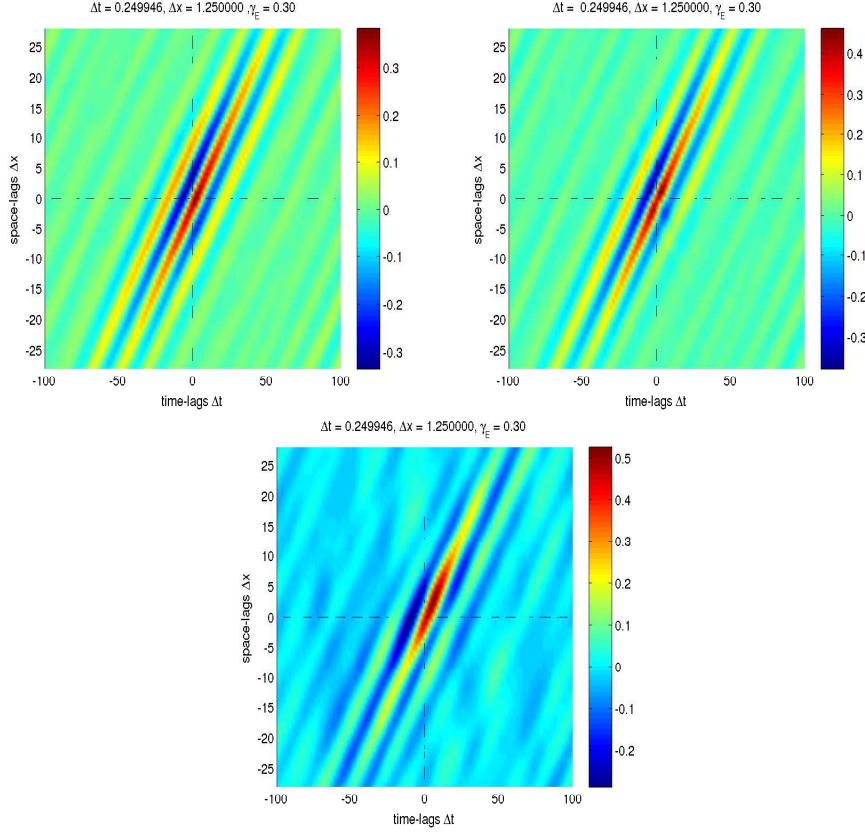


Figure 5.20: 2d Cross-correlations of zonal shear and momentum flux $R_{\omega_{E \times B, zonal} \Gamma_{||}}$ (left) and zonal shear and heat flux $R_{\omega_{E \times B, zonal} Q_i}$ (right), heat flux and momentum flux $R_{Q_i \Gamma_{||}}$ (bottom) at $\gamma_E = 0.30$

γ_E . This could be understood by writing the fluid ITG equations in Chapter 1 in field aligned coordinates and calculating the flux tube averaged parallel momentum flux. It is easy to show that the parallel momentum flux coming from the parallel velocity fluctuations driven by parallel pressure gradient fluctuations $\nabla_{||} p$ will consist of a term containing heat flux spectrum Q_k : $\int dz \sum_k (\gamma_k / |\omega_k|^2) \nabla_{||} Q_{i,k} J(z)$. This term survives only when Q_k is losses symmetry about the LFS mid-plane $z = 0$ which is brought by finite γ_E . This causes coupling of momentum and heat transport channels when γ_E is non-zero. Moreover, the correlation between $|\phi|^2$ and $\Gamma_{||}$ becomes significant compared to correlations between $|\phi|^2$ and Q_i as shown in Fig.(5.21). This is just a consequence of symmetry breaking agent γ_E .

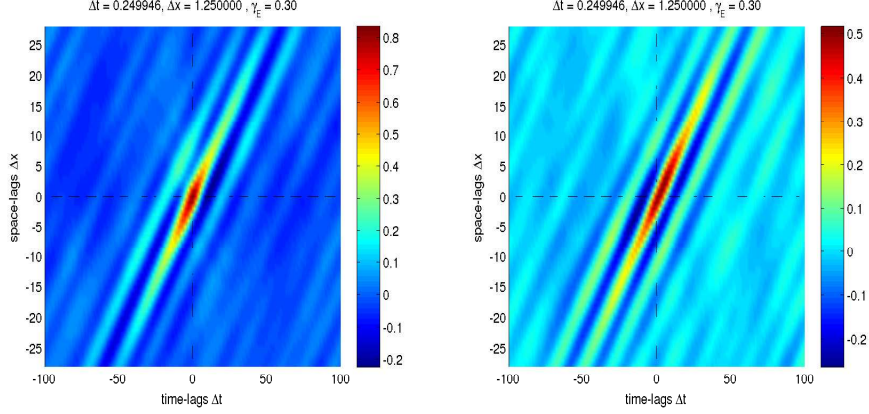


Figure 5.21: 2d Cross-correlations $R_{|\phi|^2 Q_i}$ (left) $R_{|\phi|^2 \Gamma_{||}}$ (right) at $\gamma_E = 0.30$

5.5 Discussion and Conclusions

We performed flux tube simulations of linear ITG mode exploiting the freedom of mode ballooning angle for the first time. So far flux tube simulations have only been reported for $\theta_0 = 0$ in the best of our knowledge. Following are the major findings that add to the conventional wisdom:

- High k_y modes often show maximum growth rates at θ_0 's other than 0.
- ITG instability window extends to short wavelength (SW) regime $k_y > 1$ when growth rates maximized over all ballooning angles are considered.
- The SW branch dies out on decreasing R/L_T showing behavior similar to the zero ballooning angle SWITG driven by extremely large temperature gradients.
- Though mixing length estimates of γ_{max} are slightly greater than that of γ_0 the SW branch shows insignificantly low contribution to mixing length estimates compared to the long wavelength branch.
- Loss of symmetry of potential fluctuations and loss of anti-symmetry of parallel velocity fluctuations about LFS mid plane due to finite θ_0 leads to net poloidally averaged parallel momentum flux. The parallel momentum flux is

antisymmetric with respect to θ_0 which provides a mechanism of flux reversal and hence reversal of intrinsic toroidal rotation.

- Heat flux shows even parity with respect to θ_0 .
- Un-normalized heat and momentum flux k_y spectra obtained from γ_{max} modes show peaks at $k_y = 0.5$ and 1.5 characteristic of both low k_y and high k_y spectrum of γ_{max} .

The freedom of setting arbitrary θ_0 deserves some discussion. The periodic nature of growth rates of the eigenmodes with respect to θ_0 can best be understood by calculating eigenmode averaged curvatures

$$\langle \hat{\mathcal{K}}_y \rangle = \frac{\int_{-\pi}^{+\pi} dz \hat{\mathcal{K}}_y(z) |\phi|^2(z)}{\int_{-\pi}^{+\pi} dz |\phi|^2(z)}$$

For a test eigenfunction of the type $\phi = (1 + \cos(\theta - \theta_0))$ it is easy to show that $\langle \hat{\mathcal{K}}_y \rangle$ consist of terms proportional to $\sin\theta_0$ and $\cos\theta_0$. That is an eigenmode “ballooned” at different poloidal angles samples different effective magnetic field curvatures and hence different growth rates periodic in θ_0 for effective curvature being periodic in θ_0 . This is shown in an example for $k_y = 0.6$ in Fig.(5.22). But understanding of why $\theta_0 = 0$ modes are not maximum growing modes at high k_y region requires further deep investigation which is not within the scope of this chapter.

Obviously, the freedom of choosing θ_0 is neither desirable nor self-consistent for the description of the mode. What decides ballooning angle in more realistic situation when global profile effects are considered? Eigenmode ballooning angle becomes a free parameter in flux tube simulations due to fourier decomposition of perturbations in radial direction allowed by periodic radial boundary condition which is based on assumption that the profile shearing effects are not important i.e., $\rho^* \rightarrow 0$. Hence it is natural to wonder if eigenmode ballooning angle in a global calculation with finite ρ^* correspond to $\theta_{|\gamma_{max}}$ at all. In conventional ballooning representation/formalism for 2D eigenmode structure calculation in the poloidal plane, the solution of the global eigenmode is accomplished in two steps. In the lowest order in $1/n$, where n is toroidal mode number, the eigenmode structure along the field line is calculated via an eigenvalue problem in which

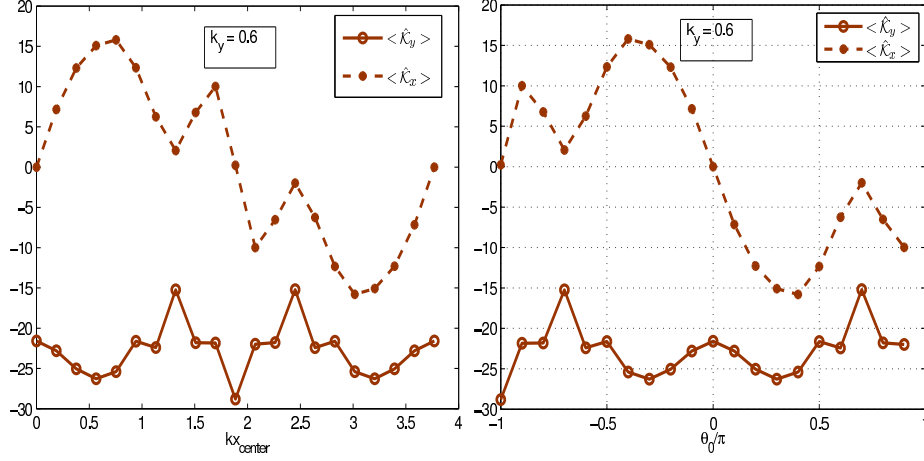


Figure 5.22: Eigenmode averaged curvatures $\langle \hat{\mathcal{K}}_x \rangle$, $\langle \hat{\mathcal{K}}_y \rangle$ vs kx_{center} (left) and θ_0 (right) for a test case of $k_y = 0.6$ when $R/L_T = 9$. The periodic nature of γ is a reflection of periodic nature of $\hat{\mathcal{K}}_y$.

θ_k , which actually appears as an operator $\theta_k = -(i/nq')d/dx$, is set to zero and local approximation to global eigenvalues are obtained[133]. θ_k is determined self-consistently from the integrability condition of the next order inhomogeneous radial envelope Equation([134]). Kim *etal* [135] and Kishimoto *etal* [136, 137] showed that in 2D envelope problem the most unstable mode is characterized by ballooning angle $\theta_0|_{\gamma_{max}} = -sign(\hat{s}\omega'_r(\omega'_r/2k_\theta\gamma_0\hat{s})^{1/3})$ where γ_0 is growth rate at zero ballooning angle and ω'_r is shear in real frequency due to equilibrium profile shear which is a finite ρ^* effect. Hence imposing finite tilts in flux tube simulations seems to violate the basic philosophy of taking $\rho^* \rightarrow 0$ in the same. A comparison of $\theta_0|_{\gamma_{max}}$ of the modes reported here with the poloidal tilt angle in global gyrokinetic simulations is desired which is left for future work.

Nonlinear simulations lead to the following conclusions.

- Nonlinear simulations with background $E \times B$ shear shows parallel momentum flux level without zonal flow shear much higher than with zonal flow shear present. However, momentum flux initially increases with $E \times B$ shear but starts to roll down due to turbulence suppression being dominant over symmetry breaking effects.
- Zonal flows shear do not produce net volume averaged parallel momentum

flux. But zonal flow shear and parallel momentum flux do show some correlations that is local in radial space x and nonlocal in time t . Heat flux is correlated with zonal flow shear non-locally in both space and time.

- Parallel momentum and heat flux channels get coupled at finite $E \times B$ shear which can be attributed to a momentum flux component driven by heat flux.

In the next Chapter we look for zonal flow generation mechanism and electromagnetic effects on zonal flow excitation and subsequent effects on transports in toroidal ITG turbulence via analytical calculations.

Secondary instability of electromagnetic ion temperature gradient modes for zonal flow generation

Having looked at radial transport of parallel momentum we now look for radial transport of poloidal momentum which manifests as radially oscillating zonal flows in the poloidal plane.

6.1 Introduction

The dependence of energy transport on plasma β ($\beta = 8\pi n_o(T_e + T_i)/B^2$, kinetic-to-magnetic pressure ratio) is of major importance for the operation and performance of a magnetic confinement fusion device. For tokamaks, the combination of high confinement and high β would allow for a high fraction of bootstrap current as well as high fusion gain and offer the promise of a more compact and economically feasible tokamak reactor operating in steady-state. The investigation of such advanced confinement regimes is presently a high priority research area in both experimental and theoretical fusion plasma physics.

Experimentally, the scaling of confinement with β has shown inconsistent results. In the commonly used empirical scaling law IPB98(y,2), a strong degradation of confinement with increasing β is predicted[138]. In dimensionless scaling experiments on the other hand, where β is varied while the other dimensionless variables are kept fixed, the strong degradation of confinement has not always been

confirmed[139, 140]. The mixed results may be due to the different turbulent types/regimes in the edge and core plasmas.

Theoretically, it is well known that the interplay between ion temperature gradient (ITG) mode turbulence and zonal flows play a crucial role for the level of turbulent transport in core plasmas. Zonal flows are radially localized flows that are driven by the turbulence and propagating mainly in the poloidal direction. The zonal flows provide a strong shear stabilization of the turbulent eddies and are hence important for the self-regulation and saturation of the turbulence[46, 47, 48, 49].

Theoretical studies of ITG turbulence and transport including finite β electromagnetic effects have usually been based on linear and quasi-linear (QL) theories. It is known that the linear ITG mode growth rate is reduced by electromagnetic fluctuations, resulting in a favorable scaling of confinement with β in QL theories[50, 51, 52, 53]. Less studied is the role of electromagnetic effects for the generation of zonal flows. Nonlinear simulations of ITG turbulence including electromagnetic effects and zonal flow dynamics have been performed using both gyrokinetic [53, 54, 55, 56, 57, 58] and gyro-fluid models[59, 60]. Recently, nonlinear gyrokinetic simulations of ITG turbulence has reported a significant reduction of transport levels with increasing β which could not be explained by the linear physics alone [53, 54].

From a theoretical point of view there are several analytical models for treating multi-scale interactions. Among the widely used models are the coherent mode coupling method (CMC), the wave kinetic equation (WKE) approach and the reductive perturbation expansion method. In comparison, the CMC model is based on a finite number of test waves, such as pump waves, zonal flows and side bands whereas the WKE analysis is based on the coupling of the micro-scale turbulence with the zonal flow through the WKE under the assumptions that there is a large separation of scales in space and time[3].

In the present chapter, electromagnetic β effects on ITG turbulence and transport is analyzed based on a two-fluid model for the ions (Refs. [141, 128, 142]) and the electrons employing the WKE model for the zonal flow generation. Note that the kinetic ballooning mode (KBM) is however not included. A system of equations is derived which describes the coupling between the background ITG turbulence, using a wave-kinetic equation, and the zonal flow mode driven by Reynolds and Maxwell stress forces. The work extends a previous study (Ref. [143]) by self-

consistently including linear as well as nonlinear β effects in the derivation. The derived dispersion relation for the zonal flow is solved numerically and the scalings of the zonal flow growth rate with plasma parameters, in particular with plasma β , is studied and the implications for ITG driven transport scaling with β are discussed.

The chapter is organized as follows. In Section 6.2 the fluid model used to describe the electromagnetic ITG modes are presented. The derivation of the zonal flow growth rate in the presence of a background of ITG modes is described in Section 6.3. In Section 6.4 the results are presented and discussed. Finally the conclusions are given in Section 6.5.

6.2 Electromagnetic toroidal ion temperature gradient driven modes

We will start by presenting the ion part of the fluid description used for toroidal ion-temperature-gradient (ITG) driven modes consisting of the ion continuity and ion temperature equations by following the Refs [52, 143]. The electromagnetic effects enter through electron fluid model via quasi-neutrality while the ion branch is identical to the electrostatic case. Combining the ion and electron fluid model through quasi-neutrality results in the dispersion relation for ITG modified by finite β effects. It has been found that the effect of parallel ion motion is weak on the reactive ITG modes and therefore it is neglected, moreover, the effects of electron trapping is neglected for simplicity. The linearized ion-continuity and ion-temperature equations can be written

$$\omega \tilde{n} = (\omega_{Di} - \omega_{\star i}) \tilde{\phi} + \omega_{Di}(\tilde{n} + \tilde{T}_i) - k_{\perp}^2 (\omega - \alpha_i \omega_{\star i}) \tilde{\phi}, \quad (6.1)$$

$$\omega \tilde{T}_i = \left(\frac{2}{3} \omega_{Di} - \eta_i \omega_{\star i}\right) \tilde{\phi} + \frac{2}{3} \omega_{Di}(\tilde{n} + \tilde{T}_i) + \frac{5}{3} \omega_{Di} \tilde{T}_i - k_{\perp}^2 (\omega - \alpha_i \omega_{\star i}) \tilde{\phi}. \quad (6.2)$$

Here we have assumed $\tau = T_i/T_e = 1$ and $\tilde{n} = (L_n/\rho_s) \delta n/n_0$, $\tilde{\phi} = (L_n/\rho_s) e \delta \phi/T_e$, $\tilde{T}_i = (L_n/\rho_s) \delta T_i/T_{i0}$ are the normalized ion particle density, the electrostatic potential and the ion temperature, respectively. We have denoted the ion diamagnetic and magnetic drift frequency as $\omega_{\star i} = -\omega_{\star e}$ and $\omega_{Di} = -\omega_{De}$ where the geometrical quantities are calculated using a semi-local model where $g_i(\theta)$ is defined by

$\omega_D(\theta) = \omega_* \epsilon_n g_i(\theta)$, with $\omega_* = k_y v_* = k_y \rho_s c_s / L_n$, see Equations(6.17) - (6.19) below. The normalized gradient scale lengths are defined as $L_f = -(d \ln f / dr)^{-1}$ ($f = \{n, T_i\}$), $\eta_i = L_n / L_{T_i}$, $\epsilon_n = 2L_n / R$ where R is the major radius and $\alpha_i = (1 + \eta_i)$. The perpendicular length scale and time are normalized by ρ_s and L_n / c_s , respectively. Here $\rho_s = c_s / \Omega_{ci}$ where $c_s = \sqrt{T_e / m_i}$ and $\Omega_{ci} = eB / m_i c$. We will start by deriving the linear ion density response of the form $\tilde{n}_i = Q\tilde{\phi}$ for this system of equations. Combining Equations(6.1) - (6.2) and eliminating the temperature perturbations we find a relation between the ion density and potential perturbations,

$$\tilde{n}_i = \frac{T}{N} \tilde{\phi} = Q\tilde{\phi}, \quad (6.3)$$

$$N = \omega^2 - \frac{10}{3} \omega_{Di} \omega + \frac{5}{3} \omega_{Di}^2, \quad (6.4)$$

$$T = \omega(\omega_{Di} - \omega_{*i}) + \omega_{*i} \omega_{Di} \left(\frac{7}{3} - \eta_i \right) - \frac{5}{3} \omega_{Di}^2 - (\omega + \alpha_i \omega_{*i}) \left(\omega - \frac{5}{3} \omega_{Di} \right) k_{\perp}^2 \quad (6.5)$$

Now we turn our attention to the electron fluid model. We will consider a low- β tokamak equilibrium with Shafranov shifted circular magnetic surfaces while omitting the parallel magnetic perturbations (the compressional Alfvén mode) and we will make use of a electric field representation of the form,

$$\vec{E} = -\nabla \tilde{\phi} - \frac{1}{c} \frac{\partial \tilde{A}_{\parallel}}{\partial t} \vec{e}_{\parallel}, \quad (6.6)$$

where $\tilde{\phi}$ is the scalar potential, \tilde{A}_{\parallel} is the parallel component of the vector potential and \vec{e}_{\parallel} is the unit vector along \vec{B} . We find from the parallel momentum equation for electrons while neglecting electron inertia a relation between the electron density, potential and parallel vector potential,

$$\tilde{n}_e = \left(\tilde{\phi} - \frac{\omega - \omega_{*e}}{ck_{\parallel}} \tilde{A}_{\parallel} \right). \quad (6.7)$$

We will now use the quasi-neutrality condition ($\tilde{n}_i = \tilde{n}_e$) in combination with the parallel electron momentum Equation(6.7) and the ion density response Equation(6.3) to determine the parallel vector potential in terms of the electrostatic

potential yielding

$$\tilde{A}_{\parallel} = ck_{\parallel} \frac{1-Q}{\omega - \omega_{\star e}} \tilde{\phi} = \Omega_{\alpha} \tilde{\phi}. \quad (6.8)$$

Here,

$$\Omega_{\alpha} = ck_{\parallel} \frac{1-Q}{\omega - \omega_{\star e}}. \quad (6.9)$$

In order to arrive at the dispersion relation, we need yet another equation relating the electrostatic potential and the vector potential, see Ref. [52]. We use the electron continuity equation to find

$$\omega \tilde{n}_e = (\omega_{\star e} - \omega_{De}) \tilde{\phi} + \omega_{De} \tilde{P}_e - \frac{1}{ne} k_{\parallel} J_{\parallel}, \quad (6.10)$$

where ω_{De} is the electron magnetic drift frequency and $\tilde{P}_e = n\tilde{T}_e + T_e\tilde{n}_e$ is the linearized electron pressure perturbation. Furthermore we assume that the electron parallel heat conductivity is large $\nabla_{\parallel} \tilde{T}_e \approx 0$ where ∇_{\parallel} is taken along the total magnetic field line giving

$$k_{\parallel} \tilde{T}_e = \eta_e \frac{k_y}{c} \tilde{A}_{\parallel}. \quad (6.11)$$

In the regime $v_{ti} \ll \frac{|\omega|}{k_{\parallel}} \approx v_A \ll v_{te}$ the parallel current is primarily carried by electrons ($v_A = \frac{B}{\sqrt{4\pi n m_i}}$ and v_t are the Alfvén and thermal speed, respectively) resulting in,

$$k_{\parallel}^2 J_{\parallel} = k_{\parallel}^2 J_{\parallel e} = ne \left((\omega_{\star e} - \omega) k_{\parallel} \tilde{\phi} + \frac{(\omega - \omega_{\star e})(\omega - \omega_{De}) + \eta_e \omega_{\star e} \omega_{De}}{c} \tilde{A}_{\parallel} \right) \quad (6.12)$$

The parallel current density (J_{\parallel}) can be determined through the parallel component of Ampère's law,

$$\nabla_{\perp}^2 \tilde{A}_{\parallel} = -\frac{4\pi}{c} J_{\parallel}, \quad (6.13)$$

yielding the second relation between the potentials ϕ and \tilde{A}_\parallel as

$$k_\parallel \tilde{\phi} = \left(1 + \frac{k_\perp^2 k_\parallel^2 v_A^2 + \omega_{De}(\omega - \omega_{*eT})}{\omega(\omega_{*e} - \omega)} \right) \frac{\omega}{c} \tilde{A}_\parallel \quad (6.14)$$

Combining Equations(6.8) and (6.14) and normalizing with ω_{*e}^2 we find the ITG mode dispersion relation as

$$-k_\perp^2 k_\parallel^2 + \beta \left(\frac{q}{\epsilon_n} \right) \left((\bar{\omega} - 1)(\bar{\omega} - \epsilon_n g_i) + \eta_e \epsilon_n g_i - \frac{(\bar{\omega} - 1)^2}{1 - Q} \right) = 0. \quad (6.15)$$

Here, we have normalized the ITG mode real frequency and growth rate as $\bar{\omega} = \frac{\omega}{\omega_{*e}}$. The geometrical quantities will be determined using a semi-local analysis by assuming an approximate eigenfunction while averaging the geometry dependent quantities along the field line. The form of the eigenfunction is assumed to be[52],

$$\Psi(\theta) = \frac{1}{\sqrt{3\pi}}(1 + \cos \theta) \quad \text{with} \quad |\theta| < \pi. \quad (6.16)$$

In the dispersion relation we will replace $k_\parallel = \langle k_\parallel \rangle$, $k_\perp = \langle k_\perp \rangle$ and $\omega_D = \langle \omega_D \rangle$ by the averages defined through the integrals,

$$\langle k_\perp^2 \rangle = \int_{-\pi}^{\pi} d\theta \Psi k_\perp^2 \Psi = k_\theta^2 \left(1 + \frac{s^2}{3}(\pi^2 - 7.5) - \frac{10}{9}s\alpha + \frac{5}{12}\alpha^2 \right), \quad (6.17)$$

$$\langle \omega_D \rangle = \int_{-\pi}^{\pi} d\theta \Psi \omega_D \Psi = \epsilon_n \omega_* \left(\frac{2}{3} + \frac{5}{9}s - \frac{5}{12}\alpha \right), \quad (6.18)$$

$$\langle k_\parallel k_\perp^2 k_\parallel \rangle = \int_{-\pi}^{\pi} d\theta \Psi k_\parallel k_\perp^2 k_\parallel \Psi = \frac{k_\theta^2}{3(qR)^2} \left(1 + s^2 \left(\frac{\pi^2}{3} - 0.5 \right) - \frac{8}{3}s\alpha + \frac{3}{4}\alpha^2 \right). \quad (6.19)$$

Here $\alpha = \beta q^2 R (1 + \eta_e + (1 + \eta_i)) / (2L_n)$ and $\beta = 8\pi n_o (T_e + T_i) / B^2$ is the plasma β , q is the safety factor and $s = rq' / q$ is the magnetic shear. The α -dependent term above (in Equation(6.17)) represents the effects of Shafranov shift. We will now study the non-linear generation of zonal flow induced by toroidal ITG modes modified by electromagnetic effects.

6.3 The model for zonal flow generation

In order to determine the zonal flow generation from the non-linear coupling of ITG modes modified by electromagnetic effects, we will need to describe the temporal evolution of the zonal flow through the vorticity equation,

$$\langle \nabla \cdot \vec{J} \rangle = \langle \nabla \cdot J_{\perp} \rangle + \langle \nabla \cdot J_{\parallel} \rangle \quad (6.20)$$

Here $\langle f(k_x, k_y) \rangle = \int d^2k f(k_x, k_y)$. The vorticity equation consists of two parts, the first including a derivative perpendicular to the field line and the second along the field line. At first, we will consider the two contributions separately where the perpendicular part can be written,

$$\begin{aligned} \langle \nabla \cdot J_{\perp} \rangle &= \langle \nabla \cdot (en_i \vec{v}_{\star i} - n_e \vec{v}_{\star e}) \rangle + \langle \nabla \cdot en_i \vec{v}_{pi} \rangle \\ &= -\frac{\partial \nabla_{\perp}^2 \Phi}{\partial t} - \langle [\tilde{\phi}, \nabla_{\perp} \tilde{\phi}] \rangle \end{aligned} \quad (6.21)$$

Here $[A, B] = \frac{\partial A}{\partial x} \frac{\partial B}{\partial y} - \frac{\partial A}{\partial y} \frac{\partial B}{\partial x}$ is the Poisson bracket. Next, we consider the contribution from the parallel derivative of the current density,

$$\begin{aligned} \langle \frac{1}{en} \nabla J_{\parallel} \rangle &= \langle \frac{1}{en} \nabla_{\parallel 0} J_{\parallel} - \frac{1}{en} \frac{e_{\parallel} \times \nabla \tilde{A}_{\parallel}}{B} \cdot \nabla J_{\parallel} \rangle \\ &= \left(\frac{v_A}{c} \right)^2 \langle [\tilde{A}_{\parallel}, \nabla_{\perp}^2 \tilde{A}_{\parallel}] \rangle \\ &= \left(\frac{v_A}{c} \right)^2 \langle |(1 - Q) \left(\frac{ck_{\parallel}}{\omega - \omega_{\star e}} \right)|^2 [\tilde{\phi}, \nabla_{\perp}^2 \tilde{\phi}] \rangle \\ &= \langle |\Omega_{\alpha}|^2 [\tilde{\phi}, \nabla_{\perp}^2 \tilde{\phi}] \rangle \end{aligned} \quad (6.22)$$

where we have used Equation(6.9) to substitute the vector potential by the electric potential and we have assumed that the variation along the field line is very small $\nabla_{\parallel 0} J_{\parallel} \approx 0$. The time evolution of the zonal flow potential (Φ) is then given by,

$$\frac{\partial}{\partial t} \nabla_{\perp}^2 \Phi = -\langle (1 - |\Omega_{\alpha}|^2) [\tilde{\phi}, \nabla_{\perp}^2 \tilde{\phi}] \rangle \quad (6.23)$$

We will now compute an estimate for the generation of zonal flows through the Reynolds stress and Maxwell stress terms. We consider the Reynolds stress,

$$\langle [\tilde{\phi}, \nabla_{\perp}^2 \tilde{\phi}] \rangle = -\nabla_X^2 \langle \frac{\partial \tilde{\phi}}{\partial x} \frac{\partial \tilde{\phi}}{\partial y} \rangle = -\nabla_X^2 Re \int d^2k k_x k_y |\tilde{\phi}|^2. \quad (6.24)$$

Here Re stands for the real part of the integral and the gradient in X acts on the spatial scale of the zonal flow. We will now assume that there exist a wave action invariant of the form $|\tilde{\phi}|^2 = C(k_x, k_y)N_k$. Now the zonal flow evolution becomes,

$$\frac{\partial}{\partial t} \nabla_{\perp}^2 \Phi = -\nabla_X^2 Re \int d^2k k_x k_y (1 - |\Omega_{\alpha}|^2) C(k_x, k_y) N_k. \quad (6.25)$$

In order to close the system of equations we need an additional relation for the action invariant (N_k) which is given by the wave kinetic equation. The wave kinetic equation (see Refs [46, 143, 144, 145, 146, 147, 148, 149]) for the generalized wave action N_k in the presence of mean plasma flow due to the interaction between mean flow and small scale fluctuations is

$$\begin{aligned} \frac{\partial}{\partial t} N_k(x, t) &+ \frac{\partial}{\partial k_x} \left(\omega_{ITG} + \vec{k} \cdot \vec{v}_0 \right) \frac{\partial N_k(x, t)}{\partial x} - \frac{\partial}{\partial x} \left(\vec{k} \cdot \vec{v}_0 \right) \frac{\partial N_k(x, t)}{\partial k_x} \\ &= \gamma_{ITG} N_k(x, t) - \Delta \omega N_k(x, t)^2 \end{aligned} \quad (6.26)$$

Here ω_{ITG} is the real frequency and γ_{ITG} is the growth rate of the small scale ITG mode fluctuations. In this analysis it is assumed that the RHS is approximately zero (stationary turbulence). The role of non-linear interactions among the ITG fluctuations (here represented by a non-linear frequency shift $\Delta \omega$) is to balance the linear growth rate. In the case when $\gamma_{ITG} N_k(x, t) - \Delta \omega N_k(x, t)^2 = 0$, the expansion of Equation(6.26) is made under the assumption of small deviations from the equilibrium spectrum function; $N_k = N_k^0 + \tilde{N}_k$ where \tilde{N}_k evolves at the zonal flow time and space scale ($\Omega, q_x, q_y = 0$) of the form $\Psi \sim e^{iq_x X - i\Omega t}$ for $\Psi = \{\Phi, \tilde{N}_k\}$, as

$$-i(\Omega_q - q_x v_{gx} + i\gamma_{ITG}) \tilde{N}_k = \frac{\partial}{\partial x} (\vec{k} \cdot \vec{z} \times \nabla (1 + \nabla_{\perp}^2) \Phi) \frac{\partial N_k^0}{\partial k_x}. \quad (6.27)$$

While using Equation(6.27) we now find the perturbed action density as,

$$\tilde{N}_k = \frac{i(\Omega_q - q_x v_{gx}) + \gamma_{ITG}}{(\Omega_q - q_x v_{gx})^2 + \gamma_{ITG}^2} k_y (\nabla_x^2 (1 + \nabla_x^2) \Phi) \frac{\partial N_k^0}{\partial k_x}, \quad (6.28)$$

and substituting Equation(6.28) into the zonal flow evolution we obtain,

$$\frac{\partial}{\partial t} \nabla_{\perp}^2 \Phi = -\nabla_x^2 Re \int d^2 k k_x k_y^2 \frac{(1 - |\Omega_{\alpha}|^2) \nabla_x^2 (1 + \nabla_x^2) \Phi}{(\Omega_q - q_x v_{gx})^2 + \gamma_{ITG}^2} C(k_x, k_y) \left(-\frac{\partial N_k^0}{\partial k_x} \right). \quad (6.29)$$

The adiabatic invariant $N_k^0 = \frac{E_k}{\omega_{rk}}$ is determined by the energy density E_k and the real frequency ω_{rk} . An approximate wave action density can be obtained using the same methodology as in Ref. [143] where the linear electron Equation(6.14) and quasi-neutrality Equation(6.8) are used to find the modified normal coordinates $\varphi = \tilde{\phi} + \alpha_k \tilde{T}_i$ for which a generalized invariant is found of the form $N_k = |\varphi|^2 = C(\vec{k}) |\tilde{\phi}|^2$. It is generally found that $C(\vec{k})$ is only weakly dependent on the wave vector \vec{k} as long as the FLR effects are small. The remaining integral displayed in Equation(6.29) can be solved in the two limits $\frac{\gamma_{ZF}}{\gamma_{ITG}} < 1$ and $\frac{\gamma_{ZF}}{\gamma_{ITG}} > 1$. We assume a certain spectral form on the action density N_k^0 and that $C(k_x, k_y)$ is weakly dependent on k_x . In the limit where the linear growth rate is much larger than the zonal flow growth $\frac{\gamma_{ZF}}{\gamma_{ITG}} < 1$ we find the dispersion relation,

$$\Omega_q = i q_x^2 (1 - q_x^2) \int d^2 k \frac{k_x k_y^2 (1 - |\Omega_{\alpha}|^2)}{\gamma_{ITG}} C(k_x, k_y) \left(-\frac{\partial N_k^0}{\partial k_x} \right). \quad (6.30)$$

Here the $1 - |\Omega_{\alpha}|^2$ represents the electromagnetic effects on the zonal flow evolution and the $1 - q_x^2$ term is the FLR stabilization. We choose the particular form of the the spectrum as a Gaussian wave packet in k_x with width Δ and delta function in k_y such that,

$$N_k^0 = N_0 e^{-\frac{(k_x - k_{x0})^2}{\Delta^2}} \delta(k_y - k_{y0}). \quad (6.31)$$

We have chosen a drift wave packet centered around the most unstable mode in k_y and a spectrum in k_x similar to that used in Ref. [150]. Now the derivative on the action density is easily found and the integral can be computed resulting in

the final zonal flow dispersion relation as,

$$\Omega_q = i(K - |\Omega_\alpha|^2)q_x^2(1 - q_x^2)\frac{k_{y0}^2\Delta\sqrt{\pi}}{\gamma_k}|\tilde{\phi}|^2. \quad (6.32)$$

Here the dispersion relation may be modified with the inclusion of the FLR nonlinearities (see e.g. Ref. [143]) by setting $K = 1 + \tau + \tau\delta_p$ where

$$\delta_p = \frac{\Delta_1\Delta_2 + \frac{2}{3}\gamma_{ITG}^2}{\Delta_2^2 + \gamma_{ITG}^2}, \quad (6.33)$$

$$\Delta_1 = \left(\eta_i - \frac{2}{3}\right) + \frac{2}{3}\omega_{ITG}, \quad (6.34)$$

$$\Delta_2 = \omega_{ITG} + \frac{5}{3}\epsilon_n g \quad (6.35)$$

and ω_{ITG} is the real frequency and γ_{ITG} is the linear growth rate of the ITG mode. Next we will consider the more interesting limit $\frac{\gamma_{ZF}}{\gamma_{ITG}} > 1$ in the integral (6.29). In this limit the zonal flows are expected to have an impact on the ITG turbulence. We assume that the coefficient $C(k_x, k_y)$ is weakly dependent on \vec{k} and that the group velocity can be written $v_{gx} = k_x k_y f(\eta_i, \eta_e, \beta, \dots)$ where $f(\eta_i, \eta_e, \beta, \dots)$ is independent of \vec{k} similar to the case in Ref [143]. We can now rewrite the integral as

$$\begin{aligned} \Omega_q &= q_x^2(1 - q_x^2)C(k_x, k_y) \int d^2k \frac{k_x k_y^2(1 - |\Omega_\alpha|^2)}{(\Omega_q - q_x v_{gx})} \left(-\frac{\partial N_k^0}{\partial k_x}\right) \\ &= q_x^2(1 - q_x^2) \frac{C(k_x, k_y)}{f(\eta_i, \eta_e, \beta, \dots)} \int d^2k \frac{k_y v_{gx}(1 - |\Omega_\alpha|^2)}{(\Omega_q - q_x v_{gx})} \left(-\frac{\partial N_k^0}{\partial k_x}\right). \end{aligned} \quad (6.36)$$

We consider the same spectral form as in Equation(6.31) and performing one partial integration the dispersion relation is readily found,

$$(\Omega_q - q_x v_{gx})^2 = -q_x^2(K - |\Omega_\alpha|^2)(1 - q_x^2)k_y\Delta\sqrt{\pi}|\tilde{\phi}|^2 \quad (6.37)$$

In the following we will use a fixed width of the spectrum with $\Delta\sqrt{\pi} = 1.0$ corresponding to a monochromatic wave packet in k_x . In the following section we will explore this dispersion relation numerically and discuss the results and its implications.

6.4 Results and discussion

The algebraic Equation(6.37) describing the zonal flow growth rate is solved numerically with the ITG eigenvalues ω_{ITG} taken from a numerical solution of the ITG dispersion relation Equation(6.15). The zonal flow growth rate is then normalized to the ITG growth rate to highlight the competition between the linear ITG drive and the stabilizing effect of the zonal flow mode through shearing of the turbulent eddies. The results are expected to give an indication of the strength of the shearing rate $\omega_s \sim \frac{d^2\Phi}{dx^2}$ (where Φ is the zonal flow component of the electrostatic potential) relative to the linear growth rate. The results for γ_{ZF}/γ_{ITG} is calculated for a turbulence saturation level, corresponding to a mixing length estimate with $\frac{e\phi}{T_e} = \frac{1}{k_x L_n} = \tilde{\phi}_0$ that is fixed. [142] In experimental tokamak plasmas the core density profiles are rather flat ($\epsilon_n > 1$) whereas the edge profiles are peaked ($\epsilon_n < 1$) with a typical experimental value of the plasma β around 1%. In Fig.(6.1) the ITG eigenvalues (normalized to the electron diamagnetic drift frequency) as a function of β are displayed with η_i as a parameter for $\epsilon_n = 2.0$, $\eta_e = 0$, $\tau = 1$, $q = 1.5$, $s = 0.5$ and $k_\perp^2 \rho^2 = 0.1$. The results are shown for $\eta_i = 3.5$ (dashed line), and for $\eta_i = 4.0$ (solid line). In the electrostatic limit $\beta \rightarrow 0$, the analytical results as obtained from Equations.(8 - 10) of Ref.[143] (neglecting FLR effects) is $\omega/\omega_{*e} = -3.03 + i0.90$ for the case $\eta_i = 3.5$ and $\omega/\omega_{*e} = -3.03 + i1.28$ for $\eta_i = 4.0$, in good agreement with the numerical results of Fig.(6.1). The results show that the ITG growth rate is reduced with increasing β as expected from previous studies ([50, 51, 52, 53, 54] and [142]).

The corresponding results for the zonal flow growth rate (normalized to the ITG growth rate) versus β are shown in Fig.(6.2). As observed, the normalized zonal flow growth increases for large β close to marginal stability. The scaling illustrates the competition between the linear and nonlinear stabilizing β effects. Close to marginal stability (for $\eta_i = 3.5$), the decrease of γ_{ITG} due to increasing β dominates resulting in a normalized zonal flow growth rate that increases with β . This would indicate that the ITG turbulence and transport decrease faster with β than expected from a purely linear analysis, in agreement with recent simulation results ([53]). For larger η_i , a decreasing zonal flow drive is observed due to Maxwell stress. We note that this result differs with that reported in Ref. ([151, 152]), using the drift-Alfven wave branch neglecting effects of curvature, where the zonal flow

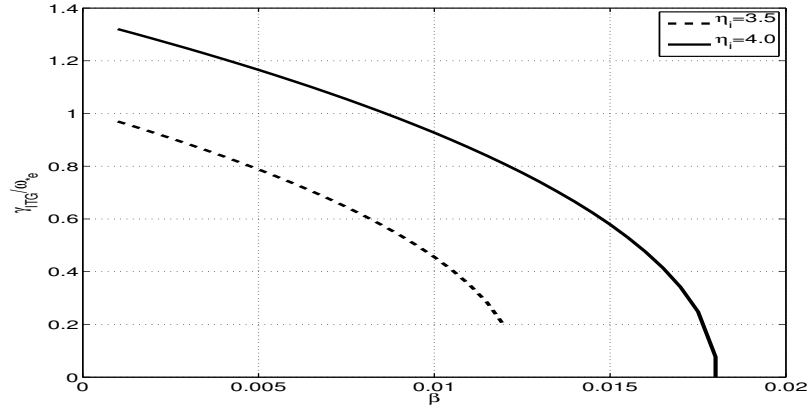


Figure 6.1: Numerical solution to Equation(6.15) displaying the ITG growth rate (normalized with ω_{*e}) versus β for $\eta_e = 0$, $q = 1.5$, $s = 0.5$, $k_{\perp}^2 \rho^2 = 0.1$, $\Delta\sqrt{\pi} = 1.0$ with ϵ_n as a parameter. Results are shown for $\eta_i = 3.5$ (dashed line) and $\eta_i = 4.0$ (solid line).

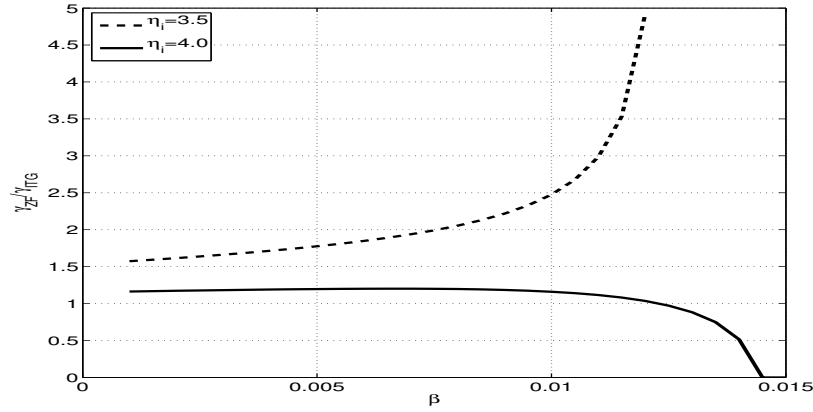


Figure 6.2: Zonal flow growth rate (normalized with γ_{ITG}) versus β with η_i as a parameter for the same parameters as in Fig.(6.1) as obtained numerically by solving Equation(6.37). A fixed ITG turbulence saturation level $\tilde{\phi} = \tilde{\phi}_0$ was used.

growth initially decreases with β and reaches a minimum and then increases. The consequence of such a β dependence is not apparent, but could indicate a transition to a more favorable confinement regime for $\beta > \beta_{min}$.

Figs.(6.3, 6.4) illustrates the ITG and zonal flow growth rates as a function of η_i with β as a parameter. The other parameters are $\epsilon_n = 2$, $\eta_e = 0$, $\tau = 1$, $q = 1.5$, $s = 0.5$ and $k_{\perp}^2 \rho^2 = 0.1$. The results are shown for $\beta = 0.1\%$ (dash-dotted line), $\beta = 0.5\%$ (dotted line), $\beta = 1.0\%$ (dashed line) and $\beta = 1.3\%$ (solid line). The linear ITG growth rates (normalized to the electron diamagnetic drift frequency) in Fig.(6.3) illustrates the typical β stabilization with a β -threshold close to the analytical result $\eta_{ith} = 3.01$ for $\beta \rightarrow 0$ (from Equation(10) of Ref. [51]). Fig.(6.4) displays the corresponding zonal flow growth rates (normalized to the ITG growth rate). The un-normalized zonal flow growth is weakly dependent on η_i , resulting in a normalized zonal flow growth rate which strongly increases when approaching the stability threshold η_{ith} . The results indicate the importance of the zonal flows close to marginal stability ($\eta_i \leq 4.0$) where $\gamma_{ZF}/\gamma_{ITG} \gg 1$ is obtained. In this region the effects of zonal flow increases with increasing β whereas for larger η_i the opposite trend is found. This is in line with the strong nonlinear upshift of the critical ion temperature gradient with increasing β and converging Dimits shift for larger β recently observed in nonlinear gyrokinetic simulations of ITG turbulence[53, 153]. However, a complete treatment of the Dimits shift requires a model for the zonal flow saturation mechanisms which is outside the scope of the present chapter. We note that the same trend, with an increase of γ_{ZF}/γ_{ITG} with increasing β is obtained in Fig.(6.2) close to marginal stability ($\eta_i = 3.5$). For larger $\eta_i > 4$, the condition $\gamma_{ZF}/\gamma_{ITG} > 1$ is however not satisfied.

6.5 Conclusions

A system of fluid equations describing the coupling between the zonal flow mode and the background ITG turbulence including finite β electromagnetic effects is derived. The model equations include the linear stabilization of the ITG mode due to finite β electromagnetic perturbations as well as the nonlinear β effects on the zonal flow entering through the Maxwell stress force. The scaling of the zonal flow growth rate with plasma parameters is studied and the implications for ITG driven

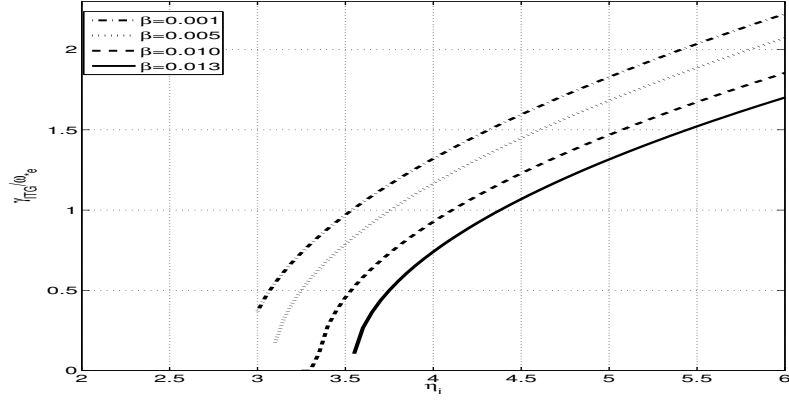


Figure 6.3: Numerical solution to Equation (6.15) showing the ITG growth rate (normalized with ω_{*e}) versus η_i for $\eta_e = 0$, $\epsilon_n = 2$, $q = 1.5$, $s = 0.5$, $k_{\perp}^2 \rho^2 = 0.1$, $\Delta\sqrt{\pi} = 1.0$ with β as a parameter. Results are shown for $\beta = 0.1\%$ (dash-dotted line), $\beta = 0.5\%$ (dashed line), $\beta = 1.0\%$ (dashed line) and $\beta = 1.3\%$ (solid line)

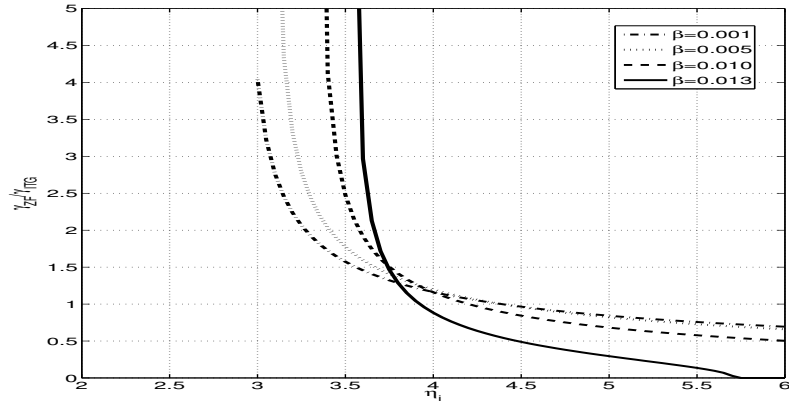


Figure 6.4: Zonal flow growth rate (normalized with γ_{ITG}) versus η_i with β as a parameter for the same parameters as in Fig.(6.3) as obtained numerically by solving Equation(6.37). A ITG turbulence saturation level $\tilde{\phi} = \tilde{\phi}_0$ was used.

transport are discussed. It is found that the ZF growth rate relative to the ITG growth rate increases with β close to marginal ITG mode stability. The result indicates a β stabilization of the ITG turbulence and transport at a faster rate than expected from a purely linear or quasi-linear analysis. Such behavior has recently been observed in nonlinear gyrokinetic simulations of ITG turbulence[53, 54]. The results are also line with the strong nonlinear upshift of the critical ion temperature gradient with increasing β and converging Dimits shift for larger β recently observed in nonlinear gyrokinetic simulations of ITG turbulence[153]. We note that close to marginal stability the increase of γ_{ZF}/γ_{ITG} is dominated by the linear stabilization of γ_{ITG} whereas for larger η_i a decreasing zonal flow drive is observed due to the competition between Reynolds and Maxwell stresses.

In the immediate future, it is of interest to complement the present model by including geometry effects and A_\perp which is important in high β plasmas relevant for spherical systems. In addition, further investigations of zonal flow stability and saturation mechanisms and their relation to transport barriers are left for future study.

The next chapter discover the possibility of zonal like mesoscale flows in the toroidal direction. This is done by including the parallel ion dynamics and following the modulational instability analysis similar to that presented in this Chapter. However for simplicity and to clearly pull out the mechanisms of toroidal zonal flow generation, the electromagnetic effects are ignored.

A new paradigm of coupled intrinsic toroidal zonal flow - ITG turbulence - poloidal zonal flow system

7.1 Introduction

Heat and particle confinement in tokamaks first deteriorates in a power ramp because of increase of free energy in the background profiles and its subsequent release by various microinstabilities. But confinement does not keep on degrading with increasing power. Beyond a critical input power the plasma settles in a high confinement state (H mode). This is an universal phenomenon seen in all fusion devices. Suppression of turbulence by macroscopic or zonal $E \times B$ shearing has been thought as a mechanism of L-H transition[13]. Fluctuations driven Reynolds stresses drive zonal flows[3] as well as mean $E \times B$ flows apart from mean $E \times B$ flow drive from pressure gradient, poloidal and toroidal flows which can be generated by external sources. Zonal flows has been shown to cause transient oscillations and eventual transition to H mode due to building of strong mean shear in a power ramp[154, 155].

Toroidal zonal flows (TZF) can also be excited via fluctuation driven toroidal Reynolds stress [156, 38], in a way exactly similar to excitation of zonal flows (here onwards dubbed as poloidal zonal flows (PZF)). However, the role of self excited TZFs in the transient dynamics of L-H transition and its effect on input power threshold has not been studied yet.

We ask and answer the following questions in this chapter:

- Is there possibility of exciting toroidal zonal flows in ITG turbulence?
- If yes, then what is the self-consistent dynamics of coupled TZF-ITG-PZF system? What is the role of TZF in LH transition?

In this chapter we show self generation of TZFs via modulation instability of the background ITG turbulence. TZFs show linear coupling with PZFs via non-linear stresses. Then we study the role of TZFs and PZFs and the transient dynamics of the L-H transition. We propose an extended 0D model for LH transition which contains the physics of mean toroidal and poloidal flows, TZFs and PZFs and the ion pressure profile, and which treats the interplay between mean and zonal flows. The model shows reduction in power threshold with increase of PZF-TZF coupling.

The chapter is organized as follows. Sec.7.2 demonstrates coupled excitation of PZFs and TZFs via modulation instability. Sec.7.3 discusses the effect of mean poloidal and toroidal shear flows on PZFs and TZFs. Sec.7.4 presents an extended 0 D model L→H transition based on the results obtained in above sections. Finally the chapter is concluded in Sec.7.5.

7.2 Coupled excitation of PZF and TZF: A new paradigm

We start with the nonlinear fluid equations describing the background toroidal ITG turbulence

$$\begin{aligned} & \left(\frac{\partial}{\partial t} + \vec{V}_0 \cdot \vec{\nabla} \right) n_i + \frac{\partial \phi}{\partial y} - \varepsilon_n g(\theta) \frac{\partial}{\partial y} (\phi + p_i) + \nabla_{\parallel} v \\ & - \left(\frac{\partial}{\partial t} + \vec{V}_0 \cdot \vec{\nabla} - K_i \frac{\partial}{\partial y} \right) \nabla_{\perp}^2 \phi - [\phi + p, \nabla_{\perp}^2 \phi] - \left[\frac{\partial p}{\partial x}, \frac{\partial \phi}{\partial x} \right] - \left[\frac{\partial p}{\partial y}, \frac{\partial \phi}{\partial y} \right] = 0 \end{aligned} \quad (7.1)$$

Parallel momentum equation, including parallel ion stress tensor [41]

$$\begin{aligned} & \left(\frac{\partial}{\partial t} + \vec{V}_0 \cdot \vec{\nabla} - 2\tau_i \varepsilon_n g \frac{\partial}{\partial y} \right) v - \hat{V}'_{\parallel 0} \frac{\partial \phi}{\partial y} - V_{\parallel 0} \varepsilon_n g \frac{\partial}{\partial y} (\phi + p) + \nabla_{\parallel} (\phi + p) \\ & + [\phi, v] = 0 \end{aligned} \quad (7.2)$$

Temperature perturbation equation

$$\left(\frac{\partial}{\partial t} + \vec{V}_0 \cdot \vec{\nabla} - \frac{5}{3}\tau_i \varepsilon_n g \frac{\partial}{\partial y}\right) T + \left(\eta_i - \frac{2}{3}\right) \frac{\partial \phi}{\partial y} - \frac{2}{3} \left(\frac{\partial}{\partial t} + \vec{V}_0 \cdot \vec{\nabla}\right) n_i + [\phi, T - \frac{2}{3}n_i] = 0 \quad (7.3)$$

Adiabatic electron response

$$n_e = \phi - \Phi_{ZF} \quad (7.4)$$

Quasineutrality

$$n_e = n_i \quad (7.5)$$

Now the zonal modes are nothing but poloidal mode number $m = 0$, toroidal mode number $n = 0$ and radial wave number $q_r \neq 0$ perturbations in the turbulence. Equations governing zonal mode evolution can be obtained by toroidal and poloidal averaging of the background turbulence equations. Following this one can identify that the PZF is driven by the so called Reynolds stress $\langle [\phi, \nabla_\perp^2 \phi] \rangle$ in a simple drift wave turbulence. In the same spirit one can expect the Reynolds stress $\langle [\phi, v] \rangle$ (from the averaged parallel momentum equation of ITG turbulence) to drive parallel zonal flow. The stresses can be expressed in terms of wave action density $N_k \equiv E_k / \omega_{r,k}$. Here E_k is the energy and $\omega_{r,k}$ is the real frequency of the k th mode. The evolution of wave action in the presence of zonal flow modulations can be described by the Wave Kinetic Equation (WKE). This forms coupled zonal flow-turbulence system. We adopt this methodology and assume that 1) the momentum diffusivity χ_ϕ is known, 2) momentum pinch is vanishing and 3) $B_\theta \ll B_\phi$ so that $\langle v_\parallel \rangle \approx \langle v_\phi \rangle$, to proceed further. The residual stress in terms of wave action or quasi-particle population density $N_k(\vec{x}, \vec{k}, t)$ can be expressed as [156]

$$\Pi^{res} = \int d\vec{k} v_{gr} k_\parallel N_k \quad (7.6)$$

The equation for intrinsic toroidal flow V_ϕ , then becomes

$$\partial_t V_\phi - \partial_r \chi_\phi \partial_r V_\phi = -\partial_r \int d\vec{k} v_{gr} k_\parallel N_k \quad (7.7)$$

The poloidal zonal flow, including the viscous damping μ , is governed by

$$\begin{aligned}\partial_t \nabla_X^2 \Phi_{pzf} - \mu \nabla_X^4 \Phi_{pzf} &= \nabla_X^2 \int d\vec{k} (1 + \tau_i + \delta_k \tau_i) k_x k_y |\phi_k|^2 \\ &= \nabla_X^2 \int d\vec{k} (1 + \tau_i + \delta_k \tau_i) k_x k_y C_k N_k\end{aligned}\quad (7.8)$$

where $\delta_k = T_k/\phi_k$ is the temperature linear response function. This term provides diamagnetic enhancement to the poloidal stress and $|\phi|^2 = C_k N_k$ has been used in the last step to express fluctuation intensity in terms of action density. The exact form of C_k can be obtained from the mode energy density and the real frequency, but it is not required here. The above equation nicely reduces to the potential vorticity equation for zonal flows generation in simple drift wave case on taking the limit $\tau_i \rightarrow 0$. The detailed structure of δ_k is provided in the next Chapter 8 since it is not needed here. The quasi-particle population density obeys the WKE given by

$$\frac{\partial N_k}{\partial t} + \frac{\partial \omega_{r,k}}{\partial \vec{k}} \cdot \frac{\partial N_k}{\partial \vec{X}} - \frac{\partial \omega_{r,k}}{\partial \vec{X}} \cdot \frac{\partial N_k}{\partial \vec{k}} = \gamma_k N_k - \Delta \omega N_k^2 \quad (7.9)$$

where $\omega_{r,k}$ and γ_k are respectively the real frequency and growth rate of the underlying turbulence in the presence of the slowly varying mesoscale zonal fields.

$$\omega_{r,k} = \omega_{itg} + \vec{k} \cdot \vec{V} \quad (7.10)$$

and $\vec{V} = \vec{V}_{pzf} + \vec{V}_{tzf}$. The above system of equations forms closed set of coupled equations describing TZF-ITG-PZF system.

Assuming the stationary turbulence as new equilibrium state, the equilibrium turbulence spectrum is given by $\gamma_k \langle N_k \rangle - \Delta \omega \langle N_k \rangle^2 = 0$. The linear population density response due to flow modulations

$$\delta N_{k,q} = R_{k,q} \left[\frac{\partial \delta \omega_{r,k}}{\partial \vec{X}} \cdot \frac{\partial \langle N_k \rangle}{\partial \vec{k}} - \delta v_{gx} \frac{\partial \langle N_k \rangle}{\partial X} + \delta \gamma_k \langle N_k \rangle \right] \quad (7.11)$$

where the propagator $R_{k,q}$ is given by

$$R_{k,q} = \frac{i}{(\Omega_q - \vec{q} \cdot \vec{v}_g + i\gamma_k)} \quad (7.12)$$

and $\delta\omega = k_y \nabla_X \Phi_{pzf} + k_{\parallel} V_{tzf} + (\partial\omega/\partial\eta_i)\delta\eta_i$, $\delta v_{gx} = (\partial\delta\omega/\partial k_x)$ and $\delta\gamma_k = (\partial\gamma_k/\partial\eta_i)\delta\eta_i$ represents respective modulations by the zonal flows. Thus the parallel residual stress can be written as

$$\Pi^{res} = \int d\vec{k} v_{gr} k_{\parallel} R_{k,q} \left[(k_y \nabla_X^2 \Phi_{pzf} + k_{\parallel} V'_{tzf}) \frac{\partial \langle N_k \rangle}{\partial \vec{k}} - \delta v_{gx} \frac{\partial \langle N_k \rangle}{\partial X} + \delta\gamma_k \langle N_k \rangle \right] \quad (7.13)$$

Similarly the poloidal stress on the r.h.s of PZF equation becomes

$$\Pi_{x,y} = \int d\vec{k} k_x k_y R_{k,q} C_k \left[(k_y \nabla_X^2 \Phi_{pzf} + k_{\parallel} V'_{tzf}) \frac{\partial \langle N_k \rangle}{\partial k_x} - \delta v_{gx} \frac{\partial \langle N_k \rangle}{\partial X} + \delta\gamma_k \langle N_k \rangle \right] \quad (7.14)$$

Assuming $\langle N_k \rangle$ to be homogeneous in X and weaker growth rate modulation by zonal flows and taking fourier transform in x one obtains the following coupled equations for TZF and PZF

$$\partial_t V'_{tzf} + \chi_{\phi} q^2 V'_{tzf} = -q^4 \sigma_1 \Phi_{pzf} + q^2 \sigma_2 V'_{tzf} \quad (7.15)$$

$$\partial_t \Phi_{pzf} + \mu q^2 \Phi_{pzf} = q^2 S_1 \Phi_{pzf} - S_2 V'_{tzf} \quad (7.16)$$

where

$$\sigma_1 = \int d\vec{k} v_{gr} k_{\parallel} R_{k,q} k_y \frac{\partial \langle N_k \rangle}{\partial k_x} \quad (7.17)$$

$$\sigma_2 = \int d\vec{k} v_{gr} k_{\parallel} R_{k,q} k_{\parallel} \frac{\partial \langle N_k \rangle}{\partial k_x} \quad (7.18)$$

$$S_1 = \int d\vec{k} k_x R_{k,q} k_y^2 C_k \left(-\frac{\partial \langle N_k \rangle}{\partial k_x} \right) \quad (7.19)$$

$$S_2 = \int d\vec{k} k_x R_{k,q} k_y k_{\parallel} C_k \left(-\frac{\partial \langle N_k \rangle}{\partial k_x} \right) \quad (7.20)$$

$$(7.21)$$

and $v_{gx} \propto -k_x k_y$. For independent modulational excitation of TZF and PZF shear the integrals σ_2 and S_1 has to be +ve definite which requires

$$\sigma_2 : -k_x \frac{\partial \langle N_k \rangle}{\partial k_x} > 0, \langle N(k_y) \rangle \neq \langle N(-k_y) \rangle \text{ or } \langle k_y \rangle \neq 0 \quad (7.22)$$

$$S_1 : -k_x \frac{\partial \langle N_k \rangle}{\partial k_x} > 0 \quad (7.23)$$

The other two integrals σ_1 and S_2 has to be definite for effective cross coupling between TZF and PZF shear.

$$\sigma_1 : -k_x \frac{\partial \langle N_k \rangle}{\partial k_x} > 0, \langle N(k_{||}) \rangle \neq \langle N(-k_{||}) \rangle \text{ or } \langle k_{||} \rangle \neq 0 \quad (7.24)$$

$$S_2 : -k_x \frac{\partial \langle N_k \rangle}{\partial k_x} > 0, \langle N(k_y, k_{||}) \rangle \neq \langle N(-k_y, -k_{||}) \rangle \text{ or } (\langle k_y \rangle, \langle k_{||} \rangle) \neq (0, 0) \quad (7.25)$$

where $\langle (...) \rangle = \int d\vec{k} \langle N_k \rangle (...)$. These coupling coefficients will feedback shear to each other. Whether this coupling will cause +ve or -ve feedback depends on the sign of σ_1 and S_2 . Obviously -ve σ_1 and S_2 will cause +ve feedback enhancing the destabilization. While condition (7.23) is easily met in the drift wave turbulence condition (7.22) can be a stringent requirement. Even if $\langle k_y \rangle = 0$ the PZF shear excited via modulational instability acts as an inhomogeneous source term in the TZF shear evolution equation leading to amplification of TZF shear. However, for the TZF shear to get unstable the parallel spectral symmetry has to be broken (i.e., $\langle k_{||} \rangle \neq 0$) which can be easily provided by background mean $E \times B$ shear[96, 112], toroidicity[41], steep density gradient as a finite ρ_s^* effect [115], up-down asymmetric equilibrium magnetic topology[42, 43] and by turbulence intensity gradient[95]. This shows coupled excitation of TZF and PZF.

The back reaction of zonal flow shear on the turbulence can be studied by the evolution equation for the mean action density under the quasilinear approximation.

$$\frac{\partial \langle N_k \rangle}{\partial t} = \left\langle \frac{\partial \delta \omega_{r,k}}{\partial \vec{X}} \cdot \frac{\partial \delta N_k}{\partial \vec{k}} \right\rangle + \langle \delta \gamma_k \delta N_k \rangle - \Delta \omega \langle \delta N_k \delta N_k \rangle \quad (7.26)$$

- The 2nd term in the Equation(7.26) eventually gives nonlinear growth of turbulence due to zonal temperature modulations, comes from term like $(\partial \gamma_k / \partial \eta_i) \delta \eta_i$.
- The 3rd term represents nonlinear pull back of turbulence.

Finally

$$\frac{\partial}{\partial t} \langle N_k \rangle = \frac{\partial}{\partial k_x} D_k \frac{\partial \langle N_k \rangle}{\partial k_x} + \Gamma_k \langle N_k \rangle - \Delta \omega \langle \delta N_k \delta N_k \rangle \quad (7.27)$$

where

$$D_k = \int d\vec{q} R_{k,q} q_x^2 |ik_y q_x \Phi_q + k_{\parallel} V_{tzf,q}|^2 \quad (7.28)$$

and the nonlinear growth is given by

$$\Gamma_k = \int d\vec{q} R_{k,q} q_x^2 \left| \frac{\partial \gamma_k}{\partial \eta} \delta \eta \right|^2 \quad (7.29)$$

7.3 Zonal flows suppression by mean shear flows

The response of drift wave spectrum δN_k to zonal flows V_{pzf} and V_{tzf} is given by the following linearized WKE

$$\begin{aligned} \partial_t \delta N_k + i q v_{gx} \delta N_k - (k_y V'_E + k_{\parallel} V'_{\parallel}) \frac{\partial}{\partial k_x} \delta N_k + \gamma \delta N_k \\ = i q (k_y V_{pzf} + k_{\parallel} V_{tzf}) \frac{\partial}{\partial k_x} \langle N_k \rangle \end{aligned} \quad (7.30)$$

Evolution equation for mean wave quanta density

$$\begin{aligned} \frac{\partial}{\partial t} \langle N_k \rangle - (k_y V'_E + k_{\parallel} V'_{\parallel}) \frac{\partial}{\partial k_x} \langle N_k \rangle \\ = \frac{\partial}{\partial k_x} \langle (k_y V'_{pzf} + k_{\parallel} V'_{tzf}) \delta N_k \rangle + \gamma \langle N_k \rangle - \Delta \omega \langle N_k \rangle^2 \end{aligned} \quad (7.31)$$

Introducing total time derivative

$$D_t = \frac{\partial}{\partial t} - (k_y V'_E + k_{\parallel} V'_{\parallel}) \frac{\partial}{\partial k_x} \quad (7.32)$$

In this coordinate,

$$D_t k_x = - (k_y V'_E + k_{\parallel} V'_{\parallel}) \quad (7.33)$$

Integrating along unperturbed, shearing ray orbit from an initial time t_0 to final time t , as done in Ref.[154, 155], yields

$$\begin{aligned} \delta N_k(q, t) = \int_{t_0}^t dt' \exp \left\{ -\gamma (t - t') - iq \int_{t'}^t dt'' v_{gx}(t'') \right\} \\ \times iq (k_y V_{pzf} + k_{\parallel} V_{tzf}) \frac{\partial \langle N_k(t') \rangle}{\partial k_x(t')} \end{aligned} \quad (7.34)$$

where the shearing by mean flows is contained in v_{gx} and $\partial \langle N_k(t') \rangle / \partial k_x(t')$. In the limit when shearing time scale of the mean flows $\tau_s >$ other dynamical time scales (i.e., $1/\gamma$, $1/v_{gx}q$ and $1/\Omega$) one can approximate $\partial \langle N_k(t') \rangle / \partial k_x(t') \sim \partial \langle N_k(t) \rangle / \partial k_x(t)$. Then using the time dependence $\exp(-i\Omega t)$ for δN_k , V_{pzf} and V_{tzf} yields

$$\delta N_k(q, \Omega) = iq (k_y V_{pzf} + k_{\parallel} V_{tzf}) R \frac{\partial \langle N_k \rangle}{\partial k_x} \quad (7.35)$$

Here the real part of R becomes

$$Re(R) \sim \frac{1}{\gamma} \left[1 - \frac{12q^2 (k_y V_E' + k_{\parallel} V_{\parallel}')^2 \omega_*^2}{\gamma^4} \right] \quad (7.36)$$

for $k_{\perp} \rho_s < 1$ and $\gamma > qv_{gx} > \Omega$. This shows weakening of response of drift wave spectrum to zonal flow via enhanced decorrelation of drift wave propagation by mean shear flows. This implies inhibition of zonal flow growth by mean shear flows.

7.4 An extended 0D empirical model: Role of TZF in L \rightarrow H transition

We present a 0D model based on the results of the sections 5.2 and 5.3 which consists of turbulence intensity ε , TZF shear V_{tzf}' , PZF shear V_{pzf}' , mean $E \times B$ shear V_E' , mean parallel (or toroidal) flow shear V_{\parallel}' , mean pressure gradient \wp and

input power Q .

$$\partial_t \varepsilon = \varepsilon \wp - a_1 \varepsilon^2 - a_2 V_E'^2 \varepsilon - a_3 V_{\parallel}'^2 \varepsilon - a_4 V_{pzf}'^2 \varepsilon - a_5 V_{tzf}'^2 \varepsilon \quad (7.37)$$

$$\partial_t V_{pzf}' = b_1 \frac{\varepsilon (b_{11} V_{pzf}' + b_{12} V_{tzf}')}{1 + (b_2 V_E' + b_3 V_{\parallel}')^2} - b_4 V_{pzf}' \quad (7.38)$$

$$\partial_t V_{tzf}' = c_1 \frac{\varepsilon (c_{11} V_{tzf}' + c_{12} V_{pzf}')}{1 + (c_2 V_E' + c_3 V_{\parallel}')^2} - c_4 \varepsilon V_{tzf}' - c_5 V_{tzf}' \quad (7.39)$$

$$\partial_t \wp = -d_1 \varepsilon \wp - d_2 \wp + Q \quad (7.40)$$

$$V_E' = e_1 \wp - e_2 V_{\parallel}' \quad (7.41)$$

where $\wp \propto \partial_r P_i$. $Q = 0.01 t^m$. Pressure curvature and mean poloidal flow not considered. Here the coefficients a_i, b_i, c_i, d_i, e_i are largely unknown but should be model dependent. However, the exact form of these coefficients are not important for the qualitative discussion presented in this chapter. Equation(7.37) describes temporal evolution of turbulence intensity: the first term on the right hand side represents turbulence generation by pressure gradient via linear instability, the second term represents its nonlinear pull back, the third, fourth, fifth and sixth terms represent suppression of turbulence by mean $E \times B$ shear, mean parallel flow shear, PZF shear and TZF shear respectively. Equation(7.38) describes temporal evolution of PZF shear: the first term on the right hand side captures zonal flow shear growth by poloidal Reynolds stress. This is +ve definite due to -ve k_x gradient of the quasiparticle population density. The second term represents coupling to TZF shear inspired by Equation(7.16) and its finiteness condition Equation(7.25). The third term is the collisional damping of PZF. The denominator of the first and second terms models suppression of PZFs growth by mean shear flows. The excitation and regulation of TZF is contained in Equation(7.39): the first term on the right hand side represents modulational excitation of TZF by finite paral-

lel(or toroidal) Reynolds stress motivated by second term of Equation(7.15) and its finiteness condition Equation(7.22). However, even if the this condition is not met in experiments the second term, coming from the other part of the toroidal Reynolds stress, the right hand side acts as a source term whose finiteness condition only requires parallel spectral asymmetry which can be naturally satisfied in a number of ways as mentioned above in section 5.2. The denominator is again to model the TZF suppression by mean shear flows. The third term represents TZF shear quenching due to turbulent toroidal momentum diffusion. The fourth term represents the neoclassical momentum diffusion. The Equation(7.40) is for mean pressure gradient evolution: the first term on the right hand side accounts for turbulent diffusion of mean pressure profile, the second term is for neoclassical transport and the third term represents input power. Equation(7.41) simply represents the radial force balance relation from the ion momentum equation. This model is an extension of the model proposed by Kim and Diamond[154, 155] and Diamond *etal*[157]. Self-consistent treatment of TZFs and PZFs coupled dynamics is what makes this model significantly different from the previous model.

Here, the input power Q controls the evolution of the system [Equations(7.37, 7.38, 7.39, 7.39, 7.40, 7.41)] for given parameters a_i , b_i , c_i , d_i , and e_i . With the increase of input power the mean pressure profile steepens leading to development of turbulence. Beyond a critical turbulence level decided by the neoclassical flow damping rate, the turbulence generates the PZF shear via modulational instability. Similarly TZF shear is excited beyond a critical turbulence amplitude determined by the neoclassical and turbulent damping rate for TZF shear. Once these zonal shears are excited they pull down turbulence level which in turn increases zonal flows shear. Thus turbulence and zonal flows (both TZF and PZF) form a self-regulating system. After a sufficiently long time and hence at sufficiently large Q , the turbulence and hence zonal flows are completely quenched transiting the system to a quiescent H mode where the slope of the profile is determined by the neoclassical transport,

$$\varepsilon = V'_{pzf} = V'_{tzf} = 0, \wp = Q/d_2 \quad (7.42)$$

We systematically explore the model numerically for linear power ramp $Q = 0.01t$ and the results are presented in Figs.(7.1 - 7.3) for different cases. First we consid-

ered the cases without zonal flows shear as shown in Fig.(7.1). Plots for turbulence intensity and pressure gradient shows that finite $E \times B$ shear causes early transition to quiescent H mode by reducing the threshold power. $E \times B$ shear increases with input power to respect radial force balance which in turn suppresses turbulence by enhancing the its decorrelation. After a sufficiently long time input power and so the $E \times B$ shear becomes so large that it completely quenches turbulence forcing the system into the quiescent state.

Then included PZF shear in the above picture with the same value of mean

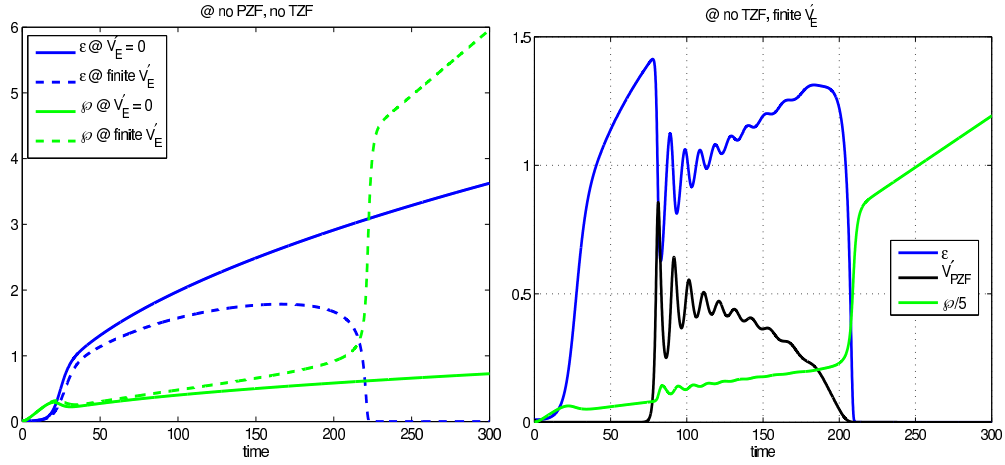


Figure 7.1: Parameters: Common: $a_1 = 0.2$, $a_2 = 0, 0.7$ (solid curves on left, otherwise), $a_3 = 0.0$, $a_4 = 0, 0.7$ (left, right), $a_5 = 0$, $b_1 = 0, 1$ (left, right), $b_{11} = 0, 1.5$ (left, right), $b_{12} = 0$, $b_2 = 1.0$, $b_3 = 0$, $b_4 = 0, 1$ (left, right), $c_1 = 0$, $c_{11} = 0.0$, $c_{12} = 0.0$, $c_2 = 0$, $c_3 = 0$, $c_4 = 0$, $c_5 = 0$, $d_1 = 1$, $d_2 = 0.5$, $e_1 = 1$, $e_2 = 0$, $V_{||}' = 0$, $m = 1$.

$E \times B$ shear (Fig.(7.1) right panel). Other parameters are shown in the caption of Fig.(7.1). It shows further reduction in the time for transition to H mode as expected from additional suppression of turbulence by zonal flows shear. However, the transition to H mode happens only via an oscillatory transient. This can be explained as follows. Increasing Q with time increases φ which grows ε which in turn excites V_{pzf}' at high enough turbulence level. But ε and φ damp by growing V_{pzf}' and ε respectively. This forms a self-regulating oscillatory system. Moreover, the net gradual rise of ε in the oscillatory phase is due to inhibition in growth of V_{pzf}' by mean shear flows. After a sufficiently long time $E \times B$ shear becomes so high that turbulence dies completely leading to death of PZF shear accompanied

by steep linear rise in pressure gradient.

Finally TZF shear V'_{tzf} is also considered in the above picture. The parameters

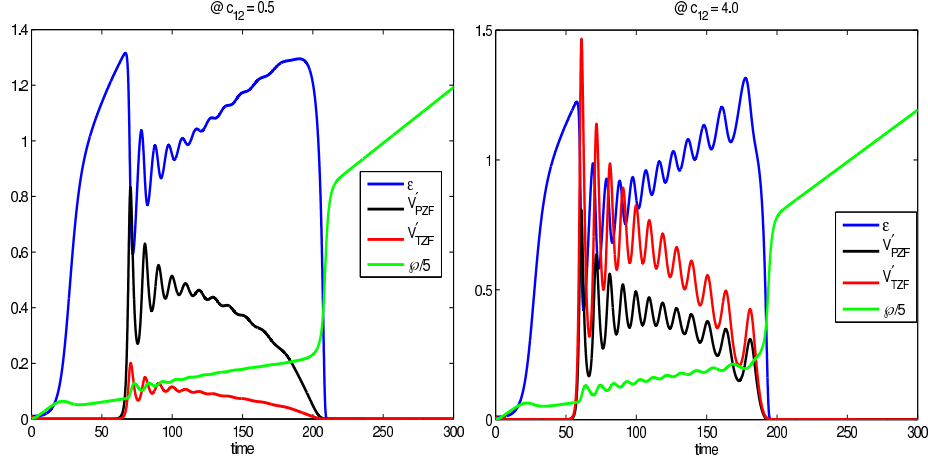


Figure 7.2: Parameters: $a_1 = 0.2$, $a_2 = 0.7$, $a_3 = 0.0$, $a_4 = 0.7$, $a_5 = 0.1$, $b_1 = 1$, $b_{11} = 1.5$, $b_{12} = 0.15$, $b_2 = 1.0$, $b_3 = 0$, $b_4 = 1$, $c_1 = 1$, $c_{11} = 0.01$, $c_{12} = 0.5$ (left panel), $c_{12} = 4.0$ (right panel), $c_2 = 1$, $c_3 = 0$, $c_4 = 1$, $c_5 = 0.5$, $d_1 = 1$, $d_2 = 0.5$, $e_1 = 1$, $e_2 = 0$, $V'_{||} = 0$, $m = 1$

are given in the caption of Fig.(7.2). In this composite picture the transition to the quiescent H mode also happens through transient oscillations in populations of different species, V'_{tzf} being an additional species here. For the chosen parameters the figure on the left shows early onset of the oscillatory region due to enhanced damping of turbulence by V'_{tzf} . V'_{tzf} is almost in the same phase as V'_{pzf} . This is due to this particular choice of parameters where $c_{11} \ll c_{12}$ for which the V'_{tzf} becomes proportional to V'_{pzf} . On increasing c_{12} to 4.0 in the right plot it is seen that the transient oscillations begin even earlier and the quiescent H mode is also achieved much earlier compared to the previous case. This is due to the fact that strong PZF→TZF coupling forces the TZF shear to grow quickly to very high levels causing strong damping of turbulence and hence reducing the threshold power.

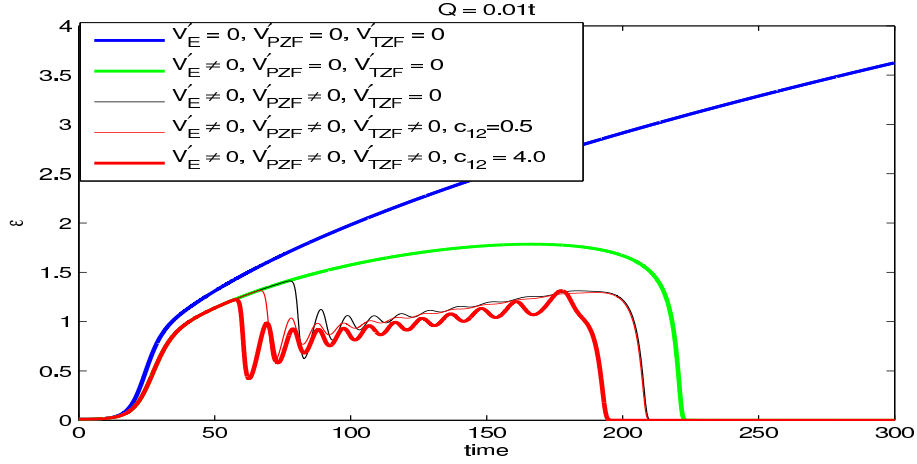


Figure 7.3: Turbulence intensity ε in different situations explained in the legend

7.5 Conclusions

We showed excitation of toroidal zonal flows by modulational decay instability of the background ion temperature gradient driven turbulence. Toroidal and poloidal zonal flow evolutions are found coupled via the nonlinear toroidal and poloidal Reynolds stresses. Two routes to this excitation are found. One is the direct and independent modulational excitation which requires following spectral properties of the background turbulence $-k_x \partial \langle N_k \rangle / \partial k_x > 0$ and $\langle k_y \rangle \neq 0$. If the later criterion is failed to get satisfied the external forcing by growing poloidal zonal flow shear provides the another route to toroidal zonal flows excitation. And this route requires $-k_x \partial \langle N_k \rangle / \partial k_x > 0$ and $\langle k_{\parallel} \rangle \neq 0$. While the first criterion is virtually satisfied in all experiments the second criterion requires various parallel symmetry breaking agents like mean $E \times B$ shear, up-down toroidal current asymmetry etc which are naturally present in most experimental conditions.

Then we considered the effect of mean poloidal and toroidal shear flows on zonal flows (both toroidal and poloidal) generation. It is found that, in weak shear limit, mean shear flows reduces the growth of zonal flows shear by enhancing the decorrelation of underlying mode propagation. Based on these observations an extended 0D model is proposed which contains the self-consistent dynamics of turbulence intensity, mean pressure gradient, mean $E \times B$ shear, mean toroidal flow shear, poloidal zonal flows and toroidal zonal flows as well. Self-consistent inclusion

of toroidal zonal flows dynamics is what creates a novel difference between this and the other models proposed so far. One of the main aspects of this new model is the linear coupling of toroidal and poloidal zonal flows via non-linear stresses. Different effects were included stepwise to explore the properties of this model. Retention of only mean $E \times B$ shear and no zonal flows shows that transition to quiescent H mode occurs early compared to the only self nonlinearity driven damping and saturation mechanism. Then inclusion of poloidal zonal flows shows that transition is triggered earlier lowering the critical input power. The transient in this case becomes oscillatory because of self-regulation of turbulence and poloidal zonal flows shear. Next inclusion of toroidal zonal flows shear and its coupling with poloidal zonal flows shear shows further reduction in critical input power for transition to the H mode. The critical input power goes down with increase of PZF→TZF coupling coefficient. Since this coupling is proportional to $\langle k_{\parallel} \rangle$, it means that the devices and regimes in which parallel spectral asymmetry is strong the threshold power will be less. This implies that the critical input power for L→H transition in a shaped equilibrium device ,where toroidal current is up-down asymmetric, will be less than in an up-down symmetric equilibrium provided other symmetry breakers are either absent or equally strong in both cases. In the next Chapter we study the stationary solutions of ITG-zonal flow sytem ignoring the parallel ion dynamics in the limit $\omega \gg k_{\parallel} c_s$ for simplicity.

Coherent non-linear structures in ITG-Zonal flows system

8.1 Introduction

Heat and particle transport in tokamak plasmas is dominantly governed by drift wave turbulence. Zonal flows are excited self-consistently via nonlinear turbulent Reynolds stresses in the drift wave turbulence which then back-react (causes induced diffusion in \vec{k} space) on the host turbulence causing it to saturate[157, 154, 155, 3, 158]. Zonal flows are defined as poloidal and toroidally symmetric ($q_\theta = q_z = 0$) potential perturbation with a finite radial scale q_r^{-1} significantly larger than the scale of underlying small scale turbulence, $q_r \ll k_r$, where \vec{q} is the wave vector of the zonal perturbations and \vec{k} is the wave vector of the background small scale turbulence. Such a renormalized weak turbulence theory [159] assumes 1) the separation in phase space velocities $\Delta(\Omega/q)$ of modulation (Ω and q correspond to frequency and radial wave number of modulation) is smaller than change in quasi-particles velocity $(\partial v_g / \partial k) \Delta k$, Δk being width of island in the phase for the quasi-particles orbit, so that island overlapping of resonances occurs. That is Chirikov parameter $\mathcal{S} = (\partial v_g / \partial k) \Delta k / \Delta(\Omega/q) > 1$. 2) the amplitude of modulation is so low that the quasi-particle trajectories are unperturbed. Alternatively this amounts to saying that the Kubo number $\mathcal{K} = \omega_b / \gamma < 1$ where ω_b is bounce frequency of the quasi-particle and $1/\gamma$ is its life time.

Such a renormalized weak turbulence theory is able to explain certain features of observed turbulence. However, numerical simulations and experiments show that

drift wave turbulence exhibits several non-Gaussian features like intermittency, bursty transport etc [67, 160, 68, 69, 70, 71]. These characteristics are related to the presence of coherent structures in the turbulence, and cannot be described by renormalized weak turbulence theories. Nonlinear coherent structure formation in simple drift wave zonal flow system has been studied by Kaw *et al*[72]. This chapter aims at describing the physics of nonlinear coherent structures in the coupled ion temperature gradient (ITG) driven turbulence and zonal flows.

The methodology used is quite similar to Kaw *et al*[72]. The short wave high frequency drift wave turbulence is treated as gas of quasi-particles which is described by the wave kinetic equation[161] for the wave action density N_k and the long scale zonal flow structures are described by an evolution equation for $m = n = 0$ component of the electrostatic potential Φ_q which is basically the flux surface averaged potential vorticity equation. The coupled equation for N_k and Φ_k shows trapping of quasi-particles in the effective potential trough generated by the zonal flow profile in strong turbulence regime $\mathcal{K} \gg 1$ but $\mathcal{S} \ll 1$. This leads to possibility of coherent structures which can be described in the form of BGK waves[65]. Reynold stresses offered by the trapped and untrapped ITG waves act in synergy to generate novel coherent structures like solitons, shocks and nonlinear wave trains in the zonal flow field in the strongly turbulent state.

8.2 Basic turbulence equations

We start with the nonlinear fluid equations for ion density perturbation n_i and ion temperature perturbation T describing the background toroidal ITG turbulence[143]

$$\begin{aligned} & \frac{\partial n_i}{\partial t} + \frac{\partial \phi}{\partial y} - \varepsilon_n \frac{\partial}{\partial y} (\phi + p_i) - \left(\frac{\partial}{\partial t} - K_i \frac{\partial}{\partial y} \right) \nabla_{\perp}^2 \phi \\ & + [\phi, n] - [\phi + p, \nabla_{\perp}^2 \phi] - \left[\frac{\partial p}{\partial x}, \frac{\partial \phi}{\partial x} \right] - \left[\frac{\partial p}{\partial y}, \frac{\partial \phi}{\partial y} \right] = 0 \end{aligned} \quad (8.1)$$

Temperature perturbation equation

$$\left(\frac{\partial}{\partial t} - \frac{5}{3} \tau_i \varepsilon_n \frac{\partial}{\partial y} \right) T + \left(\eta_i - \frac{2}{3} \right) \frac{\partial \phi}{\partial y} - \frac{2}{3} \frac{\partial n_i}{\partial t} + [\phi, T - \frac{2}{3} n_i] = 0 \quad (8.2)$$

Adiabatic electron response

$$n_e = \phi - \Phi_{ZF} \quad (8.3)$$

Quasi-neutrality

$$n_e = n_i \quad (8.4)$$

The parallel ion motion is neglected under the assumption of $\omega > k_{\parallel} c_s$. Here mixing length normalization has been used for the fluctuating quantities

$$(\phi, n_i, p) = (e\delta\phi/T_{0e}, \delta n_i/n_0, \tau_i \delta p_i/P_0) L_n/\rho_s.$$

The space-time coordinates are normalized as $x = (x - x_0)/\rho_s$, $y = y/\rho_s$, $z = z/L_n$, $t = tc_s/L_n$. And the non-dimensional parameters are $\eta_i = L_n/L_T$, $K = \tau_i(1 + \eta_i)$, $\tau_i = T_{0i}/T_{0e}$, $\epsilon_n = 2L_n/R$.

Mode energetics: Defining

$$E_{\phi} = \frac{1}{2} \int d^3x (|\phi|^2 + |\nabla_{\perp} \phi|^2) \quad (8.5)$$

and

$$E_T = \frac{3\tau_i}{2(1 + \tau_i)} \frac{1}{2} \int d^3x |T|^2 \quad (8.6)$$

it is easy to show that

$$\partial_t (E_{\phi} + E_T) = \frac{3\tau_i}{2(1 + \tau_i)} \eta_i \int d^3x T (-\partial_y \phi) \quad (8.7)$$

where we have used the identity $\int d^3x f[f, g] = 0$. This shows that the energy of the system grows as the electrostatic turbulent flux $Q_{ES} = \int d^3x T (-\partial_y \phi)$ draws energy from the mean gradients. Linearizing Equations(8.1, 8.2) and using the adiabaticity Equation(8.3) and the quasi-neutrality Equation(8.4) and eliminating ϕ and T yields the dispersion relation

$$\begin{aligned} \omega^2 (1 + k_{\perp}^2) - \omega k_y \left(1 - \left(1 + \frac{10\tau_i}{3} \right) \epsilon_n - k_{\perp}^2 \left(K + \frac{5}{3} \tau_i \epsilon_n \right) \right) \\ + \tau_i \epsilon_n k_y^2 \left(\eta_i - \frac{7}{3} + \frac{5}{3} (1 + \tau_i) \epsilon_n + \frac{5}{3} K k_y^2 \right) = 0 \end{aligned} \quad (8.8)$$

The unstable root $\omega = \omega_r + i\gamma$ from Equation(8.8) is

$$\omega_r = \frac{k_y}{2(1+k_\perp^2)} \left(1 - \left(1 + \frac{10\tau_i}{3} \right) \epsilon_n - k_\perp^2 \left(K + \frac{5}{3}\tau_i\epsilon_n \right) \right) \quad (8.9)$$

$$\gamma = \frac{|k_y|}{1+k_\perp^2} \sqrt{\tau_i\epsilon_n (\eta_i - \eta_{th})} \quad (8.10)$$

where the threshold η for the instability is given by

$$\eta_{th} \approx \frac{2}{3} - \frac{1}{2\tau} + \frac{1}{4\tau\epsilon_n} + \epsilon_n \left(\frac{1}{4\tau} + \frac{10\tau}{9} \right) \quad (8.11)$$

The effect of finite larmor radius has been neglected in obtaining the linear stability threshold while the same has been retained in the real frequency estimation as it is important for determination of dispersive effects. By taking fourier transform of Equation(8.2) the fourier amplitudes T_k and ϕ_k are related by

$$T_k = \delta_k \phi_k \quad (8.12)$$

where

$$\delta_k = \frac{\nabla_1 + i2\gamma_k/3}{\nabla_2 + i\gamma_k} \quad (8.13)$$

Here

$$\nabla_1 = \left(\eta_i - \frac{2}{3} \right) k_y + \frac{2}{3}\omega_r \quad (8.14)$$

and

$$\nabla_2 = \omega_r + \frac{5}{3}\tau_i\epsilon_n k_y \quad (8.15)$$

By using Equations(8.9) and (8.10) one can show that δ_k is independent of k up to order k_\perp^2 . In the long wavelength limit $k_\perp^2 < 1$ the real frequency can be expressed as

$$\omega_r = k_y (a - bk_\perp^2) \quad (8.16)$$

where

$$a = \frac{1}{2} \left[1 - \left(1 + \frac{10\tau_i}{3} \right) \epsilon_n \right] \quad (8.17)$$

and

$$b = \frac{1}{2} \left[1 + K - \left(1 + \frac{5}{3} \tau_i \right) \epsilon_n \right] \quad (8.18)$$

and hence the radial group velocity becomes

$$v_{gr} \approx -2k_x k_y b \quad (8.19)$$

Defining $W_* = 3\tau_i |\delta_k|^2 / (2(1 + \tau_i))$ the mode energy density ϵ_k can be obtained from Equations(8.5) and (8.6)

$$\epsilon_k = (1 + k_\perp^2 + W_*) |\phi_k|^2 \quad (8.20)$$

and so the wave action density becomes

$$N_k = \frac{1 + k_\perp^2 + W_*}{a - b k_\perp^2} |\phi_k|^2 \quad (8.21)$$

8.3 Zonal mode equations

The zonal mode equations are obtained by appropriate space-time averaging of the basic turbulence equations. Zonal modes are $m = 0$, $n = 0$ or $k_y = k_z = 0$ but radial wavenumber $q_x \neq 0$ mode in turbulence. So the evolution equations for the zonal perturbations can be obtained from the flux surface averaged vorticity equation $\langle \vec{\nabla} \cdot \vec{J} \rangle = 0$ and the flux surface averaged temperature equation[63].

$$\partial_t \nabla_x^2 \Phi_{ZF} = - (1 + \tau_i) \langle [\phi, \nabla_\perp^2 \phi] \rangle - \tau_i \langle [T, \nabla_\perp^2 \phi] \rangle + \tau_i \langle [\partial_i \phi, \partial_i T] \rangle \quad (8.22)$$

$$\partial_t T_{ZF} = - \langle [\phi, T] \rangle \quad (8.23)$$

Since

$$\langle [T, \nabla_{\perp}^2 \phi] \rangle = -\nabla_X^2 \langle \partial_y T \partial_x \phi \rangle - \langle [\partial_i T, \partial_i \phi] \rangle \quad (8.24)$$

and

$$\langle [\phi, \nabla_{\perp}^2 \phi] \rangle = -\nabla_X^2 \langle \partial_y \phi \partial_x \phi \rangle \quad (8.25)$$

and for arbitrary f and g using

$$\langle fg \rangle = Re \int d\vec{k} f_{\vec{k}} g_{\vec{k}}^* \quad (8.26)$$

the Equations(8.22) and (8.23) can be expressed as

$$\partial_t \nabla_X^2 \Phi_{ZF} = \nabla_X^2 Re \int d\vec{k} k_y k_x (1 + \tau_i + \delta_k \tau_i) |\phi_k|^2 \quad (8.27)$$

$$\partial_t T_{ZF} = -\nabla_X Re \int d\vec{k} i k_y \delta_k |\phi_k|^2 \quad (8.28)$$

In a coexisting system of ITG turbulence and zonal flow the modulations of microscale fields by mesoscale zonal flows conserve wave action density $N_k = \varepsilon_k / \omega_{r,k}$ where ε_k is the energy density of the k th mode with real frequency $\omega_{r,k}$. The action density has the generic form $N_k = N_k(|\phi_k|^2, |T|^2)$ which by using the linear fourier amplitude relations can be cast in the form $N_k = N_k(|\phi_k|^2)$. Then the modulated non-linear drivers can be expressed as a function of N_k via $\delta|\phi_k|^2 = C_k \delta N_k$. From Equation(8.21) the coefficient C_k can be obtained as

$$C_k = \frac{a - b k_{\perp}^2}{1 + k_{\perp}^2 + W_*} \quad (8.29)$$

The wave kinetic equation is used to describe the evolution of N_k in the presence of mean flows[162].

$$\frac{\partial N_k}{\partial t} + \frac{\partial \omega_{r,k}}{\partial \vec{k}} \cdot \frac{\partial N_k}{\partial \vec{X}} - \frac{\partial \omega_{r,k}}{\partial \vec{X}} \cdot \frac{\partial N_k}{\partial \vec{k}} = \gamma_k N_k - \Delta \omega N_k^2 \quad (8.30)$$

where $\omega_{r,k}$ and γ_k are respectively the real frequency and growth rate of the underlying turbulence in the presence of the slowly varying mesoscale zonal fields. The first term on the right hand side is the linear growth of the turbulence and the second term is the pull back due to nonlinear interactions. We assume the equilibrium as state of stationary turbulence. This allow us to find the equilibrium turbulence spectrum $\langle N_k \rangle$ by letting the right hand side of Equation(8.30) to vanish i.e., $\gamma_k \langle N_k \rangle - \Delta\omega \langle N_k \rangle^2 = 0$. To study the stability of such an equilibrium we can make Chapman-Enskog expansion of N_k ; $N_k = \langle N_k \rangle + \delta N_k$, where $\langle N_k \rangle$ is the slowly varying “mean” wave action density, and δN_k is the coherent perturbation to it induced by gradients of $\langle N_k \rangle$ in radius \vec{X} and \vec{k} . The linearized wave kinetic equation takes for δN_k can be written as

$$\left(\frac{\partial}{\partial t} + \vec{v}_g \cdot \frac{\partial}{\partial \vec{X}} + \gamma_k \right) \delta N_k = \frac{\partial \delta \omega_{r,k}}{\partial \vec{X}} \cdot \frac{\partial \langle N_k \rangle}{\partial \vec{k}} + \delta \gamma_k \langle N_k \rangle \quad (8.31)$$

Assuming $\Psi = \Psi_q \exp(-i\Omega t + q_X X)$ for $\Psi = (\delta N_k, \Phi_{ZF}, T_{ZF})$ the wave kinetic Equation(8.31) yields

$$\delta N_{k,q} = R_{k,q} \left[\frac{\partial \delta \omega_{r,k}}{\partial \vec{X}} \cdot \frac{\partial \langle N_k \rangle}{\partial \vec{k}} + \delta \gamma_k \langle N_k \rangle \right] \quad (8.32)$$

where the propagator $R_{k,q}$ is given by

$$R_{k,q} = \frac{i}{(\Omega_q - \vec{q} \cdot \vec{v}_g + i\gamma_k)} \quad (8.33)$$

The zonal flow being a mesoscale mode will convect the fast microturbulence modes. This effect is captured via $\partial_t \longrightarrow \partial_t + [\langle \phi \rangle, \]$. Then, in general

$$\begin{aligned} \delta \omega_{r,k} &= \frac{\delta \omega_r}{\delta \eta_i} \delta \eta_i + \vec{k}_\perp \cdot \langle V \rangle_{E \times B} \\ &= \frac{k_y k_\perp^2 \tau_i}{2(1 + k_\perp^2)} \nabla_X T_{ZF} + k_y \nabla_X (1 + \tau_i \nabla_X^2) \Phi_{ZF} \end{aligned} \quad (8.34)$$

Here the first term represents the frequency modulation due to modulation in η_i by zonal temperature perturbations T_{ZF} and the second term represents the frequency modulation due to zonal potential perturbations Φ_{ZF} . The modulation in growth

rate is given by the modulation in η_i by zonal temperature perturbations T_{ZF}

$$\delta\gamma_k = \frac{\partial\gamma_k}{\partial\eta_i}\delta\eta_i = -\frac{|k_y|}{4} \left(\frac{\epsilon_n\tau_i}{\eta_i - \eta_{th}} \right)^{1/2} \nabla_X T_{ZF} \quad (8.35)$$

Using Equations(8.34, 8.35) and ignoring the turbulent FLR effects but retaining the FLR effect for the mesoscale field yields

$$\delta N_{k,q} = R_{k,q} \left[-k_y \bar{q}^2 \Phi_q \frac{\partial \langle N_k \rangle}{\partial k_x} - i|k_y| W_\eta q T_q \langle N_k \rangle \right] \quad (8.36)$$

where $\bar{q}^2 = q^2(1 - \tau_i q^2)$ and $W_\eta = \sqrt{\epsilon_n \tau_i / (\eta_i - \eta_{th})} / 4$. Finally, using Equation(8.36) the zonal flow Equations(8.27, 8.28) takes the form

$$\partial_t \Phi_q = Re \int d\vec{k} k_y k_x (1 + \tau_i + \delta_k \tau_i) C_k R_{k,q} \left[-k_y \bar{q}^2 \Phi_q \frac{\partial \langle N_k \rangle}{\partial k_x} - i|k_y| W_\eta q T_q \langle N_k \rangle \right] \quad (8.37)$$

$$\partial_t T_q = q Re \int d\vec{k} k_y \delta_k C_k R_{k,q} \left[-k_y \bar{q}^2 \Phi_q \frac{\partial \langle N_k \rangle}{\partial k_x} - i|k_y| W_\eta q T_q \langle N_k \rangle \right] \quad (8.38)$$

Now using the \vec{k} symmetry properties of δ_k it is easy to verify that the cross coupling terms survive iff $\langle k_x \rangle \neq 0$, where $\langle k_x \rangle = \int d\vec{k} k_x N_k / \int d\vec{k} N_k$ is spectrally averaged k_x . In case $\langle k_x \rangle = 0$ the zonal potential and zonal temperature is excited independently. Note that the independent zonal potential excitation criterion is $-k_x \partial \langle N_k \rangle / \partial k_x > 0$ while any kind of spectrum can excite zonal temperature.

8.4 Coherent structures: Stationary solutions

We now look for non-linear coherent stationary structure which are exact solutions of Equations(8.27, 8.28, 8.30) when modulational instability have already saturated. We seek stationary solutions in the absence of source and sink ($\gamma_k = \Delta\omega_k = 0$) in a frame moving with velocity U . Then we may replace $\partial_t \rightarrow -U\partial_X$.

Defining zonal flow velocity as $v = \nabla_X \Phi_{ZF}$, we can write

$$(v_{gx} - U) \nabla_X N_k - \nabla_X \omega_{r,k} \frac{\partial N_k}{\partial k_x} = 0 \quad (8.39)$$

$$(\mu \nabla_X^2 - \nu) v + U \nabla_X v = -\nabla_X \int d\vec{k} k_y k_x (1 + \tau_i + Re \delta_k \tau_i) C_k N_k \quad (8.40)$$

Here μ is viscous damping coefficient and ν represents neoclassical flow damping. The Equation(8.39) conserves N_k along the characteristic given by

$$\frac{dk_x}{dx} = -\frac{k_y (d/dx) (v + \tau_i v'')}{v_{gx} - U}, \quad \frac{dk_y}{dx} = 0 \quad (8.41)$$

Equation(8.41) can be readily integrated to give the constant of motion W

$$W = -k_y (v + \tau_i v'') + b k_y k_x^2 + k_x U, \quad k_y = k_{y0} \quad (8.42)$$

This suggests an exact solution to Equation(8.39) in the form

$$N_k(k_x, k_y, x) \equiv N_k(W(k_x, x), k_y) \quad (8.43)$$

W is physically interpreted as frequency of the ITG mode as seen from a frame moving radially with velocity U including the Doppler shift effect due to zonal flow velocity perturbations. While passing regions of different v and v'' the k_x of the mode change in such a way as to keep k_y and Ω constant. The Equation(8.42) can be expressed as

$$\bar{W} = K_x^2 + f(x) \quad (8.44)$$

where $\bar{W} = W/(b k_y)$, $K_x = k_x + \bar{U}$ and $f(x) = -(\bar{U}/2)^2 - (v + \tau_i v'')/b$ and $\bar{U} = U/(b k_y)$. Since here \vec{k} acts like \vec{v} in the Liouville equation for particle probability distribution function the Equation(8.44) can be interpreted as a sum of kinetic (first term) and potential (second term) energies giving the total energy \bar{W} as the constant of motion. Now if profile of the potential function $f(x)$ is such that it has minima and maxima (f_m) then a part of drift wave population satisfying

$\bar{W} < f_m$ will get trapped around the position corresponding to the minimum of the effective potential. Another part satisfying $\bar{W} > f_m$ will remain untrapped. The characteristic ray equations can be written as

$$\frac{dx}{dt} = -2k_x k_y b \quad (8.45)$$

$$\frac{dk_x}{dt} = -k_y \frac{d}{dx} (v + \tau_i v'') \quad (8.46)$$

$$\frac{dk_y}{dt} = 0 \quad (8.47)$$

Using Equation(8.45) the equation of motion for k_x can be written as

$$\frac{d^2 k_x}{dt^2} = 2k_y^2 b \left(\frac{d^2 v}{dx^2} + \tau_i \frac{d^4 v}{dx^4} \right) k_x \quad (8.48)$$

Equation(8.48) possesses oscillatory solution when $v'' + \tau_i v'''' < 0$

$$k_x = k_{x0} \cos(\omega_b t) \quad (8.49)$$

where the quasi-particle bounce frequency ω_b is given by

$$\omega_b = \sqrt{-2k_y^2 b (v'' + \tau_i v'''')} \quad (8.50)$$

For a monochromatic zonal flow profile $v = v_0 \cos(qx)$ the drift wave quasi-particles will get trapped in the crests of zonal flow field. Near the crest the bounce frequency would be given by

$$\omega_b = \sqrt{2k_y^2 b \bar{q}^2 v_0} \quad (8.51)$$

One can also arrive at the same conclusions by looking at the equation of motion in x . How trapping happens in the zonal flow crests can be understood as follows. As the ITG quanta rolls down the zonal flow shear layer from its maximum it losses its k_x or x - momentum due to restoring force offered by radially inward group velocity. Eventually k_x^2 becomes zero and the quasi-particle gets reflected, getting

trapped in the crest. This can also be convinced from the phase space plot of (x, k_x) , shown in Fig.(8.1), obtained from numerical solutions of Equations(8.45) and (8.46) for cosine and sine zonal flow profiles which clearly shows trapped and passing trajectories.

So once we realized the existence of trapped and untrapped quasi-particles pop-

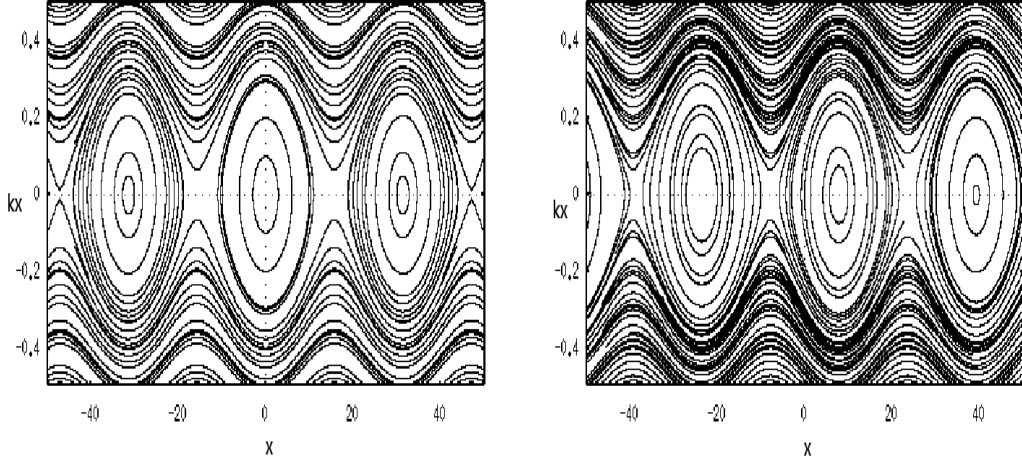


Figure 8.1: k_x vs x when $v = v_0 \cos(qx)$ (left) and when $v = v_0 \sin(qx)$ (right) with $\tau = 1$, $\epsilon_n = 0.7$, $k_y = 0.2$, $v_0 = 0.1$, $q = 0.2$.

ulation densities the solution for stationary Equations(8.39) and (8.40) can be obtained by solving the self-consistency condition:

$$\begin{aligned} & (\mu \nabla_x^2 - \nu + U \nabla_x) v = -\frac{1}{4} (1 + \tau_i + \text{Re} \delta_k \tau_i) \\ & \times \nabla_x \int_{-\infty}^{+\infty} dk_y^2 \left\{ \int_{f_m}^{\infty} d\bar{W} J N_U(\bar{W}, k_y) + \int_f^{f_m} d\bar{W} J N_T(\bar{W}, k_y) \right\} \end{aligned} \quad (8.52)$$

where N_U and N_T are the action densities for the trapped and untrapped part of the stationary drift wave turbulence and J is the Jacobian of transformation from k_x to \bar{W} given by

$$J = \frac{\left(1 - \bar{U} (\bar{W} - f)^{-1/2}\right) \left(a - b k_y^2 - b \left((\bar{W} - f)^{1/2} - \bar{U}\right)^2\right)}{1 + W_* + k_y^2 + \left((\bar{W} - f)^{1/2} - \bar{U}\right)^2} \quad (8.53)$$

The nonlinearity in Equation(8.52) is coming from the dependence of right hand side term on f which in turn is determined by the choice of trapped and untrapped action densities $N_{T,U}$. To figure out the nature of nonlinear structures supported by Equation(8.52) we make following choices of N_T and N_U

$$\frac{N_U}{N_{0U}} = \left[1 + \left(\frac{\bar{W} - f_m}{\Delta} \right)^2 \right]^{-1} \delta(k_y - k_{0y}), \quad \bar{W} > f_m \quad (8.54)$$

$$\frac{N_T}{N_{0T}} = \left[1 + \epsilon \left(\frac{f_m - \bar{W}}{\Delta} \right)^{1/2} \right] \delta(k_y - k_{0y}), \quad f < \bar{W} < f_m \quad (8.55)$$

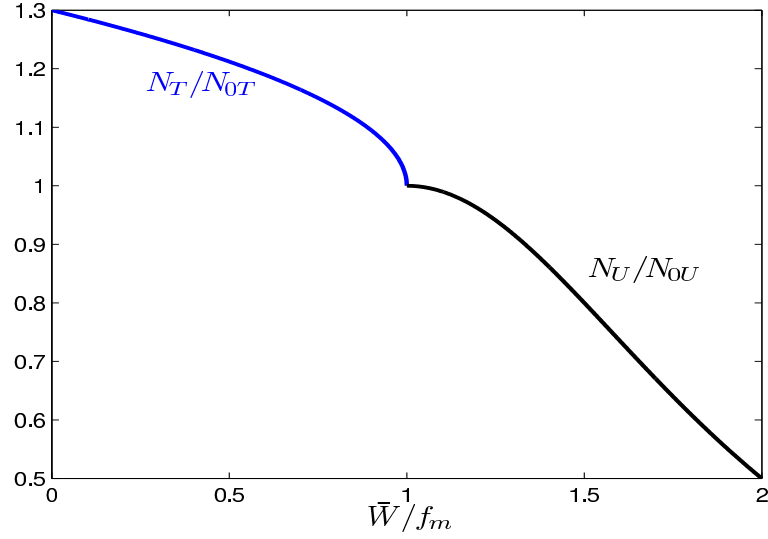


Figure 8.2: Population distributions of trapped and untrapped waves for $\epsilon = 0.3$, $\Delta/f_m = 1.0$

The two distributions are chosen to be continuous at $f = f_m$, as shown in Fig.(8.2). The monochromatic k_y spectrum might appear an extreme idealization, it safely captures the asymmetry in mode propagation direction in poloidal direction. It is extremely difficult to evaluate the integrals on the right hand side of Equation(8.52) with the Jacobian given by Equation(8.53). Hence some sensible simplifications are desirable. Assuming $k_\perp^2 < 1$ and $v_{gx} > U$ and expanding the J up to k_\perp^2 allows us to write

$$J = \frac{a}{1 + W_*} [1 - \bar{b}k_y^2 - \bar{b}(\bar{W} - f)] \quad (8.56)$$

where $\bar{b} = b/a + 1/(1 + W_*)$. Using this Jacobian the trapped and untrapped integrals in Equation(8.52) are evaluated in the appendixB which yields

$$(\mu \nabla_x^2 - \nu + U \nabla_x) v = -\nabla_x \left[\alpha (f_m - f) + \beta (f_m - f)^{3/2} + \alpha_1 (f_m - f)^2 + \beta_1 (f_m - f)^{5/2} \right] \quad (8.57)$$

where $f_m - f = (v - v_{min} + \tau_i(v'' - v''_{min}))/b$ since maximum of f corresponds to minimum of v and

$$\alpha = \bar{a}(N_{0T}\Delta(1 - \bar{b}k_{y0}^2) - N_{0U}\Delta\bar{b}\pi/2)/2 \quad (8.58)$$

$$\beta = \bar{a}N_{0T}\Delta\epsilon(1 - \bar{b}k_{y0}^2)/3 \quad (8.59)$$

$$\alpha_1 = \bar{a}N_{0T}\Delta\bar{b}(\Delta/2 - 1)/2 \quad (8.60)$$

$$\beta_1 = \bar{a}N_{0T}\Delta\epsilon\bar{b}(2\Delta/5 - 2/3) \quad (8.61)$$

Here $\bar{a} = (1 + \tau_i + Re\delta_k\tau_i)(ak_{y0})/(1 + W_*)$. Coefficients containing $N_{0T}(N_{0U})$ corresponds to contributions from trapped(untrapped) waves.

Now in the following the Equation(8.57) is investigated in different limits. First taking fourier transform in x of the linearized equation gives the dispersion relation $U = -\alpha(1 - \tau_i q^2)/b$. Since α is made of Reynolds stresses both from trapped and untrapped wave contributions this indicates that coupling to trapped and untrapped waves converts the zonal flow perturbations into radially propagating dispersive waves. Here no growth term appears because the resonant waves leading to modulational excitation of zonal flows has already been trapped in the large amplitude zonal flows at saturation. The structure of the nonlinear stationary state is determined by the nonlinear trapped wave contributions i.e., the terms with β , α_1 and β_1 in Equation(8.57). Neglecting ν and retaining terms up to order 3/2 Equation(8.57) becomes

$$V'' + \bar{\mu}V' - \kappa V + \bar{\beta}V^{3/2} = 0 \quad (8.62)$$

where $V = v - v_{min}$, $\bar{\mu} = \mu/(\alpha\tau_i)$, $\kappa = -(U + \alpha/b)/(\alpha\tau_i)$, $\bar{\beta} = \beta/(\alpha\tau_i b^{3/2})$. Note that the $V^{3/2}$ nonlinearity arises due to trapped wave population which vanish at low zonal flow amplitudes. We now obtain the solutions for Equation(8.62) in various limits. For $\bar{\mu} = 0$ and defining $\xi = x - Ut$, Equation(8.62) gives the

quadrature

$$\frac{1}{2} \left(\frac{dV}{d\xi} \right)^2 + \Psi(V) = \text{const.} \quad (8.63)$$

where the effective potential is given by

$$\Psi(V) = -\kappa \frac{V^2}{2} + \frac{2}{5} \bar{\beta} V^{5/2} \quad (8.64)$$

Such a pseudo-potential will have a minimum iff $\kappa > 0$ or $Ub + \alpha < 0$ which is

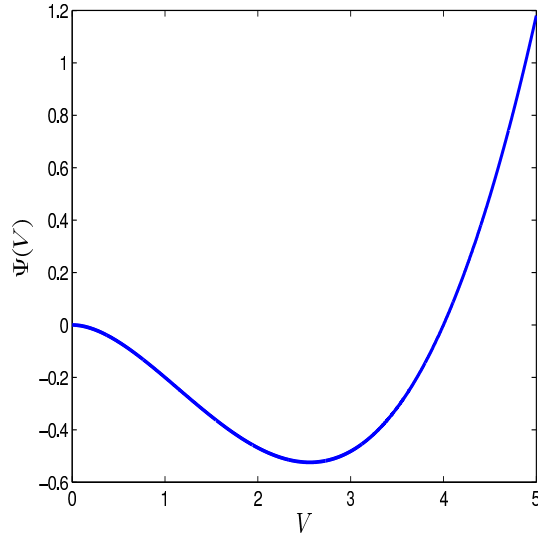


Figure 8.3: Sketch of Sagdeev Potential for $\kappa = 0.8$ and $\bar{\beta} = 0.5$

important for coherent structure formation. A schematic of the Sagdeev pseudo-potential is shown in Fig.(8.3). A pseudo-particle starting at $V > 0$ will oscillate back and forth in the well with a frequency dependent on the amplitude of oscillations. In real space this situation corresponds to a nonlinear periodic zonal flow V wave train propagating in x with speed U and having spatial period dependent on amplitude. As the initial V approaches zero the amplitude as well as the period of the nonlinear wave increases. As V starts from zero, the period is infinite and we get a solitary pulse or soliton. In such a case an exact soliton solution can be

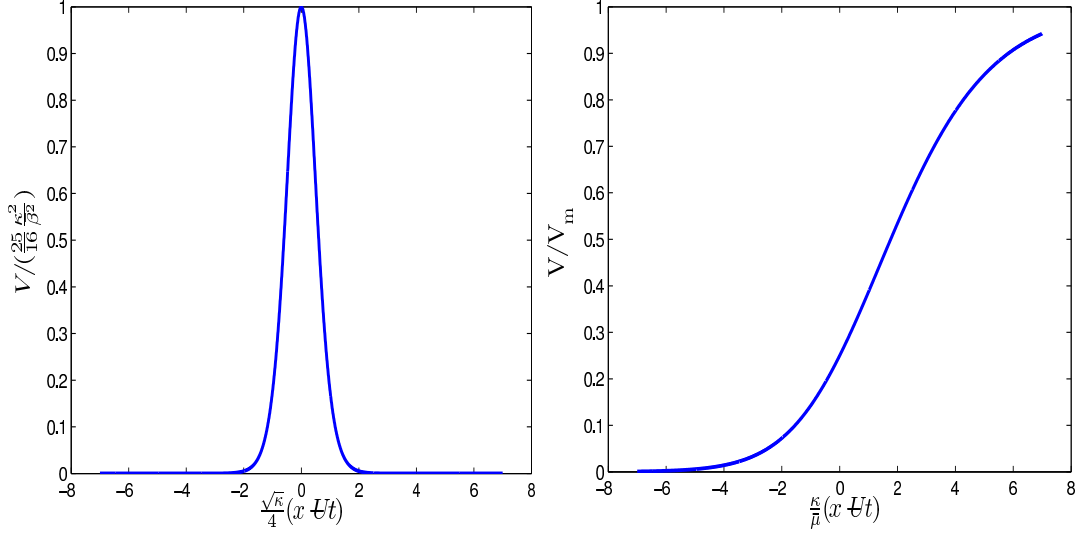


Figure 8.4: Left: Zonal flow soliton. Right: Zonal flow shock

written as

$$V = \frac{25}{16} \frac{\kappa^2}{\bar{\beta}^2} \text{sech}^4 \left[\frac{\sqrt{\kappa}}{4} (x - Ut) \right] \quad (8.65)$$

This soliton structure is a back to back zonal velocity shear layer, as shown in left panel of Fig.(8.4), with a significant fraction of ITG quasi-particles trapped between them and held together by Reynolds stresses offered by a background population of untrapped quasi-particles and propagating radially in(out), due to coupling between trapped and untrapped quasi-particle populations, when a/b is $+ve(-ve)$. Now with dissipative terms retained the pseudo-particle suffers a damped oscillation in the pseudo-potential and eventually settles down at the minimum value $V_m = \kappa^4/\bar{\beta}^2$. This corresponds to a shock like structure in zonal flow field $V(\xi)$, see right panel of Fig.(8.4), with V going from 0 to V_m after oscillating a few times around the final value. For large damping rate, there is no ringing and the shock solution goes monotonically from 0 to V_m . If the dominant dissipation is from viscosity ($\nu = 0$, μ large) then a shock solution can be obtained as

$$V = V_m \left[\frac{\exp(\kappa(x - Ut)/\bar{\mu})}{(1 + \exp(\kappa(x - Ut)/2\bar{\mu}))^2} \right] \quad (8.66)$$

8.5 Conclusions

Motivated by the non-Gaussian and intermittent character of observed turbulence, we studied the possibility of coherent structures formation in zonal flow field, such as nonlinear wave train, solitons and shocks, in ion temperature gradient driven turbulence in tokamaks in strongly nonlinear regime. The basic methodology employed is to look for stationary solutions for the coupled set of equations describing ITG turbulence (without source and sink) and zonal flows. The major findings in this chapter are:

- ITG quasi-particles get trapped in the “effective potential well” formed by the zonal flow profile which actually corresponds to the -ve flow curvature regions. The trapping happens when $\nu < \gamma_q < \omega_b$ where ν is collisionality, γ_q is the growth rate of the modulational instability and ω_b is the typical bounce frequency of the ITG quanta in the modulation envelope.
- When trapping is important a variety of radially propagating structures such as periodic nonlinear wave-trains, solitons and shocks in the zonal flow field may appear. These solutions in fact represent alternate saturated states of zonal flow generated via the modulational instabilities of the ITG turbulence. In this highly nonlinear regime coherence and quasi-particle trapping is dominant while the usual saturated states (when $\mathcal{K} < 1$ and $\mathcal{S} > 1$) are dominated by stochastic quasi-particle motion and diffusion in phase space[159].

Some of the limitations of the present analysis are: a) Stationary solutions were obtained only for zonal potential assuming Bohm-Gross like stationary distribution function for the wave action density in k_x and delta distribution in k_y . b) It is also assumed that the linear coupling of zonal potential and zonal temperature arising via the nonlinear stresses is weak so that the zonal potential and zonal temperature evolution equations can be effectively decoupled. Improving over these limitations and looking for stationary solutions for zonal temperature self-consistently and stability of the stationary states are left as a future challenging task.

9

Conclusions

In this thesis few aspects of anomalous momentum transport in ion temperature gradient driven microturbulence in tokamaks have been studied. Motivated by increasing number of experimental evidences of external torque free intrinsic toroidal and poloidal rotation studies on toroidal and poloidal momentum/velocity transport have been carried out in normal and reverse shear configuration. Most of the analytical calculations have been done in sheared slab geometry. Residual stress/flux is identified as driver of intrinsic rotation. Several mechanisms for generation of residual stress have been obtained. Electromagnetic effects on zonal flow generation have been looked and possibility of excitation of zonal like toroidal flows have been studied via modulational instability mechanism using wave kinetics method. And finally possibility of coherent structures in the modulation envelope of zonal flows have been investigated as stationary solutions of toroidal ITG turbulence-zonal flows system of equations.

9.1 Summary

Reynolds stress, from the view point of mean field theory, has been shown to be consist of diffusive, pinch and residual components. Parallel residual stress is generated by $E \times B$ shear via k_{\parallel} symmetry breaking and poloidal residual stress is generated by V'_{\parallel} via k_r symmetry breaking. k_{\parallel} symmetry breaking arise due to radial eigenmode shift off the rational surface by $E \times B$ shear. This causes exchange of roles of diffusive and non diffusive components in the poloidal and parallel stresses leading to their coupling. This causes coupling of toroidal and poloidal intrinsic

flows. Polarization drift assisted parallel residual stress is generated by $\langle k_{\parallel} k_x \rangle$ symmetry breaking which does not require radial asymmetry of the eigenmode. However nominally in drift wave ordering parallel polarization stress is one order higher in ρ_s^* compared to fluctuating $E \times B$ drift assisted k_{\parallel} symmetry breaking induced parallel residual stress. Relative to fluctuating $E \times B$ drift assisted parallel residual stress the strength of polarization drift assisted parallel residual stress is dominant in the low temperature gradient regions. No poloidal polarization stress exist.

Density gradient as ρ_s^* effect generates parallel residual stress which is of the same order of parallel polarization stress, may become comparable to $E \times B$ shear driven parallel residual stress in small L_n region, can also overtake the turbulence intensity gradient driven parallel residual stress in strong density gradient region whereas the later one is dominant in the strong profile curvature region.

Radial asymmetry of the eigenmode is not a necessary condition for the survival of residual parallel stress at q_{min} . That is $\langle k_{\parallel} \rangle \neq 0$ and $\langle Re k_x \rangle \neq 0$ even for symmetric eigenfunction leading to spontaneous toroidal and poloidal flow generation at q_{min} .

Linear gyrokinetic flux tube simulations for parallel momentum transport in the ITG turbulence reveals the following. k_y spectrum of linear growth rates maximized over all ballooning angles show a short wavelength branch which dies out near marginal temperature gradients. Finite ballooning angle θ_0 breaks eigenmode symmetry about the LFS mid plane and generates a parallel residual stress which reverses sign with θ_0 . This could have important implications for toroidal flow reversal in situations in which θ_0 naturally changes sign such as ITG to TEM transition with increasing density gradient. Nonlinear simulations with background macroscopic $E \times B$ shear shows parallel residual stress generation by symmetry breaking of the eigenmode about the LFS mid plane. Parallel residual increases with $E \times B$ rate at small values of $E \times B$ but starts to roll over at larger values of $E \times B$ rates because turbulence stabilization takes over symmetry breaking mechanism. Nonlinear simulations shows spatially local and temporally non-local 2d cross correlations between the self-consistent zonal flow shear and parallel residual stress. However the volume averaged stress is found to vanish when background $E \times B$ shear is absent. Parallel residual flux and heat flux are correlated when $E \times B$ shear is finite, indicating coupling of the two transport channels.

Study of electromagnetic effects on zonal flow generation in toroidal ITG turbulence show that near marginality the ratio γ_{ZF}/γ_{ITG} increases with β whereas for larger η_i the zonal flow drive reduces due to the competition between Reynolds and Maxwell stresses.

Toroidal zonal flows can be excited via modulational instability similar to poloidal zonal flow excitation in ITG turbulence. Toroidal and poloidal zonal flow shears are coupled linearly via non-linear stresses. Input power threshold for L-H transition reduces with $PZF \rightarrow TZF$ coupling coefficient which depends on k_{\parallel} symmetry breaking mechanisms.

Coherent nonlinear structures like solitons, shocks, nonlinear wave trains appear in zonal flow field in strong turbulence regime of electrostatic toroidal ITG turbulence due to Reynolds stresses offered by trapped and untrapped ITG waves.

9.2 Future directions

The parallel and poloidal momentum transport calculations presented in Chapters 2, 3, 4 are for electrostatic slab ITG turbulence. Extending this to toroidal ITG turbulence and including full electromagnetic effects on parallel and poloidal momentum transport could be of considerable interest. Scaling of parallel residual stress with β is extremely important in order to understand the physics behind the Rice scaling.

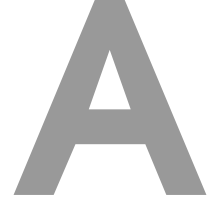
All calculations in Chapters 2, 3, 4 were performed for electrostatic slab ITG mode where electrons were treated to be adiabatic. These calculations can be extended to toroidal ITG mode including trapped electron species. This would be laborious but straightforward which will yield effect of trapped electrons on parallel and poloidal momentum transport.

Gyrokinetic flux tube simulations performed in Chapter 5 shows that the parallel momentum flux reverses sign with the eigenmode ballooning angle θ_0 . Sign reversal of residual flux is related to reversal of intrinsic rotation direction. However note that θ_0 can be chosen arbitrarily in flux tube formalism which is forbidden in global formalism. θ_0 is self consistently determined by the profile shearing effects and is found to change sign when the mode transits from ITG to TEM type on increasing density gradient. This might provide an understanding of core toroidal flow rever-

sal observed in density ramp experiments in TCV and other tokamaks. Hence it is worth doing global gyrokinetic simulations on parallel momentum transport in ITG /TEM transition regime.

From the Chapters 6, 7 and 8 presenting zonal flows generation studies, following future directions emerge. It would be interesting to complement the model of electromagnetic effects on zonal flow generation presented in Chapter 6 by including the geometry effects and parallel magnetic field fluctuations which is important in high β plasmas relevant for spherical systems. In addition, further investigations of zonal flow stability and saturation mechanisms retaining the electromagnetic effects are left for future study.

The coupling of toroidal and poloidal zonal flows via k_{\parallel} symmetry breaking and effect of toroidal zonal flows on transport can be studied via gyrokinetic simulations to validate the toroidal zonal flow generation studies presented in Chapter 7. Stationary solution of ITG-zonal flow system were studied in Chapter 8. The access to the assumed Bohm-Gross type distribution of trapped and untrapped quasi-particles requires further research. Destruction of zonal flow shear layer obtained as coherent solutions will lead to a burst in transport. Hence it will be worth doing stability analysis of stationary solutions. The parallel ion dynamics was ignored in this chapter. Including the parallel ion dynamics will facilitate calculation of nonlinear stationary structure in toroidal zonal flow field as well.



Perturbative calculation of eigenfunction at q_{min}

Consider Equations(4.8) and (4.10) with $\hat{s} = 0$, $\hat{V}'_E = \hat{V}'_{\parallel} = 0$

$$\frac{d^2\phi_k}{dx^2} - \rho_s^* \frac{d\phi_k}{dx} + U(x, \Omega)\phi_k = 0 \quad (\text{A.1})$$

$$U(x, \Omega) = A_1 + A_3x^2 + A_5x^4 \quad (\text{A.2})$$

where

$$A_1 = -k_y^2 + \frac{1 - \Omega}{K + \Omega} + \frac{k_z^2}{k_y^2\Omega^2} \quad (\text{A.3})$$

$$A_3 = \frac{1}{k_y^2\Omega^2} \left\{ -\frac{2k_yk_z\hat{s}_dL_n}{q_0R} \right\} \quad (\text{A.4})$$

$$A_5 = \frac{1}{k_y^2\Omega^2} \left(\frac{k_y\hat{s}_dL_n}{q_0R} \right)^2 \quad (\text{A.5})$$

Using the transformation

$$\xi = (-A_3)^{1/4} \left(x + \frac{A_2}{2A_3} \right) \quad (\text{A.6})$$

the Equation(A.1) becomes

$$\frac{d^2\phi_k}{d\xi^2} - (-A_3)^{-1/4}\rho_s^* \frac{d\phi_k}{d\xi} + \left(E - \xi^2 + \frac{A_5}{(-A_3)^{3/2}}\xi^4 \right) \phi_k = 0 \quad (\text{A.7})$$

where

$$E = \left(A_1 - \frac{A_2^2}{4A_3} \right) / \sqrt{-A_3} \quad (\text{A.8})$$

Now using the transformation

$$\phi_k = \Phi_k \exp \left(\frac{1}{2} \int (-A_3)^{-1/4} \rho_s^* d\xi \right) \quad (\text{A.9})$$

the first derivative can be removed. The resulting equation in Φ_k is

$$\frac{d^2 \Phi_k}{d\xi^2} + \left(E^* - \xi^2 + \frac{A_5}{(-A_3)^{3/2}} \xi^4 \right) \Phi_k = 0 \quad (\text{A.10})$$

where now

$$E^* = E - \left(\frac{(-A_3)^{-1/4} \rho_s^*}{2} \right)^2 \quad (\text{A.11})$$

The quartic term in the potential can be treated perturbatively, similar to perturbation theories in quantum mechanics.

$$\phi = \phi_0 + \phi_1 + \phi_2 + \dots \quad (\text{A.12})$$

$$E = E_0 + E_1 + E_2 + \dots \quad (\text{A.13})$$

Using Equations(A.12) and (A.13) in Equation(A.10) we get at zero order

$$\frac{d^2 \Phi_0}{d\xi^2} + (E_0^* - \xi^2) \Phi_0 = 0 \quad (\text{A.14})$$

whose solution is

$$\Phi_0^l = \varphi_l H_l(\xi) \exp\left(-\frac{\xi^2}{2}\right), \quad \varphi_l = (2^l l! \sqrt{\pi})^{-1/2} \quad (\text{A.15})$$

when

$$E_0^{*l} = 2l + 1, \quad l = 0, 1, 2, \dots etc. \quad (\text{A.16})$$

At first order

$$\left(\frac{d^2}{d\xi^2} + E_0^{*l} - \xi^2 \right) \Phi_1^l + \left(E_1^{*l} + \frac{A_5}{(-A_3)^{3/2}} \xi^4 \right) \Phi_0^l = 0 \quad (\text{A.17})$$

Taking $\Phi_1^l = \sum_m a_m^l \Phi_0^m$, multiplying Equation(A.17) by Φ_0^n and integrating over all ξ and using the property of self adjointness of the operator and orthogonality of the set $\{\Phi_0^l\}$, gives

$$a_n^l (E_0^{*l} - E_0^{*n}) 2^n n! + E_1^{*l} \delta_{n,l} 2^n n! + \frac{A_5}{(-A_3)^{3/2}} [2^{n-4} n! \delta_{n,l+4} + 2^{n-2} (2n-1) n! \delta_{n,l+2} + 3 \cdot 2^{n-2} (2n^2 + 2n + 1) n! \delta_{n,l+0} + 2^n (2n+3) (n+2)! \delta_{n,l-2} + 2^n (n+3)! \delta_{n,l-4}] = 0 \quad (A.18)$$

Setting $n = l$ in Equation(A.18) gives the solvability condition of Equation(A.17) which are nothing but the perturbed eigenvalues

$$E_1^{*l} = -\frac{A_5}{(-A_3)^{3/2}} [3 \cdot 2^{-2} (2l^2 + 2l + 1)] \quad (A.19)$$

Setting $n \neq l$ determines a_n^l

$$a_n^l = -\frac{1}{E_0^{*l} - E_0^{*n}} \frac{A_5}{(-A_3)^{3/2}} [2^{n-4} n! \delta_{n,l+4} + 2^{n-2} (2n-1) n! \delta_{n,l+2} + 3 \cdot 2^{n-2} (2n^2 + 2n + 1) n! \delta_{n,l+0} + 2^n (2n+3) (n+2)! \delta_{n,l-2} + 2^n (n+3)! \delta_{n,l-4}] \quad (A.20)$$

The corrected eigenvalue up to first order for $l = 0$ radial quantum number is

$$E^{*0} = E_0^{*0} + E_1^{*0} \quad (A.21)$$

which gives the dispersion relation as

$$-k_y^2 + \frac{1 - \Omega}{K + \Omega} + \frac{k_z^2}{k_y^2 \Omega^2} - \left(\frac{\rho_s^*}{2} \right)^2 = \frac{1}{k_y \Omega} \left\{ \frac{2k_y k_z \hat{s}_d L_n}{q_0 R} \right\}^{1/2} - \frac{3}{4} \left(\frac{k_y \hat{s}_d L_n}{2k_z q_0 R} \right) \quad (A.22)$$

The eigenfunction corrected up to first order for $l = 0$ radial quantum number is

$$\Phi^0 = \Phi_0^0 + a_2^0 \Phi_0^2 + a_4^0 \Phi_0^4 \quad (A.23)$$

Substituting the value of coefficients a_n^l from Equation(A.20) in the above Equation(A.23) gives

$$\begin{aligned}\Phi^0 = \varphi_0 \exp\left(-\frac{\xi^2}{2}\right) + \frac{A_5}{(-A_3)^{3/2}} \left[\varphi_2 \frac{3}{16} (4\xi^2 - 2) \right. \\ \left. + \varphi_4 2^{-7} (16\xi^4 - 48\xi^2 + 12) \right] \exp\left(-\frac{\xi^2}{2}\right)\end{aligned}\quad (\text{A.24})$$

where $\varphi_n = (2^n n! \sqrt{\pi})^{-1/2}$ Hence the total eigenfunction ϕ for the $l = 0$ radial quantum number, given by Equation(A.9), including the ρ_s^* effect becomes

$$\begin{aligned}\phi^0 = \varphi_0 \exp\left(-\frac{\xi^2}{2} + \frac{1}{2}(-A_3)^{-1/4} \rho_s^* \xi\right) + \frac{A_5}{(-A_3)^{3/2}} \left[\varphi_2 \frac{3}{16} (4\xi^2 - 2) \right. \\ \left. + \varphi_4 2^{-7} (16\xi^4 - 48\xi^2 + 12) \right] \exp\left(-\frac{\xi^2}{2} + \frac{1}{2}(-A_3)^{-1/4} \rho_s^* \xi\right)\end{aligned}\quad (\text{A.25})$$

B

Derivation of Equation(8.57)

The trapped and untrapped integrals in Equation(8.52) are evaluated first.

Trapped integral (I_T):

$$\begin{aligned} I_T &= \int_f^{f_m} d\bar{W} J N_T(\bar{W}, k_y) \\ &= \int_f^{f_m} d\bar{W} \frac{a}{1 + W_*} [1 - \bar{b}k_{y0}^2 - \bar{b}(\bar{W} - f)] N_{0T} \left[1 + \epsilon \left(\frac{f_m - \bar{W}}{\Delta} \right)^{1/2} \right] \end{aligned} \quad (\text{B.1})$$

Let $\frac{f_m - \bar{W}}{\Delta} = x$ so that $-d\bar{W} = \Delta dx$ then

$$I_T = \frac{aN_{0T}\Delta}{1 + W_*} \int_0^{f_m - f} dx [1 - \bar{b}k_{y0}^2 - \bar{b}(f_m - f - x\Delta)] [1 + \epsilon x^{1/2}] \quad (\text{B.2})$$

$$\begin{aligned} &= \frac{aN_{0T}\Delta}{1 + W_*} \int_0^{f_m - f} dx [1 - \bar{b}k_{y0}^2 - \bar{b}(f_m - f) + \\ &\quad \epsilon (1 - \bar{b}k_{y0}^2 - \bar{b}(f_m - f)) x^{1/2} + \bar{b}\Delta x + \bar{b}\Delta\epsilon x^{3/2}] \\ &= \frac{aN_{0T}\Delta}{1 + W_*} \left[(1 - \bar{b}k_{y0}^2) (f_m - f) + \frac{2}{3}\epsilon (1 - \bar{b}k_{y0}^2) (f_m - f)^{3/2} \right. \\ &\quad \left. + \bar{b} \left(\frac{\Delta}{2} - 1 \right) (f_m - f)^2 + \bar{b}\epsilon \left(\frac{2}{5}\Delta - \frac{2}{3} \right) (f_m - f)^{5/2} \right] \end{aligned} \quad (\text{B.3})$$

Untrapped integral(I_U):

$$\begin{aligned}
 I_U &= \int_{f_m}^{\infty} d\bar{W} J N_U(\bar{W}, k_y) \\
 &= \int_{f_m}^{\infty} d\bar{W} \frac{a}{1+W_*} [1 - \bar{b}k_{y0}^2 - \bar{b}(\bar{W} - f)] N_{0U} \left[1 + \left(\frac{\bar{W} - f_m}{\Delta} \right)^2 \right]^{-1} \quad (\text{B.4})
 \end{aligned}$$

Let $\frac{\bar{W}-f_m}{\Delta} = x$ so that $d\bar{W} = \Delta dx$ then

$$I_U = \frac{aN_{0U}\Delta}{1+W_*} \int_0^{\infty} dx [1 - \bar{b}k_{y0}^2 - \bar{b}(f_m - f + x\Delta)] [1 + x^2]^{-1} \quad (\text{B.5})$$

$$= \frac{aN_{0U}\Delta}{1+W_*} [1 - \bar{b}k_{y0}^2 - \bar{b}(f_m - f)] \frac{\pi}{2} \quad (\text{B.6})$$

In evaluating the last step the other diverging integral $\int_0^{\infty} dx x(1+x^2)^{-1}$ has been ignored, as it is a mathematical artifact of the expansion of FLR terms in Equation(8.53).

Using the values of I_T and I_U obtained above yields the desired Equation(8.52).

Bibliography

- [1] J D Lawson. Some criteria for a power producing thermonuclear reactor. *Proceedings of the Physical Society*, 70(Section B), 1957.
- [2] J Wesson. *Tokamaks*. Oxford Science Publications, 1997.
- [3] P. H Diamond, S.I. Itoh, K. Itoh, and T. S. Hahm. *Plasma Phys. Controlled Fusion*, 47:R35, 2005.
- [4] Akihide Fujisawa. A review of zonal flow experiments. *Nucl. Fusion*, 49:013001, 2009.
- [5] Steven A. Balbus and John F. Hawley. Instability, turbulence, and enhanced transport in accretion disks. *Rev. Mod. Phys.*, 70:1–53, Jan 1998.
- [6] Gareth P. Williams. Planetary circulations: 1. barotropic representation of jovian and terrestrial turbulence. *J. Atmos. Sci.*, 35:1399–1426, 1978.
- [7] H. Biglari, P. H. Diamond, and P. W. Terry. *Phys. Fluids*, B 2(1):1, 1990.
- [8] T. S. Hahm. Rotation shear induced fluctuation decorrelation in a toroidal plasma. *Phys. Plasmas*, 1:2940, 1994.
- [9] T. S. Hahm and K. H. Burrell. *Phys. Plasmas*, 2:1648, 1995.
- [10] T. S. Hahm and K. H. Burrell. *Plasma Phys. Control. Fusion*, 38:1427, 1996.
- [11] G. R. Mckee, P. Gohil, D.J. Schlossberg, J.A. Boedo, K.H. Burrell, J.S. deGrassie, R.J. Groebner, R.A. Moyer, C.C. Petty, T.L. Rhodes, L. Schmitz, M.W. Shafer, W.M. Solomon, M. Umansky, G.Wang, A.E. White, and X. Xu. *Nucl. Fusion*, 49:115016, 2009.
- [12] R C Wolf. Internal transport barriers in tokamak plasmas. *Plasma Phys. Control. Fusion*, 45(1):R1–R91, 2003.
- [13] K. H. Burrell. Effects of $\mathbf{e} \times \mathbf{b}$ velocity shear and magnetic shear on turbulence and transport in magnetic confinement devices. *Phys. Plasmas*, 4(5):1499–1518, 1997.

- [14] E. J. Strait, T. S. Taylor, A. D. Turnbull, J. R. Ferron, L. L. Lao, B. Rice, O. Sauter, S. J. Thompson, and D. Wróblewski. Wall stabilization of high beta tokamak discharges in diiii-d. *Phys. Rev. Lett.*, 74(13):2483–2486, Mar 1995.
- [15] A. M. Garofalo, A. D. Turnbull, M. E. Austin, J. Bialek, M. S. Chu, K. J. Comer, E. D. Fredrickson, R. J. Groebner, R. J. La Haye, L. L. Lao, E. A. Lazarus, G. A. Navratil, T. H. Osborne, B. W. Rice, S. A. Sabbagh, J. T. Scoville, E. J. Strait, and T. S. Taylor. Direct observation of the resistive wall mode in a tokamak and its interaction with plasma rotation. *Phys. Rev. Lett.*, 82(19):3811–3814, May 1999.
- [16] L.-J. Zheng, M. Kotschenreuther, and M. S. Chu. Rotational stabilization of resistive wall modes by the shear alfvén resonance. *Phys. Rev. Lett.*, 95(25):255003, Dec 2005.
- [17] L. J. Zheng, M. T. Kotschenreuther, and J. W. Van Dam. Rotational stabilization of resistive wall modes in iter advanced tokamak scenarios. *Phys. Plasmas*, 17(5):056104, 2010.
- [18] T. C. Hender, J. C. Wesley, J. Bialek, A. Bondeson, A. H. Boozer, R. J. Buttery, A. Garofalo, T. P. Goodman, R. S. Granetz, Y. Gribov, O. Gruber, M. Gryaznevich, G. Giruzzi, S. Günter, N. Hayashi, P. Helander, C. C. Hegna, D. F. Howell, D. A. Humphreys, G. T. A. Huysmans, A. W. Hyatt, A. Isayama, S. C. Jardin, Y. Kawano, A. Kellman, C. Kessel, H. R. Koslowski, R. J. La Haye, E. Lazzaro, Y. Q. Liu, V. Lukash, J. Manickam, S. Medvedev, V. Mertens, S. V. Mirnov, Y. Nakamura, G. Navratil, M. Okabayashi, T. Ozeki, R. Paccagnella, G. Pautasso, F. Porcelli, V. D. Pustovitov, V. Riccardo, M. Sato, O. Sauter, M. J. Schaffer, M. Shimada, P. Sonato, E. J. Strait, M. Sugihara, M. Takechi, A. D. Turnbull, E. Westerhof, D. G. Whyte, R. Yoshino, H. Zohm, Disruption ITPA MHD, and Magnetic Control Topical Group. *Nucl. Fusion*, page S128, 2007.
- [19] R. J. Hawryluk, D. J. Campbell, G. Janeschitz, P.R. Thomas, R. Albanese, R. Ambrosino, C. Bachmann, L. Baylor, M. Becoulet, I. Benfatto, J. Bialek, A. Boozer, A. Brooks, R. Budny, T. Casper, M. Cavinato, J.-J. Cordier,

- V. Chuyanov, E. Doyle, T. Evans, G. Federici, M. Fenstermacher, H. Fujieda, K. G' al, A. Garofalo, L. Garzotti, D. Gates, Y. Gribov, P. Heitzenroeder, T.C. Hender, N. Holtkamp, D. Humphreys, I. Hutchinson, K. Ioki, J. Johnner, G. Johnson, Y. Kamada, A. Kavin, C. Kessel, R. Khayrutdinov, G. Kramer, A. Kukushkin, K. Lackner, I. Landman, P. Lang, Y. Liang, J. Linke, B. Lipschultz, A. Loarte, G.D. Loesser, C. Lowry, T. Luce, V. Lukash, S. Maruyama, M. Mattei, J. Menard, M. Merola, A. Mineev, N. Mitchell, E. Nardon, R. Nazikia, B. Nelson, C. Neumeyer, J.-K. Park, R. Pearce, R.A. Pitts, A. Polevoi, A. Portone, M. Okabayashi, P.H. Rebut, V. Riccardo, J. Roth, S. Sabbagh, G. Saibene, G. Sannazzaro, M. Schaffer, M. Shimada, A. Sen, A. Sips, C.H. Skinner, P. Snyder, R. Stambaugh, E. Strait, M. Sugihara, E. Tsitrone, J. Urano, M. Valovic, M. Wade, J. Wesley, R. White, D.G. Whyte, S. Wu, M. Wykes, and L. Zakharov. Principal physics developments evaluated in the iter design review. *Nucl. Fusion*, 49:065012, 2009.
- [20] R. Hemsworth, H. Decamps, J. Graceffa, B. Schunke, M. Tanaka, M. Dremel, A. Tanga, H.P.L. De Esch, F. Geli, J. Milnes, T. Inoue, D. Marcuzzi, P. Sonato, and P. Zaccaria. *Nucl. Fusion*, 49:045006, 2009.
- [21] N. Holtkamp. The status of the iter design. 2008. Proc. 22nd Int. Conf. on Fusion Energy 2008 (Geneva Switzerland, 2008)(Viena: IAEA) OV/2-1.
- [22] J. E. Rice, A. Ince-Cushman, J.S. deGrassie, L.-G. Eriksson, Y. Sakamoto, A. Scarabosio, A. Bortolon, K.H. Burrell, B.P. Duval, C. Fenzi-Bonizet, M.J. Greenwald, R.J. Groebner, G.T. Hoang, Y. Koide, E.S. Marmor, A. Pochelon, and Y. Podpaly. *Nucl. Fusion*, 47:1618, 2007.
- [23] A. Bortolon, B. P. Duval, A. Pochelon, and A. Scarabosio. Observation of spontaneous toroidal rotation inversion in ohmically heated tokamak plasmas. *Phys. Rev. Lett.*, 97:235003, 2006.
- [24] J. E. Rice, J. W. Hughes, P. H. Diamond, Y. Kosuga, Y. A. Podpaly, M. L. Reinke, M. J. Greenwald, Ö. D. Gürcan, T. S. Hahm, A. E. Hubbard, E. S. Marmor, C. J. McDevitt, and D. G. Whyte. Edge temperature gradient as intrinsic rotation drive in alcator *c*-mod tokamak plasmas. *Phys. Rev. Lett.*, 106:215001, May 2011.

- [25] J. E. Rice, I. Cziegler, P. H. Diamond, B. P. Duval, Y. A. Podpaly, M. L. Reinke, P. C. Ennever, M. J. Greenwald, J. W. Hughes, Y. Ma, E. S. Marmor, M. Porkolab, N. Tsujii, and S. M. Wolfe. Rotation reversal bifurcation and energy confinement saturation in tokamak ohmic l -mode plasmas. *Phys. Rev. Lett.*, 107:265001, Dec 2011.
- [26] M.L. Reinke Y.A. Podpaly A. Bortolon R.M. Churchill I. Cziegler P.H. Diamond A. Dominguez P.C. Ennever C.L. Fiore R.S. Granetz M.J. Greenwald A.E. Hubbard J.W. Hughes J.H. Irby Y. Ma E.S. Marmor R.M. McDermott M. Porkolab N. Tsujii J.E. Rice, B.P. Duval and S.M. Wolfe. Observations of core toroidal rotation reversals in alcator c-mod ohmic l-mode plasmas. *Nucl. Fusion*, 51(8):083005, 2011.
- [27] J. E. Rice, M. J. Greenwald, Y. A. Podpaly, M. L. Reinke, P. H. Diamond, J. W. Hughes, N. T. Howard, Y. Ma, I. Cziegler, B. P. Duval, P. C. Ennever, D. Ernst, C. L. Fiore, C. Gao, J. H. Irby, E. S. Marmor, M. Porkolab, N. Tsujii, and S. M. Wolfe. Ohmic energy confinement saturation and core toroidal rotation reversal in alcator c-mod plasmas. *Physics of Plasmas*, 19(5):056106, 2012.
- [28] C. S. Chang, C. K. Phillips, R. White, S. Zweben, P. T. Bonoli, J. E. Rice, M. J. Greenwald, and J. deGrassie. Generation of plasma rotation by ion cyclotron resonance heating in tokamaks. *Physics of Plasmas*, 6(5):1969–1977, 1999.
- [29] F. W. Perkins, R. B. White, P. T. Bonoli, and V. S. Chan. Generation of plasma rotation in a tokamak by ion-cyclotron absorption of fast alfvén waves. *Physics of Plasmas*, 8(5):2181–2187, 2001.
- [30] V. S. Chan, S. C. Chiu, and Y. A. Omelchenko. Radio-frequency-driven radial current and plasma rotation in a tokamak. *Physics of Plasmas*, 9(2):501–510, 2002.
- [31] L. G. Eriksson and F. Porcelli. Toroidal plasma rotation induced by fast ions without external momentum injection in tokamaks. *Nuclear Fusion*, 42:959, 2002.

- [32] A. L. Rogister, J. E. Rice, A. Nicolai, A. Ince-Cushman, and S. Gangadhara. Theoretical interpretation of the toroidal rotation velocity observed in alcator c-mod ohmic h-mode discharges. *Nucl. Fusion*, 42:1144, 2002.
- [33] A. J. Cole, C. C. Hegna, and J. D. Callen. Effect of neoclassical toroidal viscosity on error-field penetration thresholds in tokamak plasmas. *Phys. Rev. Lett.*, 99:065001, Aug 2007.
- [34] J.S. deGrassie, R.J. Groebner, K.H. Burrell, and W.M. Solomon. Intrinsic toroidal velocity near the edge of diii-d h-mode plasmas. *Nucl. Fusion*, 49:085020, 2009.
- [35] B. Coppi. Accretion theory of 'spontaneous' rotation in toroidal plasmas. *Nucl. Fusion*, 42:1, 2002.
- [36] K. C. Shaing. Theory for toroidal momentum pinch and flow reversal in tokamaks. *Phys. Rev. Lett.*, 86:640–643, Jan 2001.
- [37] O. D. Gurcan, P. H. Diamond, T. S. Hahm, and Singh R. *Phys. Plasmas*, 14:042306, 2007.
- [38] W.X. Wang, T.S Hahm, S. Ethier, G. Rewoldt, W.W. Lee, W.M Tang, and P.H. Kaye, S.M.and Diamond. *Phys. Rev. Lett.*, 102:035005, 2009.
- [39] C. J. McDevitt, P.H. Diamond, O.D. Gurcan, and T.S. Hahm. *Phys. Plasmas*, 16:052302, 2009.
- [40] C. J. McDevitt, P.H. Diamond, and O.D. Gurcan. *Phys. Rev. Lett.*, 103:205003, 2009.
- [41] J. Weiland, R. Singh, H. Nordman, P. Kaw, A.G. Peeters, and D. Strinzi. Symmetry breaking effects of toroidicity on toroidal momentum transport. *Nuclear Fusion*, 49(6):065033, 2009.
- [42] Y. Camenen, A. G. Peeters, C. Angioni, F. J. Casson, W. A. Hornsby, A. P. Snodin, and D. Strintzi. *Phys. Rev. Lett.*, 102:125001, 2009.
- [43] Y. Camenen, A. G. Peeters, C. Angioni, F. J. Casson, W. A. Hornsby, A. P. Snodin, and D. Strintzi. *Phys. Plasmas*, 16:062501, 2009.

- [44] W. M. Solomon, K. H. Burrell, R. Andre, L. R. Baylor, R. Budny, P. Gohil, R. J. Groebner, C. T. Holcomb, W. A. Houlberg, and M. R. Wade. Experimental test of the neoclassical theory of impurity poloidal rotation in tokamaks. *Physics of Plasmas*, 13(5):056116, 2006.
- [45] T. Tala, Y. Andrew, K. Cromb-År, P.C. de Vries, X. Garbet, N. Hawkes, H. Nordman, K. Rantamäki, P. Strand, A. Thyagaraja, J. Weiland, E. Asp, Y. Baranov, C. Challis, G. Corrigan, A. Eriksson, C. Giroud, M.-D. Hua, I. Jenkins, H.C.M. Knoop, X. Litaudon, P. Mantica, V. Naulin, V. Parail, K.-D. Zastrow, and JET-EFDA contributors. Toroidal and poloidal momentum transport studies in jet. *Nuclear Fusion*, 47(8):1012, 2007.
- [46] P. H. Diamond, S.-I. Itoh, K. Itoh, and T. S. Hahm. Zonal flows in plasma - a review. *Plasma. Phys. Cont.*, 47(5):R35–R161, 2005.
- [47] A. Hasegawa, C. G. McClellan, and Y. Kodama. *Phys. Fluids*, 22:122.
- [48] P. B. Snyder and G. W. Hammett. *Phys. Plasmas*, 8:744, 2001.
- [49] P. B. Snyder and G. W. Hammett. *Phys. Plasmas*, 8:3199, 2001.
- [50] L. Laborde, D. C. McDonald, and I. Voitsekhovitch. *Phys. Plasmas*, 15:102507, 2008.
- [51] H. Nordman, P. Strand, J. Weiland, and J.P. Christiansen. *Nucl. Fusion*, 39:1157, 1999.
- [52] A. Jarmén, P. Malinov, and H. Nordman. *Plasma Phys. Controlled Fusion*, 40:2041, 1998.
- [53] M. J. Pueschel and F. Jenko. *Phys. Plasmas*, 17:062307.
- [54] M. J. Pueschel, M. Kammerer, and F. Jenko. *Phys. Plasmas*, 15:102310, 2008.
- [55] Y. Chen, S. E. Parker, B. I. Cohen, A. M. Dimits, W. M. Nevins, D. Shumaker, V. K. Decyk, and J. N. Leboeuf. *Nucl. Fusion*, 43:1121, 2003.
- [56] S. E. Parker, Y. Chen, W. Wan, B. I. Cohen, and W. M. Nevins. *Phys. Plasmas*, 11:2594, 2004.

- [57] J. Candy. *Phys. Plasmas*, 12:072307, 2005.
- [58] F. Jenko and W. Dorland. *Plasma Phys. Controlled Fusion*, 43:A141, 2001.
- [59] B. D. Scott. *Phys. Plasmas*, 7:1845, 2000.
- [60] B. D. Scott. *Plasma Phys. Controlled Fusion*, 48:B2777, 2006.
- [61] F L Hinton and M N Rosenbluth. Dynamics of axisymmetric and poloidal flows in tokamaks. *Plasma Physics and Controlled Fusion*, 41(3A):A653, 1999.
- [62] B. N. Rogers, W. Dorland, and M. Kotschenreuther. Generation and stability of zonal flows in ion-temperature-gradient mode turbulence. *Phys. Rev. Lett.*, 85:5336–5339, Dec 2000.
- [63] Eun jin Kim and P. H. Diamond. Dynamics of zonal flow saturation in strong collisionless drift wave turbulence. *Physics of Plasmas*, 9(11):4530–4539, 2002.
- [64] A. I. Smolyakov, P. H. Diamond, and M. Malkov. Coherent structure phenomena in drift wave–zonal flow turbulence. *Phys. Rev. Lett.*, 84:491–494, Jan 2000.
- [65] I Bernstein, J M Greene, and M D Krushkal. *Phys. Rev.*, 108:546, 1957.
- [66] Predhiman Kaw, Kunioki Mima, and Kyoji Nishikawa. Envelope solutions for random-phase plasmons. *Phys. Rev. Lett.*, 34:803–806, Mar 1975.
- [67] R. Jha, P. K. Kaw, S. K. Mattoo, C. V. S. Rao, Y. C. Saxena, and ADITYA Team. Intermittency in tokamak edge turbulence. *Phys. Rev. Lett.*, 69:1375–1378, Aug 1992.
- [68] S. Benkadda, T. Dudok de Wit, A. Verga, A. Sen, ASDEX team, and X. Garbet. Characterization of coherent structures in tokamak edge turbulence. *Phys. Rev. Lett.*, 73:3403–3406, Dec 1994.
- [69] M. Endler, H. Niedermeyer, L. Giannone, E. Kolzhauer, A. Rudyj, G. Theimer, and N. Tsois. *Nucl. Fusion*, 35:1307, 1995.

- [70] B. A. Carreras, C. Hidalgo, E. Sánchez, M. A. Pedrosa, R. Balbín, I. García-Cortés, B. van Milligen, D. E. Newman, and V. E. Lynch. Fluctuation-induced flux at the plasma edge in toroidal devices. *Physics of Plasmas*, 3(7):2664–2672, 1996.
- [71] B. A. Carreras et al. Long-range time correlations in plasma edge turbulence. *Phys. Rev. Lett.*, 80:4438–4441, May 1998.
- [72] P Kaw, R Singh, and P H Diamond. *Plasma Phys. Controlled Fusion*, 44:51, 2002.
- [73] J. E. Rice, M. Greenwald, I.H. Hutchinson, E.S. Marmor, Y. Takase, S.M. Wolfe, and F. Bombarda. *Nucl. Fusion*, 38:75, 1998.
- [74] H. K. Moffatt. *Magnetic Field Generation in Electrically Conducting Fluids*. (Cambridge: Cambridge University Press), 1978.
- [75] Robert H. Kraichnan. Inertial ranges in two-dimensional turbulence. *Phys. Fluids*, 10(7):1417–1423, 1967.
- [76] M. G. Shats, H. Xia, and H. Punzmann. *Phys. Rev. Lett.*, 99:164502, 2007.
- [77] H K Moffat. *Reflections on Magnetohydrodynamics Perspectives in Fluid Dynamics* ed G.K. Batchelor, H.K. Moffatt, and M.G. Worster. (CUP).
- [78] X. Garbet. *Proc. 22nd Int. Conf. on Fusion energy Geneva, 2008* (Vienna: IAEA) CD-ROM file[Geneva, Switzerland] and <http://www-naweb.iaea.org/napc/physics/FEC/FEC2008/html/index.htm>, 2008.
- [79] N. Mattor and P. H. Diamond. *Phys. Fluids*, 31:1180, 1988.
- [80] S. D. Scott, P. H. Diamond, R. J. Fonck, R. J. Goldston, R. B. Howell, K. P. Jaehnig, G. Schilling, E. J. Synakowski, M. C. ZarnstorA, C. E. Bush, E. Fredrickson, K. W. Hill, A. C. Janos, D. K. Mansfield, D. K. Owens, H. Park, G. Pautasso, A. T. Ramsey, J. Schivell, G. D. Tait, W. M. Tang, and G. Taylor. *Phys. Rev. Lett.*, 64:531, 1990.
- [81] I. Holod and Z. Lin. *Phys. Plasmas*, 15:092302, 2008.

- [82] T. S. Hahm, P. H. Diamond, O. D. Gurcan, , and G. Rewoldt. *Phys. Plasmas*, 14:072302, 2007.
- [83] O. D. Gurcan, P. H. Diamond, and T. S. Hahm. *Phys. Rev. Lett.*, 100:135001, 2008.
- [84] A. G. Peeters, C. Angioni, and D. Strintzi. *Phys. Rev. Lett.*, 98:265003, 2007.
- [85] M. Yoshida, Y. Kamada, H. Takenaga, Y. Sakamoto, H. Urano, N. Oyama, and G. Matsunaga. *Phys. Rev. Lett.*, 100:105002, 2008.
- [86] P.H Diamond and Y.B. Kim. *Phys. Fluids*, B3:1626, 1991.
- [87] U. Frisch. *Turbulence*. (Cambridge: Cambridge University Press), 1995.
- [88] P. H. Diamond, C. J. McDevitt, Ö. D. Gürcan, T. S. Hahm, and V. Naulin. Transport of parallel momentum by collisionless drift wave turbulence. *Phys. Plasmas*, 15(1):012303, 2008.
- [89] W. X. Wang, T. S. Hahm, S. Ethier, G. Rewoldt, W. W. Lee, W. M. Tang, S. M. Kaye, and P. H. Diamond. Gyrokinetic studies on turbulence-driven and neoclassical nondiffusive toroidal-momentum transport and the effect of residual fluctuations in strong $e \times b$ shear. *Phys. Rev. Lett.*, 102(3):035005, 2009.
- [90] T. S. Hahm, P. H. Diamond, O. D. Gurcan, and G. Rewoldt. Nonlinear gyrokinetic theory of toroidal momentum pinch. *Phys. Plasmas*, 14(7):072302, 2007.
- [91] Ö. D. Gürcan, P. H. Diamond, and T. S. Hahm. Turbulent equipartition and homogenization of plasma angular momentum. *Phys. Rev. Lett.*, 100(13):135001, 2008.
- [92] N. Kluy, C. Angioni, Y. Camenen, and A. G. Peeters. Linear gyrokinetic calculations of toroidal momentum transport in the presence of trapped electron modes in tokamak plasmas. *Phys. Plasmas*, 16:122302, 2009.
- [93] E. S. Yoon and T. S. Hahm. *Nuclear Fusion*, 50:064006, 2010.

- [94] C. J. McDevitt and P. H. Diamond. Transport of parallel momentum by drift-alfven turbulence. *Phys. Plasmas*, 16(1):012301, 2009.
- [95] Ö. D. Gürcan, P. H. Diamond, P. Hennequin, C. J. McDevitt, X. Garbet, and C. Bourdelle. Residual parallel reynolds stress due to turbulence intensity gradient in tokamak plasmas. *Phys. Plasmas*, 17(11):112309, 2010.
- [96] Ö. D. Gürcan, P. H. Diamond, T. S. Hahm, and R. Singh. Intrinsic rotation and electric field shear. *Phys. Plasmas*, 14(4):042306, 2007.
- [97] D.G. Whyte, A.E. Hubbard, J.W. Hughes, B. Lipschultz, J.E. Rice, E.S. Marmor, M. Greenwald, I. Cziegler, A. Dominguez, T. Golfinopoulos, N. Howard, L. Lin, R.M. McDermott, M. Porkolab, M.L. Reinke, J. Terry, N. Tsujii, S. Wolfe, S. Wukitch, Y. Lin, and the Alcator C-Mod Team. *Nuclear Fusion*, 50:105005, 2010.
- [98] K. Ida, Y. Yoshimura, K. Nagaoka, M. Osakabe, S. Morita, M. Goto, M. Yokoyama, H. Funaba, S. Murakami, K. Ikeda, H. Nakano, K. Tsumori, Y. Takeiri, O. Kaneko, and L. H. D. experiment group. *Nucl. Fusion*, 50:064007, 2010.
- [99] W. X. Wang, P. H. Diamond, T. S. Hahm, S. Ethier, G. Rewoldt, and W. M. Tang. Nonlinear flow generation by electrostatic turbulence in tokamaks. *Phys. Plasmas*, 17:072511, 2010.
- [100] F. J. Casson, A. G. Peeters, Y. Camenen, W. A. Hornsby, A. P. Snodin, D. Strintzi, and G. Szepesi. Anomalous parallel momentum transport due to $\mathbf{e} \times \mathbf{b}$ flow shear in a tokamak plasma. *Phys. Plasmas*, 16(9):092303, 2009.
- [101] W. X. Wang, T. S. Hahm, S. Ethier, L. E. Zakharov, and P. H. Diamond. Trapped electron mode turbulence driven intrinsic rotation in tokamak plasmas. *Phys. Rev. Lett.*, 106:085001, 2011.
- [102] Rameswar Singh, R Ganesh, R Singh, P Kaw, and A. Sen. Intrinsic toroidal and poloidal flow generation in the background of its turbulence. *Nuclear Fusion*, 51(1):013002, 2011.

- [103] Z. Yan, M. Xu, C. Holland P. H. Diamond, S. H. Muller, G. R. Tyan, and J. H. Yu. *Phys. Rev. Lett.*, 104:065002, 2010.
- [104] S. H. Müller, J. A. Boedo, K. H. Burrell, J. S. deGrassie, R. A. Moyer, D. L. Rudakov, and W. M. Solomon. *Phys. Rev. Lett.*, 106:115001, 2011.
- [105] S. Hamaguchi and W. Horton. Effects of sheared flows on ion-temperature-gradient-driven turbulent transport. *Physics of Fluids B: Plasma Physics*, 4(2):319–328, 1992.
- [106] N. Mattor and P. H. Diamond. Momentum and thermal transport in neutral beam heated tokamaks. *Phys. Fluids*, 31(5):1180–1189, 1988.
- [107] L. Bai, A. Fukuyama, and M. Uchida. Flow-shear stabilization of ion temperature gradient-driven instability in a tokamak: Slab theory. *Phys. Plasmas*, 5(4):989–999, 1998.
- [108] D. H. E. Dubin, J. A. Krommes, C. Oberman, and W. W. Lee. *Phys. Fluids*, 26:3524, 1983.
- [109] A. Brizard. Nonlinear gyrofluid description of turbulent magnetized plasmas. *Phys. Fluids B*, 4(5):1213 – 1228, 1992.
- [110] M. N. Rosenbluth and F. L. Hinton. Poloidal flow driven by ion-temperature-gradient turbulence in tokamaks. *Phys. Rev. Lett.*, 80(4):724–727, Jan 1998.
- [111] Jiquan Li, Y Kishimoto, and T Tuda. *Plasma Physics and Controlled Fusion*, 42:443, 2000.
- [112] Rameswar Singh, R Ganesh, R Singh, P Kaw, and A. Sen. Intrinsic toroidal and poloidal flow generation in the background of itg turbulence. *Nuclear Fusion*, 51(1):013002, 2011.
- [113] L Bai, A Fukuyama, and M Uchida. *Physics of Plasmas*, 5:989, 1998.
- [114] J Q Li, L Huang, and W X Qu. *Physics of Plasmas*, 5:959, 1998.
- [115] Rameswar Singh, R Singh, P Kaw, P H Diamond, O D Gurcan, and H Norman. Symmetry breaking effects of density gradient on parallel momentum transport: A new ρ_s^* effect. *Phys. Plasmas*, 19:012301, 2012.

- [116] F. Jenko, W. Dorland, M. Kotschenreuther, and B. N. Rogers. Electron temperature gradient driven turbulence. *Physics of Plasmas*, 7(5):1904–1910, 2000.
- [117] A.G. Peeters, Y. Camenen, F.J. Casson, W.A. Hornsby, A.P. Snodin, D. Strintzi, and G. Szepesi. The nonlinear gyro-kinetic flux tube code gkw. *Computer Physics Communications*, 180(12):2650 – 2672, 2009.
- [118] M. A. Beer, S. C. Cowley, and G. W. Hammett. Field-aligned coordinates for nonlinear simulations of tokamak turbulence. *Physics of Plasmas*, 2(7):2687–2700, 1995.
- [119] J. Chowdhury, R. Ganesh, J. Vaclavik, S. Brunner, L. Villard, and P. Angelino. Short wavelength ion temperature gradient mode and coupling with trapped electrons. *Physics of Plasmas*, 16(8):082511, 2009.
- [120] Zhe Gao, H. Sanuki, K. Itoh, and J. Q. Dong. Temperature gradient driven short wavelength modes in sheared slab plasmas. *Physics of Plasmas*, 10(7):2831–2839, 2003.
- [121] Zhe Gao, H. Sanuki, K. Itoh, and J. Q. Dong. Short wavelength ion temperature gradient instability in toroidal plasmas. *Physics of Plasmas*, 12(2):022502, 2005.
- [122] A. Hirose, M. Elia, A. I. Smolyakov, and M. Yagi. Short wavelength temperature gradient driven modes in tokamaks. *Physics of Plasmas*, 9(5):1659–1666, 2002.
- [123] Xavier Lapillonne. *Local and global Eulerian gyrokinetic simulations of microturbulence in realistic geometry with applications to the TCV Tokamak*. PhD thesis, CRPP Association Euratom École Polytechnique Fédérale de lausanne, 2010.
- [124] Florian Merz. *Gyrokinetic simulation of multimode plasma turbulence*. PhD thesis, der Westfälischen Wilhelms-Universität Münster, 2010.
- [125] Y Camenen, Y Idomura, S. Jolliet, and A.G. Peeters. Consequences of profile shearing on toroidal momentum transport. *Nuclear Fusion*, 51:073039, 2011.

- [126] M. Artun and W. M. Tang. Gyrokinetic analysis of ion temperature gradient modes in the presence of sheared flows. *Physics of Fluids B: Plasma Physics*, 4(5):1102–1114, 1992.
- [127] J. Q. Dong and W. Horton. Kinetic quasitoroidal ion temperature gradient instability in the presence of sheared flows. *Physics of Fluids B: Plasma Physics*, 5(5):1581–1592, 1993.
- [128] R. E. Waltz, G. D. Kerbel, and A. J. Milovich. *Phys. Plasmas*, 1:2229, 1994.
- [129] R. E. Waltz, G. M. Staebler, W. Dorland, G. W. Hammett, M. Kotschenreuther, and J. A. Konings. A gyro-landau-fluid transport model. *Physics of Plasmas*, 4(7):2482–2496, 1997.
- [130] R. E. Waltz, R. L. Dewar, and X. Garbet. Theory and simulation of rotational shear stabilization of turbulence. *Physics of Plasmas*, 5(5):1784–1792, 1998.
- [131] J. E. Kinsey, R. E. Waltz, and J. Candy. Nonlinear gyrokinetic turbulence simulations of $e \times b$ shear quenching of transport. *Physics of Plasmas*, 12(6):062302, 2005.
- [132] R. E. Waltz, G. D. Kerbel, J. Milovich, and G. W. Hammett. Advances in the simulation of toroidal gyro-landau fluid model turbulence. *Physics of Plasmas*, 2(6):2408–2416, 1995.
- [133] F Romalnelli and F Zonca. The radial structure of ion-temperature-gradient-driven mode. *Physics of Fluids B*, 5(11):4081, 1993.
- [134] R J Hastie, K W Hesketh, and J B Taylor. Shear damping of two-dimensional drift waves in a large-aspect-ratio tokamak. *Nuclear Fusion*, 19:1223, 1979.
- [135] J. Y. Kim, Y. Kishimoto, M. Wakatani, and T. Tajima. Poloidal shear flow effect on toroidal ion temperature gradient mode: A theory and simulation. *Physics of Plasmas*, 3(10):3689–3695, 1996.
- [136] Y Kishimoto, J Y Kim, W Horton, T Tajima, M J LeBrun, and S Shirai. Toroidal mode structure in weak and reversed magnetic plasmas and its role

- in internal transport barrier. *Plasma physics and controlled fusion*, 40:A663, 1998.
- [137] Y Kishimoto, J Y Kim, W Horton, T Tajima, M J LeBrun, S A Dettrick, J Q Li, and S Shirai. Discontinuity model for internal transport barrier formation in reversed magnetic shear plasmas. *Nuclear Fusion*, 40:667, 2000.
- [138] ITER Physics Basis Team. *Nuclear Fusion*, 39:2175, 1999.
- [139] D. C. McDonald, J. G. Cordey, C. C. Petty, M. Beurskens, R. Budny, I. Coffey, M. de Baar, C. Giroud, E. Joffrin, P. Lomas, A. Meigs, J. Ongena, G. Saibene, R. Sartori, I. Voitsekhovitch, and JET EFDA contributors. *Plasma Phys. Controlled Fusion*, 46:A215, 2004.
- [140] C. C. Petty, T. C. Luce, D. C. McDonald, J. Mandrekas, M. R. Wade, J. Candy, J. G. Cordey, V. Drozdov, T. E. Evans, J. R. Ferron, R. J. Groebner, A. W. Hyatt, G. L. Jackson, R. J. La Haye, T. H. Osborne, and R. E. Waltz. *Phys. Plasmas*, 11:2514.
- [141] G. Hammett, M. Beer, W. Dorland, S.C. Cowley, and S.A. Smith. *Plasma Phys. Controlled Fusion*, 35:937, 1993.
- [142] J. Weiland. *Collective Modes in Inhomogeneous Plasmas, Kinetic and Advanced Fluid Theory*. IOP Publishing Bristol, 2000.
- [143] J. Anderson, H. Nordman, R. Singh, and J. Weiland. *Phys. Plasmas*, 9:4500, 2002.
- [144] A. I. Smolyakov, P. H. Diamond, and M. V. Medvedev. *Phys. Plasmas*, 7:3987, 2000.
- [145] A. I. Smolyakov, P. H. Diamond, and Y. Kishimoto. *Phys. Plasmas*, 9:3826, 2002.
- [146] J. A. Krommes and C. B. Kim. Interactions of disparate scales in drift-wave turbulence. *Phys. Rev E*, 62(6, Part B):8508–8539, 2000.
- [147] J. Anderson, H. Nordman, R. Singh, and J. Weiland. *Plasma Phys Controlled Fusion*, 48:651, 2006.

- [148] J. Anderson and Y. Kishimoto. *Phys. Plasmas*, 14:012308, 2007.
- [149] A. A. Vedenov, A. V. Gordeev, and L. I. Rudakov. *Plasma Phys.*, 9:719, 1967.
- [150] M. A. Malkov, P. H. Diamond, and A. Smolyakov. *Plasma Phys.*, 8:1553, 2001.
- [151] P. N. Guzdar, R. G. Kleva, and L. Chen. *Phys. Plasmas*, 8:459, 2001.
- [152] P. N. Guzdar, R. G. Kleva, and N. Chakrabarti. *Phys. Plasmas*, 11:3324, 2004.
- [153] A. M. Dimits, G. Bateman, M. A. Beer, B. I. Cohen, W. Dorland, G. W. Hammett, C. Kim, J. E. Kinsey, M. Kotschenreuther, A. H. Kritz, L. L. Lao, J. Mandrekas, W. M. Nevins, S. E. Parker, A. J. Redd, D. E. Shumaker, R. Sydora, and J. Weiland. Comparisons and physics basis of tokamak transport models and turbulence simulations. *Phys. Plasmas*, 7(3):969–983, 2000.
- [154] E J kim and P H Diamond. *Phys. Rev. Lett.*, 90:185006, 2003.
- [155] E J kim and P H Diamond. *Phys. Plasmas*, 10:1698, 2003.
- [156] P. H. Diamond, C. J. McDevitt, Ö. D. Gürcan, T.S. Hahm, W. X. Wang, E.S. Yoon, I. Holod, Z. Lin, V. Naulin, and R.Singh. Physics of non-diffusive turbulent transport of momentum and the origins of spontaneous rotation in tokamaks. *Nuclear Fusion*, 49(4):045002, 2009.
- [157] P. H. Diamond, Y.-M. Liang, B. A. Carreras, and P. W. Terry. Self-regulating shear flow turbulence: A paradigm for the l to h transition. *Phys. Rev. Lett.*, 72(16):2565–2568, Apr 1994.
- [158] M. A. Malkov and P. H. Diamond. Analytic theory of L to H transition, barrier structure, and hysteresis for a simple model of coupled particle and heat fluxes. *Phys. Plasmas*, 15(12), 2008.
- [159] P H Diamond, S I Itoh, and K Itoh. *Modern Plasma Physics:Volume 1: Physical Kinetics of Turulent Plasmas*. Cambridge University Press, 2010.

- [160] B. K. Joseph, R. Jha, P. K. Kaw, S. K. Mattoo, C. V. S. Rao, and Y. C. Saxena Aditya Team. Observation of vortex-like coherent structures in the edge plasma of the aditya tokamak. *Physics of Plasmas*, 4(12):4292–4300, 1997.
- [161] T H Stix. *Waves in Plasma*. New York: American Institute of Physics, 1992.
- [162] A. I. Smolyakov and P. H. Diamond. Generalized action invariants for drift waves-zonal flow systems. *Phys. Plasmas*, 6(12):4410–4413, 1999.